

NASA/CR-2002-211438



Transition Documentation on a Three-Element High-lift Configuration at High Reynolds Numbers — Analysis

Arild Bertelrud
Analytical Services and Materials, Inc., Hampton, Virginia

February 2002

The NASA STI Program Office . . . in Profile

Since its founding, NASA has been dedicated to the advancement of aeronautics and space science. The NASA Scientific and Technical Information (STI) Program Office plays a key part in helping NASA maintain this important role.

The NASA STI Program Office is operated by Langley Research Center, the lead center for NASA's scientific and technical information. The NASA STI Program Office provides access to the NASA STI Database, the largest collection of aeronautical and space science STI in the world. The Program Office is also NASA's institutional mechanism for disseminating the results of its research and development activities. These results are published by NASA in the NASA STI Report Series, which includes the following report types:

- TECHNICAL PUBLICATION. Reports of completed research or a major significant phase of research that present the results of NASA programs and include extensive data or theoretical analysis. Includes compilations of significant scientific and technical data and information deemed to be of continuing reference value. NASA counterpart of peer-reviewed formal professional papers, but having less stringent limitations on manuscript length and extent of graphic presentations.
- TECHNICAL MEMORANDUM. Scientific and technical findings that are preliminary or of specialized interest, e.g., quick release reports, working papers, and bibliographies that contain minimal annotation. Does not contain extensive analysis.
- CONTRACTOR REPORT. Scientific and technical findings by NASA-sponsored contractors and grantees.
- CONFERENCE PUBLICATION. Collected papers from scientific and technical conferences, symposia, seminars, or other meetings sponsored or co-sponsored by NASA.
- SPECIAL PUBLICATION. Scientific, technical, or historical information from NASA programs, projects, and missions, often concerned with subjects having substantial public interest.
- TECHNICAL TRANSLATION. English-language translations of foreign scientific and technical material pertinent to NASA's mission.

Specialized services that complement the STI Program Office's diverse offerings include creating custom thesauri, building customized databases, organizing and publishing research results . . . even providing videos.

For more information about the NASA STI Program Office, see the following:

- Access the NASA STI Program Home Page at <http://www.sti.nasa.gov>
- Email your question via the Internet to help@sti.nasa.gov
- Fax your question to the NASA STI Help Desk at (301) 621-0134
- Telephone the NASA STI Help Desk at (301) 621-0390
- Write to:
NASA STI Help Desk
NASA Center for AeroSpace Information
7121 Standard Drive
Hanover, MD 21076-1320

NASA/CR-2002-211438



Transition Documentation on a Three-Element High-lift Configuration at High Reynolds Numbers — Analysis

Arild Bertelrud
Analytical Services and Materials, Inc., Hampton, Virginia

National Aeronautics and
Space Administration

Langley Research Center
Hampton, Virginia 23681-2199

Prepared for Langley Research Center
under Contract NAS1-96014

February 2002

Available from:

NASA Center for AeroSpace Information (CASI)
7121 Standard Drive
Hanover, MD 21076-1320
(301) 621-0390

National Technical Information Service (NTIS)
5285 Port Royal Road
Springfield, VA 22161-2171
(703) 605-6000

CONTENTS

SYMBOLS	4
SUMMARY	6
1. GENERAL	7
1.1 Code validation issues	7
1.2 The role of transition documentation.	8
1.3 Testing in LTPT.	8
1.4 Conditions influencing the experiment	9
1.5 Characteristics of the present experiment.	10
2. DESCRIPTION OF THE TRANSITION EXPERIMENT	12
2.1 Facility and model	12
2.2 Run procedure	12
2.3 Configurations	13
2.4 Repeatability of reference conditions	14
3. METHODOLOGY	15
3.1 Lift coefficients	15
3.1.1 Integrated model pressures	15
3.1.2 Integrated ceiling and floor pressures	16
3.1.3 Balance data	16
3.2 Wake profiles	17
3.3 Pressure distributions	18
3.3.1 Definition of pressure coefficients	18
3.3.2 Mach number distributions	19
3.3.3 Repeatability assessment.	19
3.3.4 Stagnation points and suction peaks	20
3.3.5 Engineering predictions	23
3.3.6 Comparisons with previous tests	23
3.4 Hot film signals	24
3.4.1 Mean bridge voltage	25
3.4.2 Standard deviation	25
3.4.3 Skewness	26
3.4.4 Flatness	26
3.4.5 Scales	26
3.4.6 Phase relations.	27
3.4.7 Cross-correlations	27
3.4.8 Spectra	27
3.4.9 Stationarity	28
3.4.10 Repeatability	28
3.4.11 Transition location	28
4. ANALYSIS OF LOADS	30
4.1 Effect of configuration	30
4.2 Effect of Mach number.	30

4.3	Effect of Reynolds number	31
4.4	Tunnel wall loads	31
5.	ANALYSIS OF MERGED HOT FILM AND PRESSURE DATA	32
5.1	30P/30N Mach=0.2 Re=9 mill.	32
5.1.1	Slat flow	32
5.1.2	Main flow	33
5.1.3	Flap flow	34
5.1.4	Slat cove	35
5.1.5	Main cove	36
5.1.6	Three-dimensional effects	36
5.2	30P/30N Reynolds number effects	36
5.2.1	Slat flow	37
5.2.2	Main flow	37
5.2.3	Flap flow	38
5.3	30P/30N Mach number effects	38
5.3.1	Slat flow	38
5.3.2	Main flow	39
5.3.3	Flap flow	39
5.4	30P/30AD	39
5.4.1	Slat flow	39
5.4.2	Main flow	39
5.4.3	Flap flow	40
5.5	30P/35T	40
5.5.1	Slat flow	40
5.5.2	Main flow	41
5.5.3	Flap flow	41
5.6	Three-dimensional effects	41
5.7	Wake flows	43
6.	CONCLUSIONS	44
	REFERENCES	45
	APPENDICES.	48
A1.	TRANSITION TABLES	48
A2.	IMPLEMENTATION OF EXPERIMENTAL TRANSITION LOCATIONS	57
A2.1	Coordinate systems.	57
A2.2	Experimental flow features	57
A2.3	Interpretation of flow features	57
A2.4	Tables relating surface coordinates to nested coordinates	58
A3.	ASSESSMENT OF EXPERIMENTAL VALIDITY	62
A3.1	Film sheet effect	62
A3.2	Three-dimensionality	63
A3.3	Sidewall mass-flow	63
A3.4	BLT (Boundary-Layer-Traverse) influence	63

	A3.5	Comparisons with previous tests	. . .	64
A4.		LOGBOOK TABLES	65
	A4.1	Hot film records and corresponding pressure data	65
	A4.2	Clean model pressure data	70
	A4.3	Wake data	71
		LIST OF FIGURES	72
		FIGURES	76

SYMBOLS

Alpha,ALPHA	Angle of attack [deg]
ax, az	Bezier coefficient - third power element
bx, bz	Bezier coefficient - second power element
c, C	Chord
cx, cz	Bezier coefficient - linear element
CDinf	Drag coefficient, under infinity (undisturbed) conditions
CDS1	Drag coefficient measured by balance
CDTOT2	Drag coefficient at measurement location, probe 2
Cf	Local skin friction coefficient
CFSP	Wind tunnel wall correction factor
CL	Lift coefficient
CLCOMBO	Lift coefficient, determined through integration of pressure distributions on all elements (centerline)
CLFLAP	Lift coefficient for flap, determined through integration of pressure distribution on flap (centerline)
CLS1	Lift coefficient, determined from force balance
CLSLAT	Lift coefficient for slat , determined through integration of pressure distribution on the slat (centerline)
CLwall	Lift coefficient determined from integrated ceiling and floor pressure distributions (centerline)
CLWBOX	Lift coefficient for main wing , determined through integration of pressure distribution on the main element (centerline)
CMCOMBO	Moment coefficient, determined through integration of pressure distributions on all elements (centerline)
CMFLAP	Moment coefficient for flap, determined through integration of pressure distribution on flap (centerline)
CMS1	Moment coefficient, determined from force balance
CMSLAT	Moment coefficient for slat, determined through integration of pressure distribution on the slat (centerline)
CMWBOX	Moment coefficient for main wing , determined through integration of pressure distribution on the main element (centerline)
CMYS	Moment coefficient (around y-axis), determined from force balance
Cp	Static pressure coefficient
dCL	Lift-coefficient difference
dCp	Pressure-coefficient difference
dMACH	Mach-number difference
dRN	Reynolds- number difference
M,Mach,MACH	Mach number
Mloc	Local Mach number
p	Pressure
Re	Reynolds number
RN	Reynolds number [mill]
s	Coordinate along element surface
slope0(i)	Derivative at (start) point X0,Z0 of Bezier curve i.
slope3(i)	Derivative at (end) point X3,Z3 of Bezier curve i.

t	Bezier parameter, $t \in \{0,1\}$
U	Velocity, longitudinal, variable in Bezier representation
U2	Velocity, longitudinal component, measured with probe 2 on the wake rake.
Ue	Free stream velocity
Us	Wake center velocity defect
V2	Velocity, vertical component, measured with probe 2 on the wake rake
V	Fluctuating voltage
W2	Velocity, transverse component, measured with probe 2 on the wake rake
X0,X3	End point coordinate, Bezier curve
X1,X2	Control point coordinate, Bezier curve
x	Coordinate, longitudinal
y	Coordinate, vertical
Z2	Coordinate in wake, vertical
Z0,Z3	End point value, Bezier curve
Z1,Z2	Control point value, Bezier curve
z	Coordinate, transverse
β	Wake velocity defect
λ	Transverse length-scale
θ	Momentum thickness
ρ	Cross-correlation
ξ	Non-dimensional, transverse coordinate
τ	Time-delay

Subscripts

COVE	Slat or main element cove (lower side, cusp to rear)
flap	Flap conditions
main	Main element conditions
ReattF	Forwardmost limit of reattachment region
ReattB	Rearmost limit of reattachment region
slat	Slat conditions
stagnation	Stagnation point conditions, either element
TrB	Beginning of transition
TrE	End of transition
t	total conditions
U	
∞	infinity

Abbreviations

AD	Analog-to-digital conversion
BLC	Boundary Layer Control
BLT	Boundary-Layer-Transpose (mechanism)
CFD	Computational Fluid Dynamics
LTPT	Low Turbulence Pressure Tunnel
MCARS	Multi Channel Anemometry & Recording System
MDA	McDonnell Douglas Aircraft Company
SIF	Standard Interface Format. File format used for reduced data from LTPT, ASCII/binary or ASCII

SUMMARY

The ongoing High Lift Flow Physics Experiment at NASA Langley Research Center includes experiments on the McDonnell-Douglas LB546 High-Lift model in the Low Turbulence Pressure Tunnel (LTPT). As part of the effort to establish salient flow properties of a two-dimensional high lift configuration for comparison with Computational Fluid Dynamics (CFD) code output, pressure distributions, wake profiles and Reynolds stress profiles were obtained in a series of experiments starting in 1996.

Transition location is another important parameter which, more often than not, is needed as input to CFD codes. To define the transition location (or region) between laminar and turbulent flow, a series of experiments was conducted on the LB546 model utilizing surface hot films.

The present report contains the analysis of the surface hot film data obtained in the LTPT experiment, in terms of transition locations on the three elements. It also includes relevant information regarding the pressure loads and distributions and the wakes behind the model to aid in the interpretation of the transition data. For some configurations the pressure data has been compared with data obtained for the same configurations during earlier wind tunnel entries with the same three-element model.

The methodology used to determine the regions of transitional flows is outlined and each configuration tested has been analyzed and commented. A discussion of the validity of the data due to interference effects, repeatability and three-dimensionality of the flow is included.

The experimental information utilized is available in a database. A separate Contractor Report (Bertelrud and Johnson [1]) describes how to access the database utilizing a set of codes included in the database.

Due to resource limitations only approximately 70 % of the test conditions has been processed and included in reports or database.

1. GENERAL

Prediction of the performance and flow physics of multi-element, high-lift configurations has been the purpose of an extensive effort over the past decades. Early codes combined inviscid panel methods with boundary layer techniques for confluent flows and utilized empirical correlations to arrive at a prediction of the flow properties. While most of these codes were two-dimensional (Goradia & Colwell [2]) some of the early codes were set up to deal with the high-lift problem for infinite swept wings (Dvorak [3]). This approach did not represent the true three-dimensionality since the spanwise gradients were missing, but some of the three-dimensional flow features such as attachment-line transition and the possibility of relaminarization could be taken into account.

While many previous high-lift system designs attained their higher lift performance through the use of up to 5 elements, in the recent past there has been a return to the basic three-element configurations involving a leading edge slat and a trailing-edge flap (Dillner et. al. [4]), and use of new codes based on Navier-Stokes formulations (Dominik [5], Mani and Bush [6]). A combination of larger and faster computers in combination with improved grid generation approaches and more efficient numerical techniques have allowed considerable improvements in reliability. Considerable experience has been gained in utilization of turbulence models, and a large number of models of varying complexity are in use for design purposes.

1.1 Code validation issues

One fundamental issue remaining is the direct validation of the codes; i.e. given the reference conditions, how good is the detailed agreement between physical reality and the prediction? Agreement can be considered in three levels:

- Pressure distributions
- Mean flow
- Turbulence characteristics

Unless all three are validated separately, the comparison is inadequate and inconclusive.

It appears that agreement in pressure distributions (and hence lift coefficients) for most conditions is possible in most cases of interest, i.e. conditions where no massive separation is present. However, Mach number, Reynolds number and configuration change trends may not even be of the correct sign if the local flow (mean flow and turbulence) is not understood.

Experimentally, documentation of the mean flow properties such as measurement of velocity profiles is feasible but due to practical limitations associated with testing time they are in general carried out for a limited number of points on the model. Transition from laminar to turbulent flow is an important parameter, since it determines both the sensitivity to separation for the flow on the elements, as well as having a profound influence on the characteristics and strength of attached and separated shear layers. The question of possible spanwise non-uniformity of transition, compressibility, longitudinal curvature and lateral convergence/divergence are important both for the evaluation of the two-dimensionality of the experiment as well as for the choice of equations to use and turbulence models to employ.

The turbulence models used in the codes quite often contain non-physical or hard-to-measure parameters, adding to the complexity of validating the computational methods. Most often it is virtually impossible to determine whether the experiment or the computational trend (or both) are wrong, since the amount of information describing the experimental flow conditions, in general, is too limited.

Throughout the years a series of experimental investigations have been conducted to provide data for code validation, see e.g. Djatmiko et.al.[7], Pocheron and Thibert [8]. In addition to the ongoing discussion of the applicability of two-dimensional testing to three-dimensional high-lift configurations (Butter [9]), there are overriding problems regarding Reynolds number and other scaling effects and limitations in the amount and quality of data that can be obtained in wind tunnel tests. Reynolds number differences can be expected to both change the type of flow phenomena encountered (e.g. transition or laminar separation) as well as alter the quantitative values for a phenomenon. Thus the size and shape of separated regions along with boundary layer thicknesses are expected to change when the Reynolds number is changed.

1.2 The role of transition documentation

One of the critical issues is knowledge of the transition location for the flow on both sides of each element. Currently this is commonly used as input in the codes, and is thus a critical element for code validation. If (or rather when) there are disagreements between the measured and predicted flow, great care must be exercised in judgment whether the mean flow representation and/or turbulence modeling causes the discrepancy.

In the present report two approaches to the data are taken:

- Documentation of transition locations for use as input to computational codes. Providing a transition region definition allows the user of the data to make an interpretation depending on the type of modeling used.
- Description and discussion of the flow properties of value for a physical interpretation of the flow fields and flow field differences between configurations known to have differences in performance.

1.3 Testing in LTPT

For close-to-flight Reynolds number testing, the Low Turbulence Pressure Tunnel (Figure 1) at NASA Langley has been used extensively, see e.g. Paschal et.al. [10]. Over the past years a variety of different configurations have been examined. It is therefore important to have a clear definition of which models (hardware) and riggings were used in each of the tests.

Some related experiments in LTPT with the same or similar models may be of interest:

Nakayama, Kreplin and Morgan [11] made extensive documentation of the mean flow field and turbulence characteristics for a similar model, with emphasis on the effects of BLC. Valarezo et.al. carried out an optimization experiment [12].

Chin, Peters, Spaid and McGhee [13] presented results for the same physical model and the same riggings.

Mani and Bush [6] performed computations on the model at Mach=0.2, Re=9 mill, as used in a NASA Computational workshop in 1993.

Dominik [5] dealt with the same model, but used different notations for the riggings (A=30P/30N & B=30P/30AD).

Most experiments performed in the LTPT facility have been aimed at performance optimization. In the present test the target has been to explore the flow characteristics of configurations not necessarily being the best but with similar flow features as an optimum configuration.

The three configurations chosen for the current experiment were close to optimum regarding high lift performance, and thus the variations in terms of transition locations may not be excessive. This is, in particular, the case on the suction side of the elements, where the adverse pressure gradients are so large that the transition region lengths are very short and can be expected to be driven by the pressure gradient.

One aspect of interest is whether a separation bubble exists close to the suction peaks. While transition to turbulent flow in general is advantageous (since the turbulent layer can tolerate a higher pressure gradient before it separates), an excessive turbulent run length may also cause a problem since a thicker layer is more prone to separate than a thin one.

The two scaling parameters of primary interest for the investigation are the Reynolds number and the Strouhal number. For atmospheric tunnels, the upper limit in Reynolds number often is 3-4 million. For the current 22-inch model, atmospheric runs corresponds to Re=2.6 million. If this model were representative of a 14 ft. chord airplane wing, testing in LTPT at a full scale Reynolds number of 20 million could be accomplished but the unsteady shedding from the elements would be significantly different. Since the model would be 1:7.5 of full scale the shedding frequencies would be almost an order of magnitude too high (Bertelrud and Liandrat [14]). As a consequence the model test might exhibit flow features not existing in flight and vice versa.

1.4 Conditions influencing the experiment

While an experiment in LTPT provides a very high Reynolds number, and thus should be reliable from the point of Reynolds number scaling, there are several issues that need consideration for an assessment of the experiment as a code validation tool. Among these are:

- wind tunnel wall effects/three-dimensionality.

While sidewall suction can alleviate the problem to some extent (as has been done in the present experiment through adjusting the amount of suction to yield small spanwise pressure gradients at 16 degrees angle of attack), there will always be a three-dimensional effect that has to be considered when drawing conclusions. This has been discussed in Appendix A2 on how to interpret the data for Navier-Stokes computation usage.

- wind tunnel turbulence.

It is a well-known phenomenon that the flow is affected by wind tunnel turbulence level, length scale and structure; it is not always true that a low turbulence level in a wind tunnel corresponds to a late transition. Both level and anisotropy depend on the streamwise location in the test section, and a high-

lift configuration close to maximum lift also may alter the turbulence characteristics from the empty-tunnel values. Depending on the scale of separated regions or vortices, significant interactions may exist.

-model scale.

High-lift configurations contain several sources of organized vortex shedding, as indicated above. The most dominant may be assumed to be the transverse vorticity streets mentioned previously, assumed to emanate from the slat cove and the main element cove, as well as possibly from the flap (Kreplin and Höhler [15], Savory and Toy [16]. (i.e. Karman street) These scale with the Strouhal number rather than the Reynolds number, and in the current analysis an effort has been made to assess the existence of transverse shedding.

The other type of vorticity of concern is the longitudinal vortices emanating from brackets etc. These presumably interact with the quasi-two-dimensional flow field, and may in fact increase the indicated lift coefficient, since longitudinal vortices, in general, are advantageous (vortex generators on wings). However this type of spanwise non-uniformity is almost impossible to characterize in this type of an experiment, and the best one can do is to try keeping the sensors away from bracket wakes etc.

-surface roughness/imperfections.

Depending on the unit Reynolds number of the tunnel and the surface finish of the model, this may cause a discrepancy from full-scale flight conditions. In the present experiment the surface roughness of the model is not known. However, the main roughness effect can be anticipated to be caused by the hot film sheet with its sensors and leads. Two different issues are of concern: whether or not the roughness causes transition and on the other hand whether the leads make the turbulent boundary layer a rough one. Both issues are discussed in Appendix A3.

Several of the factors described will influence the flow situation at any given time, and as discussed in Appendix A3 (in particular A3.5), the flow three-dimensionality in particular close to stall is influenced by separated regions in the upper surface flap corners. The flow may be steered in one or the other lateral direction depending on minute changes in the flow conditions. This directional effect influences both the measured flow properties locally (i.e. at the 74 % span location where the hot films and Reynolds stress measurements are done) as well as the integrated center line values.

A large number of experiments have been carried out to serve as guidance in the assessment of code performance. In general, the pressure distribution has been used as the common denominator between experiment and computations. This is due to both the fact that the static pressure is readily measurable with common instrumentation, and also that to obtain agreement in terms of pressure distributions is not too hard.

If the requirement for comparison is extended to mean velocity profiles, the job is much tougher. Yet this is a requirement for comparison before the performance of turbulence models can be assessed.

1.5 Characteristics of the present experiment

In the present experiment, the pressure distributions are used along with several statistical properties of the hot-film signals to assess the flow conditions. The films define a transition region, but the statistical parameters do not give all details of interest. Therefore the information is augmented in certain cases by cross correlation function estimates to assess whether flow is turbulent or separated and also which

direction the flow is moving. In addition spectra occasionally have been used to evaluate how fast the turbulent layer is developing and whether any particular frequencies can be identified in laminar, transitional and turbulent regions.

Throughout the analysis, it is necessary to bear in mind the deficiencies of the hot film systems (a nearly unknown transfer function for the dynamic signals). The Constant-Temperature-Anemometry used has been verified up to 20 kHz information frequency (50 kHz sampling rate), but as in most experiments the actual response of individual films to flow dynamics is not verified. The approach therefore is to assume that the response of adjacent films and for all films in general is the same. Through analogies, it is possible to make a judgment as to whether or not there is a big difference between sensors; i.e. to what extent the data provides space-correlations of value.

2. DESCRIPTION OF THE TRANSITION EXPERIMENT

This chapter contains a limited description of the experiment, as needed to utilize the transition information provided. The separate database report contains a comprehensive description of the experiment to the extent needed for further analysis of the experimental database.

2.1 Facility and model

The hot film experiment and the subsequent Reynolds stress experiment are designated 397 in LTPT's system and LB546k in (McDonnell-Douglas) MDA's nomenclature. Here LB546 is the model name and the letter k designates the tunnel entry in question. The test was conducted between August 5 and August 21, 1996 with the model mounted in the wind tunnel in the traditional manner, centered on turn tables containing the suction boxes.

The model consists of the LS12 slat, the W10BB wing box assembly and the F22 flap. The model has pressure taps mainly in the mid-span region of the three elements, with one additional chordwise row on the flap close to the hot film location. Four spanwise rows exist, one on the slat, one on the main element and two on the flap. Figure 2 illustrates the location of the pressure tap rows.

The 350 hot films were located in a single row at 74 % span (Figure 3).

The MCARS (Johnson and Bertelrud [17 , 18]) anemometry system was used. This system allows 14 surface hot films to be operated simultaneously, and has internal switching capability between seven groups (banks) of films. This means that 98 films may be run without modifying the physical hookup. In the test the wind tunnel conditions were kept constant while three different hookups were utilized. until, $3 \times 98 = 294$ films were used.

Throughout almost the entire experiment, the 294 films of highest importance for transition detection were used. In the very last part of the test (see below) films located in the slat and main cove regions were hooked up to explore these regions and if possible determine reattachment regions. Some details regarding the hot film system is found in a separate report describing the database (Bertelrud and Johnson [1]).

2.2 Run procedure

The runs were made at fixed angles-of-attack: 4, 8, 10, 12, 16, 19, 21, 22 and 23 degrees. Due to the amount of time involved in setting proper sidewall venting, and commensurate with common practice in LTPT, the sidewall suction was applied to make the spanwise pressure distributions uniform only at 16 degrees. At lower and higher angles the sidewall suction settings remained at the values chosen for the 16-degree configuration. This resulted in some spanwise non-uniformities at the angles-of-attack close to stall. Most atmospheric facilities employ sidewall control adjusted for each angle of incidence.

In addition runs were made where the model was swept continuously through the angle-of-attack regime. The data has been included in the database, but is not discussed further here.

After a polar (a series of angle of attack conditions) had been tested, the hot film system was changed to handle another set of 98 sensors, and the angle-of attack sequence was repeated.

2.3 Configurations

The configurations are defined through combinations of deflections, gaps and overhangs for the slat and flap elements, as follows (Figure 4):

Configuration	SLAT			FLAP		
	Deflection, deg	Overhang, %	Gap, %	Deflection, deg	Overhang, %	Gap, %
30P/30N	30	-2.5	2.95	30	0.25	1.27
30P/30AD	30	-2.5	2.95	30	0.25	1.50
30P/35T	30	-2.5	2.95	35	0.00	0.95

The configurations (riggings) used were done in the following sequence:

- 30P/30N was tested through the available Mach number and Reynolds number regimes. Some repeat runs were made and also some angle-of-attack sweeps. Standard hot film sensor selection was used.
- 30P/30AD was tested at the standard condition (Mach=0.2 at Re=9 million) plus one extra Mach number and Reynolds number regimes. Standard hot film sensor selection was used.
- 30P/35T was tested at two Reynolds numbers. Standard hot film sensor selection was used.
- 30P/30N was tested at the standard conditions. The cove sensor selection was used.

In Chapter 5 on results, the data from the two sets of 30P/30N data have been merged. Figure 5 illustrates the Mach number versus Reynolds number combinations run for the different configurations. 30P/30N and to a lesser degree 30P/30AD were tested to explore both Reynolds number and Mach number trends, while only Reynolds number was explored for 30P/35T.

In addition to the hot film runs, pressure data from the two subsequent tests have been included in the present report, since they serve as comparison information to the transition data set:

- 30P/30N was tested at standard conditions (Mach=0., with bare model; i.e. the film sheet was removed. This data set serve as baseline for configuration performance.
- 30P/30N was tested at standard conditions, with bare model as above, but with the Boundary Layer Traverse (BLT) present.
- 30P/35T was tested at limited conditions, with bare model as above, but with the Boundary Layer Traverse (BLT) present.

During some of the hot film runs, the wake rake mounted behind the model was used to determine the wake profile. This has been included in the database, and some results are included in the present report.

Appendix A4 contains an account of the run and point numbers for the various sets of data. It serves as a guide only, primary information is found in the database access codes.

It should be noted that due to cost- and time constraints only 2/3 of the data acquired has been analyzed. It is available in raw, binary form in the database, but no processed files exist.

2.4 Repeatability of reference conditions

In order to combine data from several points, it is necessary to have some knowledge of the repeatability in reference conditions. In particular the angle of attack is critical. There was a concern that the use of three connector sets to gather the required amount of data from $3 * 98 = 294$ hot films would cause problems due to the repeatability of the angle-of-attack parameter. A series of tests from the initial series showed that the repeatability of angle-of-attack was satisfactory (data gathered with varying connector set and constant angle-of-attack compared well with data gathered when the connector set was retained and the angle-of-attack changed). The latter procedure became the standard operating procedure since it offered substantial time saving and a more reliable accounting of which connector set was hooked up at any given time.

Consider the repeatability of angle-of-attack, Reynolds number and Mach number, exemplified by the 30P/30N data, throughout the entire Mach number Reynolds number and angle-of-attack regime. The data set for these parameters is shown in Figure 6a and 6b. The average, root-mean square deviations and maximum difference for the separate parameters are:

	Mean	Standard deviation	Max. difference
Mach number	0.0005	± 0.0010	± 0.003
Reynolds number	-0.02 %	$\pm 0.58 \%$	$\pm 2 \%$
Angle-of-attack	0.0025 deg	± 0.0094 deg	± 0.03 [deg]

No regions of particularly large deviations could be identified, as the plot as function of angle of attack shows (Figure 6b).

The numbers above are valid for repeatability only - it can be anticipated that the accuracy of the parameters is considerably different. Experience in other tunnels indicate that there may be subtle differences in the way the tunnel flow conditions result in differences in the performance, especially close to maximum lift.

The tunnel calibration factor, CFSP, which is a measure of the sidewall suction mass flow, is mainly a function of Reynolds number as Figure 6c illustrates. There is a Mach number dependence, but (not shown) no clear trend with angle-of-attack. The latter is to be expected since the setting was not changed with angle-of-attack.

3. METHODOLOGY

This chapter describes the different flow features examined, and their determination. Information for the standard configuration, 30P/30N at Mach=0.2, Reynolds number = 9 million. is used to illustrate the information. Figure 7 illustrates how different parts of the experimental information from the pressure measurements on the model, on the tunnel walls, and in the wake are combined with balance data to create checks and provide redundancy in the measurements.

All data used was extracted from ASCII SIF-files provided by standard LTPT wind tunnel data reduction. No wind tunnel correction has been applied to the integrated coefficients.

3.1 Lift coefficients

There are three separate sources of lift coefficient available: integrated pressure on each of the three model elements, integrated ceiling and floor pressure, and balance lift data.

3.1.1 Integrated pressure from model pressure taps

The lift coefficients are based on the customary integration of the pressure data in the data reduction of LTPT. The lift coefficients are determined as a sum of all elements as well as separately for the slat, the main element wing box and for the flap element (CLCOMBO, CLSLAT, CLWBOX and CLFLAP). The force data is also available in the SIF files. The moment coefficients were also available in the database (CMCOMBO, CMSLAT, CMWBOX and CMFLAP), but they have not been used in the present analysis.

It is possible to examine Reynolds number, Mach number, configuration effects, and affected elements by the plotting the force polars. Cases where global effects are observed can then be examined in more detail.

Figure 8 shows an example of repeatability for the lift coefficient as function of angle of attack for the entire configuration (CLCOMBO). Figure 9 shows the repeatability in lift coefficient for the three elements, the slat, the wing box (main element) and the flap. In the figures data from 30P/30N, Mach=0.2, Re=9 million is used, illustrating three identical polars, 7 through 9, and can be seen as an indication of the typical repeatability for integrated pressures.

Also shown are the integrated lift coefficients from the current tunnel entry (dashed) taken without the hot film sheet present. There is a difference throughout the angle-of-attack regime, getting significant above 19 degrees. Figures 9a and b indicate that the effect is due to both the slat and the main wing element. The influence of hot film sheets is discussed further in Appendix A3.

This effect is important as it changes the maximum lift and also the angle of attack for maximum lift. It also changes stall behavior dramatically, presumably due to transition effects.

3.1.2 Integrated ceiling and floor pressure taps

As a separate check of the information from pressure taps on the model, a technique often used in early wind tunnel testing for estimation of lift coefficients and performance optimization has been used. The pressure distributions on the ceiling and the floor are used to estimate the overall lift coefficient. Figure 10 shows an example of the distributions found for various angles of attack. Note that the lift created by the model is spread over 7 chords length on the tunnel walls and the shape of distributions on the walls do not change appreciably as the angle-of-attack is varied.

In Figure 11 this pressure information has been integrated, scaled by the projected nested chord (i.e. divided by $\cos \alpha$), and is denoted CLwall. Data from two subsequent polars can be seen. The agreement is fair between the two techniques for the entire configuration, as can be expected. It appears that trends in the CLCOMBO data are detected also in the CLwall data. Thus the integrated ceiling and floor static pressures is a data set of measurements independent of CLCOMBO and is suitable for use in trend analysis where it is critical that erroneous pressure tap information is properly handled.

3.1.3 Balance data

The configuration was mounted on a balance, and although usually not considered as accurate as the integrated model pressures, it provides the third independent set of data for use in the analysis. The lift coefficient in the SIF-files is denoted CLS1.

The balance data also includes a drag coefficient, CDS1. Since the lift coefficients for high-lift experiments are high, the accuracy of the drag measurement traditionally is considered inferior. Note that while the integrated pressure could provide a pressure drag (which theoretically is zero, d'Alambert's paradox) and the wake measurement can be interpreted as viscous drag, the balance data should be the combination of the two.

Figure 12 illustrates balance drag polars for 30P/30N at the nominal conditions, Mach=0.2, Re=9 million, for the three repeat polars discussed earlier. The comparison with data for the clean configuration provides the expected result that the drag of the clean configuration is significantly lower throughout the angle-of-attack regime.

The moment curves for the configuration are also of importance for practical use of the data. In the present experiment, it is a measure of the pressure distribution on each element, and the combination, CMCOMBO, can be compared with the corresponding balance moment coefficient. Note that the SIF-files contain the pressure-integrated moment coefficients at the leading edge, while the balance moment coefficient, CMYS1, has been referred to the 25% chord point.

Illustrated in Figure 13 is the lift-moment polar of integrated pressure (CLCOMBO and CMCOMBO) for cases throughout the Reynolds number regime. No significant trends are visible. Comparison with the balance data reveals a significant difference (Figure 14) both between pressure and balance data as function of angle of attack as well as in repeatability for the balance data. The integrated pressures appear much more repeatable than the balance data.

The SIF-files also includes the information for each element, as shown in Figure 15, allowing judgment regarding any movement of center of pressure for each of the elements.

3.2 Wake profiles

The wakes behind the configuration elements are important diagnostics of the flow characteristics on each element (Bertelrud and Ljungström [19]) and for an assessment of element interaction. The wake behind the configuration provides an overall performance characterization. It is convenient to probe the wake at a location several chords behind the trailing edge (far wake) since recovery of downwash and static pressure make both the measurement and its interpretation much easier.

In the present experiment, the wake profiles were obtained using a traversing rake with two 5-hole probes located 4 inches apart (vertical direction) at midspan. The entire rake was traversed vertically, taking a data point every 0.2 inches. Depending on the angle-of-attack and flow condition, the measurement range was adjusted to cover the entire wake. For most of the figures in the present report, probe 2 was used, since it was considered to have the best calibration and covered the entire wake region.

Figure 16 shows the horizontal (longitudinal or streamwise) component of the non-dimensional velocity, U_2 , as a function of the vertical coordinate Z_2 for a set of wakes behind the configuration 30P/30N at Mach=0.2 and Re=9 million. The velocity components U_2 , V_2 and W_2 are non-dimensionalized by the tunnel reference velocity. The wake shape is nearly symmetric at this location, and the main effect is a vertical displacement. $Z_2=0$ The center plane of the wind tunnel corresponds to $Z_2=0$. The figure shows the typical overall velocity gradient in the flow field behind a configuration with circulation. Over the 12-inch high measurement region the free stream velocity changes by roughly 5% of the tunnel reference velocity.

For wakes it is common to non-dimensionalize the velocity defect by the maximum velocity defect and use $\beta=U_s/U_e$ as a wake characteristic (Tennekes & Lumley [20]), where U_s is the maximum velocity defect:

$$U_s = (U_{e,c} - U_c) / U_e$$

Here $U_{e,c}$ = velocity at wake centerline (Z_c) (interpolated, $\approx U_e$)

U_c = velocity at wake centerline (measured)

The vertical coordinates of the wake are transformed to a coordinate system centered at the maximum velocity defect and scaled by the integral properties of the wake.

Assume a simple, Gaussian wake shape $f = [U_e - U] / U_s = \exp(-0.5 \xi^2)$ where ξ is a transverse coordinate and U is the local velocity in the wake. For a plane wake, the transverse length scale, λ , is then defined by:

$$\lambda / \theta = 0.398 / \beta \quad \text{where } \theta = \text{momentum thickness of the wake}$$

The non-dimensionalized transverse coordinate system is given using

$$\xi = (Z - Z_c) / \lambda$$

Figure 17 shows two of the wakes of Figure 16 non-dimensionalized. It is seen that this configuration has near-gaussian shape wakes irrespective of angle-of-attack. This non-dimensional representation makes it easier to draw conclusions from the wake data, since symmetry estimates and self-

preservation predictions can be made. Note that the coordinate $|\xi| = 3$ corresponds to 1 % of the velocity defect remaining and for practical purposes can be regarded as the wake width.

The vertical component (or downwash) V_2 is shown in Figure 18 as function of the non-dimensional distance (vertical location scaled by the integral length scale). In terms of downwash, the values of V_2 indicate flow angles at this streamwise location varying from 6 to 8 degrees as the angle of attack increases from 4 to 16 degrees, compared with a downwash on the lower side of the wake of roughly 5 degrees.

Figure 19 shows the transverse component, W_2 , also non-dimensionalized by the tunnel reference velocity. The values are small, and the accuracy may be in question for the velocity component in the transverse direction. However, the interpreted skewing through the wake is of order 1 degree for centerline measurements in the nominally two-dimensional experiment.

The drag coefficient evaluated in the LTPT wake data reduction scheme and available in the SIF files, CDTOT2, and the value determined from the wake profiles integrated and related to the far field using Squire-Young's equations [21] , CD_{inf} , are shown in Figure 20. There is a general agreement between the results from the two data reduction techniques. Also, it appears that the hot film sheets (located between 74 % span and the sidewall) have negligible effects on the viscous losses at the model centerline.

3.3 Pressure distributions

The pressure distributions were obtained to:

- allow assessment of stagnation points and suction peaks.
- verify the configuration performance.
- compare with earlier tunnel entries in LTPT with the same configurations.

3.3.1 Definition of the pressure coefficients

Three different definitions of the pressure coefficients are used:

- The standard procedure used in earlier test entries, where each pressure is corrected for the vented mass flow. This definition is denoted: *standard*.
- A coefficient based on the measured pressure; i.e. no tunnel correction (CFSP=1). This definition is denoted: *original*.
- A coefficient based on the assumption that the value of the total pressure at the slat stagnation point is representative of the total pressure for the wind tunnel. Since the stagnation points on the other elements and any reattachment points will be subject to viscous losses as well as possible shocks, their stagnation pressure will be lower than that of the slat. This definition is denoted: *slat special*.

In the access code used for analyzing the pressures, any of these definitions of the pressure coefficients can be used. In the present report the standard procedure for evaluation of LTPT data is used (CFSP>1). Normally the difference is small, and problems usually arise only in the stagnation regions of the three elements if the measured pressures need to be interpreted as Mach numbers. Figure 21 shows typical differences between the standard and original values for the pressure distributions in the suction peak region of the main wing where the differences are the largest. In this example, the

differences are minor, and the only problem would be interpretation of the stagnation region Mach number distribution. In an approximate sense, since the reference pressure is the main difference between the three techniques, the differences amount to shifting the curves vertically.

3.3.2 Mach number distributions

At any given point the local Mach number is given by the ratio of total pressure and static pressure. Upstream of the model, the total pressure is approximately constant. However, due to the finite size of the wind tunnel, there will, in general, be a varying static pressure.

In the data reduction procedure of LTPT, a total pressure rake output is combined with a static pressure measurement at a somewhat different location. The tunnel reference Mach number is determined from the two. However, if the static pressure somewhere else is used, the reference Mach number would be given differently. Figure 22 illustrates that although the floor and ceiling Mach numbers range from 0.15 to 0.25, the reference Mach number would change very little if the average of the ceiling and floor pressures of Figure 22 were used.

Although the reference Mach number is approximately 0.2, the local Mach numbers on the elements can be much higher, and as seen in Figure 23 can reach 0.75 on the slat at 16 degrees angle-of-attack. For maximum lift coefficients, the highest Mach number is close to 1. This means that not only will the total pressure over the main and flap elements be influenced by viscous losses, but may also have shock losses included. The only location free from any of these losses would be the stagnation point of the slat. With a reference Mach number of 0.2, this coefficient should be $C_p = 1.010$. This in turn determines the appropriate reference pressure for the tunnel, and is the basis for the *slat special* data reduction mentioned in the previous section.

3.3.3 Repeatability assessment.

The hot film data was obtained during (at least) three polars where conditions were repeated (See 2.4), and through observation of the repeatability, the reliability of the transition data can be estimated. Previously the repeatability in terms of overall loads was discussed. For the transition location data it is important to also make an assessment of the repeatability of pressure distributions. Figures 24a and 24b show examples of good repeatability, indicating that there is a small shift in level for both the main element and to some extent also on the flap. The main element pressure distribution appears to indicate an angle of attack decrease from Point 65 to Point 74. However, the measured angle of attack does not confirm this, and also the trend in pressure change on the flap is opposite of what an angle-of-attack change would give, so the reason for the variation is unclear.

Figure 25 shows the typical deviations for the entire main element. It is clear that the deviations are the largest in the suction peak region. The deviations in the figure could not be attributed to an angle of attack change or to any of the reference parameters, Mach number and Reynolds number.

In the current analysis of hot film data, the experimental pressure distributions from the first polar of each case was used, since no systematic difference due to sequence could be detected.

3.3.4 Stagnation points and suction peaks

The tunnel Mach numbers were 0.15, 0.2 and 0.23. If the measured pressures are interpreted as Mach number, it is clear that the local flow is compressible in many of the cases. At high alpha the flow at the suction peak of the slat is sonic or slightly supersonic for Mach=0.2 and 0.23, compressible over the main element and in general incompressible over the flap.

Figure 26 illustrates the relation between the local Mach number and the pressure coefficient, assuming perfect gas and a full total pressure at the stagnation point. This is true for the slat but as previously mentioned a rough approximation on the main element and the flap where viscous losses cause a lower stagnation pressure.

To determine the location and pressure at the stagnation points accurately, it is necessary to transform the pressures to Mach numbers, as described earlier.

The Mach number distributions and the stagnation and suction peaks were determined as follows (details given in the database report), utilizing measured pressures rather than regression analysis.

Stagnation point:

There is a need to determine both location and pressure at the stagnation point accurately, since even small errors will cause a velocity distribution unsuitable for boundary layer computations.

In Figure 27, the measured pressure in the slat stagnation region is illustrated for 16 degrees angle-of-attack. The stagnation point is the point where the dividing streamline intersects with the element. It is a physically well-defined location, since any streamline above it will pass on the suction side of the element, and any streamline below it will pass on the pressure side of the element. However, the pressure distribution around the stagnation point does not exhibit any sharp peaks, and hence is difficult to determine accurately from the pressure coefficients.

As Figure 27 illustrates, the possible stagnation region is fairly large, of order 2 % chord since it is unknown on which side of the maximum measured pressure the stagnation point is located. The Mach number distributions based on either the standard, original or slat special definition of the pressure coefficient are determined. Figure 28 illustrates how the distributions are interpreted, using a simplified version of the technique for swept wings described in (Bertelrud & Graves [22]). Using the Mach number with an opposite sign for all positions on the lower side of the maximum pressure, the minimum Mach number may either be positive or negative.

Figures 28a through 28c shows the interpretation of the information for the three elements. The open symbols are the values of Mach number, without taking the flow direction into account, $|\text{Mach}|$. The smaller filled symbols takes into account the flow direction - Mach numbers that for certain are located below the stagnation point, are negative.

The highest measured pressure is also converted to Mach number, either positive or negative (triangle). (If the chosen pressure coefficient definition is incorrect, the Mach number may be non-physical.) The true stagnation point must be located between a line between points of both sides of the maximum pressure point and in the other end the low Mach number (stagnation. point) that does not cause an inflection in Mach number distribution at the stagnation point.

The results indicate a considerable improvement in stagnation point determination.

The following procedure can be implemented in a data reduction code and be used to determine the stagnation points on the elements:

- A. Determine the local Mach number for each pressure value, assuming the total pressure coefficient to be the ideal. Do not use the highest measured pressure, as described above the true stagnation location will be on either side of it.
- B. Change sign for the Mach number below the highest measured pressure.
- C. Make a curve fit through the points, either a straight line fit through adjacent points to the 'stagnation. This determines the LOCATION of the stagnation point.
- D. For the slat stagnation point the pressure coefficient, C_{pt} , is assumed given by $p_t/p_\infty = (1 + M_\infty^2)^{3.5}$ and $C_{pt} = (p_t/p_\infty - 1)/(0.7 M_\infty^2)$.
For the Mach number range 0.15 to 0.23 this means $C_{pt, stagnation} = 1.0056$ to 1.0133 .

For the main element and the flap, the values are found by using the measured pressures only, since there is no certain way of estimating the coefficient at stagnation, a priori. In these cases the stagnation pressure is determined as an average of using points ahead of and behind the stagnation point, making a polynomials going through zero slope at the stagnation point location.

The suction peak:

The exact value is not as critical as for the stagnation point, but the location is critical since it determines the run length for a laminar boundary layer under an adverse pressure gradient.

The suction peak is determined through a similar approach where a Bezier curve is used based on the value and slope of the Mach number curve upstream and downstream of the lowest pressure measured.

To represent the pressure distribution and in particular the suction peak, it is necessary to interpret the measured pressures to obtain smooth curves usable for engineering estimates. The computational model of the high-lift elements usually have an order of magnitude better resolution than the experimentally determined pressures. Since boundary layers and separations in general are sensitive to the pressure distributions and the changes in pressure gradient, a smooth interpolation routine is needed.

The interpolated curve should go through the measured data, since the measurement accuracy often is very good, and certainly better than a regression fit.

Bezier curves [23] are used for the present data, and experimental data is handled as function of s/c , as before.

A Bezier curve with continuity in function value U (pressure coefficient, Mach number or velocity) is defined over the interval $s/c (i)$ to $s/c (i+1)$ through experimental tap locations and measured values of the parameters:

coordinates: $X0 = s/c (i)$ and $X3 = s/c (i+1)$

and velocities: $Z0 = U(i)$ and $Z3 = U(i+1)$

as well as the slopes at the end points $(X0, Z0)$ and $(X3, Z3)$ respectively.

The Bezier curve goes through the end points, 0 and 3, and have two control points, 1 and 2, guiding the curve. Figure 29a illustrates the suction peak on the main element for 30P/30N at Mach=0.2, Re=9 mill, Alpha=16 deg.

Depending on the measured points available and the purpose of the interpretation the slopes may be chosen using one of several different techniques.

The following choice provides continuous slope :

$$\text{slope0}(i) = [U(i+1) - U(i-1)] / [s/c(i+1) - s/c(i-1)]$$

$$\text{slope3}(i) = [U(i+2) - U(i)] / [s/c(i+2) - s/c(i)]$$

The coefficients in the Bezier curve are given by

$$cx = X3 - X0$$

$$cz = cx \text{ slope0}(i)$$

$$bz = 3.0 (Z3 - Z0) - cx \text{ slope0}(i) + \text{slope3}(i)$$

$$az = Z3 - Z0 - bz - cz$$

Since s/c (unlike x/c) is monotonously increasing, the control points can be chosen so that sharp corners and multiple value curves are avoided. The control points do not need to be evaluated to generate the Bezier curve, but are given below for reference:

$$X1 = X0 + (X3 - X0) / 3 \quad \text{and} \quad X2 = X0 + 2 (X3 - X0) / 3$$

$$Z1 = Z0 + \text{slope0}(i) (X3 - X0) / 3 \quad \text{and} \quad Z2 = Z3 - \text{slope3}(i) (X3 - X0) / 3$$

The value of velocity, pressure or Mach number at any s/c position are found from:

$$t = [s/c - s/c(i)] / cx$$

$$U = az t^3 + bz t^2 + cz t + U(i)$$

The first and second derivatives with respect to s/c are very simple since t is proportional to s/c:

$$dU/d(s/c) = [3 az t^2 + 2 bz t + cz] / cx$$

$$d^2U / d(s/c)^2 = [6 az t + 2 bz] / cx^2$$

As mentioned above, the parameter to be fit may be either Cp, Ue or Me.

Figure 29b shows the suction peak of the interpolated pressure distribution curves for 30P/30N. The figure shows a segment of the curve, including the control points. As described earlier, the Bezier curve is chosen to with a requirement on the slope of the curve at the measured points. The curve can be described by any number of distinct points.

there is a need to emphasize that different spanwise locations of midspan pressure taps and quarter-span surface hot films.

In Figure 33 the difference between test g and k has been explored for three angles of attack. The differences are, as will be shown later, of the same order as the repeatability from run to run.

Another matter of interest is the question whether or not Reynolds number trends are consistent from test to test. This has been explored in Figures 34a through 34c, for the angles 8, 16 and 19 degrees angle of attack, where the difference between pressure distributions for the main element at $Re=5$ mill. and $Re=9$ mill. have been determined from tests g and k separately.

As an example, Figures 34a and 34c indicate a consistent pattern for the tests at 8 and 19 degrees while Figure 34b indicates that there is a slight level shift upper rear for 16 degrees and some discrepancies close to the suction peak. However, in all three cases the differences are small compared with the repeatability within each test and the accuracy of measurement. Thus, as far as the transition measurements are concerned, the pressure distributions appear repeatable. Regarding the overall flow characteristics in the tunnel, these are discussed further in Appendix 3.5.

3.4 Hot film signals

In this section a description is given of the hot film signal features studied in order to determine the transition locations on the different elements. The statistical information for each of the sensors was, in general, obtained as the average of 8 to 15 1024 sample data sets, taken over at least 6 seconds for each angle of attack. 30P/30N information is given as examples of the types of data utilized.

Figures 35a through 35c illustrate the pressure distributions on the three elements, since information regarding the local pressure gradient is essential for any estimate of flow behavior. The portion to be used with the hot film data is re-plotted in Figure 36a-36c for $s/c=-0.02$ to 0.10. Note that all plots for the hot films are made in terms of s/c rather than x/c .

On the slat the 8 degrees case (as well as 4 degrees, not shown) is distinctly different, since it does not show a suction peak. Also, at high angles of attack, the slat has very high-pressure coefficient, increasing with angle of attack. The main wing shows similar trends, although not as strong. However, already at 8 degrees there is a strong suction peak present.

In contrast, the flap has the highest suction peak at low angles of attack. As the angle of attack increases, the load on the flap gradually is relieved.

The anomaly at the slat suction peak is believed to be caused by damage at one of the taps; it tracks the rest of the pressures but with a shift.

The graphs are organized as follows - in all cases the information concerns 30P/30N at Mach=0.2, $Re=9$ million, $\alpha=8, 16$ and 19 degrees:

Content	Slat	Main	Flap
Pressure distribution - overall	35a	35b	35c
Pressure distribution	36a	36b	36c
Standard deviation	37a	37b	37c
Skewness	38a	38b	38c
Flatness	40a	40b	40c

3.4.1 Mean bridge voltage

The value of the mean bridge voltage is a measure of the wall shear. However, it is not accurate and requires individual film information to be utilized. In the transition study it has been used to determine the quality of the individual sensor data, and data with a mean voltage below a certain level has been disregarded. It is not meaningful to present the mean voltage without a more thorough presentation of individual calibration data - considered to be outside the scope of the present report.

In a separate analysis the mean flow data is used together with the dynamic data to identify possible separated regions.

3.4.2 Standard deviation

The standard deviation of the hot film signal is commonly used for transition detection. In general an increase in amplitude ratio of two to three exists between laminar and turbulent flow, while transitional (intermittent) flows usually exhibit much higher levels.

Figure 37a - c illustrate the types of distributions of the standard deviation for 8, 16 and 19 degrees angle-of-attack, for each of the three elements. Transition, in general, is considered to occur where there is a higher level of standard deviation. However, as is evident from the figures, this is often far from true for (at least) the suction side of high lift configurations.

The interpretation of standard deviations is influenced by the mean level of the signal. The nonlinearity of the hot film response results in higher sensitivity to fluctuations when the mean level is low. Thus, the standard deviations in the laminar regions typically are in the range 1.5 mVolts, while for zero-flow conditions it is 2.5-3 mVolts. Also, notice that for sensors very close to the stagnation point, the standard deviation is usually high. This is due to the very low level of shear, which in some cases is also associated with higher, single frequency fluctuations due to shedding.

In contrast, when transition occurs in connection with high levels of shear (high dynamic pressure) the level of the standard deviation is rather low. In general, high-pressure coefficient values may coincide with high shear, i.e. low output. However, if the adverse pressure gradient is so large that the wall shear is reduced (in cases approaching separation), the sensitivity to fluctuations will be large even where the pressure coefficient is appreciable.

3.4.3 Skewness

This is a measure of asymmetry of the signal. Typically pure laminar and turbulent flows exhibit nearly zero skewness. Transitional flow will correspond to one sign in the beginning of transition, zero close to where the intermittency factor is 0.5, and then a reversal in sign.

Figure 38a - c illustrates the skewness distribution for the three elements. Most often the two peaks are evident, as can be expected for flow going through a region of increasing intermittency. As mentioned, laminar and turbulent flows have skewness close to zero. However, it is not uncommon in the present experiment to see deviations in regions right behind transition. This feature has not yet been examined.

3.4.4 Flatness

Flatness is also called kurtosis or crest factor. Typically it has a value close to 3, for laminar and turbulent flows, while transitional flows correspond to large values. Figure 39 shows the relation between Skewness and Flatness for an ideal, intermittent (transitional) boundary layer consisting of periods of pure laminar and pure turbulent flow only. The intermittency is also indicated. In reality the signals are not perfectly laminar or turbulent, and use of intermittency as an indicator is not practical since there is no clearly defined procedure for its estimation and its value may depend on signal filtering in a way that is hard to predict.

Figure 40a - c illustrates the flatness distribution for the three elements. Locally the flatness values can be very high, and most often two peaks can be found, corresponding to the ideal indications of Figure 39. If transition occur over a very short distance, it may not be possible to distinguish two peaks of flatness (or skewness). The conditions on the slat and the main element for 19 degrees angle of attack are examples of this.

In reality the transitional flow does have a variety of states, containing fluctuation of varying amplitude and spectral content in laminar as well as turbulent portions of the intermittent flow. Figure 41 illustrates results from flap sensors, where data has been plotted irrespective of location. As can be seen sensors in front of the transitional regime (laminar) are very close to the Gaussian value of 3. The transitional data covers both the early part of transition and late parts of transition.

In cases where there is a strong adverse pressure gradient bringing the boundary layer close to separation, the flatness may stay at an elevated value before it returns to the near-Gaussian value of 3. The flap flow in Figure 40c is an example of this. To determine if the flow is attached or reversed, it is not sufficient to look at the single-sensor statistics. Cross-correlations of the signals or spectra from pairs of sensors must be used.

3.4.5 Scales

The autocorrelation function is used to provide information on the Taylor microscale and the Integral length scale. In the analysis the scales have been used to indicate spectral information. The scales were used only as a rough guide to identify sensors that might exhibit a problem or a region of strong correlation.

3.4.6 Phase relations

In the stagnation region of an airfoil, the phase relations between a pair of films may be utilized used to estimate the location of the stagnation point, since films on either side will exhibit 180-degree phase reversal, as long as the amplitude is sufficiently large to have valid data. This technique is not always applicable on a multi-element airfoil since the free stream may contain strong structures.

3.4.7 Cross-correlations

The cross-correlation function was used to determine time-delay between maximum correlation. This was used to identify stagnation or reattachment regions, but also in general to identify the coherent structures in the turbulent part of the boundary layers.

The cross-correlation function is defined as:

$$\rho_{ij}(\Delta\tau) = \int v_i(t) v_j(t+\Delta\tau) / v_i(t) v_j(t)$$

In essence one looks for the maximum correlation between signals and how far from 0 this maximum correlation is shifted.

Considerable care must be taken in drawing conclusions from cross-correlations between surface hot film sensors:

- Since each individual film has a different transfer function, the use of cross correlations described previously suffer from the same limitation (to a smaller degree the statistical properties above) since the analysis assumes that the films have similar transfer functions.
- Reattachment regions, as well as separation regions, are notoriously unsteady, at a shedding frequency that is at best single-valued, and that is available through the standard analysis routines.
- The data records limit the analysis. For example, 1024 points sampled at 50 kHz means that the maximum sample length is 20.48 msec. This means that a frequency below 100 Hz is not measurable. As mentioned, the digital signal has no high pass filtering. Although this in principle is an advantage, it means that any low frequency content may enter into the estimates of averages and to some extent the higher moments.

3.4.8 Spectra

Although the transfer functions for each film is unknown, the spectra are used to identify several features:

- existence or development of a low frequency oscillations
- power line influence on the signal; either 60Hz or 400Hz harmonics
- common mode (high frequency, uncorrelated) noise due to coax cables
- AD saturation crosstalk; i.e. whether or not saturation in one channel may be influencing the others.

Due to task limitations, no spectra have been included in the present report.

3.4.9 Stationarity

Stationarity is determined through examination of all data sets available in all the buffers, and verify whether or not the statistical values change. Since the length of each 1024 sample data set is only 20.5 msec, frequencies below 100 Hz may be present (and observed) in the data but are not resolved.

3.4.10 Repeatability

Repeatability is verified through examination of similar data points taken on different occasions. Two types of repeatability are considered. One is the repeatability without anemometer bridge setup changes. This has been illustrated in Figure 33 for the standard deviation and flatness on the main element. The other is the change due to overheat where the flow is nominally the same but the overheat has been changed.

3.4.11 Transition location

The transition region is determined from a combination of the standard deviation, the skewness and the flatness of the hot film signals. The scales are used as a guide along with samples of the signals to make sure that any noise or disturbance that might be present is not interpreted a transition.

Two of the ground rules for the analysis are:

- Each element is handled separately
- A merged data file is used per angle-of-attack, containing all chordwise pressure information and all validated hot film statistical data.

The following is the sequence used to determine the transition region:

1. Assess the pressure distribution; i.e. identify stagnation regions and possible suction peaks
2. Assess the distribution of standard deviations; i.e. identify regions of high standard deviation due to:
 - Stagnation
 - Transition
 - Separation
 - Reattachment
 - Turbulent & turbulent low-shear flow
3. Utilize Skewness and Flatness to determine which flow phenomena is present
4. Utilize time-domain analysis to Identify stagnation points separation/reattachment points and separated regions:
 - Crosscorrelation function: Time shift of maximum correlation and value of maximum correlation.
 - ‘Conditional’ sampling to identify structures in turbulent boundary layer
 - Signal display - phase shift identifies stagnation region.
5. In specific areas ALL data sets are utilized to verify the stationarity of the signals.

6. Crossplots of data throughout polar are used to identify trends that are not otherwise identified due to sensor physical separation etc.

As described, the pressure distribution is included in the comparisons, since it usually provide a good indication of where transition can be expected to occur, and more importantly indicate the sensitivity of the hot films. Another feature of the hot film signals is their behavior in a stagnation point region, where the mean shear approaches zero. In some of the figures a higher standard deviation is visible in the stagnation region. This is mainly due to the non-linear effects of the hot film. The skewness and flatness are used to verify that this indeed is not a transitional signal but a stagnation point feature. These regions are explored separately.

The most conclusive test once general regions have been determined based on the statistical parameters, is to examine the signals directly, evaluate the cross-correlation function and make decisions based on direct signal interpretation.

In addition to the single-point analysis above, where each Point is handled separately, the transition tables have been modified to accommodate for trends observed when either angle-of-attack, Reynolds number or Mach number has been used as free parameter.

An example of the relationship between the different transition indicators and the resulting assumed transition location is shown in Figure 42. As is seen not only the extent of the regions is included, but also peaks for the different statistical properties: one peak for the Standard deviation (does not move with angle of attack), and two peaks each for the Skewness and Flatness. As can be seen the Flatness peaks move closer (and forward) as the angle of attack is increased - indicating a shorter intermittent region.

Also, notice that in this case there is an appreciable difference between the suction peak position at the centerline and at the 25 % line (which corresponds to the hot film array,). Thus the transitional region indicated by the Flatness starts at the suction peak (for the 25 % line).

4. ANALYSIS OF LOADS

To obtain an overall indication of the overall performance of the high-lift configurations, the integrated loads and their dependence due to parameters, such as configuration, Mach number and Reynolds number are examined.

4.1 Effect of configuration

In earlier tests in LTPT, it was found that 30P/30N was one of the best overall in terms of maximum lift coefficient, 30P/30AD somewhat inferior at high angles while 30P/35T had a separated flap and provided the least attractive performance of the three.

Figure 43 through 46 show comparisons between the configurations for 5 and 9 million Reynolds number. While the 30N and 30 AD configuration appear almost identical, 35T (not shown) is significantly inferior. The possible influence of the sheet of hot films on the measured pressure distributions is discussed in Appendix A3.1.

Figure 43 and 44 show the development of lift coefficient as function of angle of attack for the configurations 30P/30N and 30P/30AD at $Re=5$ mill at high angles of attack. The two Figures indicate similar results whether the integrated pressures, CLCOMBO z (Figure 43), are used or the balance data, CLS1 (Figure 44) is presented.

In the region close to maximum lift, the integrated pressure values, CLCOMBO, indicates that 30N peaks higher, while 30AD appears to have less of repeatability. In particular it appears that Polar 40 has a different behavior than Polars 41 and 42. The balance values, CLS1, indicate the same general trends although the absolute lift coefficients are 6-7 % lower.

Figures 45a and 45b presents separate accounts of the integrated pressures for the two configurations 30N and 30AD. Overall the load distributions for the two configurations are very similar, both regarding overall and each element.

Figure 46 provides a clearer indication of the difference between configuration at $Re=5$ mill, showing the average of the three polars for each of the conditions, and indicating balance data as well as pressure data. Although different in level, the trends depending on configuration is similar for the two techniques.

4.2 Effect of Mach number

Figure 36 illustrates that there is an effect of Mach number even at $M=0.15$ - a consistent trend at the highest Angles of attack indicates a higher maximum lift value for lower Mach numbers.

The reasons for indicated Mach number effects at lower lift coefficients/angles of attack are not clear, but possibly is within repeatability from polar to polar. Since the local Mach number is highest on the slat, it might be expected that this element contained the bulk of the Mach number effect. This is not the case, since the main element also is demonstrated to be considerably affected.

4.3 Effect of Reynolds number

The Reynolds number effect is opposite in sign for 30N and 30AD, as is clear from Figure 45a and 45b respectively. The Reynolds number effect is largest between 5 and 9 millions. This is the case for all three configurations tested.

To explore the trends further, delta-CL values were determined between $Re=5$ and 9 mill with the results shown in Figure 48. Filled symbols denoted changes in CLCOMBO; open symbols represent the corresponding wall load integrations.

In Figure 49 the Reynolds number trend at $Re=9$ to 12 mill is shown. Both pressures and force balance data (not shown) were found to have a cyclic variation as angle of attack changes. It is not established how significant these variations are. However, Figure 49 indicates that the wing box is responsible for the trends indicated. The slat may have an influence close to maximum lift.

Since the differences shown in Figure 49 are the result of integrated pressure distributions, it is useful to explore the differences in terms of local pressure values. In Figures 50a and 50b this has been done at $Re=12$ mill and 21 degrees angle-of-attack. Probably the suction peak of the main element in combination with the rear lower surface are the main discrepancies that may cause the observed 'oscillation' effects. These are the only two regions where there is a difference in pressure. The decrease in suction peak of 0.2 is contrary to the expected development, but may be associated with changes in the slat gap causing a change in the stagnation point flow on the main element.

4.4 Tunnel wall loads

The trends observed in the present data may not necessarily be typical of observed trends in previous test series. To substantiate the validity of the results from the present test, Figure 48b show the trends for traditionally determined loads, $dCLCOMBO$, and the agreement with tunnel wall data, $dCLwall$. As the figure indicates the agreement is good throughout the angle-of-attack region. While the Figures show very good agreement in measured trends, the differences found due to Reynolds number change are so small that it is difficult to argue that the oscillations with angle of attack are significant. They may be the result of repeatability level for the wind tunnel, as discussed previously or may be the result of a complex flow characteristic development. It is clear that the interaction between the elements is going through a series of different phases as the angle-of-attack is changed.

5. ANALYSIS OF MERGED HOT FILM AND PRESSURE DATA

The statistical analysis is based on sample sets of 1024 samples, averaged over approx. 15 sets per hot film for each of the 294 hot films for each of the (typically) 9 angles of attack, i.e. roughly 40,000 data sets per configuration. The tables in Appendix A1 contain a complete account of the determined transition locations and other flow features. The figures of the present section contain selected information and features used to illustrate an argument.

To a large extent results are given in the form of changes compared to the 30P/30N standard case (Mach=0.2 and Re=9 mill.). The transition graphs obtained within the scope of the task are organized as follows:

Configuration	Mach	Re [mill]	Slat	Main	Flap
30P/30N	0.2	9	51a	51b	51c
30P/30N	0.2	5	67a	67b	67c
30P/30AD	0.2	9	79a	79b	79c

5.1 30P/30N Mach=0.2 Re=9 mill.

Figures 51a through 51c illustrate the movement of transition for each of the three elements as function of angle-of-attack. All plots are done as function of the surface coordinate s/c , since this is the appropriate physical dimension for the surface flow on the configuration. Figure 52 through 55 illustrate flow features in the slat/front main region and the rear main/flap region respectively.

The cove information is discussed separately in Appendix A4, regarding both the techniques for analysis and the results.

5.1.1 Slat flow (30N-0.2-9)

Figure 51a shows the coordinate s/c on the ordinate. The apex of the slat is at $s/c=0$. The upper trailing edge is located at $s/c=0.16$ on the top of the figure. The lower side stretches from apex down to the cusp at $s/c=-0.06$. The cove region covers from $s/c=-0.06$ back to the trailing edge at $s/c=-0.20$. Since the s/c coordinate system wraps around the slat $s/c=0.16$ and $s/c=-0.20$ is the same point.

The slat flow stagnation point starts out at apex (i.e. close to $y/c=0$, where $s/c=0$). As the angle of attack increases, the stagnation points moves down and back, until stagnation occurs almost on the lower edge of the slat. Meanwhile, there is no suction peak for $\text{Alpha}=4$ degrees; there is a smooth acceleration all the way to the trailing edge on the suction side. From 8 degrees on a suction peak appears close to the apex. This suction peak moves very little - of the order 1 % chord - as the Angle of attack is increased to 23 degrees.

The transition region moves forward from being at the rear upper edge for alpha 4 degrees, until it occurs almost immediately behind the suction peak at high angles of attack. It appears that the beginning to end of transition in general is 2 % chord, except for 4 degrees where transition starts close

to the upper trailing edge and probably sheds as an intermittent shear layer, possibly causing spanwise non-uniformities.

When determining transition location, the standard deviation shows a sensor-dependent pattern typical of the results where differences in overheat/bridge voltage provides a variation that is not a flow feature, but rather an illustration of hot film setup limitations. This is evident in the plots of standard deviations of Figure 37a through 37c.

Figures 56a through 56c exhibit the dependence of the distributions of statistical parameters on angle of attack for the slat. For clarity only 4 to 12 degrees are illustrated. Figure 37a, 38a and 39a show also higher angles.

For 4 degrees only the standard deviation indicates a non-laminar flow, and only at the very last sensors. The standard deviation is seen to exhibit a clear transitional region only at 8 degrees, where it covers 5-6 sensors. The skewness shows the expected two-sided deviation while the flatness over the same sensor give two same-sign peaks, but with a longer transition region. It is clear from the figures that it is increasingly difficult to characterize transition as the angle of attack increases, and the excursions in Flatness get less and less pronounced.

Note that the peaks in the region of the stagnation point are mainly a result of the low shear in the region, resulting in a very high sensitivity of the films. Spectra show an indication of a low frequency oscillation in the region, but its source is not clear. Away from the stagnation point it is not detectable.

The upper side transition for angles of attack higher than 8 degrees is almost undetectable, indicating that it happens over an extremely short distance. This may be explained by the very high adverse pressure gradients where transition is nearly to instantaneous either through attached bypass transition or through a closed separation bubble.

The flow topology for the slat is illustrated in Figure 52 for the 4-degree alpha case. On the suction side the flow is laminar/early transitional; as mentioned the suction side does not have a suction peak - the region of minimum pressure is located at the trailing edge. The free shear layer leaving the cusp is probably laminar despite an appreciable distance from the stagnation point undergoes free shear layer transition and reattaches almost at the lower side trailing edge.

The corresponding sketch for 16 degrees of Figure 53 shows a suction peak and associated transition very close to apex, a stagnation point close to the cusp and a reattaching shear layer in the cove region well ahead of the trailing edge. Another difference from 4 degrees is that at 16 degrees angle of attack, also the main element has a distinct suction peak and transition region.

5.1.2 Main flow (30N-0.2-9)

The flow features found on the main element are illustrated in Figure 51b, some of the plots of the statistical properties from the hot film signals are found in Figures 37b, 38b and 37b.

The pressure distributions in Figure 57 illustrates virtually no movement of the low-pressure region, only a successively higher pressure coefficient values as the angle-of-attack is increased. The suction peak stays close to $s/c=0.01$, but the values are considerably lower than on the slat. The surface curvature region close to $s/c=0.1$ provides a pressure distribution resembling the shape normally cause

by a reattaching laminar separation bubble (at high Reynolds numbers). However, for most of the angles-of-attack, there was no evidence of reversed flow in the hot film data, and also transition occurs almost immediately behind the suction peak. For 4 degrees, the flatness factor indicates a clear transitional region from $s/c=0.01$ to 0.06 . At higher angles it becomes very short, and is centered around $s/c=0.02$.

The reason for the high flatness at 16 degrees from $s/c=0.16$ to 0.25 is not clear.

On the lower side of the main, the stagnation point moves back somewhat, as the detailed pressure distribution in Figure 58 shows. A major feature is the existence of slight suction peak mid-chord at low angles and an associated region of favorable pressure gradient. The suction peak moves back and the favorable gradient becomes weaker as the angle-of-attack increases. The hot film statistics indicate that this causes transition start to move from $s/c=-0.33$ to -0.4 at the two lowest angles, and jump back for higher angles. In fact, it appears that the flow over the lower trailing edge of the main is transitional for all angles above 8 degrees. This may have an influence on the main element cove flow and the subsequent flap flow.

5.1.3 Flap flow (30N-0.2-9)

The flow features found on the main element are illustrated in Figure 51c, some of the plots of the statistical properties from the hot film signals are found in Figures 37c, 38c and 39c.

The pressure distributions over the flap for the centerline and the extra row (close to the hot film locations), are shown in Figures 59 and 60. The suction peak for the main row moves slowly from $s/c=0.02$ to 0.03 as the angle of attack is increased, while it is further forward for the extra tap row. Up to 19 degrees the changes are mostly in scaling. For higher angles it appears that there is separation or near separation. The standard deviation distribution shows transition in the region s/c 0.04 to 0.06 , except for 23 degrees where it is further forward. The high level in the rear ($s/c>0.20$) for 8 degrees is uncertain. For 23 degrees the high level may indicate simply low shear or reversed low (check). However, neither the skewness nor the flatness indicates anything other than low shear, attached flow. Here is an example where the cross-correlation of the sensors can provide information on the flow status.

On the lower part of the flap, the hot film signals indicate that the flow is laminar; the non-stationarity found in the rear is associated with a fairly low frequent oscillation that could be caused by the main cove vortex shedding.

Figure 54 provides an illustration of flow topology for the main cove/flap region at 4 degrees alpha. The flow from the main element lower side is turbulent. The appreciable difference in suction peak location for the two spanwise stations is visible. The relatively long transitional region on the upper side is also visible. At 16 degrees (Figure 55) the changes for the time-averaged flow on the flap are very modest. The main change is that the free shear layer from the main element cusp is laminar/early transitional.

The value of the pressure coefficient at the suction peak and at the trailing edge are often instructive regarding the general flow features, and these have been plotted in Figure 61 for the flap flow of all three configurations at Mach=0.2 and Re=9 mill. A high suction peak usually leads to a local separation at high angles of attack. Complete pressure recovery (stagnation) at the trailing edge would

mean $C_p=1$ (approx.) In reality attached flow and thin boundary layers would have a pressure coefficient at the trailing edge close to 0.2. As the load increases, the boundary layers get thicker and nearly separate, the coefficient reaches zero. If there is a separation, the pressure will become negative, and for an open separation (without reattachment) adjust to the pressure in the separated region.

30P/30N exhibits a smooth development over angle-of-attack with a slightly less loaded peak region than 30AD, and much less than 35T, as is to be expected with the higher flap angle. As mentioned, the viscous losses often manifest themselves as a loss in pressure recovery at the trailing edge, and even here 30P/30N appears better than the other two.

5.1.4 Slat cove (30N-0.2-9)

To investigate the flow in the cove region, it is not sufficient to utilize only the single-sensor statistical information, since the flow direction is not a priori known. The few static pressure taps provide some information, but it is not even possible to determine the Mach number distribution, since the total pressure is unknown.

The next set of figures show results from the cross-correlation of signals from adjacent sensors in the slat cove, providing some insight into the flow features. Since the 0.1-in. separation used for the hot films in the cove region was small relative to the longitudinal flow structure, high cross-correlation values were observed.

Figure 62 shows the maximum cross-correlation coefficients as function of location for different angles. The symbol locations correspond to the mid-point between the adjacent sensors used in the analysis. It can be seen that for each angle the correlation is high, except in some region, where one may argue that there is a probability of a reattachment occurring.

The time shift of the maximum correlation indicates how long time it took a typical flow structure to move from one sensor to the other. This is expressed in number of time samples the maximum cross-correlation has been time shifted. As shown in Figure 63 where data for 4, 16 and 21 degrees angle of attack have been used as examples, the time shift indicated by the data appears to change sign approximately where the data is uncorrelated. The trailing edge of the cove is at $s/c=-0.22$, the $s/c=-0.10$ is further forward.

A curvefit has been included for the 4-degree points. Forward of $s/c=-0.14$ there is typically a time shift of 7 samples between adjacent sensors. By considering the information in Figure 63, an estimate of propagation velocity can be made as a sanity check of the correlations. The data is sampled at 50,000 Hz, which means that the typical delay of 7 samples, corresponds to $7/50=0.14$ msec. With sensors 0.1 in. apart that means a propagation velocity of

$\Delta U = 0.00254 \text{ [m]} / 0.00014 \text{ [sec]} \approx 18 \text{ m/s}$ which is roughly 25 % of the reference speed of the tunnel.

Fairing lines through the zero-time shift data and assuming that correlations below 0.3 are essentially uncorrelated, it is possible to interpret the data as shown in Figure 64, where reattachment regions have been plotted against angle of attack. The locations should be seen as rough estimates. It is clear that the flow is unsteady.

To get a clearer physical picture of the meaning of the plots, Figure 52 showed the presumed reattachment point in terms of physical coordinates for the slat cove for the 4-degree case. The evolution through the angle of attack regime has been illustrated in Figure 65 where the accuracy of the reattachment region determination has also been indicated.

One may also compare the presumed reattachment region and the flow to the single-sensor statistics. This has been done in Figure 66. The standard deviation shows a higher level in the recirculating part of the cove ($s/c = -0.15$ to -0.10 and forward). This may be due to differences in wall shear. The flatness indicates a minimum where the reattachment region is found.

5.1.5 Main cove (30N-0.2-9)

This data was obtained in the same series of runs where the slat cove flow was documented, and a similar technique was used to examine the space-time-correlations and determine the reattachment region. The film signals from the main cove were considerably more noisy than the signals from the slat cove. Within the accuracy of the technique, it was not possible to establish any angle-of-attack effect.

5.1.6 Three-dimensional effects (30N-0.2-9)

Three-dimensional effects are always present in two-dimensional experiments, and it is therefore necessary to view the results with caution. In the present experiment, as in a majority of others, the three-dimensionality is expressed in terms of pressure distributions. If additional information is available in terms of visualization of transition patterns (IR-photos) or separation patterns (oil flows), these are more direct proof of three-dimensional effects.

It is common to use sidewall suction or blowing to attain quasi-two-dimensional pressure distributions. Since the required mass flow (distribution) is dependent on the angle-of-attack, this is a time-consuming technique, and for LTPT it is common practice to set it for minimum variation in spanwise pressure at 16 degrees angle of attack. For lower angles, this approximate setting is reasonably good, but for 19 degrees and higher there is a marked spanwise pressure gradient, particularly on the flap.

As described in Appendix A2, one may look at three-dimensional effects as composed of a skewing (or distortion) of the flow field. The skewing means that there is a need to interpret the experimental transition locations to alleviate the skewing. The three-dimensionality in terms of truly spanwise flow is harder to deal with.

5.2 30P/30N Reynolds number effect

The Reynolds number effect for 30P/30N has been documented over four Reynolds numbers: 5,9,12 and 15 millions based on configuration chord, albeit with the highest Reynolds number data being taken at Mach=0.18 instead of 0.2. Also the highest Reynolds number data was only taken at three angles of attack, 4, 8 and 16 degrees. A complete interpreted transition data set has been illustrated in

Figure 67a-c for the three elements at one Reynolds number: 5 million. Similar data sets can be created for each additional Reynolds number.

5.2.1 Slat flow (30N-0.2)

For Reynolds number 5 million, only the slat flow pressure distribution at low angles of attack (e.g. 8 degrees) is altered noticeably (Although the stagnation point also moves slightly as the Reynolds number is decreased). Figure 67a shows the transition pattern to be similar to the 9 million case. Figure 68 illustrates movement of stagnation point and suction peak as well as beginning and end of transition for $Re=5$ and 9 mill.

The stagnation point stays basically unaltered when the Reynolds number is reduced to 5 million. The transition region on the upper side moves right behind the suction peak to actually happening over the almost constant pressure region behind the suction peak. While the standard deviation indicates transition from $s/c=0.067$ to 0.105 , the skewness as well as the flatness provide an estimate of: $s/c=0.06$ to 0.11 . On the pressure (lower side) the C_p distribution barely changes and the main effect is a slight movement of the stagnation point towards apex.

At high angles-of-attack, a very moderate change of the pressure distribution is found, and there is very minor transition adjustment occurs. In most of the cases, there is a trend of movement of transition further back as the Reynolds number is decreased.

Figure 69 shows the changes in pressure distributions on the slat for $Re=5, 9, 12$ and 15 mill. at 8 degrees angle of attack. The two issues demonstrated in the figure are that for 8 degrees angle of attack:

- the slat pressure distribution does not change from $Re=9$ up to 15 mill.
- Transition moves forward between 5 and 9 mill; for increasing Reynolds number above 9 mill only the length of the transition region gets shorter.

5.2.2 Main flow (30N-0.2)

The flow conditions on the main element at $Re=5$ mill are illustrated in Figure 67b. The most dominant difference from $Re=9$ mill is the movement of transition on the lower side towards the main element cusp/cove.

Figure 70a and 70b illustrate the flow changes with Reynolds number on the main element for 8 degrees angle of attack. The pressure distribution of the main for $Re=5$ mill. is barely noticeably different from 9 mill, as seen in Figure 71. Yet the transition on the suction side has moved somewhat back by 0.05 in s/c , while the transition on the lower side is moved downstream by considerable 25 % chord, from -0.4 to -0.65 . Notice though, that for 8 degrees the end of transition still occurs in front of the cove 'entry'.

The pressure distribution is barely affected at 8 degrees angle of attack, but transition moves back on the suction side. Comparing with the distributions of standard deviations obtained at 9 million Reynolds number, there is a marked change, with two distinct peaks existing around $s/c=0.015$ and 0.045 . (Figure 72a and 72b). Based on the logic below, it is suggested that the two peaks correspond to a reattaching (closed, short) laminar separation bubble that is not predominant at 9 millions.

The most convenient way of exploring the data is to go back to the time-space relations for the region, at $Re=5$ mill. Figure 73 shows time series for parts of the region of interest. The signals suggest a separation and reattachment where there is phase reversal and loss of correlation. In the present case the signals indicate separation between films 160 and 161, and reattachment further back between films 156 and 157. The flow is laminar for films 164 and 163. The subsequent films indicate an UNSTEADY bubble where the fluctuations for films 156 through 152 are seen as an indicator of how far the bubble moves. If the present region was one of natural transition, there would have been a convective pattern throughout, and not the phase reversal.

The pattern was also explored using the cross-correlation function, as depicted in Figures 74. There is an indicative time shift changing sign twice, but perhaps more indicative is the high correlation except for two distinct locations, roughly corresponding to the phase reversals of the signal traces.

It is argued that a similar pattern exists for the flow at 19 degrees and above, but there the resolution involved preclude a proper analysis.

On the pressure side transition moves back almost all the way to the trailing edge. As the angle-of-attack is increased there is still some movement of the transition location, but the pressure distribution over the flap is basically unaltered from the 9 million case.

5.2.3 Flap flow (30N-0.2)

Figure 67c shows the flow features on the flap at $Re=5$ mill. Predominant features are the relatively long transitional region on the suction side, approximately 4 % chord, and also the large difference between the mid-span and the auxiliary tap row suction peaks. Figure 75 shows the pressure distribution and the standard deviation distribution on the flap. The pressure distribution is basically not altered, while the beginning of transition on the suction side has moved back by roughly 0.5 to 1 %. In the region 12 to 16 degrees angle of attack transition beginning did not move at all.

The end of transition moved from 7% chord at small angles-of-attack and 6% at the high angles, by 1% when the Reynolds number is reduced from 9 mill to 5 mill.

5.3 30P/30N Mach number effect

The Mach number effect is not readily described, partly because only a limited part of the data could be analyzed under the task. The data presented below concerns the conditions for 19 degrees angle of attack. The full range of angles-of-attack has been documented experimentally but not analyzed.

5.3.1 Slat flow (30N- -9)

Figure 76 shows the pressure distributions in the suction peak region. It appears that at least one tap is bad. The trend is to have slightly higher suction peak, while the effect on transition of an increase in Mach number appears to be that of increasing the transitional region's length. The existence of a shock can not be ruled out for the $Mach=0.23$ case and the possibility of local separations has not been examined due to time limitations.

5.3.2 Main flow (30N- -9)

The Mach number effect on the main element is more clearly defined. Figure 77 indicates a suction peak that moves back and increases with increasing Mach number. Meanwhile the transition moves forward until it starts literally at the suction peak. The length of the region does not change; the entire process appears to happen within roughly 1 % chord. Again, note that the pressure distribution belongs to mid-span while the hot film data was taken at 74% span.

5.3.3 Flap flow (30N- -9)

On the flap, the midspan pressure distribution does not change with Mach number, while the auxiliary row at 74% indicates a lowering value and a distribution moving forward; see Figure 78, but with pressure gradients roughly as at mid span. The transition region is basically unchanged, extending over 3% chord length.

5.4 30P/30AD

Based on MDA's previous experience, this configuration is assumed to be one of the best, but noticeably inferior to 30P/30N. The transition graphs are shown in Figures 79a - 79c, and as expected the follow similar trends and have comparable features to those of 30P/30N. Most of the discussion in the subsequent section will be concentrated of differences between the configurations.

As an example 19 degrees angle of attack is chosen and in the figures the results are compared with the similar reference conditions for 30P/30N.

5.4.1 Slat flow 30P/30AD

Examination of the pressure distributions for the slat (not shown) indicates almost no noticeable differences. Figures 80a to 80c present the hot film data for the slat flow. Figure 80a shows the standard deviation indicating that the transition at 8 degrees has moved back almost 2% when compared with 30P/30N. The skewness distributions confirm the same shift in transition location, see Figure 80b. Also the flatness is in agreement, except the first peak is not distinct. This latter occurrence is assumed to be due to lack of resolution.

5.4.2 Main flow 30P/30AD

Figures 81a through 81c provide the hot film information for the main element. On the main element there is likewise virtually no change in pressure distribution. The main difference between 30N and 30AD is found on the lower side, where transition appears to be moved back 25 % chord. This is clearly seen for the standard deviation distributions, but can also be seen in skewness and flatness.

5.4.3 Flap flow 30P/30AD

The flap indicates some change in pressure distribution, but the transition occurs at an unchanged location for 30P/30AD. Figure 82 shows the distribution of standard deviation where the main difference between 30N and 30AD appears to be a lower level for the turbulent flow in the latter.

The figure illustrates an instrumentation problem present during parts of the run. The level for the laminar region is higher for the AD configuration. One of the two systems was subject to an electrical disturbance, causing spikes in the signal and AD saturation, which in turn caused crosstalk over all 7 channels for that system. This caused a moderate change in standard deviation, as illustrated by the higher levels from $s/c = -0.05$ to 0.03 . (The data has been included to illustrate the effects. Skewness and Flatness were affected, but are not shown.) Further back on the suction side of the flap, data was taken with the other, undisturbed, system; hence the transition data is real and unaffected.

5.5 30P/35T

The hot film data taken for this configuration was not of the same high quality as the 30N and 30AD data. This was caused by problems with parts of the hot film sheet on the flap developing an air bubble underneath the between the sensors and the wall. Repair attempts were not successful. Also, during part of the test with 35T, there were electrical noise problems, so only a part of the data is reliable. Thus only very limited information is included for the main element, where the main disturbances occurred.

In this section some additional information on 30P/30AD has been included for $Re = 5$ million, since it is natural to do the comparison between the three configuration. Three angles of attack for 30P/30AD and 30P/35T were analyzed at this Reynolds number. Mainly the standard deviation will be examined.

The figures illustrating standard deviation distributions for all three configurations are organized as follows:

Angle-of-attack	Element	Re=9 million	Re=5 million
8	Slat	83a	83b
16	Slat	84	-
19	Slat	-	85
8	Main	86	-
8	Flap	87a	87b
16	Flap	88	-
19	Flap	-	89
21	Flap	-	90

5.5.1 Slat flow 30P/35T

The pressure distribution was basically unchanged from the other configurations. Initially we will concentrate on the 8 degrees angle of attack case. Figure 83a illustrates 35T data on the slat compared with 30N and 30AD for $Re = 9$ million. 35T has transition occurring in the same region as 30AD, but interestingly 30N has transition occurring further forward. The stagnation point location is very evident through the peak in standard deviation.

If the Reynolds number is reduced to 5 million, as depicted in Figure 83b, 30N transition has moved back to 35T, while 30AD has moved further back. 30AD also appears to have the stagnation point moved slightly to the lower side of the slat.

Looking at conditions for 16 degrees angle of attack, all three configurations agree for $Re=9$ mill, (Figure 84). When the Reynolds number is reduced to 5 million, no change is visible. (Figure 85).

5.5.2 Main flow 30P/35T

The pressure distribution was basically unchanged from the other configurations.

Figure 86 shows the standard deviation on the main element. Note that the data has spikes, which probably are noise. The analysis of this data indicates very small changes from configuration to configuration.

5.5.3 Flap flow 30P/35T

The pressure distribution was somewhat changed from the other configurations. First 8 degrees angle of attack data is presented. Starting with $Re=9$ mill, Figure 87a illustrates the 35T data on the slat compared with the 30N and the 30AD for the flap. The 35T data has transition occurring in the same region as 30AD and 30N, i.e. the change in pressure distribution was not significant enough to matter. However, it may be interesting to note that, on the slat, the 30AD transition deviated from the other two for this Reynolds number and angle of attack. On the flap transition appears to occur at the same location as the 30N and the 30AD, but the standard deviation level is different in the turbulent regime.

At $Re=5$ million, some disturbances are present for 35T, but transition remains roughly unchanged (Figure 87b). Increasing the angle of attack to 16 degrees, Figure 88 and 89 illustrates very small changes. Only when the angle of attack is increased to 21 degrees, as depicted in Figure 90, is there a difference between 35T and the other two configurations; start of transition moved forward somewhat and the level for the turbulent flow is also noticeably different.

5.6 Three-dimensional effects

It is necessary to distinguish between at least two different terms regarding three-dimensional effects:

- Spanwise non-uniformity, which sets up spanwise differences but in general, does not cause noticeable crossflow. This can be viewed as comparable to strip-'theory' for finite wings.
- Three-dimensional flow ranging from embedded vortices created by brackets, corners etc. in an almost any two-dimensional flow, to fully developed crossflow caused by spanwise non-uniformity.

There are several different techniques available to determine three-dimensional effects, ranging from fully three-dimensional flow field measurements providing all three velocity components, through surface flow visualization and IR imaging of a transition front to the status in the present experiment: merely documenting spanwise pressure distributions in addition to the chordwise ones.

More comprehensive investigations are considered for the next experimental phases, but for the time being the pressure distributions are the only source of information.

Only 9 million Reynolds number is considered since all angles-of-attack have been analyzed at this Reynolds number. The three configurations are examined, but since the possible effects of the film sheets are discussed, this information has been included in the Appendix.

The four spanwise (suction side) distributions examined are one on the slat (5% chord), one on the main element (82.5%) and two on the flap (74% and 100%). Note that the % chord positions are given as stowed coordinates, so that in reality the 82.5% main element row is upstream of the 74% flap row.

The plots of spanwise pressure distributions corresponding to the transition graphs, Mach=0.2, Re=9 million, are tabulated below:

Configuration	Slat(5%)	Main (82.5%)	Flap (74%)	Flap (100%)
30P/30N	91a	91b	91c	91d
30P/30AD	92a	92b	92c	92d
30P/35T	93a	93b	93c	93d

The pressure distribution on the slat appears to be very uniform for all three configurations, and there is no indication its non-uniformity should be strong enough to create problems on the main element.

On the main element up to 16 degrees angle of attack, only a slight variation exists between 70 and 100 % span. At higher angles, the variation increase until there is a variation of almost 0.6 compared to the left side. On the front spanwise row of the flap the difference has increased to a high of 0.9 which may seem not too different until one realizes that the value at the suction peak on the flap is 1/3 of what it is on the main element.

A good indicator on the overall effects on the configuration can be found in the 100% (trailing edge) pressure coefficients, which is a measure of the pressure recover. Inviscid flow should have a trailing edge pressure equal to the stagnation pressure. In reality, for practical airfoils, a value of around 0.15 - 0.2 for the pressure coefficient can be considered to indicate attached flow. However, if the pressure coefficient goes to zero or becomes negative, there is a high probability that the flow is separated over the trailing edge. Based on this it appears that the flow may be marginally separated in the rear corner of the flap close to 100 % span. Successively, the separated region appears to grow until it is felt at the midspan for 22 degrees angle of attack. The information on the other two configurations has been plotted with the 30P/30N information shown as dashed lines. For 30AD the slat, as expected, has small variations, the main element has the same general pattern, which leads to the conclusion that whatever (unknown) three-dimensional effects there are, they must be similar. The flap looks similar along the 74 % chord line, but for the 22 degree trailing edge data there is an indication of a more limited separated region than 30P/30N.

30P/35T slat information can be found in Figure 93a. Here it is clear that there may be more than negligible differences for angles of attack 16 degrees and up, exhibiting a difference up to 0.2. It is not a three-dimensional effect, but may instead be a result of load redistribution due to the flap setting. This is confirmed by the same pattern as observed previously recurring over the main element. The main difference is found in Figure 93d, where the trailing edge pressure distributions for the flap have been documented. All angles above 8 degrees exhibit significant differences between 35T and 30N, and it appears that for all angles above 16 degrees, the separated region in all probability is larger for 35T.

5.7 Wake flow

The streamwise velocity profiles for the wakes are shown in Figure 16 for 30P/30N and in Figure 94a and 94b for 30P/30AD and 30P/35T, respectively. As the angle of attack increases from 4 degrees to 16 degrees, the main change is a vertical shift of the wake of roughly 4 inches for the 30N and 30AD wakes. While the 30AD wakes are well-behaved and close to symmetrical (similar to 30N), the wakes of 35T up to 12 degrees exhibit a smaller downshift, asymmetry and unsteadiness signified by the jagged upper side of the wakes. For 16 degrees angle-of-attack it appears better ordered.

Note that the behavior of the wake is mostly influenced by the conditions at 77% where the information in the previous section showed substantial differences between 30N, 30AD versus 35T.

In Figures 17, 95a and 95b, the non-dimensional shape has been plotted. It is clear that both 30N and 30AD have well behaved, symmetrical shapes, while the wakes behind 35T even at 16 degrees angle of attack exhibit non-stationarity as well as asymmetry.

Figure 96 illustrates the location of the wake center for the different configurations as function of angle-of-attack, while Figure 97 shows the maximum velocity defect. Again, 35T stands out. The drag coefficients are illustrated in Figure 98, and the wakes from 8 through 12 degrees clearly have a much higher drag for the 35T.

6. DISCUSSION AND CONCLUSIONS

The present report should be viewed as part of a set of three where the other two describe the database and how to access it as well as a description of the hot film anemometry system used to gather and organize the raw, digital data.

Based on a large amount of data obtained at different Mach numbers and Reynolds numbers for three- configurations (riggings) of a three-element MDA model, several conclusions and comments can be made.

- The transition regions have been established, based on multiple transition criteria.

- Localized reattachment regions in the slat cove and the main cove have been identified.

- Local separated regions on the flap have been identified and characterized.

- In general, there is very little difference in pressure distributions for different configurations. At high angles of attack the three-dimensionality of the distributions appear to be larger than the difference between configurations.

- The general flow characteristic of the model is similar to earlier tests. However there is an influence of the hot film sheet that has to be considered when using the data. The transitional regions were not known a priori, so the number of hot films used had to be very large to obtain transition data of acceptable resolution.

- Only the Mach number effects for the slat shows any significant differences, mainly due to the extreme Mach number there, sonic or slightly supersonic.

- The transition locations were obtained off center line, i.e. at a spanwise station corresponding to that of the Reynolds stress measurements, but not corresponding to the main measurement row of pressures.

- Even seemingly small difference in pressure distributions can be accompanied by significant and major differences in viscous flow characteristics, such as separations, transition region extent and physical characteristics.

- Spanwise non-uniformities can explain some of the seemingly strange trends observed in some of the global data, compared with old data available from previous test series.

REFERENCES

1. Bertelrud,A. and Johnson,S.: “Documentation of Transition on a Three-Element High-Lift Configuration at High Reynolds Numbers - Database.” NASA/CR-2002-211439, 2002.
2. Goradia,S.H. and Colwell,G.T.: “Analysis of High-Lift Wing Systems.” *Aeronautical Quarterly*, May 1975, pp. 88-108.
3. Dvorak,F.A., Woodward,F.A. and Maskell,B.: “A Three-Dimensional Viscous/Potential Flow Interaction Analysis Method for Multi-Element Wings.”NASA CR-152012, 1977.
4. Dillner,B., May,F.W. and McMasters,J.H.: “Aerodynamic Issues in the design of High-Lift Systems for Transport Aircraft.”In AGARD-CP-365 Improvement of Aerodynamic Performance Through Boundary Layer Control and High Lift Systems, Brussels, Belgium, 21-23 May, 1984.
5. Dominik,C.J.: “Application of the Incompressible Navier-Stokes Equations to High-Lift Flows.” AIAA Paper 94-1872, presented at the AIAA 12th Applied Aerodynamics Conference, June 20-23, 1994, Colorado Springs, Colorado.
6. Mani,M. and Bush,R.H.: “Overlapping Grid Method of High-Lift and Store Carriage Applications.” AIAA Paper 93-3428, presented at the AIAA Applied Aerodynamics Conference, August 9-11, 1993, Monterey,CA.
7. Djatmiko, B., Sudira, I. G. N., Cakrawala, A., van-den-Berg, B., Chintamani,S.H. and Mack,M.D., “The Effect of Wing Sweep on the Flow Around a Slat and Its Performance.” Proceedings of the 19th ICAS Congress, Anaheim, CA, Sept. 18-23, 1994, Vol. 1 (A94-31534 10-01), Washington, DC, American Inst. of Aeronautics and Astronautics, Inc., 1994, p. 109-118A.
8. Porcheron, B. and Thibert,J.J.: “Etude detaillee de l'Ecoulement Autour d'un Profil Hypersustense. Comparaisons avec les Calculs.” In AGARD-CP-365 Improvement of Aerodynamic Performance Through Boundary Layer Control and High Lift Systems, Brussels, Belgium, 21-23 May, 1984.
9. Butter,D.J.: “Recent Progress on Development and Understanding of High Lift Systems.”In AGARD-CP-365 Improvement of Aerodynamic Performance Through Boundary Layer Control and High Lift Systems, Brussels, Belgium, 21-23 May, 1984.
10. Paschal,K., Goodman,W., McGhee,R., Walker,B. and Wilcox,P.A.: “Evaluation of Tunnel Sidewall Boundary-layer Control Systems for High-Lift Airfoil Testing. AIAA Paper 91-3243, September 1991.
11. Nakayama,A., Kreplin,H.-P. and Morgan,H.L.: “ Experimental Investigation of Flowfield About a Multielement Airfoil.” *AIAA Journal*, vol. 28, No. 1, January 1990, pp. 14-21.

12. Valarezo,W.O., Dominik,C.J., McGhee,R.J., Goodman,W.L. and Paschal,K.B.: “Multi-Element Airfoil Optimization for Maximum Lift at High Reynolds Number.” AIAA Paper 91-3332, presented at the AIAA 9th Applied Aerodynamics Conference, September 23-25, 1991, Baltimore, Maryland.
13. Chin,V.D., Peters,D.W., Spaid,F.W.: “Flowfield Measurements About a Multi-Element Airfoil at High Reynolds Numbers.” AIAA Paper 93-3137 presented at AIAA 24th Fluid Dynamics Conference, July 6-9, 1993, Orlando, Florida.
14. Bertelrud, A. and Liandrat, M-P., “Large Eddy Breakup Devices at Low and High Reynolds Numbers,” AIAA Paper 90-1601, AIAA 21st Fluid Dynamics, Plasma Dynamics and Lasers Conference, Seattle, WA, June 1990.
15. Kreplin, H.-P. and Höhler,G.: “Anwendungen von Multisensor-Heissfilmfolien.” in DGLR-FA T 2.2-Sitzung “Flächige Strömungsmessverfahren.”, Berlin, Germany, March 2-3, 1995.
16. Savory,E., Toy, N. , Tahouri,B. and Dalley,S.: “ The flow regimes in the Cove regions Between a Slat and a Wing and the Flap on a Multi-element Airfoil.” in Engineering turbulence - Modeling and Experiments (Rodi and Ganic, Eds.), Elsevier, 1990.
17. Johnson, S. and Bertelrud,A.: “NASA LaRC FIB Multi Channel Anemometry Recording System, MCARS User’s manual”. NASA/CR-2002-211440, 2002.
18. Bertelrud,A., Johnson,S., Lytle,C. and Mills,C.: “A System for Analysis of Transition Characteristics on a High-Lift Configuration at High Reynolds Numbers.” presented at the 17th ICIASF , September 29 - October 2, 1997, Monterey,CA
19. Bertelrud,A. and Ljungström,B.L.G.: “The Viscous Flow Around a Two Dimensional High Lift Wing.” FFA TN AU-1155, 1974.
20. Tennekes,H. and Lumley,J.L.: “A First Course in Turbulence.” The MIT Press, Cambridge, Mass. U.S.A. and London, England, 1972.
21. Squire ,H.B. and Young, A.D.: “The Calculation of the Profile Drag of Aerofoils.” ARC R&M 1838, 1937.
22. Bertelrud, A. and Graves, S.: “Analysis of Flight Flow Characteristics in the Leading Edge Region of Swept Wings at Subsonic and Transonic Speeds” AIAA Paper 94-2152 presented at the 7th Biennial AIAA Flight Test Conference, Colorado Springs, CO, June 20-23, 1994
23. Enns,S.:”Free-Form Curves on your Micro-Implement Bezierand B-spline Curves for Interactive Graphics” BYTE, December 1986,pp.225-230.
24. White,F.M.: “Viscous Fluid Flow.” McGraw-Hill, New York, 1974.

25. Mann,A.R. and Whitten,P.D. General Dynamics Convair Aerosp. Div. Rep. ERR-FW-1094, Fort Worth,TX (1970)
26. Michel,R. : “Etude de la transition sur les profils d'aile. Etablissement d'un critere de détermination du point de transition et calcul de la traînée de profil en incompressible.”ONERA Report 1/1578-A (1951)
27. Govindarajan, R. and Narasimha, R.: “The role of residual, non-turbulent disturbances on transition onset in two-dimensional boundary layers.” J. Fluids Eng., March 1981, Vol 113, pp.147-149.
28. Weibust,E., Bertelrud, A. and Ridder,S.O.: “Experimental Investigation of Laminar Separation Bubbles and comparison with Theory.” Journal of Aircraft, Vol. 24, No. 5, May 1987, pp. 291-297.

APPENDIX 1 TRANSITION LOCATIONS

This appendix contains the transition locations in tabulated form. Below is a chart of configurations with indication of which cases were analyzed.

The symbols mean:

- Ø Processed and analyzed
- O Processed only.
- Not analyzed
- Not run

Angle-of-attack: 4 deg. 8 deg. 10 deg. 12 deg. 16 deg. 19 deg. 21 deg. 22 deg. 23 deg.

Config	Mach	Re [million]	4 deg.	8 deg.	10 deg.	12 deg.	16 deg.	19 deg.	21 deg.	22 deg.	23 deg.
1. 30P/30N	0.2	9 Ø	Ø	Ø	Ø	Ø	Ø	Ø	Ø	Ø	Ø
2. 30P/30N	0.15	9 Ø	Ø	-	-	-	Ø	Ø	-	-	
3. 30P/30N	0.23	9 -	Ø	-	-	-	Ø	Ø			
4. 30P/30N	0.2	5 Ø	Ø	Ø	Ø	Ø	Ø	Ø	Ø	Ø	Ø
5. 30P/30N	0.2	12 -	O	-	-	-	O	O	-	-	
6. 30P/30N	0.18	15	Ø	Ø			Ø				
7. 30P/30AD	0.2	9	Ø	Ø	Ø	Ø	Ø	Ø	Ø	Ø	Ø
8. 30P/30AD	0.23	9	O	-	-	-	-	-	O	O	-
9. 30P/30AD	0.2	5 -	O	-	-	-	O	O	-	-	
10. 30P/35T	0.2	9	Ø	Ø		Ø	Ø	Ø	Ø Ø	Ø	Ø
11. 30P/35T	0.2	5 -	O	-	-	-	-	O	O	-	

As can be seen a total of 46 test cases have been processed and analyzed, another 12 have been processed but not analyzed in terms of establishing the locations of characteristic features.

The processed data for all 58 cases has been included on a CD in terms of 'merged data' i.e. both pressure data (pressure coefficients, C_p) and hot film statistics (Standard deviation, Skewness, Flatness) are available as function of streamwise location, s/c , for each element.

The data files contain all measured points, and no smoothing has been done.

Table 1

Configuration:	30P/30N								
Mach:=0.2	Reynolds number:= 9 million								
Angle-of-attack:	4 deg.	8 deg.	10 deg.	12 deg.	16 deg.	19 deg.	21 deg.	22 deg.	23 deg.
SLAT									
Stagnation	-0.002	-0.013	-0.018	-0.025	-0.035	-0.050	-0.050	-0.055	-
Upper									
Suction peak	n/a	0.015	0.011	0.009	0.007	0.006	0.006	0.006	-
Transition B	0.145	0.030	0.025	0.020	0.014	0.010	0.010	0.008	0.007
Transition E	0.160	0.060	0.050	0.034	0.025	0.020	0.020	0.021	0.021
Lower									
Suction peak	n/a	n/a	n/a	n/a	n/a	n/a	n/a	n/a	-
Transition B	n/a	n/a	n/a	n/a	n/a	n/a	n/a	n/a	n/a
Transition E	n/a	n/a	n/a	n/a	n/a	n/a	n/a	n/a	n/a
Cove									
Reattachment F	-0.185	-0.180	-0.170	-0.165	-0.155	-0.145	-0.140	-0.140	-
Reattachment R		-0.195	-0.190	-0.185	-0.175	-0.165	-0.155	-0.150	-0.150 -
MAIN									
Stagnation	-0.068	-0.070	-0.080	-0.090	-0.100	-0.110	-0.130	-0.140	-
Upper									
Suction peak	-0.001	0.000	0.006	0.006	0.006	0.008	0.010	0.010	-
Transition B	0.015	<u>0.012</u>	0.012	0.011	0.012	0.016	0.018	-	0.017
Transition E	0.045	*0.025	0.025	0.023	0.025	0.025	0.028	-	0.028
Lower									
Suction peak	-0.500	-0.510	-0.530	-0.560	-0.610	-0.620	-0.620	-0.620	-
Transition B	-0.340	-0.405	-0.480	-0.640	-0.660	-0.670	-0.670	-0.670	n/a
Transition E	-0.5000	-0.510	-0.7000	n/a	n/a	n/a	n/a	n/a	n/a
Cove									
Reattachment F	n/a	n/a	n/a	n/a	n/a	n/a	n/a	n/a	-
Reattachment R	n/a	n/a	n/a	n/a	n/a	n/a	n/a	n/a	-
FLAP									
Stagnation	-0.010	-0.010	-0.010	-0.010	-0.010	-0.010	-0.010	-0.010	-
Upper									
Suction peak	0.027	0.026	0.025	0.024	0.024	0.024	0.024	0.024	-
Transition B	0.030	0.030	0.035	0.040	0.040	0.030	0.028	0.020	0.015
Transition E	0.070	0.070	0.065	0.065	0.065	0.060	0.058	0.058	0.060
Lower									
Suction peak	n/a	n/a	n/a	n/a	n/a	n/a	n/a	n/a	-
Transition B	n/a	n/a	n/a	n/a	n/a	n/a	n/a	n/a	n/a
Transition E	n/a	n/a	n/a	n/a	n/a	n/a	n/a	n/a	n/a
Extra tap row									
Suction peak	0.0200	0.020	0.0200	0.0200	0.018	0.016	0.0110	0.0100	-

* Indication of bubble ending at 0.048

Table 2

Configuration:	30P/30N								
Mach = 0.15	Reynolds number:		9 mill.						
Angle-of-attack:	4 deg.	8 deg.	10 deg.	12 deg.	16 deg.	19 deg.	21 deg.	22 deg.	23 deg.
SLAT									
Stagnation	-0.002	-0.012				-0.050	-0.052		
Upper									
Suction peak	0.146	0.020				0.005	0.006		
Transition B	0.140	0.048				0.015	0.015		
Transition E	n/a	0.065				0.020	0.020		
Lower									
Suction peak	n/a	n/a				n/a	n/a		
Transition B	n/a	n/a				n/a	n/a		
Transition E	n/a	n/a				n/a	n/a		
MAIN									
Stagnation	-0.065	-0.065				-0.130	-0.130		
Upper									
Suction peak	-0.011	-0.002				0.004	0.005		
Transition B	0.021	0.016				0.021	0.021		
Transition E	0.044	0.030				0.032	0.032		
Lower									
Suction peak	-0.430	-0.440				-0.640	-0.640		
Transition B	-0.350	-0.430				n/a	n/a		
Transition E	-0.480	-0.600				n/a	n/a		
FLAP									
Stagnation	-0.009	-0.010				-0.012	-0.012		
Upper									
Suction peak	0.027	0.027				0.024	0.023		
Transition B	0.026	0.026				0.026	0.026		
Transition E	0.070	0.068				0.059	0.059		
Lower									
Suction peak	n/a	n/a				n/a	n/a		
Transition B	-0.290	n/a				n/a	n/a		
Transition E	n/a	n/a				n/a	n/a		
Extra tap row									
Suction peak	0.020	0.020				0.016	0.015		

Table 3

Configuration:	30P/30N						
Mach:=	0.23						
Angle-of-attack:	Reynolds number:= 9 million.						
	4 deg.	8 deg.	10 deg.	12 deg.	16 deg.	19 deg.	21 deg.
SLAT							
Stagnation		-0.011				-0.043	-0.047
Upper							
Suction peak		0.015				0.007	0.007
Transition B		0.052				0.011	0.007
Transition E		0.070				0.025	0.020
Lower							
Suction peak		n/a				n/a	n/a
Transition B		n/a				n/a	n/a
Transition E		n/a				n/a	n/a
MAIN							
Stagnation		-0.008				-0.120	-0.120
Upper							
Suction peak		0.006				0.013	0.013
Transition B		<u>0.012</u>				0.016	0.016
Transition E		0.048				0.025	0.025
Lower							
Suction peak		-0.510				-0.6200	-0.620
Transition B		-0.420				-0.6600	-0.660
Transition E		-0.530				n/a	n/a
FLAP							
Stagnation		-0.008				-0.008	-0.008
Upper							
Suction peak		0.024				0.024	0.024
Transition B		0.030				0.030	0.028
Transition E		0.070				0.060	0.060
Lower							
Suction peak		n/a				n/a	n/a
Transition B		n/a				n/a	n/a
Transition E		n/a				n/a	n/a
Extra tap row							
Suction peak		0.021				0.014	0.012

Table 4

Configuration:

30P/30N

Mach: = 0.2

Reynolds number := 5 million.

Angle-of-attack:

4 deg. 8 deg. 10 deg. 12 deg. 16 deg. 19 deg. 21 deg. 22 deg. 23 deg.

SLAT

Stagnation	-0.002	-0.008	-0.0185	-0.025	-0.035	-0.050	-0.050	-0.049	-0.049
Upper									
Suction peak	n/a	0.020	0.012	0.009	0.008	0.006	0.006	0.003	0.002
Transition B	0.145	0.067	0.038	0.0295	0.015	0.013	0.0156	-0.005	-0.005
Transition E	n/a	0.105	0.056	0.038	0.029	0.029	0.025	0.025	0.025
Lower									
Suction peak	n/a	n/a	n/a	n/a	n/a	n/a	n/a	n/a	n/a
Transition B	n/a	n/a	n/a	n/a	n/a	n/a	n/a	n/a	n/a
Transition E	n/a	n/a	n/a	n/a	n/a	n/a	n/a	n/a	n/a

MAIN

Stagnation	-0.068	-0.070	-0.080	-0.090	-0.100	-0.110	-0.130	-0.150	-0.150
Upper									
Suction peak	-0.001	0.000	0.006	0.006	0.006	0.008	0.010	0.006	0.006
Transition B	<u>0.012</u>	0.039	0.040	0.039	0.039	<u>0.012</u>	<u>0.012</u>	<u>0.010</u>	<u>0.010</u>
Transition E	0.060	0.062	0.057	0.060	0.060	0.050	0.048	0.060	0.060
Lower									
Suction peak	-0.430	-0.510	-0.530	-0.560	-0.600	-0.620	-0.620	n/a	n/a
Transition B	-0.605	-0.634	-0.650	-0.660	-0.670	-0.670	-0.690	-0.67	-0.67
Transition E	-0.660	-0.684	-0.730	n/a	n/a	n/a	n/a	n/a	n/a

FLAP

Stagnation	-0.010	-0.010	-0.010	-0.010	-0.010	-0.010	-0.010	-0.012	-0.012
Upper									
Suction peak	0.027	0.026	0.025	0.024	0.024	0.024	0.024	0.025	0.025
Transition B	0.040	0.040	0.040	0.040	0.040	0.027	0.027	0.003	0.030
Transition E	0.080	0.080	0.075	0.072	0.072	0.073	0.068	0.080	0.080
Lower									
Suction peak	n/a								
Transition B	n/a	-0.295	-0.295	n/a	n/a	n/a	n/a	n/a	n/a
Transition E	n/a								
Extra tap row									
Suction peak	0.020	0.020	0.020	0.020	0.018	0.016	0.011	0.014	0.014

Table 5

Configuration: 30P/30N
 Mach = 0.18 Reynolds number := 15 million.
 Angle-of-attack: 4 deg. 8 deg. 10 deg. 12 deg. 16 deg. 19 deg. 21 deg. 22 deg. 23 deg.

	4 deg.	8 deg.	10 deg.	12 deg.	16 deg.	19 deg.	21 deg.	22 deg.	23 deg.
SLAT									
Stagnation	-0.003	-0.013							-0.038
Upper									
Suction peak	0.140	0.016							-0.005
Transition B	0.143	*0.040							0.016
Transition E	n/a	*0.055							0.025
Lower									
Suction peak	n/a	n/a							n/a
Transition B	-0.043	n/a							n/a
Transition E	n/a	n/a							n/a
MAIN									
Stagnation	-0.085	-0.080							-0.130
Upper									
Suction peak	-0.009	-0.050							0.0040
Transition B	*-0.007	*-0.010							*-0.010
Transition E	-0.003	*-0.004							*-0.004
Lower									
Suction peak	-0.470	-0.470							-0.580
Transition B	-0.380	*-0.360							-0.560
Transition E	-0.450	-0.440							-0.620
FLAP									
Stagnation	0.010	-0.008							-0.010
Upper									
Suction peak	0.025	0.025							0.024
Transition B	0.025	0.025							0.028
Transition E	0.040	0.040							0.040
Lower									
Suction peak	n/a	n/a							n/a
Transition B	*-0.290	*-0.290							*-0.290
Transition E	n/a	n/a							n/a
Extra tap row									
Suction peak	0.020	0.021							0.020

Table 6

Configuration:	30P/30AD								
Mach: =	0.2								
Angle-of-attack:	Reynolds number: = 9 million.								
	4 deg.	8 deg.	10 deg.	12 deg.	16 deg.	19 deg.	21 deg.	22 deg.	23 deg.
SLAT									
Stagnation	-0.002	-0.012	-0.017	-0.022	-0.035	-0.045	-0.050	-0.052	-0.054
Upper									
Suction peak	0.140	0.015	0.012	0.010	0.010	0.008	0.008	0.008	0.008
Transition B	0.140	0.052	**	0.025	0.016	0.012	0.008	0.008	0.008
Transition E	n/a	0.070	**	0.034	0.025	0.020	0.020	0.020	0.020
Lower									
Suction peak	n/a	n/a	n/a	n/a	n/a	n/a	n/a	n/a	n/a
Transition B	-0.040	n/a	n/a	n/a	n/a	n/a	n/a	n/a	n/a
Transition E	n/a	n/a	n/a	n/a	n/a	n/a	n/a	n/a	n/a
MAIN									
Stagnation	-0.0700	-0.070	-0.080	-0.100	-0.110	-0.110	-0.160	-0.150	-0.150
Upper									
Suction peak	-0.015	0.000	0.007	0.008	0.009	0.010	0.008	0.008	0.008
Transition B	0.012	<u>0.010</u>	<u>0.010</u>	0.010	0.012	0.015	-0.001	0.016	0.016
Transition E	0.050	0.050	0.050	0.030	0.025	0.030	0.033	0.030	0.030
Lower									
Suction peak	-0.470	-0.510	-0.520	-0.530	-0.640	-0.640	-0.640	-0.640	-0.640
Transition B	-0.595	-0.610	-0.625	-0.642	-0.680	*n/a	n/a	-0.680	-0.680
Transition E	-0.630	-0.675	-0.690	n/a	n/a	n/a	n/a	n/a	n/a
FLAP									
Stagnation	-0.010	-0.010	-0.009	-0.010	-0.011	-0.012	-0.011	-0.010	-0.01
Upper									
Suction peak	0.027	0.027	0.027	0.026	0.025	0.024	0.023	0.023	0.023
Transition B	0.027	0.027	0.027	0.027	0.030	0.033	0.033	0.027	0.027
Transition E	0.068	0.067	0.067	0.067	0.065	0.058	0.056	0.050	0.059
Lower									
Suction peak	n/a	n/a	n/a	n/a	n/a	n/a	n/a	n/a	n/a
Transition B	-0.290	n/a	n/a	n/a	n/a	n/a	n/a	n/a	n/a
Transition E	n/a	n/a	n/a	n/a	n/a	n/a	n/a	n/a	n/a
Extra tap row									
Suction peak	0.018	0.012	0.012	0.012	0.013	0.013	0.012	0.011	0.011

*Transition has started before cove.

Table 7

Configuration:	30P/35T								
Mach = 0.2	Reynolds number = 9 million.								
Angle-of-attack:	4 deg.	8 deg.	10 deg.	12 deg.	14 deg.	16 deg.	19 deg.	21 deg.	22 deg.
SLAT									
Stagnation	-0.003	-0.011	-0.017	-0.025	-0.035	-0.039	-0.046	-0.048	-0.048
Upper									
Suction peak	0.137	0.012	0.012	0.010	0.010	0.010	0.010	0.010	0.010
Transition B	0.143	0.047	0.034	0.017	0.017	0.015	0.010	0.006	**
Transition E	n/a	0.070	0.047	0.034	0.029	0.025	0.025	0.020	**
Lower									
Suction peak	n/a	n/a	n/a	n/a	n/a	n/a	n/a	n/a	n/a
Transition B	-0.050	n/a	n/a	n/a	n/a	n/a	n/a	n/a	n/a
Transition E	n/a	n/a	n/a	n/a	n/a	n/a	n/a	n/a	n/a
MAIN									
Stagnation	-0.065	-0.066	-0.067	-0.075	-0.110	-0.145	-0.150	-0.170	-0.160
Upper									
Suction peak	-0.008	0.000	0.005	0.007	0.009	0.010	0.009	0.009	0.009
Transition B	**	**	**	**	**	**	**	**	**
Transition E	**	**	**	**	**	**	**	**	**
Lower									
Suction peak	-0.450	-0.510	-0.510	-0.510	-0.510	-0.520	-0.520	-0.580	-0.620
Transition B	**	**	**	**	**	**	**	**	**
Transition E	**	**	**	**	**	**	**	**	**
FLAP									
Stagnation	-0.020	-0.020	-0.020	-0.0200	-0.0150	-0.0150	-0.0180	-0.0180	-0.014
Upper									
Suction peak	0.025	0.025	0.025	0.025	0.025	0.025	0.025	0.024	0.020
Transition B	0.030	0.030	0.032	0.032	0.033	0.027	0.027	0.027	0.018
Transition E	0.060	0.060	0.060	0.060	0.052	0.055	0.055	0.055	0.045
Lower									
Suction peak	n/a	n/a	n/a	n/a	n/a	n/a	n/a	n/a	n/a
Transition B	-0.180	n/a	-0.210	n/a	n/a	n/a	n/a	n/a	n/a
Transition E	n/a	n/a	n/a	n/a	n/a	n/a	n/a	n/a	n/a
Extra tap row									
Suction peak	0.010	0.010	0.010	0.011	0.012	0.012	0.012	0.012	0.012

APPENDIX 2 IMPLEMENTATION OF EXPERIMENTAL TRANSITION LOCATIONS

Since it is not self evident how to implement the experimentally determined transition locations on the high-lift model for Navier-Stokes codes, this note is written to clarify the experimental results and suggest how to utilize the information.

A2.1. COORDINATE SYSTEMS

- All coordinates used are NESTED (also denoted STOWED), i.e. independent of angle of attack and rigging.
- All coordinates are non-dimensionalized by chord (= 22 inches)
- All coordinates were obtained from the model description drawings (or in the case of the hot film locations from sensor sheet data files.

x/c	Longitudinal
y/c	Normal
	Nose/apex, slat (nested) is $x/c=0, y/c=0$
	Trailing edge/flap, flap (nested) is $x/c=1, y/c=0$
s/c	Surface coordinate, positive on the suction side, negative on the pressure side. $s/c=0$ when $y/c=0$ on the forward part of each element, which in general does not corresponding to the stagnation point. The s/c values 'wraps around', i.e. continue past corners into the cove areas. (Note that in the coves s/c is not accurate due to the ambiguity in definition of the corners.

A2.2. EXPERIMENTAL FLOW FEATURES

All experimental pressure distributions, hot film data and interpretations of these are primarily done in terms of s/c , since the purpose of the test is transition determination. x/c can be provided, but are immaterial - see A.2.3. All hot films were located at 73.4% span, while most pressure taps were located at 50 % span. (The second flap row was located at 76.9 % span).

Up through 16 degrees angle-of-attack the discrepancies in pressure distributions were moderate. Even though the films are located at 0.1-in. pitch in the most dense regions, particularly the high angle-of-attack flows may have fairly short transition regions so that only 1 or 2 films pick up the feature.

A2.3. INTERPRETATION OF FLOW FEATURES

For each element the experimental flow features are given in terms of s/c (See Appendix1):

Stagnation point	1
Suction peak(s)	1 or 2 (upper/lower)
Transition beginning	1 or 2 (upper/lower)
Transition end	1 or 2 (upper/lower)

Transition was determined based on a combination of standard deviation, skewness and flatness plus in most cases an examination of the signal traces for data quality check and exploration of auto- or cross correlations. Afterwards a quality assurance using the pressure distribution was done.

The procedure to use the information should be as follows:

A. Determine the location of the suction peak, s/c_{SP} . This will in general be different both in location and magnitude from the computed one, s/c_{SP-C} .

B. Determine the location of transition beginning and end, s/c_B & s/c_E .
Compute:

$$\Delta s/c_B = s/c_B - s/c_{SP} \quad \text{and} \quad \Delta s/c_E = s/c_E - s/c_{SP}$$

C. The transition location for the N-S computations given as:

$$s/c_{B-C} = s/c_{SP-C} + \Delta s/c_B \quad \text{and} \quad s/c_{E-C} = s/c_{SP-C} + \Delta s/c_E$$

If the suction peak is non-existent or weak (most lower surfaces), the experimental transition location can be used as is.

The logic behind the procedure is that the flow (at least for distinct suction peaks) should be assumed to have canonical pressure distributions:

- That transition or separation is mainly a result of a pressure gradient behind the suction peak and the run length (viscous) of the laminar boundary layer.
- Except for the very highest angles-of-attack, the pressure gradients in the region are off by at most a moderate percentage.
- Three-dimensional effects showing in the experiment are partly chordwise 'displacements' partly true three-dimensionality. The approach above takes care of the 'displacement'.

A2.4 TABLES RELATING SURFACE COORDINATES TO NESTED COORDINATES

FLAP				Hot films 1 -105							
no.	x/c	y/c	s/c	no.	x/c	y/c	s/c	no.	x/c	y/c	s/c
1	0.9947	0.0043	0.3178	36	0.7000	0.0082	0.0087	71	0.8480	0.0044	-0.1504
2	0.9772	0.0091	0.2996	37	0.7006	0.0038	0.0041	72	0.8526	0.0048	-0.1549
3	0.9596	0.0138	0.2814	38	0.7024	-0.0004	-0.0004	73	0.8571	0.0051	-0.1595
4	0.9420	0.0181	0.2632	39	0.7055	-0.0037	-0.0049	74	0.8616	0.0054	-0.1640
5	0.9242	0.0219	0.2451	40	0.7092	-0.0063	-0.0095	75	0.8662	0.0056	-0.1686
6	0.9063	0.0253	0.2269	41	0.7132	-0.0083	-0.0140	76	0.8707	0.0058	-0.1731
7	0.8884	0.0284	0.2087	42	0.7175	-0.0098	-0.0186	77	0.8753	0.0061	-0.1777
8	0.8704	0.0311	0.1905	43	0.7219	-0.0109	-0.0231	78	0.8798	0.0062	-0.1822
9	0.8524	0.0337	0.1723	44	0.7264	-0.0115	-0.0277	79	0.8843	0.0064	-0.1868
10	0.8344	0.0357	0.1541	45	0.7310	-0.0114	-0.0322	80	0.8889	0.0065	-0.1913
11	0.8163	0.0371	0.1360	46	0.7355	-0.0109	-0.0368	81	0.8934	0.0066	-0.1959
12	0.7981	0.0378	0.1178	47	0.7400	-0.0102	-0.0413	82	0.8980	0.0066	-0.2004
13	0.7935	0.0378	0.1132	48	0.7445	-0.0095	-0.0458	83	0.9025	0.0066	-0.2049
14	0.7890	0.0378	0.1087	49	0.7489	-0.0087	-0.0504	84	0.9071	0.0066	-0.2095
15	0.7844	0.0378	0.1041	50	0.7534	-0.0079	-0.0549	85	0.9116	0.0065	-0.2140

16	0.7799	0.0377	0.0996	51	0.7579	-0.0071	-0.0595	86	0.9162	0.0064	-0.2186
17	0.7754	0.0375	0.0951	52	0.7624	-0.0064	-0.0640	87	0.9207	0.0063	-0.2231
18	0.7708	0.0373	0.0905	53	0.7669	-0.0056	-0.0686	88	0.9252	0.0060	-0.2277
19	0.7663	0.0370	0.0860	54	0.7713	-0.0049	-0.0731	89	0.9298	0.0058	-0.2322
20	0.7617	0.0366	0.0814	55	0.7758	-0.0042	-0.0777	90	0.9343	0.0055	-0.2368
21	0.7572	0.0362	0.0769	56	0.7803	-0.0035	-0.0822	91	0.9388	0.0051	-0.2413
22	0.7527	0.0356	0.0723	57	0.7848	-0.0028	-0.0868	92	0.9434	0.0048	-0.2458
23	0.7482	0.0350	0.0678	58	0.7893	-0.0022	-0.0913	93	0.9479	0.0044	-0.2504
24	0.7437	0.0343	0.0632	59	0.7938	-0.0015	-0.0958	94	0.9524	0.0039	-0.2549
25	0.7392	0.0335	0.0587	60	0.7983	-0.0009	-0.1004	95	0.9569	0.0035	-0.2595
26	0.7348	0.0325	0.0541	61	0.8028	-0.0003	-0.1049	96	0.9615	0.0030	-0.2640
27	0.7304	0.0315	0.0496	62	0.8073	0.0003	-0.1095	97	0.9660	0.0025	-0.2686
28	0.7260	0.0302	0.0451	63	0.8118	0.0008	-0.1140	98	0.9705	0.0019	-0.2731
29	0.7217	0.0288	0.0405	64	0.8164	0.0014	-0.1186	99	0.9750	0.0013	-0.2777
30	0.7175	0.0272	0.0360	65	0.8209	0.0019	-0.1231	100	0.9795	0.0007	-0.2822
31	0.7134	0.0252	0.0314	66	0.8254	0.0024	-0.1277	101	0.9840	-0.0001	-0.2868
32	0.7095	0.0229	0.0269	67	0.8299	0.0028	-0.1322	102	0.9885	-0.0008	-0.2913
33	0.7059	0.0201	0.0223	68	0.8344	0.0033	-0.1368	103	0.9929	-0.0016	-0.2958
34	0.7028	0.0167	0.0178	69	0.8390	0.0037	-0.1413	104	0.9974	-0.0025	-0.3004
35	0.7008	0.0127	0.0132	70	0.8435	0.0041	-0.1459				

MAIN

Hot films 106 -283

no.	x/c	y/c	s/c	no.	x/c	y/c	s/c	no.	x/c	y/c	s/c
105	0.8696	0.0323	0.8343	166	0.0485	-0.0017	-0.0020	227	0.5408	-0.0437	-0.5248
106	0.8337	0.0377	0.7980	167	0.0463	-0.0056	-0.0066	228	0.5453	-0.0431	-0.5293
107	0.7976	0.0426	0.7616	168	0.0447	-0.0099	-0.0111	229	0.5498	-0.0425	-0.5339
108	0.7615	0.0467	0.7252	169	0.0439	-0.0143	-0.0157	230	0.5543	-0.0419	-0.5384
109	0.7253	0.0503	0.6889	170	0.0441	-0.0189	-0.0202	231	0.5589	-0.0413	-0.5430
110	0.6891	0.0532	0.6525	171	0.0456	-0.0231	-0.0248	232	0.5634	-0.0407	-0.5475
111	0.6528	0.0558	0.6161	172	0.0483	-0.0267	-0.0293	233	0.5678	-0.0401	-0.5521
112	0.6165	0.0578	0.5798	173	0.0519	-0.0295	-0.0339	234	0.5723	-0.0394	-0.5566
113	0.5802	0.0594	0.5434	174	0.0562	-0.0309	-0.0384	235	0.5769	-0.0388	-0.5611
114	0.5438	0.0606	0.5070	175	0.0607	-0.0318	-0.0430	236	0.5813	-0.0381	-0.5657
115	0.5075	0.0614	0.4707	176	0.0652	-0.0326	-0.0475	237	0.5858	-0.0374	-0.5702
116	0.4711	0.0618	0.4343	177	0.0696	-0.0335	-0.0521	238	0.5903	-0.0367	-0.5748
117	0.4347	0.0619	0.3979	178	0.0741	-0.0343	-0.0566	239	0.5948	-0.0360	-0.5793
118	0.3984	0.0615	0.3616	179	0.0786	-0.0350	-0.0611	240	0.5993	-0.0353	-0.5839
119	0.3620	0.0607	0.3252	180	0.0831	-0.0358	-0.0657	241	0.6038	-0.0345	-0.5884
120	0.3257	0.0596	0.2889	181	0.0876	-0.0365	-0.0702	242	0.6083	-0.0338	-0.5930
121	0.3075	0.0588	0.2707	182	0.0920	-0.0372	-0.0748	243	0.6128	-0.0330	-0.5975
122	0.2893	0.0580	0.2525	183	0.0965	-0.0378	-0.0793	244	0.6172	-0.0323	-0.6020
123	0.2712	0.0570	0.2343	184	0.1010	-0.0385	-0.0839	245	0.6217	-0.0315	-0.6066
124	0.2530	0.0560	0.2161	185	0.1056	-0.0391	-0.0884	246	0.6262	-0.0307	-0.6111
125	0.2349	0.0548	0.1980	186	0.1101	-0.0397	-0.0930	247	0.6307	-0.0300	-0.6157
126	0.2168	0.0535	0.1798	187	0.1146	-0.0403	-0.0975	248	0.6352	-0.0292	-0.6202
127	0.2122	0.0531	0.1752	188	0.1191	-0.0409	-0.1020	249	0.6396	-0.0284	-0.6248
128	0.2077	0.0528	0.1707	189	0.1236	-0.0415	-0.1066	250	0.6441	-0.0276	-0.6293
no.	x/c	y/c	s/c	no.	x/c	y/c	s/c	no.	x/c	y/c	s/c

129	0.2032	0.0524	0.1661	190	0.1281	-0.0420	-0.1112	251	0.6486	-0.0267	-0.6339
130	0.1986	0.0520	0.1616	191	0.1326	-0.0425	-0.1157	252	0.6531	-0.0259	-0.6384
131	0.1941	0.0516	0.1570	192	0.1371	-0.0430	-0.1202	253	0.6575	-0.0251	-0.6430
132	0.1896	0.0512	0.1525	193	0.1416	-0.0435	-0.1248	254	0.6620	-0.0243	-0.6475
133	0.1851	0.0508	0.1479	194	0.1462	-0.0440	-0.1293	255	0.6665	-0.0235	-0.6520
134	0.1805	0.0504	0.1434	195	0.1507	-0.0445	-0.1339	256	0.6709	-0.0226	-0.6566
135	0.1760	0.0500	0.1389	196	0.1552	-0.0449	-0.1384	257	0.6754	-0.0218	-0.6612
136	0.1715	0.0495	0.1343	197	0.1597	-0.0454	-0.1430	258	0.6799	-0.0210	-0.6657
137	0.1670	0.0490	0.1298	198	0.1643	-0.0458	-0.1475	259	0.6843	-0.0201	-0.6702
138	0.1624	0.0486	0.1252	199	0.1688	-0.0462	-0.1521	260	0.6888	-0.0193	-0.6748
139	0.1579	0.0480	0.1207	200	0.1733	-0.0466	-0.1566	261	0.6933	-0.0185	-0.6793
140	0.1534	0.0474	0.1161	201	0.1778	-0.0470	-0.1612	262	0.6977	-0.0177	-0.6839
141	0.1490	0.0466	0.1116	202	0.1824	-0.0474	-0.1657	263	0.7022	-0.0168	-0.6884
142	0.1445	0.0457	0.1070	203	0.1869	-0.0478	-0.1702	264	0.7000	0.0140	-0.7275
143	0.1401	0.0446	0.1025	204	0.1914	-0.0481	-0.1748	265	0.7000	0.0236	-0.7371
144	0.1357	0.0436	0.0979	205	0.1960	-0.0485	-0.1793	266	0.7696	0.0321	-0.8151
145	0.1312	0.0424	0.0934	206	0.2005	-0.0488	-0.1839	267	0.7787	0.0321	-0.8242
146	0.1269	0.0413	0.0889	207	0.2050	-0.0492	-0.1884	268	0.7878	0.0321	-0.8333
147	0.1225	0.0400	0.0843	208	0.2096	-0.0495	-0.1930	269	0.7923	0.0321	-0.8378
148	0.1181	0.0387	0.0798	209	0.2141	-0.0498	-0.1975	270	0.7968	0.0321	-0.8424
149	0.1138	0.0373	0.0752	210	0.2186	-0.0501	-0.2020	271	0.8014	0.0321	-0.8469
150	0.1095	0.0359	0.0707	211	0.2232	-0.0504	-0.2066	272	0.8059	0.0321	-0.8515
151	0.1052	0.0344	0.0661	212	0.2277	-0.0507	-0.2112	273	0.8105	0.0321	-0.8560
152	0.1009	0.0328	0.0616	213	0.2322	-0.0509	-0.2157	274	0.8150	0.0321	-0.8605
153	0.0967	0.0311	0.0570	214	0.2368	-0.0512	-0.2202	275	0.8196	0.0321	-0.8651
154	0.0925	0.0294	0.0525	215	0.2413	-0.0515	-0.2248	276	0.8241	0.0321	-0.8697
155	0.0884	0.0276	0.0480	216	0.2595	-0.0524	-0.2430	277	0.8287	0.0321	-0.8742
156	0.0842	0.0256	0.0434	217	0.2776	-0.0531	-0.2611	278	0.8332	0.0321	-0.8787
157	0.0802	0.0236	0.0389	218	0.2958	-0.0537	-0.2793	279	0.8377	0.0321	-0.8833
158	0.0762	0.0214	0.0343	219	0.3140	-0.0541	-0.2975	280	0.8423	0.0321	-0.8878
159	0.0722	0.0192	0.0298	220	0.3503	-0.0545	-0.3339	281	0.8514	0.0321	-0.8969
160	0.0684	0.0168	0.0252	221	0.3867	-0.0543	-0.3702	282	0.8605	0.0319	-0.9060
161	0.0646	0.0142	0.0207	222	0.4231	-0.0532	-0.4066	283	0.8696	0.0312	-1.5957
162	0.0610	0.0115	0.0161	223	0.4594	-0.0513	-0.4430				
163	0.0575	0.0085	0.0116	224	0.4956	-0.0485	-0.4793				
164	0.0542	0.0054	0.0070	225	0.5318	-0.0447	-0.5157				
165	0.0512	0.0020	0.0025	226	0.5363	-0.0442	-0.5202				

SLAT

Hot films 284 -359

no.	x/c	y/c	s/c	no.	x/c	y/c	s/c	no.	x/c	y/c	s/c
284	0.1432	0.0464	0.1566	309	0.0316	0.0257	0.0430	334	0.0410	-0.0102	-0.0842
285	0.1387	0.0459	0.1521	310	0.0273	0.0241	0.0384	335	0.0449	-0.0021	-0.0933
286	0.1341	0.0454	0.1475	311	0.0231	0.0225	0.0339	336	0.0476	0.0016	-0.0978
287	0.1296	0.0448	0.1430	312	0.0190	0.0206	0.0294	337	0.0506	0.0050	-0.1024
288	0.1251	0.0442	0.1384	313	0.0149	0.0185	0.0248	338	0.0538	0.0082	-0.1069
289	0.1206	0.0436	0.1339	314	0.0110	0.0162	0.0202	339	0.0573	0.0112	-0.1115
290	0.1161	0.0430	0.1293	315	0.0074	0.0134	0.0157	340	0.0608	0.0140	-0.1160
291	0.1116	0.0424	0.1248	316	0.0042	0.0102	0.0112	341	0.0645	0.0166	-0.1206
292	0.1071	0.0417	0.1203	317	0.0016	0.0065	0.0066	342	0.0683	0.0191	-0.1251

293	0.1026	0.0410	0.1157	318	0.0002	0.0022	0.0021	343	0.0722	0.0215	-0.1296
294	0.0981	0.0403	0.1112	319	0.0002	-0.0023	-0.0025	344	0.0761	0.0238	-0.1342
295	0.0936	0.0396	0.1066	320	0.0018	-0.0066	-0.0070	345	0.0802	0.0259	-0.1388
296	0.0892	0.0389	0.1021	321	0.0044	-0.0102	-0.0116	346	0.0843	0.0279	-0.1433
297	0.0847	0.0381	0.0975	322	0.0077	-0.0134	-0.0161	347	0.0884	0.0298	-0.1478
298	0.0802	0.0373	0.0930	323	0.0114	-0.0160	-0.0207	348	0.0926	0.0316	-0.1524
299	0.0757	0.0365	0.0884	324	0.0154	-0.0182	-0.0252	349	0.0968	0.0332	-0.1569
300	0.0713	0.0356	0.0839	325	0.0195	-0.0202	-0.0297	350	0.1010	0.0348	-0.1615
301	0.0668	0.0347	0.0794	326	0.0237	-0.0219	-0.0343	351	0.1054	0.0363	-0.1660
302	0.0624	0.0338	0.0748	327	0.0279	-0.0235	-0.0388	352	0.1097	0.0377	-0.1706
303	0.0579	0.0328	0.0702	328	0.0323	-0.0249	-0.0434	353	0.1140	0.0390	-0.1751
304	0.0535	0.0318	0.0657	329	0.0366	-0.0261	-0.0479	354	0.1184	0.0402	-0.1796
305	0.0491	0.0307	0.0612	330	0.0410	-0.0273	-0.0525	355	0.1228	0.0413	-0.1842
306	0.0447	0.0296	0.0566	331	0.0454	-0.0284	-0.0570	356	0.1273	0.0423	-0.1887
307	0.0403	0.0284	0.0521	332	0.0452	-0.0268	-0.0660	357	0.1317	0.0432	-0.1933
308	0.0360	0.0271	0.0475	333	0.0405	-0.0192	-0.0751	358	0.1361	0.0442	-0.1978
								359	0.1406	0.0452	-0.2024

APPENDIX 3

ASSESSMENT OF VALIDITY OF THE EXPERIMENT

In this section some of the conditions that may affect the validity and usefulness of the data are discussed - assessments are included throughout the report. It is important to distinguish between local and global disturbances, local disturbances alter the flow only at the disturbance location and will not have any measurable effects downstream or to the sides, while global disturbances (e.g. tripping transition) will have effects that may jeopardize the test as a code validation case.

A3.1 Film sheet effect

The hot films were applied to each of the three elements deposited on separate polyamide film sheets wrapping around each element. The sheet was 0.002 in. thick and the glue layer thickness was approximately 0.002 in., i.e. a total of 0.004 in., or roughly 0.02% of chord. Since 30P/30N has a gap of 1.27% and 30P/30AD 1.50%, the values would change to 1.25% and 1.48% respectively, while the overhang of nominally 0.25 % would go to 0.23 %.

A number of concerns exist:

- Sheet thickness. The geometry of the elements are somewhat changed, but it is doubtful that the gaps may be sufficiently modified to alter the flow. The radius of curvature is different, but probably not enough to matter.
- Surface roughness. The leads were also deposited on the sheets, and there is in certain instances concern that the surface roughness is affecting the turbulent boundary layer.
- Sheet bubbling occurred at least during the last part of the test over the flap region.
- Sheet edge. This was initially smooth, but there may be some effects both initially and as the test progressed.

The overall effect of the film sheet could be observed in several of the parameters. Figure A3.1 illustrates the overall effect on the lift coefficient, as expressed in CLCOMBO. It is clear that although the effect at low angles-of-attack is of the same order of magnitude as the repeatability, the behavior at high angles is appreciable. The figure exemplifies data taken early and late in the test, corresponding to the initial (early) 30P/30N runs in the beginning of the experiment, and late, corresponding to data obtained during the last part of the test, when the cove sensors were used.

Splitting the information up into the three elements, it is clear that the main effect occurs for the wing box .The local effects are found in the pressure distributions demonstrated in Figure A3.2. The effects at mid span appear negligible, but a comprehensive assessment of the effects involves performing boundary layer computations for the two cases.

Splitting the information up into the three elements, it is clear that the main effect occurs for the wing box .The local effects are found in the pressure distributions exemplified in Figure A3.2. As can be seen the effects at mid span appear negligible, but a comprehensive assessment of the effects involves performing boundary layer computations for the two cases.

The viscous effects of the films are shown in Figure A3.3a and A.3.3b. The wakes have essentially similar drag characteristics, but are displaced vertically - suggesting that there is a redistribution of the spanwise loading of the high-lift configuration rather than an increase in drag, as will be illustrated later in the Appendix.

It would have been desirable to make comparisons also at $Re=5$ million, but unfortunately no clean wing data is available.

A3.2 Three-dimensionality

This is due to tunnel inflow conditions, sidewall boundary layers, flap brackets etc. No thorough effort was carried through during the experiment to investigate these effects, and throughout the report the main information used is the spanwise pressure distributions on the elements along with the secondary chordwise row on the flap.

Figures A3.4a through A.3.4d show spanwise pressure distributions for each element as function of angle of attack, for the most benign configuration, 30P/30N at Mach=0.2, $Re=9$ mill, clean surface. To further illustrate the effect of the hot film sheet, spanwise pressure distributions with and without film sheet present have been compared in Figures A3.5a through A.3.5d. As expected, the spanwise non-uniformity increases with angle of attack, and is more pronounced on the flap, compared with conditions further forward.

It is clear that the film had a moderate effect on the spanwise pressure distribution for angles of attack up to maximum lift. At higher angles the discrepancies are appreciable.

A3.3 Sidewall mass-flow

The sidewall suction is estimated from a series of rakes in the suction box arrangement, integrated to provide the mass flow. The suction setting was done to minimize spanwise pressure gradients at 16 degrees angle-of-attack. The main tunnel correction done for the pressure data is in terms of a correction to each pressure measured (CFSP) computed from the estimated mass flow. Figure 6c shows the typical value for the tunnel correction as function of reference parameters. Since the tunnel calibration factors used in the previous tests are not available, further comparisons will not be included in the present report.

A3.4 BLT (Boundary-layer-Traversal) influence

During the Reynolds stress measurements (also denoted test 397 or K), the model was bare, but to hold the traversing x-wire, a fairly bulky traversing device had to be used (BLT), to ensure that the high air loads could be accommodated. Figure A3.6 illustrates that the device had a measurable effect even as far as the integrated lift coefficients are concerned. Figure A3.7 illustrates that the effect on flap pressure distributions at midspan is moderate. To confirm the effects, the suction peak and rear regions have been replotted in Figures A3.8a and A.3.8b.

As can be expected, the effects are larger on the flap pressure distribution at the same spanwise location as where the BLT was located. Figure A3.9 shows the distributions for various BLT locations at 19 degrees angle of attack.

A3.5 Comparisons with previous tests

The model hardware has been tested in LTPT several times earlier, and also the current riggings have been explored. Figure A3.10 contains a comparison of pressure distributions on the slat for low angles of attack. There are clear differences, but no further evaluation is considered part of this report, since the information available on tunnel venting, data processing etc. is available. In Figure A3.10 the main difference appears to be a difference in reference pressure, corresponding to a shift in C_p values of 0.02 - 0.04.

At higher angles of attack the difference increases somewhat, as illustrated in Figure A3.11. The large difference in suction peak value may be attributable to local leading edge imperfections that may have affected the measurements.

The main element pressure distributions confirm the reference level shift. Figures A3.12a through c shows details of the comparison, illustrating moderate differences, as shown later combined with lateral pressure redistribution.

Figures A3.13a and A3.13b show that the Reynolds number effects from 5 to 9 million are, within measurement accuracy, similar during tests K and G for the main element.

Another issue is the repeatability and comparison of spanwise pressure distributions. In Figures A3.14a through A3.14d the spanwise distributions have been plotted for high angles of attack. It is clear that up through 19 degrees the agreement is fair. The spanwise redistribution has been further documented.

The repeatability is documented in Figure A3.15, where the distributions at the trailing edge of the flap are illustrated. It is clear that the repeatability within tests is better than the repeatability from test to test. The figure also indicates that test K deviates whether or not the film sheet was present.

APPENDIX 4 LOGBOOK TABLES

A4.1 Hot film records and corresponding pressure data

This section contains a list of data points and tunnel conditions along with an indication of whether or not the data has been analyzed. For accessing the original raw or reduced data, the database report should be used.

Point-1 has been used for the merged data, while Point-2 and -3 in general has not been analyzed since they are repeat runs as far as the pressure is concerned but contains additional hot film data.

File denotes the name of the original pressure file for each run.

Each record in the database has its unique name, and through recording this name along with the statistical output from the codes, it is possible at any stage to go back and revalidate or enhance the data. Typically this means that the same record can be reanalyzed using more recent techniques if need arises.

The convention is as follows:

Since System A and System B files are separate, the record name applies to both:

<Date><file letter><record number in file>.

Film-1, -2 and -3 provides the record names for the hot film data. For example, the hot film records for data taken during Point 51 (30P/30N, Mach=0.2, Re=9 mill, 8 degrees angle of attack) which were recorded on August 5, can be found in the files 5A.hfc and 5B.hfc (System A or B), records 66 through 193.

Points 79 through 103 (Pressure files asc010 through asc012) contain repeat runs of 30P/30N taken in a different sequence than normal, to sort out repeatability issues. They are not included in the processed database.

Comments relate to how the data has been utilized. 'Not processed' means that it is not available in the database, often due to time limitations for the work. 'Not analyzed' means that it exists in processed form and may be part of the present report, but the information has not been interpreted as transition data.

Configuration: 30P/30N

Date: August 5, 1996

Mach number: 0.2

Reynolds number: 9 mill.

α	Point-1	Point-2	Point-3	Film-1	Film-2	Film-3	Comment
4	50	61	70	b450-c81	e418-f65	h18-h145	
8	51	62	71	c82-c209	f66-f193	h146-h273	
10	52	63	72	c210-c337	f194-f321	h274-h417	
12	53	64	73	c338-c449	f322-f449	h418-i033	
16	54	65	74	c450-d97	f450-g97	i34-i161	
19	55	66	75	d98-d225	g98-g209	i62-i289	
21	56	67	76	d226-d369	g210-g337	i290-i417	
22	57	68	77	d370-e33	-	i418-j65	
23	58	69	78	e34-e161	g338-h17	j66-j177	
File	asc007	asc008	asc009				

Configuration: 30P/30N

Date: August 7, 1996

Mach number: 0.15

Reynolds number: 9 mill.

α	Point-1	Point-2	Point-3	Film-1	Film-2	Film-3	Comment
4	110	120	129	b96-b287	e464-f175	j144-j335	
8	111	121	130	b288-b479	f324-g47	j336-k63	
10	113	122	131	c1-c191	g48-g255	k64-k255	Not processed
12	114	123	132	c192-c399	g256-g463	k256-k463	Not processed
16	115	124	133	c400-d111	h64-h271	k464-l175	Not processed
19	116	125	134	d112-d319	h272-h463	l176-l383	
21	117	126	135	d320-e31	h464-i175	l384-m95	
22	118	127	136	e32-e239	i176-i383	m96-m287	Not processed
23	119	128	137	e240-e463	i384-j143	m288-n15	Not processed
File	asc014	asc015	asc016				

Configuration: 30P/30N

Date: August 7, 1996

Mach number: 0.23

Reynolds number: 9 mill.

α	Point-1	Point-2	Point-3	Film-1	Film-2	Film-3	Comments
4	138	146	154	n16-n207	p464-q175	t225-t431	Not processed
8	139	147	156	n208-n431	q176-q367	t624-t815	
10	140	148	157	n432-o63	q368-r79	t816-t1023	Not processed
12	142	149	158	o64-o255	r80-r271	t1024-t1087	Not processed
16	143	150	160	o256-o447	r272-r463	t1329-t1519	Not processed
19	144	151	161	o448-p191	r464-s175	t1520-t1679	
21	145	152	162	p192-p383	s240-s463	t1680-t1887	
File	asc017	asc018	asc019				

Configuration: 30P/30N

Date: August 8, 1996

Mach number: 0.20

Reynolds number: 5 mill.

α	Point-1	Point-2	Point-3	Film-1	Film-2	Film-3	Comments
4	178	188	197	a48-a239	e49-e240	j340-k64	
8	179	189	198	a240-a431	e241-e432	k65-k256	
10	180	190	199	a432-b143	e433-f160	k257-k448	
12	181	191	200	b144-b335	f161-f368	k449-l176	
16	182	192	201	b336-c79	f369-g80	l177-l384	
19	183	193	202	c80-c271	g81-g272	l385-m112	
21	186	194	203	d145-d336	g273-g464	m113-m304	
22	185	195	204	c400-d144	g465-h176	m305-n32	Not analyzed
23	187	196	205	d337-e48	h177-h400	n33-n240	Not analyzed
File	asc022	asc023	asc024				

Configuration: 30P/30N

Date: August 8, 1996

Mach number: 0.20

Reynolds number: 12 mill.

α	Point-1	Point-2	Point-3	Film-1	Film-2	Film-3	Comments
4	208	217	224	o337-p48	s177-s343	t1089-t1233	Not processed
8	209	218	225	p49-p256	s388-t80	t1295-t1456	Not analyzed
10	211	219	226	p385-q112	t81-t247	t1457-t1614	Not processed
12	212	220	227	q113-q304	t281-t447	t1676-t1791	Not processed
16	213	221	228	q305-r16	t483-t626	t1868-t1982	Not processed
19	214	222	229	r17-r208	t674-t848	-	Not analyzed
21	215	223	230	r209-r400	t849-t1051	t2239-t2247	Not analyzed
22	216	-	-	r465-s176	-	-	Not processed
23	-	-	-	-	-	-	Not processed or checked
File	asc025	asc026	asc027				

Configuration: 30P/30N

Date: August 9, 1996

Mach number: 0.18

Reynolds number: 15 mill

α	Point-1	Point-2	Point-3	Film-1	Film-2	Film-3	Comments
4	233	237	241	b304-c15	d200-d415	e448-f159	
8	234	238	242	c16-c207	e416-e127	f160-f351	
16	235	239	244	c208-c399	e128-e239	f352-g63	
File	asc028	asc029	asc030				

Configuration: 30P/30AD

Date: August 12, 1996

Mach number: 0.20

Reynolds number: 9 mill.

α	Point-1	Point-2	Point-3	Film-1	Film-2	Film-3	Comments
4	251	261	271	b74-b255	f128-f319	j1-j191	
8	252	262	272	b261-b445	f320-g47	j192-j383	
10	253	263	274	b464-c173	g48-g255	k80-k287	
12	254	264	277	c183-c383	g256-g463	k288-k479	
16	255	265	279	c407-d95	g464-h175	l1-l191	
19	256	266	280	d112-d287	h176-h367	l192-l415	
21	258	267	281	e1-e207	h368-i79	l416-m159	
22	259	268	282	e208-e399	i80-i287	m160-m367	
23	260	269	283	e400-f127	i288-i479	m368-n79	
File	asc032	asc033	asc034				

Configuration: 30P/30AD

Date: August 13, 1996

Mach number: 0.23

Reynolds number: 9 mill.

α	Point-1	Point-2	Point-3	Film-1	Film-2	Film-3	Comments
4	287	295	303	b48-b223	f144-g15	j16-j207	Not analyzed
8	288	296	304	b224-b383	g16-g287	j208-j400	Not processed
10	289	297	305	b384-c127	g288-h15	j401-k111	Not processed
12	290	298	306	c128-c335	h16-h207	k112-k303	Not processed
16	291	299	307	c336-d47	h208-h399	k304-l15	Not processed
19	292	300	308	d48-d239	h400-i111	l16-l182	Not analyzed
21	293	301	309	d240-d431	i112-i303	m1-m127	Not analyzed
22	294	302	310	d432-e143	i304-j15	m128-m351	Not processed
File	asc036		asc037	asc038			

Configuration: 30P/30AD

Date: August 14, 1996

Mach number: 0.2

Reynolds number: 5 mill.

α	Point-1	Point-2	Point-3	Film-1	Film-2	Film-3	Comments
4	-	324	337	-	f324-g47	j368-k94	Not processed
8	314	325	338	b242-b431	g48-g175	k95-k287	Not analyzed
10	315	327	339	b432-c143	g416-h127	k288-k479	Not processed
12	316	329	340	c144-c335	h128-h334	l1-l223	Not processed
16	317	330	341	c336-d63	h336-i47	l224-l415	Not processed
19	318	331	342	d64-d239	i48-i239	l46-m127	Not analyzed
21	319	333	343	d240-d431	i240-i447	m128-m319	Not analyzed
22	321	334	344	d432-e159	i448-j159	m320-n31	Not processed
23	322	336	345	e160-e360	j160-j367	n68-n271	Not processed
File	asc040	asc041	asc042				

Configuration: 30P/35T

Date: August 19, 1996

Mach number: 0.2

Reynolds number: 9 mill.

α	Point-1	Point-2	Point-3	Film-1	Film-2	Film-3	Comments
4	356	369	379	b48-b255	f400-g110	j320-k47	
8	357	370	380	b256-b447	g111-g303	k48-k239	
10	358	371	381	b448-c159	g304-h31	k240-k463	
12	359	372	382	c160-c353	h32-h223	k464-l175	
14	366	373	383	e368-f79	h272-h479	l176-l383	
16	360	374	384	c354-d63	i1-i191	l384-m95	
19	361	376	385	d64-d255	i192-i383	m96-m303	
21	363	377	386	d256-d447	i392-j95	m404-n15	
22	364	378	387	d448-e191	j96-j303	n16-n159	
23	365	-	-	e192-e367	-	-	Not processed
File	asc049	asc050	asc051				

Configuration: 30P/35T

Date: August 19, 1996

Mach number: 0.2

Reynolds number: 5 mill.

α	Point-1	Point-2	Point-3	Film-1	Film-2	Film-3	Comments
4	389	398	407	n368-o79	r288-r479	t1072-t1263	Not processed
8	390	399	409	o128-o335	s1-s190	t1264-t1455	Not analyzed
10	391	400	411	o336-p47	s191-s383	t1456-t1663	Not processed
12	392	401	412	p48-p255	s385-t95	t1664-t1855	Not processed
14	393	402	413	p256-p447	t96-t287	t1856-t2047	Not processed
16	394	403	414	p448-q159	t288-t479	t2048-t2239	Not processed
19	395	404	415	q160-q367	t480-t671	t2240-t2431	Not analyzed
21	396	405	416	q368-r95	t572-t863	t2432-t2639	Not analyzed
22	397	406	417	r96-r287	t864-t1071	t2640-t2831	Not processed
File	asc052	asc053	asc054				

Configuration: 30P/30N

Date: August 21, 1996

Mach number: 0.2

Reynolds number: 5 mill.

Arrangement: Coves

α	Point-1	Point-2	Point-3	Film-1	Film-2	Film-3	Comments
4	420	429	-	b309-b361	f464-g303	-	
8	421	430	-	c48-c100	g304-h143	-	
10	422	433	-	c312-c480	h304-i142	-	
12	423	435	-	d73-d248	i143-i463	-	
16	424	436	-	d296-d480	i464-j287	-	
19	425	437	-	e21-e239	j288-k111	-	
21	426	438	-	e240-e463	k112-k431	-	
22	427	439	-	e464-f223	k432-l287	-	
23	428	-	-	f224-f463	-	-	
File	asc055	asc056					

A4.2 Clean model pressure data

Points run with Clean model (film sheets removed, polished) after the hot film runs are listed below. Only configuration 30P/30N was documented.

Mach	0.2	0.2	0.2
Re [mill]	9	12	9
α [deg]			
4	462	471	-
8	463	472	480
10	464	473	-
12	465	474	-
16	466	475	-
19	467	476	-
21	468	477	-
22	469	478	-
23	470	479	-
File	asc071	asc072	asc073

After the hot film experiment was finished, the Reynolds stress measurements were carried out. During these measurements, Points of pressure data were taken with the Boundar Layer Traverse (BLT) present. All data pertain to 30P/30N and 30P/35T, and had a target Mach \approx 0.2, and have been included in the processed database:

File	Configuration	Mach	Re [mill]	BLTposition	$\alpha=8$	$\alpha=19$	$\alpha=21$
asc077	30P/30N	0.2	9	0.85	495,496	497	498
asc078	30P/30N	0.2	9	0.7175	509	510	511
asc079	30P/30N	0.2	5	0.7175	513	514	515
asc080	30P/30N	0.2	9	0.1075	520	521	522
asc085	30P/30N	0.2	9	0.15	544	545	546
asc087	30P/30N	0.19	15	0.87	552	553	554
asc088	30P/30N	0.2	9	0.85	558	559	560
asc089	30P/35T	0.2	9	0.7175	566	567	568
asc090	30P/35T	0.2	9	0.87	572	573	574

A4.3 Wake data

The traversing wake rake was used at approximately the 74 % span location during the hot film test both with the hot film sheet mounted and (from Point 462 on) after the film sheet had been removed. No comment below means hot film sheets were mounted, standard set of films were active. 'Repeat' means that the film sheets are present but 'Cove' sensor arrangement active. 'Clean' model means that the film sheets have been removed and the model polished. Processed data is available in the database for all indicated Points below. Note that the Points for some tunnel conditions are not among the ones used for the hot film analysis (see Appendix A4.1).

Wake rake data was obtained during the following Points:

Configuration	Mach	Re[mill]	Angle of attack [deg]						Comments
			4	8	10	12	14	16	
30P/30N	0.2	9	50	51	52	53	-	54	
30P/30N	0.15	9	110	111	-	-	-	115	
30P/30N	0.23	9	138	-	140	-	-	143	
30P/30N	0.2	5	165	166	-	-	-	169	
30P/30N	0.2	12	208	210	-	-	-	213	
30P/30AD	0.2	9	270	273	275	276	-	278	
30P/30AD	0.23	9	287,303	304	-	-	-	307	
30P/30AD	0.2	5	313	314	-	-	-	317	
30P/35T	0.2	9	356	357	358	359	373	360	
30P/35T	0.2	5	389	390	-	-	-	394	
30P/30N	0.2	9	420	421	422	423	-	424	Repeat
30P/30N	0.2	9	462	463	464	465	-	466	Clean model
30P/30N	0.2	12	471	472	-	-	-	475	Clean model
30P/30N	0.2	9	-	480	-	-	-	-	Clean model

LIST OF FIGURES

- 1 LTPT wind tunnel
- 2a Location of tap rows, upper side
- 2b Location of tap rows, lower side
- 3 Location of hot films
- 4a Riggings - slat
- 4b Riggings - flap
- 4c Riggings - configuration
- 5 Mach vs. Re for different configurations
- 6a Repeatability of Mach/Re
- 6b Repeatability, dRN vs Alpha
- 6c Repeatability , CFSP vs RN
- 7 Experimental information - parameters
- 8 Repeatability. CLCOMBO vs ALPHA
- 9a Repeatability. CLSLAT vs ALPHA
- 9b Repeatability. CLWBOX vs ALPHA
- 9c Repeatability. CLFLAP vs ALPHA
- 10 Ceiling & floor pressures for different Alpha
- 11 Comparison CLwall & CLCOMBO
- 12 Repeatability. Drag polars CLS1 vs CDS1
- 13 Polar. CLCOMBO vs CMCOMBO for different Re.
- 14 Comparison & repeatability. CMCOMBO & CMYS vs ALPHA
- 15 Moment coefficients for each element vs ALPHA
- 16 Wake profile example, U2 vs Z2
- 17 Wake profiles, non-dimensional velocity vs x
- 18 Wake profile example, V2 vs x
- 19 Wake profile example, W2 vs Z2
- 20 Viscous Drag (Squire-Young & CDTOT2) vs ALPHA
- 21 Pressure distr. main , standard amd original.
- 22 Mach number distributions on tunnel walls, ceiling/floor/average
- 23 M.local distributions on slat, main and flap
- 24a Repeatability, Cp.main
- 24b Repeatability, Cpmain
- 25 Repeatability, dCp. main
- 26 Relation between local Mach vs Cp for different Mach.ref.
- 27 Cp.slat in stagn. region
- 28a Mach.slat in stagn. region
- 28b Mach.main in stagn. region
- 28c Mach.flap in stagn. region
- 29a Cp.main suction peak - Bezier
- 29b Cp.main sucron peak - Bezier detail
- 30 Cp.main upper - Computed & experimental transition locations
- 31 Ue & Cf main lower - Computed & experimental transition locations
- 32 Cp.main - comparison g & k. Alpha=16 deg.
- 33 Cp.main differences g & k. Alpha=8,16 & 19 deg.
- 34a Cp.main. Differences Re=5 & 9 mill. Alpha = 8 deg.
- 34b Cp.main. Differences Re=5 & 9 mill. Alpha = 16 deg.
- 34c Cp.main. Differences Re=5 & 9 mill. Alpha = 19 deg.

- 35a Cp.slat Alpha=8, 16 and 19 deg.
- 35b Cp.main Alpha=8, 16 and 19 deg.
- 35c Cp.flap Alpha=8, 16 and 19 deg.
- 36a Cp.slat Alpha=8, 16 and 19 deg. Nose region.
- 36b Cp.main Alpha=8, 16 and 19 deg. Nose region.
- 36c Cp.flap Alpha=8, 16 and 19 deg. Nose region.
- 37a Standard deviation.slat Alpha=8, 16 and 19 deg. Nose region.
- 37b Standard deviation.main Alpha=8, 16 and 19 deg. Nose region.
- 37c Standard deviation.flap Alpha=8, 16 and 19 deg. Nose region.
- 38a Skewness.slat Alpha=8, 16 and 19 deg. Nose region.
- 38b Skewness.main Alpha=8, 16 and 19 deg. Nose region.
- 38c Skewness.flap Alpha=8, 16 and 19 deg. Nose region.
- 39 Flatness and intermittency versus Skewness. Ideal.
- 40a Flatness.slat Alpha=8, 16 and 19 deg. Nose region.
- 40b Flatness.main Alpha=8, 16 and 19 deg. Nose region.
- 40c Flatness.flap Alpha=8, 16 and 19 deg. Nose region.
- 41 Flatness vs Skewness. Flap. Alpha=10 to 16 deg.
- 42 Transition region characteristics. Flap.
- 43 CLCOMBO vs Alpha for 30N & 30AD close to CLmax. 5 mill.
- 44 CLS1 vs Alpha for 30N & 30AD close to CLmax. 5 mill.
- 45a CLCOMBO etc for 30P/30N. Re=5 & 9 mill.
- 45b CLCOMBO etc for 30P/30AD. Re=5 & 9 mill.
- 46 Average of 3 polars; CLCOMBO & CLS1 vs Alpha. Re=5 mill.
- 47 Mach effect on CLCOMBO etc. 30P/30N
- 48 dCL(Re) 5 & 9 mill vs Alpha; CLCOMBO & CLwall.
- 49 dCL(Re) 9 & 12 mill vs Alpha. CLCOMBO + elements.
- 50a Cp.main at 9 & 12 mill. Alpha=21 deg.
- 50b Cp.main at 9 & 12 mill. Alpha=21 deg. Zoom of differences.
- 51a Transition 30P/30N Re=9 mill. Slat.
- 51b Transition 30P/30N Re=9 mill. Main.
- 51c Transition 30P/30N Re=9 mill. Flap.
- 52 Flow features. Slat. Alpha=4 deg
- 53 Flow features. Slat. Alpha=16 deg
- 54 Flow features. Flap. Alpha=4 deg
- 55 Flow features. Flap. Alpha=16 deg
- 56a Standard deviation.slat Alpha=4,8,10,12 deg.
- 56b Skewness.slat Alpha=4,8,10,12 deg.
- 56c Flatness.slat Alpha=4,8,10,12 deg.
- 57 Cp.main. Alpha=4,8,10,12 deg.
- 58 Cp.main.Zoom lower. Alpha=4,8,10,12 deg.
- 59 Cp.flap. Alpha=4,8,16,19,21,23 deg.
- 60 Cp.flap & Cp.flap.aux. Alpha=4,21,23 deg.
- 61 Cp.flap.suction peak & trailing edge vs Alpha. 30N,30AD & 35T
- 62 Cross-correlation vs s/c.slatcove. 30N M=0.2 Re=9 mill. Various Alpha
- 63 Time shift vs s/c.slatcove. 30N M=0.2 Re=9 mill. Various Alpha
- 64 s/c.slat of flow features in cove vs Alpha.
- 65 Slat flow features; stagnation,transition,reattachment. Various alpha
- 66 Stdev & Flatness vs s/c.slat Alpha = 19 deg.
- 67a Transition 30P/30N Re=5 mill. Slat.

67b Transition 30P/30N Re=5 mill. Main.
67c Transition 30P/30N Re=5 mill. Flap.
68 Re effect Transition 30P/30N. Slat.
69 Re effect. Cp distr. slat 5,9,12 & 15 mill.
70a Cp & std.dev. main. Re= 5 mill. Alpha=8 deg
70b Cp & std.dev. main. Re=15 mill. Alpha=8 deg
71 Cp.main Comparison 5 & 9 mill Nose region. Alpha=4 deg
72a Stdev .main nose. Re=5 mill, Alpha 4-21 deg.
72b Stdev .main nose. Re=9 mill, Alpha 4-21 deg.
73 Signal traces Main, Re=5 mill. Alpha=4 deg
74 Cross-correlation. Main. Re=5 mill. Shows bubble. Alpha=4 deg
75 Cp & std.dev. flap. Re= 5 mill. Alpha=8 deg
76 Mach number effect on slat. 30P/30N Alpha=19 deg.
77 Mach number effect on main. 30P/30N Alpha=19 deg.
78 Mach number effect on flap. 30P/30N Alpha=19 deg.
79a Transition 30P/30AD Re=9 mill. Slat.
79b Transition 30P/30AD Re=9 mill. Main.
79c Transition 30P/30AD Re=9 mill. Flap.
80a Comparison 30N & 30AD. Alpha=8 deg. Slat. Standard deviation.
80b Comparison 30N & 30AD. Alpha=8 deg. Slat. Skewness.
80c Comparison 30N & 30AD. Alpha=8 deg. Slat. Flatness.
81a Comparison 30N & 30AD. Alpha=8 deg. Main. Standard deviation.
81b Comparison 30N & 30AD. Alpha=8 deg. Main. Skewness.
81c Comparison 30N & 30AD. Alpha=8 deg. Main. Flatness.
82 Comparison 30N & 30AD. Alpha=8 deg. Flap. Standard deviation.
83a Comparison 30N,30AD and 35T. Alpha=8 deg. Slat. Std.dev. Re=9 mill.
83b Comparison 30N,30AD and 35T. Alpha=8 deg. Slat. Std.dev. Re=5 mill.
84 Comparison 30N,30AD and 35T. Alpha=16 deg. Slat. Std.dev. Re=9 mill.
85 Comparison 30N,30AD and 35T. Alpha=19 deg. Slat. Std.dev. Re=5 mill.
86 Comparison 30N,30AD and 35T. Alpha=8 deg. Main. Std.dev.Re=5 mill.
87a Comparison 30N,30AD and 35T. Alpha=8 deg. Flap. Std.dev. Re=9 mill.
87b Comparison 30N,30AD and 35T. Alpha=8 deg. Flap. Std.dev. Re=5 mill.
88 Comparison 30N,30AD and 35T. Alpha=16 deg. Flap. Std.dev.Re=9 mill.
89 Comparison 30N,30AD and 35T. Alpha=19 deg. Flap. Std.dev.Re=5 mill.
90 Comparison 30N,30AD and 35T. Alpha=21 deg. Flap. Std.dev.Re=5 mill.
91a Spanwise Cp. 30P/30N M=0.2 Re=9 mill. Slat 5%.
91b Spanwise Cp. 30P/30N M=0.2 Re=9 mill. Main 82.5 %.
91c Spanwise Cp. 30P/30N M=0.2 Re=9 mill. Flap 74 %.
91d Spanwise Cp. 30P/30N M=0.2 Re=9 mill. Flap 100 %.
92a Spanwise Cp. 30N & 30AD M=0.2 Re=9 mill. Slat 5%.
92b Spanwise Cp. 30N & 30AD M=0.2 Re=9 mill. Main 82.5 %.
92c Spanwise Cp. 30N & 30AD M=0.2 Re=9 mill. Flap 74 %.
92d Spanwise Cp. 30N & 30AD M=0.2 Re=9 mill. Flap 100 %.
93a Spanwise Cp. 30N & 35T M=0.2 Re=9 mill. Slat 5%.
93b Spanwise Cp. 30N & 35T M=0.2 Re=9 mill. Main 82.5 %.
93c Spanwise Cp. 30N & 35T M=0.2 Re=9 mill. Flap 74 %.
93d Spanwise Cp. 30N & 35T M=0.2 Re=9 mill. Flap 100 %.
94a Wake profiles 30P/30AD M=0.2 Re=9 mill.
94b Wake profiles 30P/35T M=0.2 Re=9 mill.

- 95a Non-dimensional wake profiles 30P/30AD M=0.2 Re=9 mill.
- 95b Non-dimensional wake profiles 30P/35T M=0.2 Re=9 mill.
- 96 Vertical location of max. velocity defect. M=0.2 Re=9 mill.
- 97 Non-dimensional max. velocity defect. M=0.2 Re=9 mill.
- 98 Viscous drag CDTOT2 for the three configurations.
-
- A3.1 The overall effect of hot film sheets on CLCOMBO.
- A3.2 Cp.main with and without film sheets
- A3.3a The viscous effects of the films on the wakes. Alpha=4 deg.
- A3.3b The viscous effects of the films on the wakes. Alpha=12 deg.
- A3.4a Spanwise Cp for slat as function of Alpha. Clean.30N,M=0.2,Re=9 mill
- A3.4b Spanwise Cp for main as fn. of Alpha.Clean.30N,M=0.2,Re=9 mill
- A3.4c Spanwise Cp for flap as fn. of Alpha. Clean.30N,M=0.2,Re=9 mill
- A3.4d Spanwise Cp for flapTE as fn. of Alpha.Clean.30N,M=0.2,Re=9 mill
- A3.5a Spanwise Cp for slat for different Alpha. Effect of film
- A3.5b Spanwise Cp for main different Alpha. Effect of film
- A3.5c Spanwise Cp for flap different Alpha. Effect of film
- A3.5d Spanwise Cp for flap TE different Alpha. Effect of film
- A3.6 BLT influence on integrated pressures, CLCOMBO.
- A3.7 BLT effect on flap pressure distributions midspan.
- A3.8a BLT effect on flap pressure distributions midspan- suction peak region.
- A3.8b BLT effect on flap pressure distributions midspan- rear region region.
- A3.9 BLT effect on flap pressure distributions at auxiliary row.
- A3.10 Cp.slat, tests K and G, 30P/30N, M=0.2, Re=9 mill.Alpha=4 and 8 deg.
- A3.11 Cp.slat, tests K and G, 30P/30N, M=0.2, Re=9 mill.Alpha=16,19&23 deg.
- A3.12a Cp.main, K & G, 30P/30N, M=0.2, Re=9 mill.Alpha=16-23 deg.Lower.
- A3.12b Cp.main, K & G, 30P/30N, M=0.2, Re=9 mill.Alpha=16-23 deg.Nose.
- A3.12c Cp.main, K & G, 30P/30N, M=0.2, Re=9 mill.Alpha=16-23 deg.Rear.
- A3.13a dCp.main. K & G. Re-effect, 5 & 9 mill. Alpha=8 deg.
- A3.13b dCp.main. K & G. Re-effect, 5 & 9 mill. Alpha=16 deg.
- A3.14a Spanwise Cp. Tests K & G. 30P/30N M=0.2 Re=9 mill. Slat 5%
- A3.14b Spanwise Cp. Tests K & G. 30N M=0.2 Re=9 mill. Main 82.5%
- A3.14c Spanwise Cp. Tests K & G. 30N M=0.2 Re=9 mill. Flap 74%
- A3.14d Spanwise Cp. Tests K & G. 30N M=0.2 Re=9 mill. Flap 100%
- A3.15 Spanwise Cp. Tests K,Kclean, G&H. M=0.2 Re=9 mill. Flap 100%

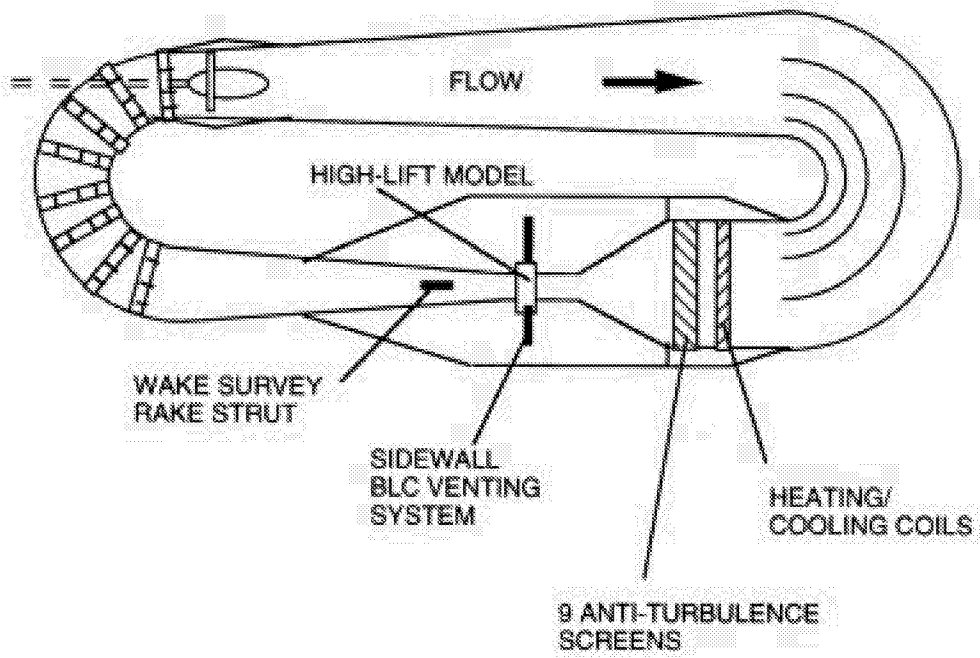


Figure 1 Sketch of the NASA Langley Low Turbulence Pressure Tunnel, LTPT.

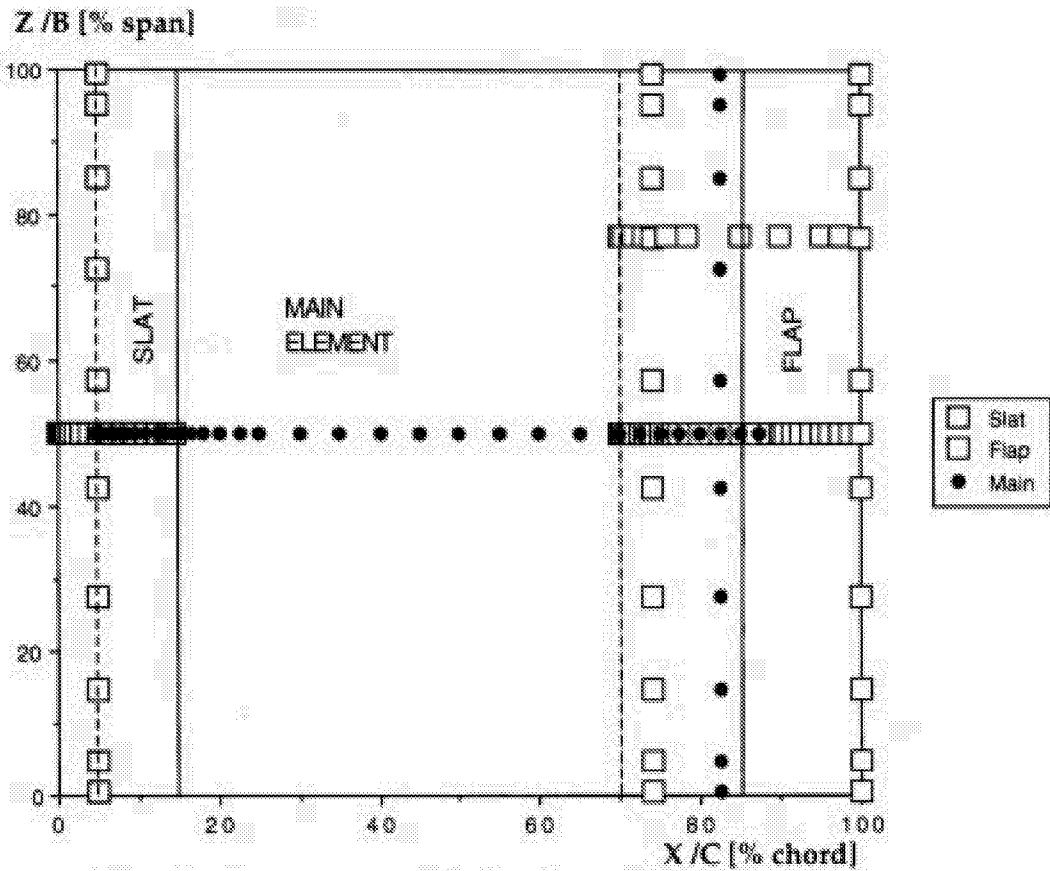


Figure 2a Pressure taps on the three-element high-lift model.
 Chord=22 in. Span=36 in. Upper side.

Zlower [%] span

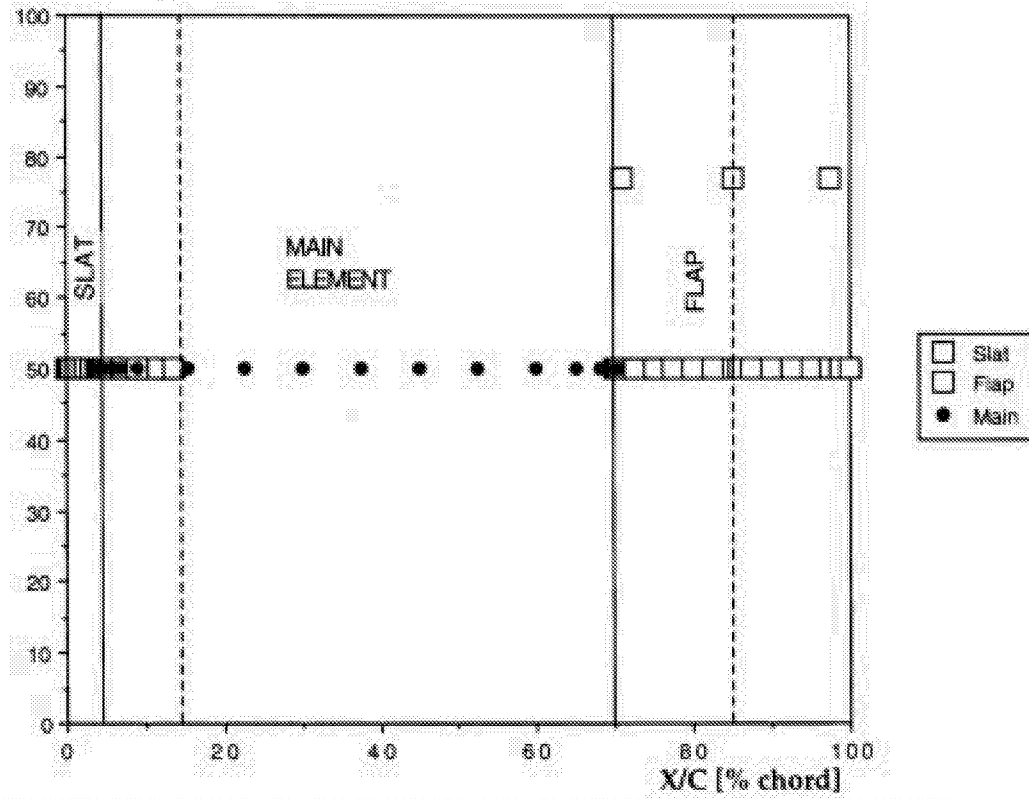


Figure 2b Pressure taps on the three-element high-lift model. Slat taps include cover. Chord=22 in. Span=36 in. Lower side.

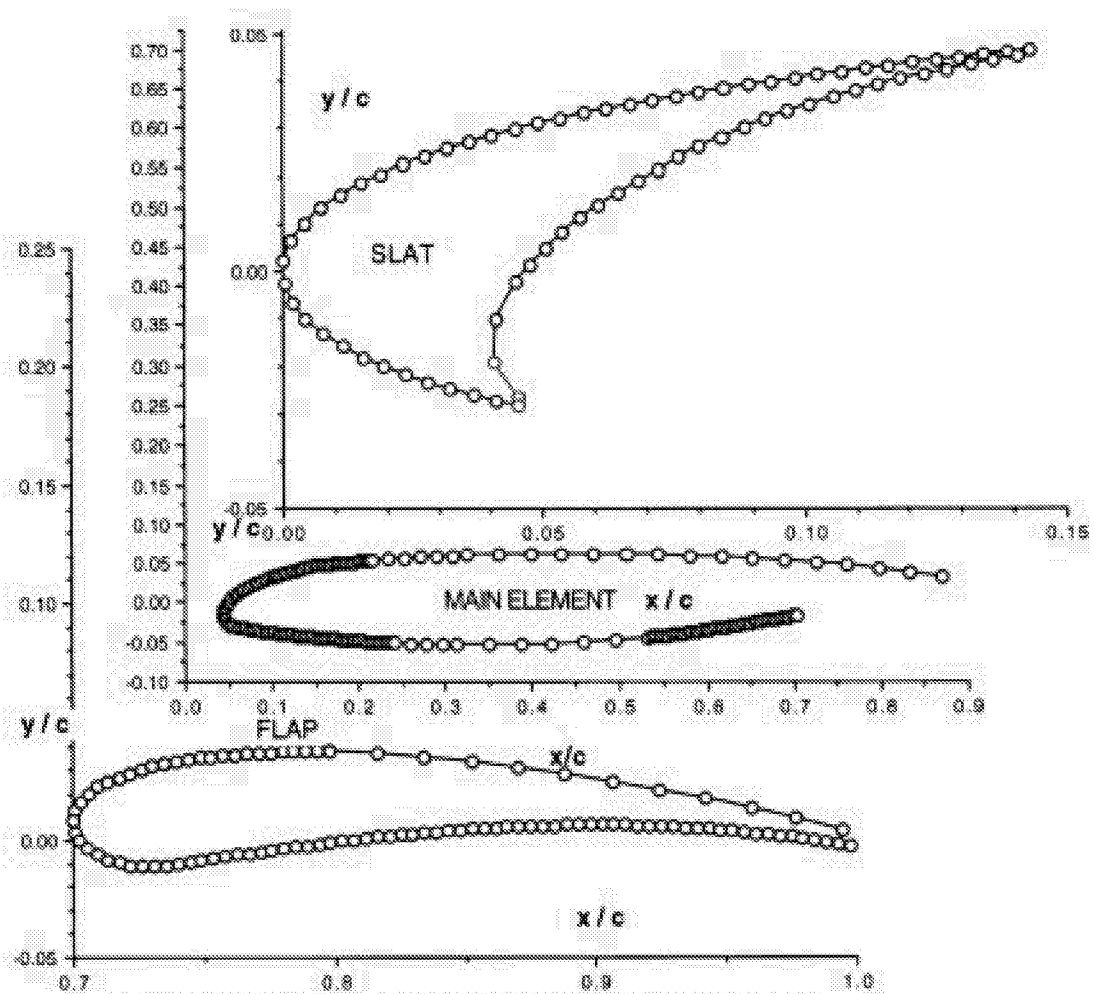


Figure 3 Hot film sensor locations on the three elements.

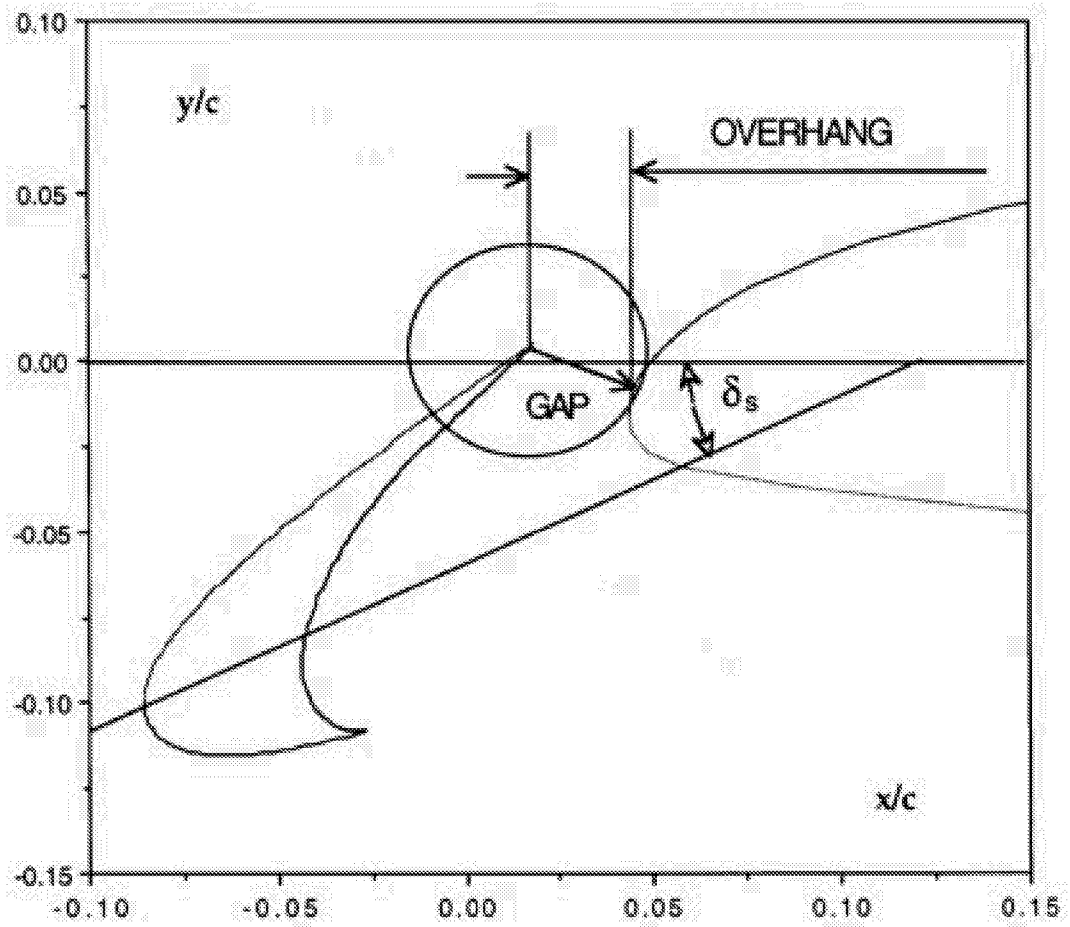


Figure 4a Definition of configuration (rigging). Slat

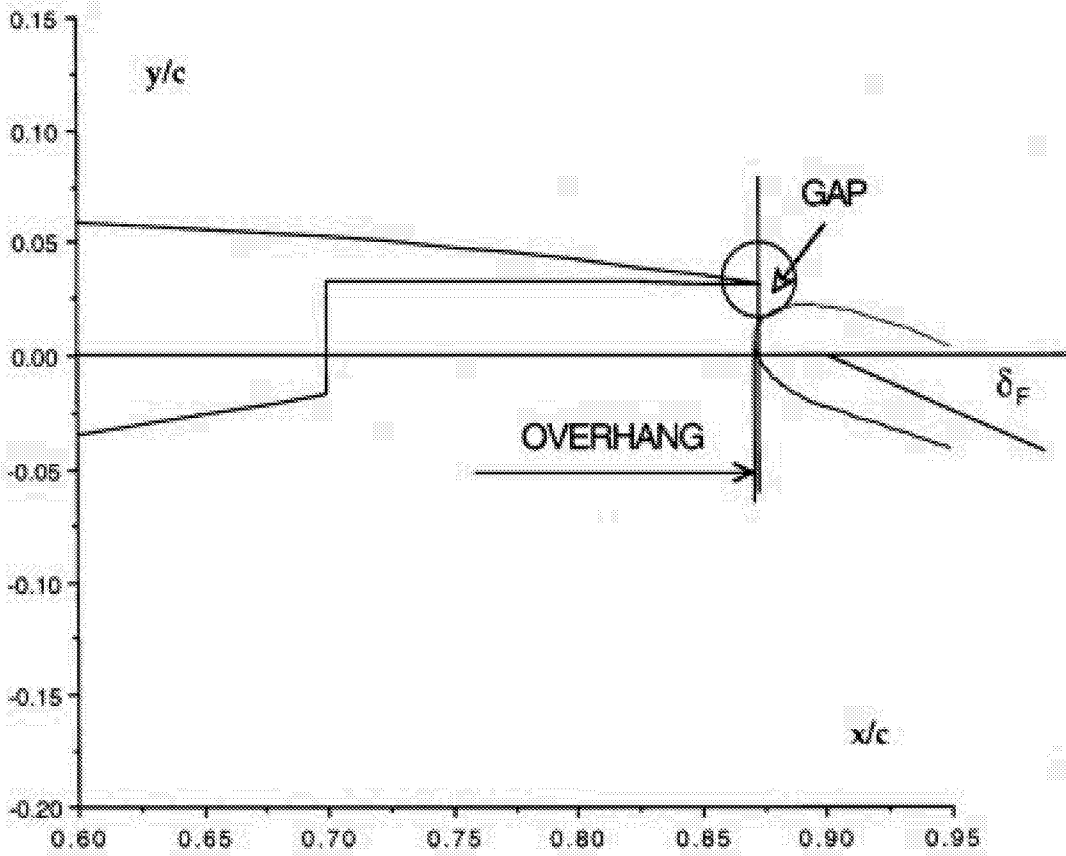


Figure 4b Definition of configurations (rigging). Flap.

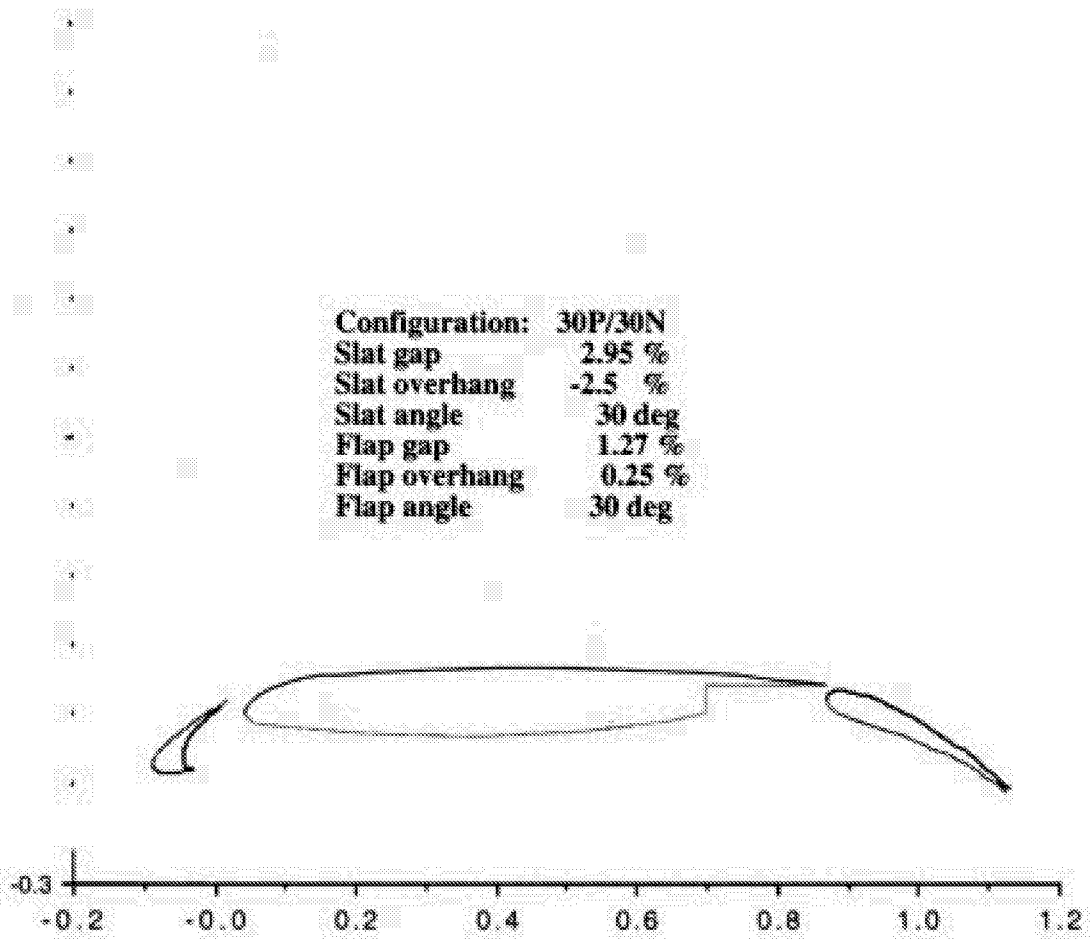


Figure 4c MDA 3-element high-lift model, - 30P/30N rigging

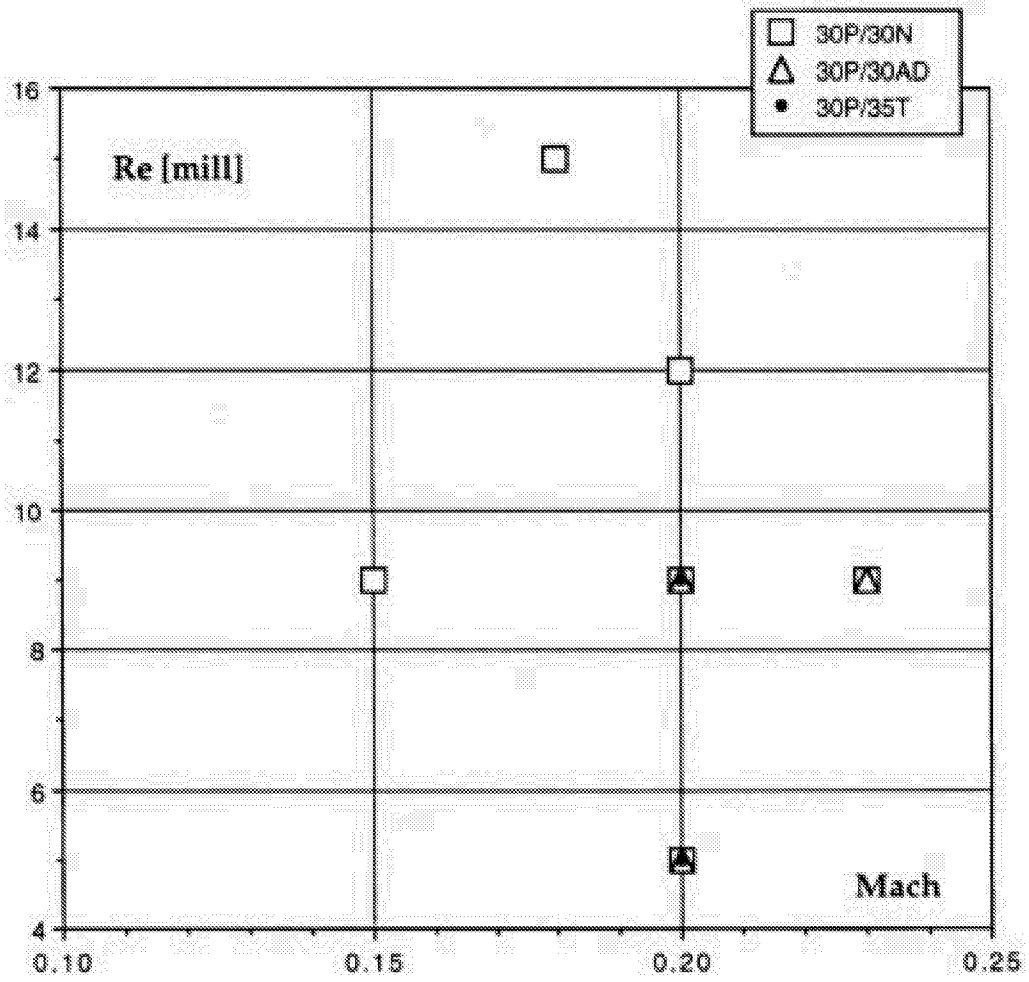


Figure 5 Nominal reference conditions tested for the three riggings.

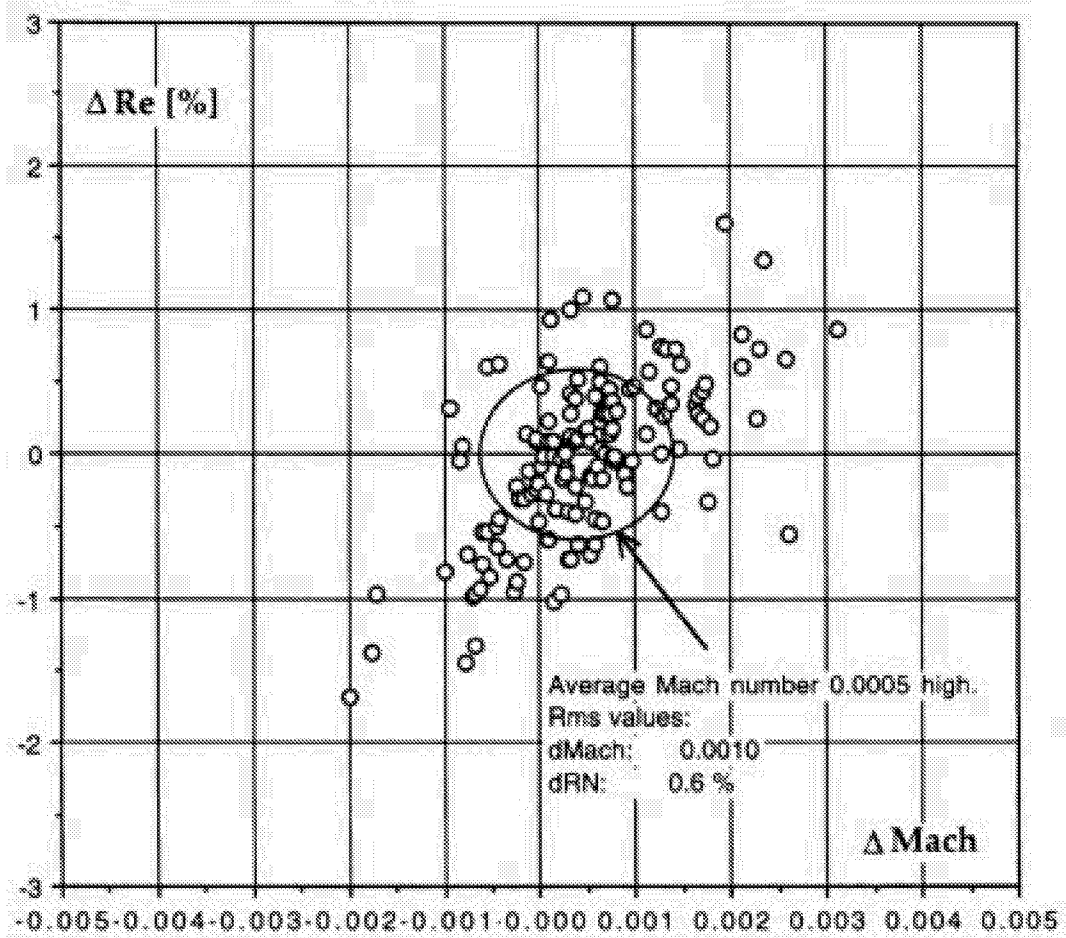


Figure 6a Repeatability of reference conditions for 30P/30N throughout the Mach- and Reynolds number regime.

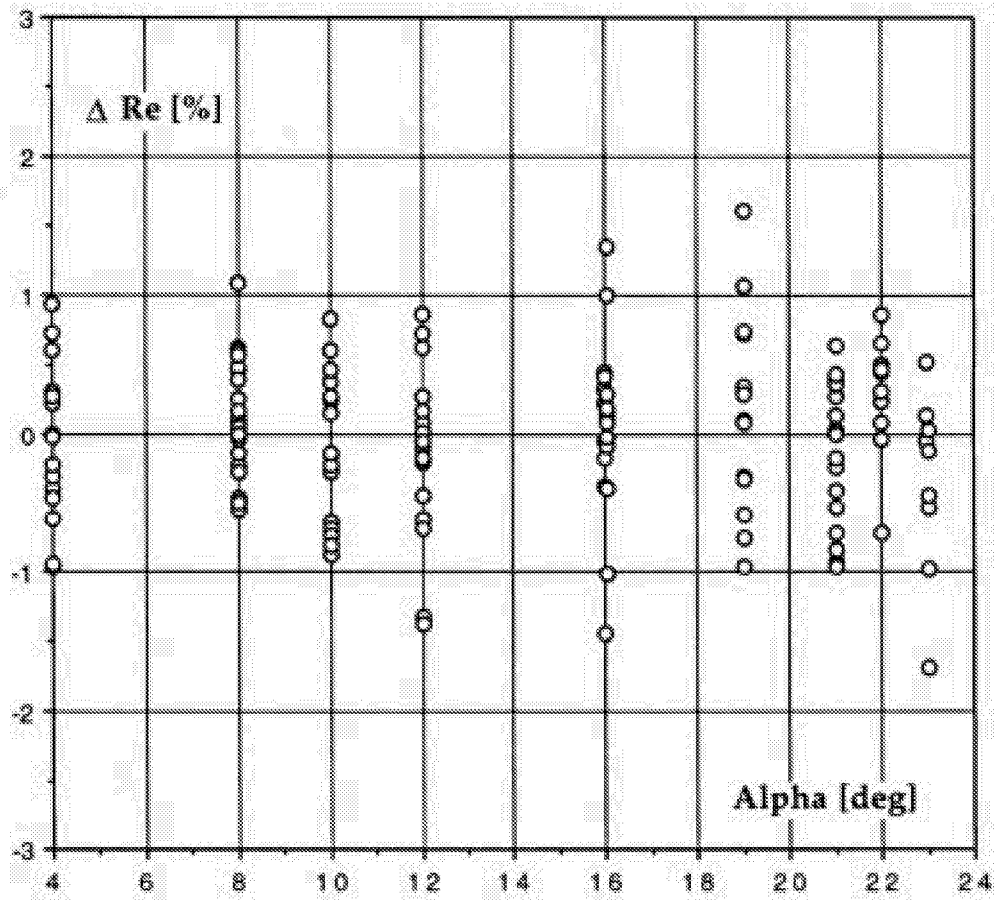


Figure 6b Reynolds number deviation as function of angle-of-attack.

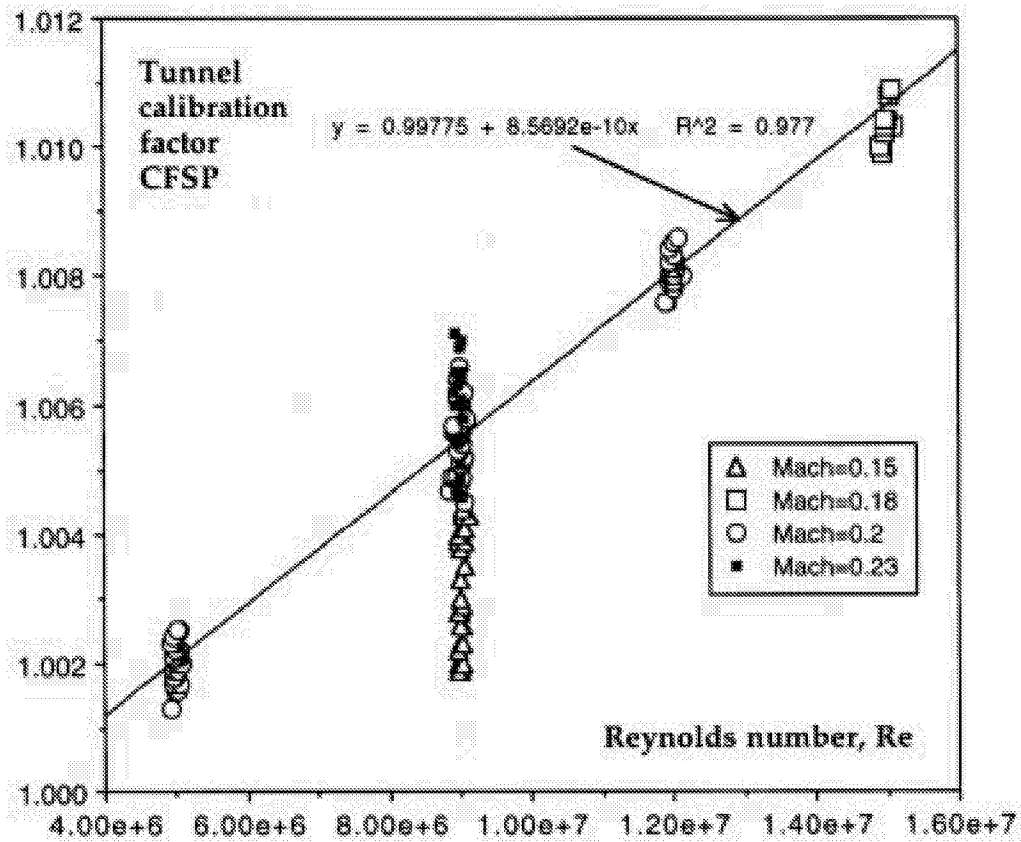


Figure 6c Tunnel calibration factor, CFSP, as function of Reynolds number and Mach number for 30P/30N.

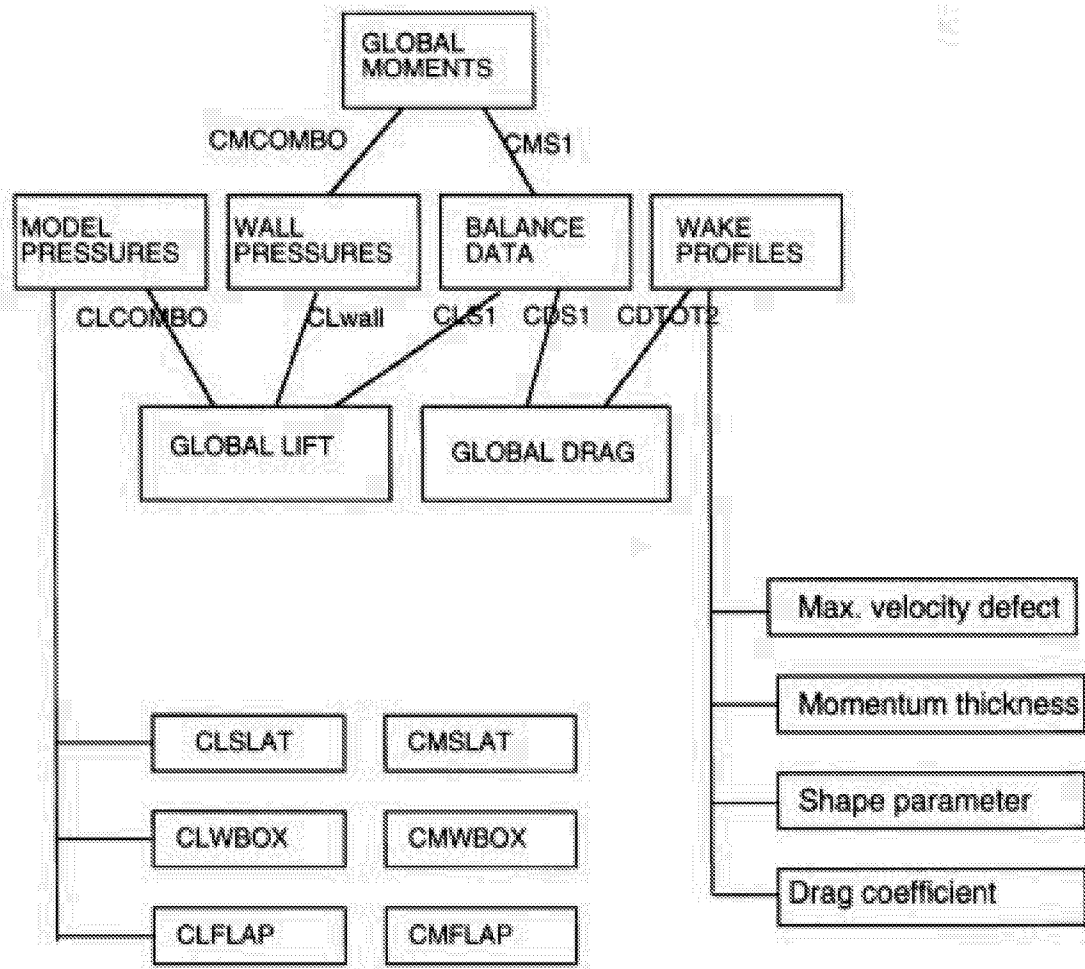


Figure 7 Pressure and force data parameters

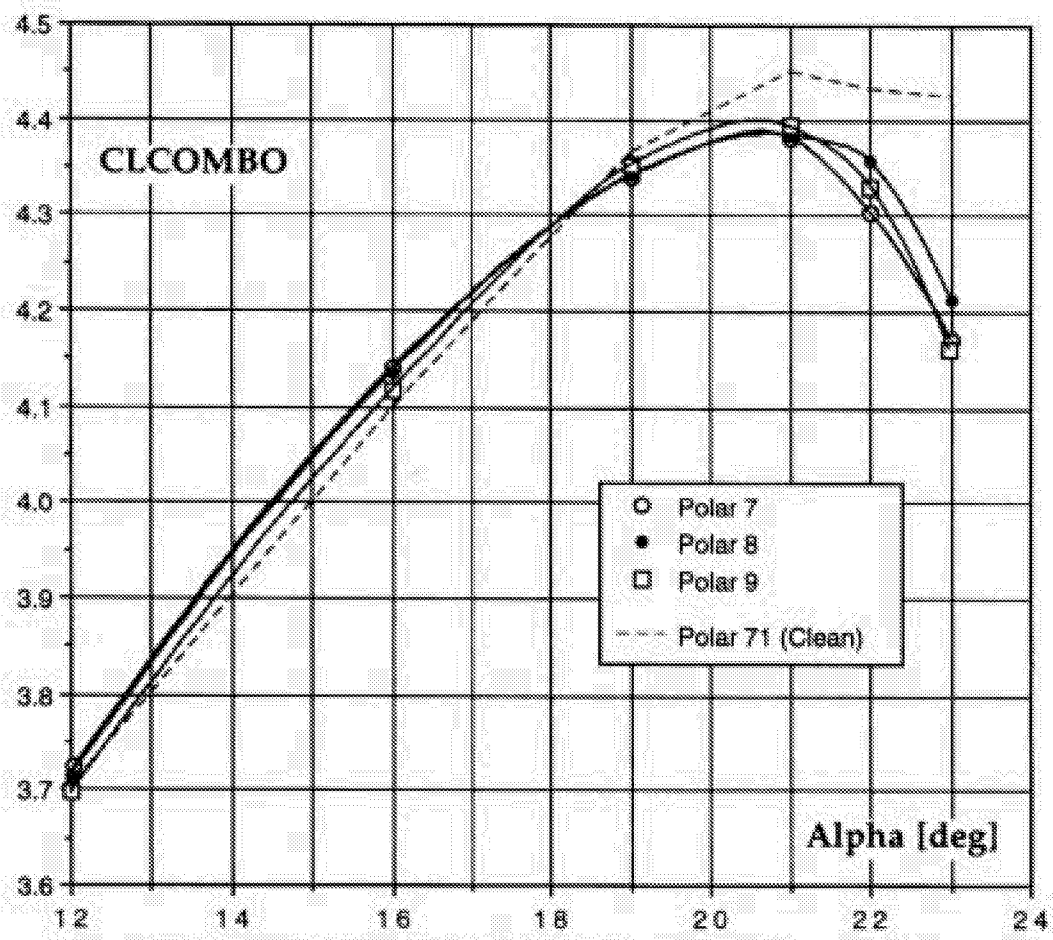


Figure 8 Repeatability of CLCOMBO (based on integrated pressure)
 30P/30N Mach=0.2 Re=9 million

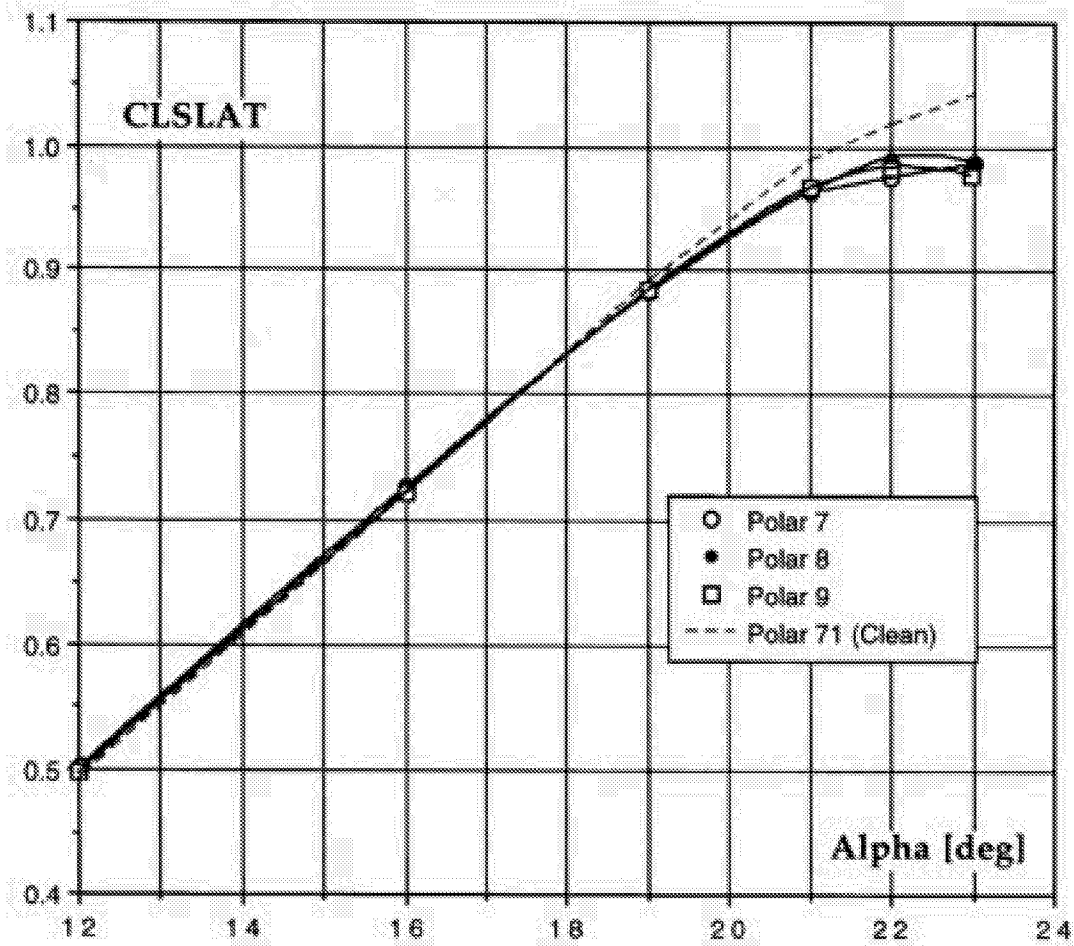


Figure 9a Repeatability of CLSLAT (based on integrated pressure)
 30P/30N Mach=0.2 Re=9 million

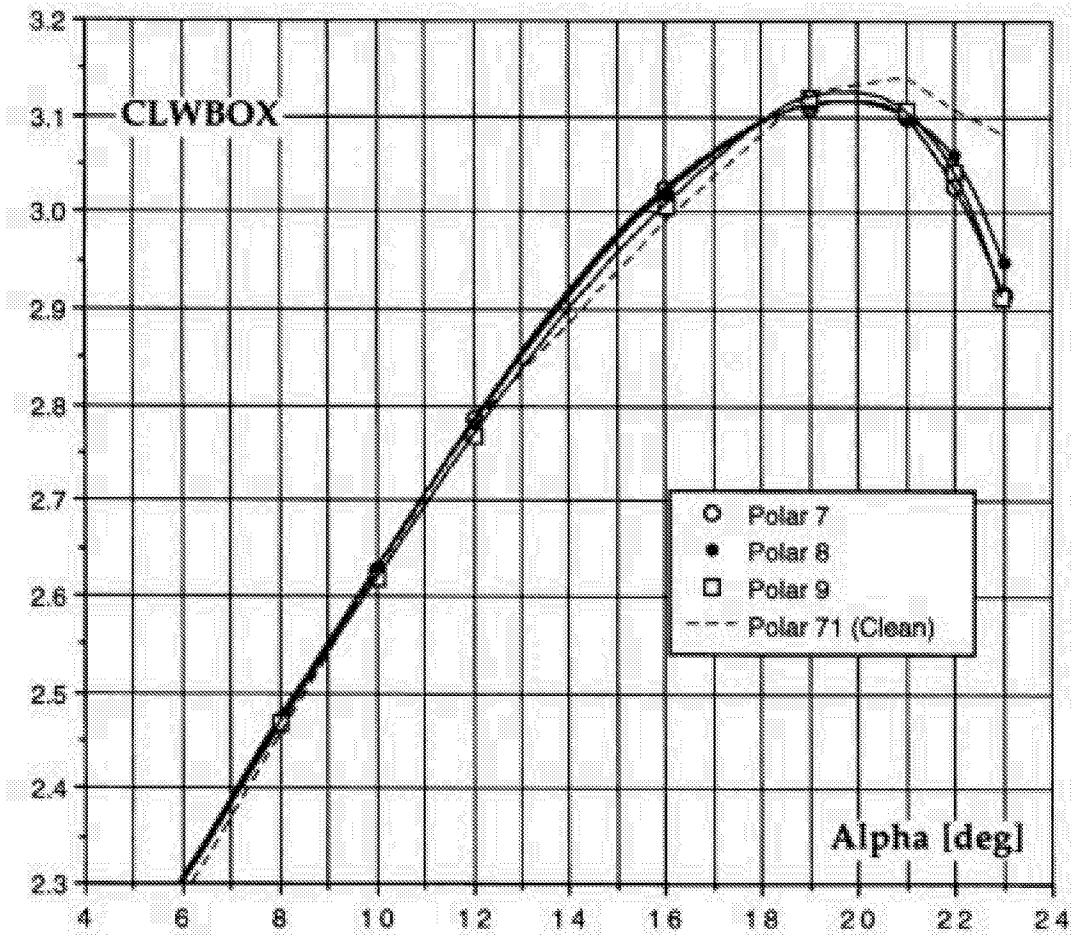


Figure 9 b Repeatability of CLWBOX (based on integrated pressure)
 30P/30N Mach=0.2 Re=9 million

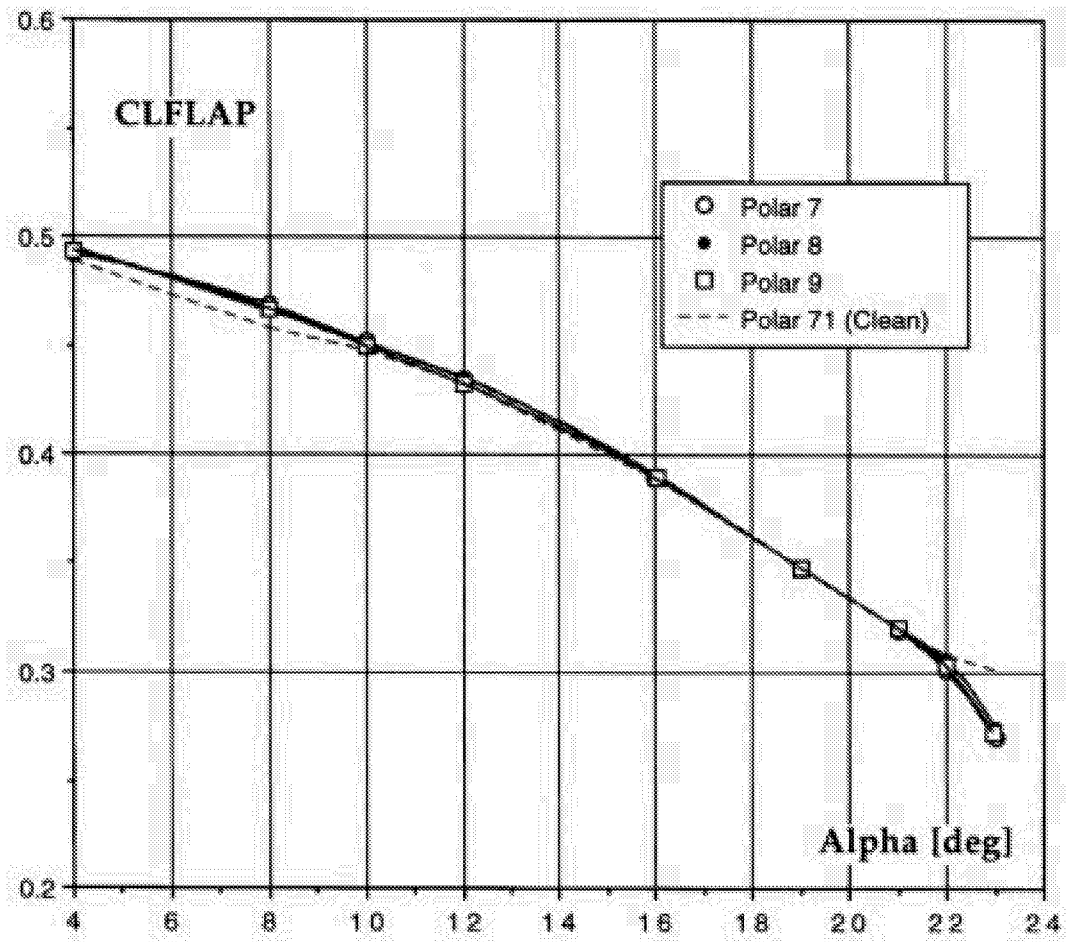


Figure 9 c Repeatability of CLFLAP (based on integrated pressure)
 30P/30N Mach=0.2 Re=9 million

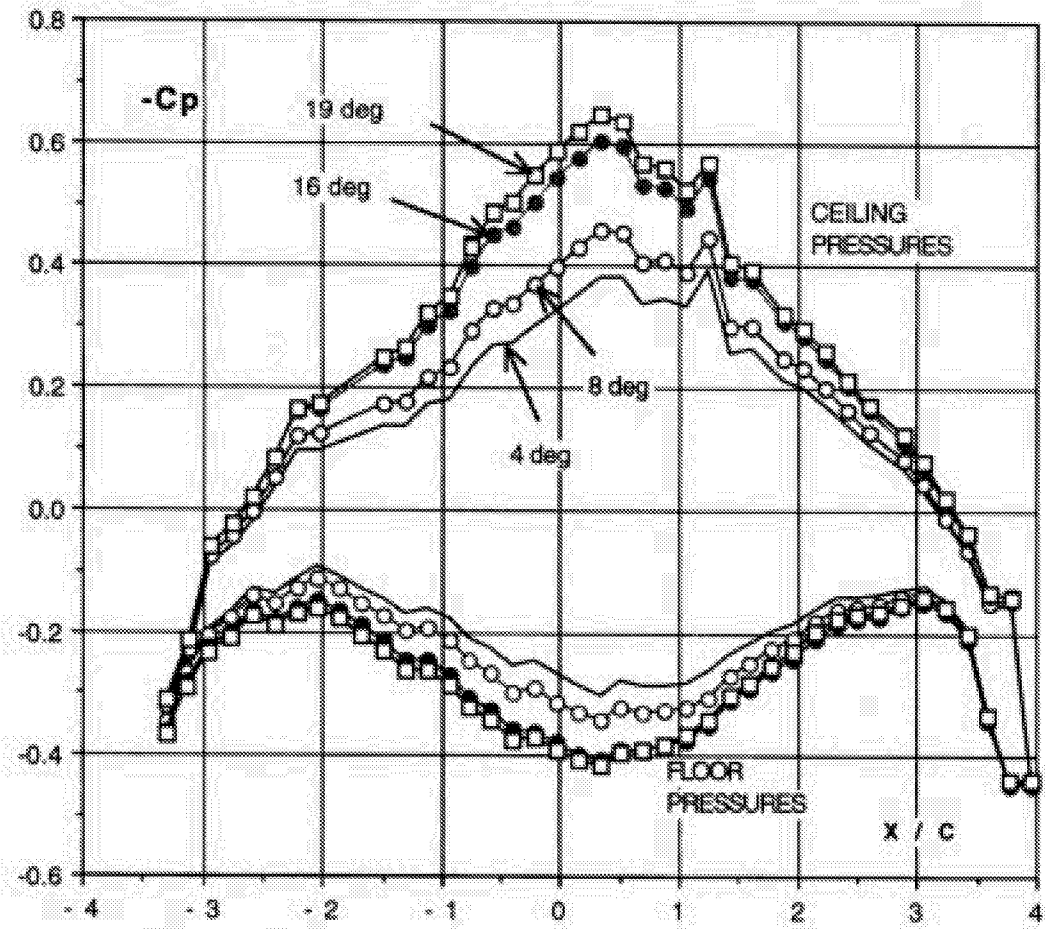


Figure 10 Tunnel ceiling and floor pressure distributions. 30P/30N Mach=0.2 Re=9 mill. Points 50,51,54 and 56.

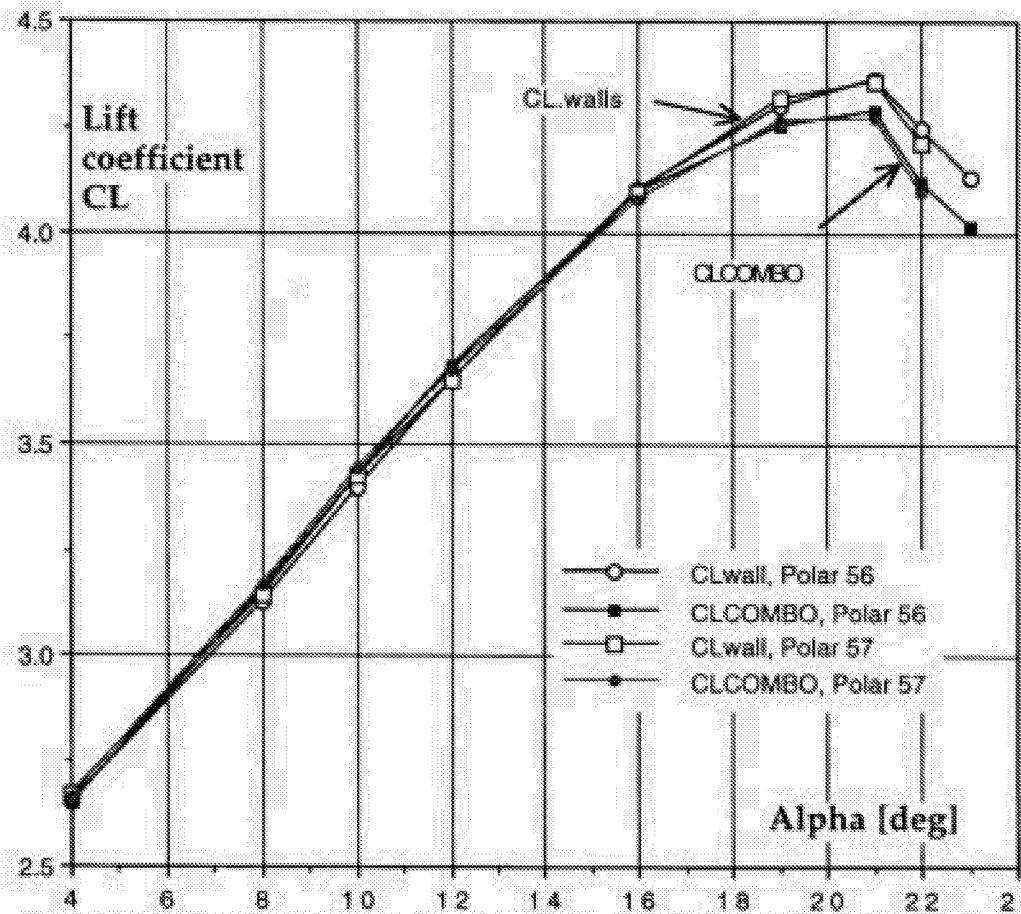


Figure 11 Comparison between pressures integrated on the model and on the wind tunnel walls. 30P/30N Mach=0.2 Re=9 million Repeatability is also illustrated.

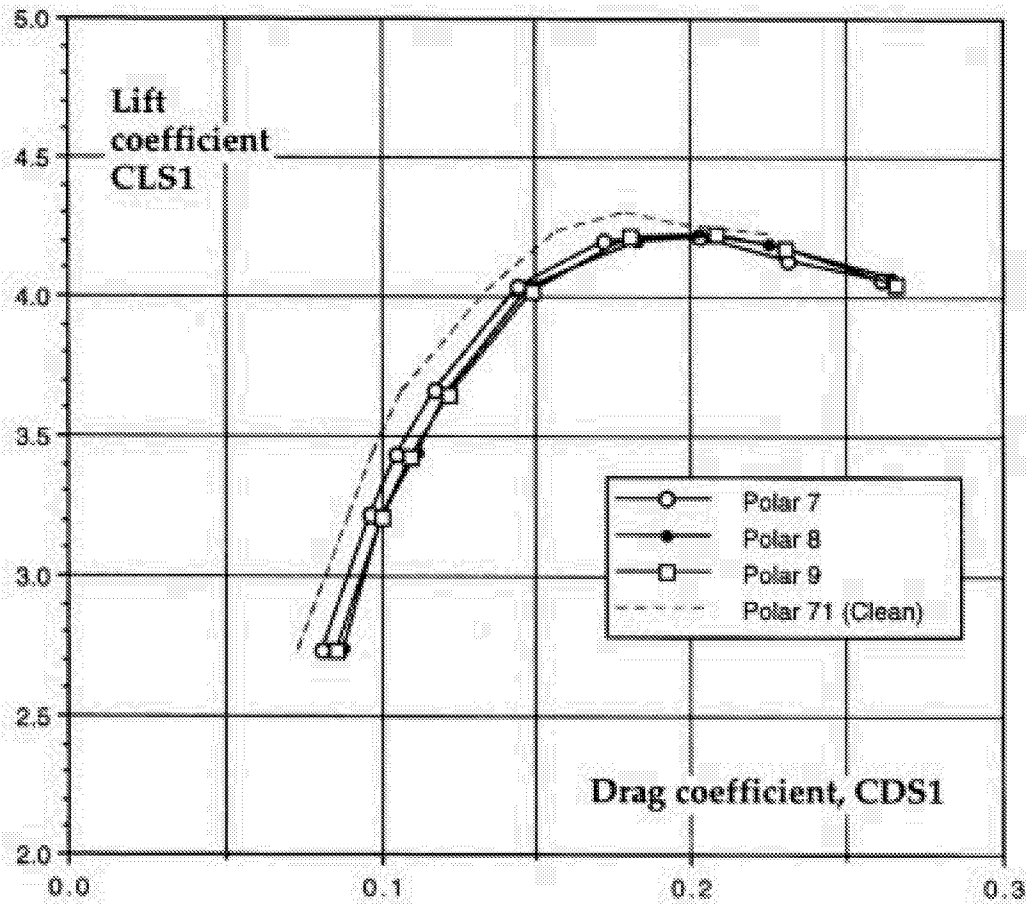


Figure 12 Repeatability of balance data. 30P/30N Mach=0.2 Re=9 million
 A polar without any hot films present (clean) is included.

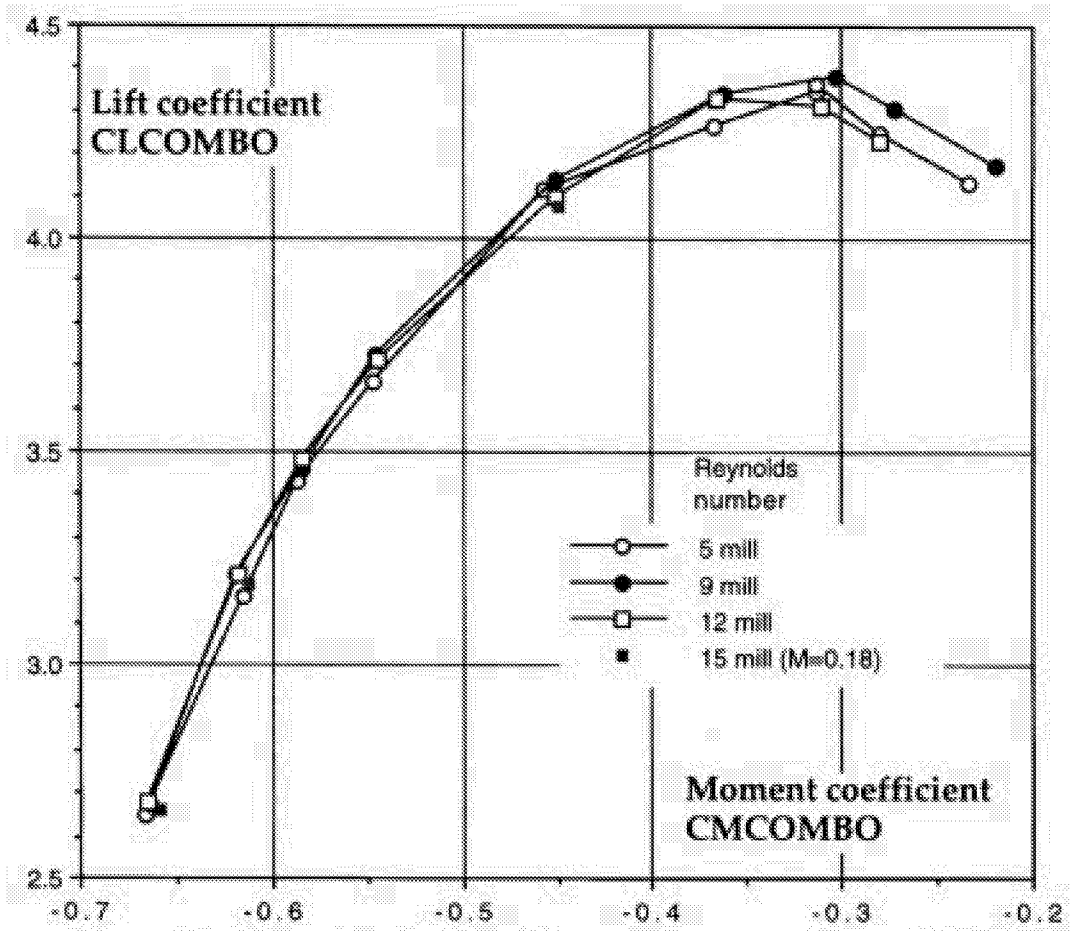


Figure 13 Moment polar from integrated pressure data. 30P/30N
Mach=0.2 Several Reynolds numbers included. Hot films present.

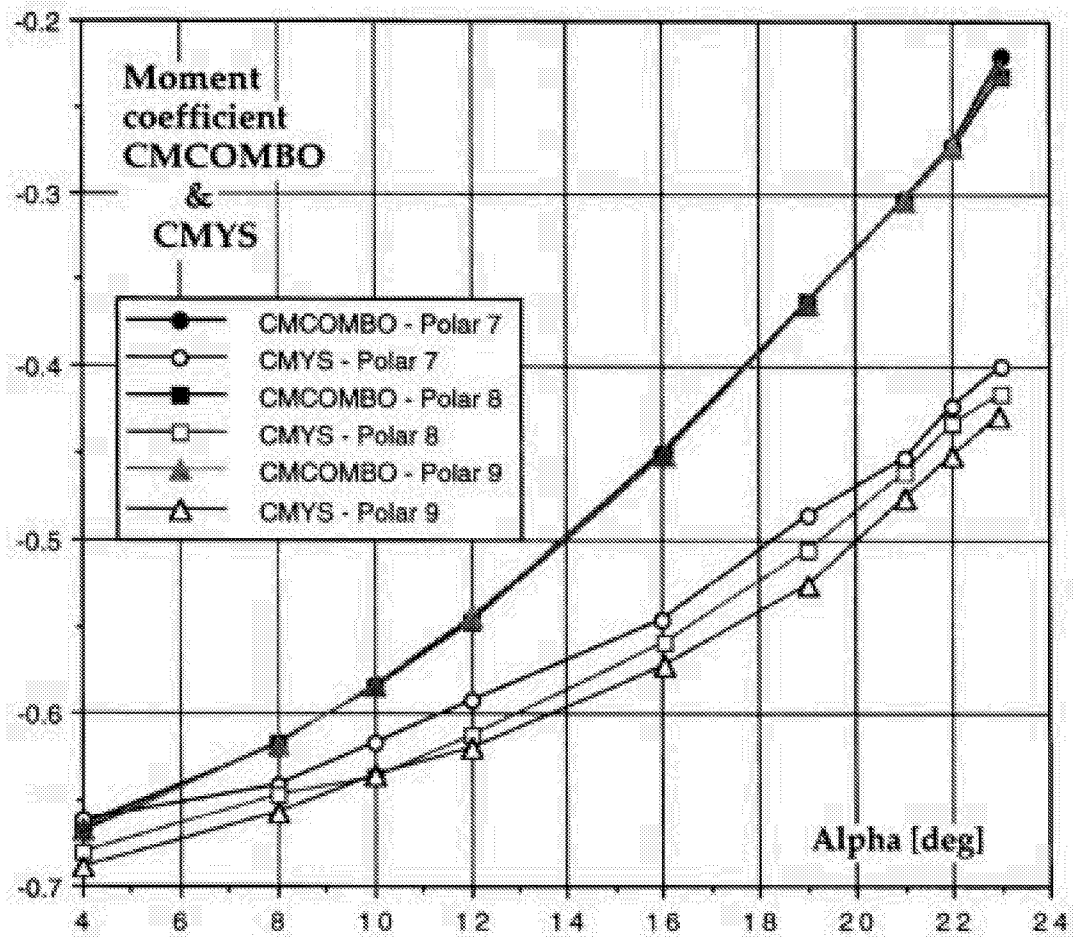


Figure 14 Comparison and repeatability of moment coefficients
 30P/30N Mach=0.2 Re=9 million

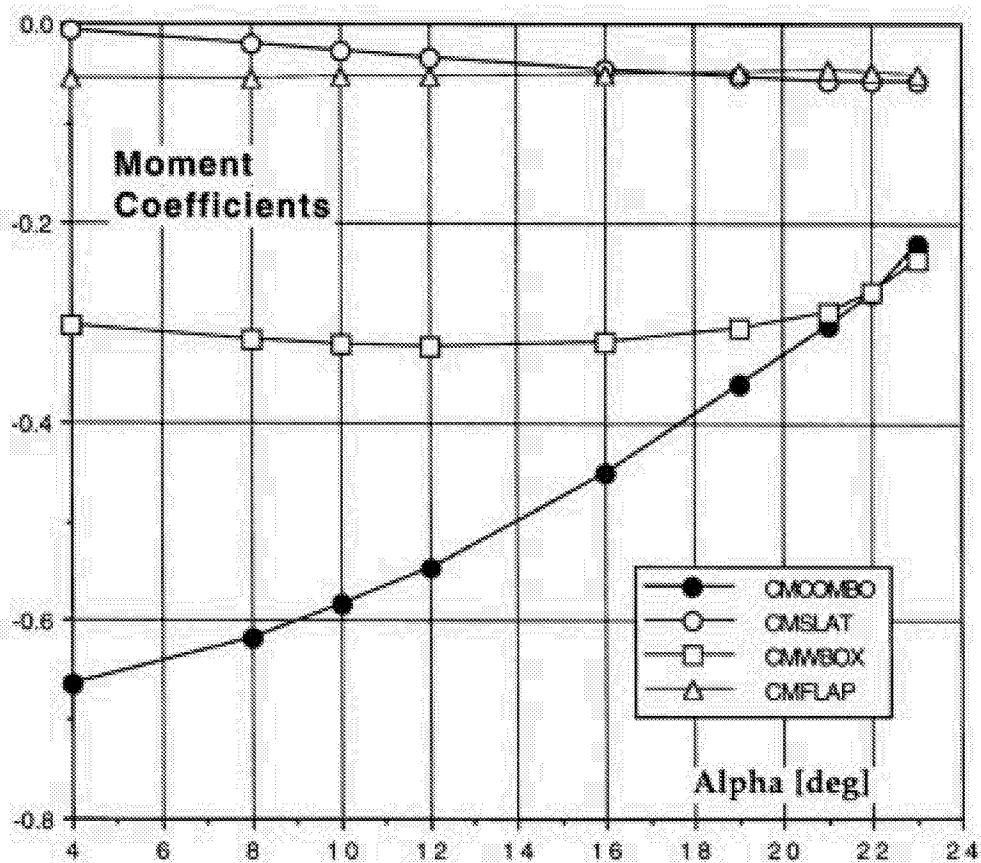


Figure 15 Moment coefficients for each of the elements, Polar 7 30P/30N Mach=0.2 Re=9 million Moment coefficients are referred to the leading edge of each element.

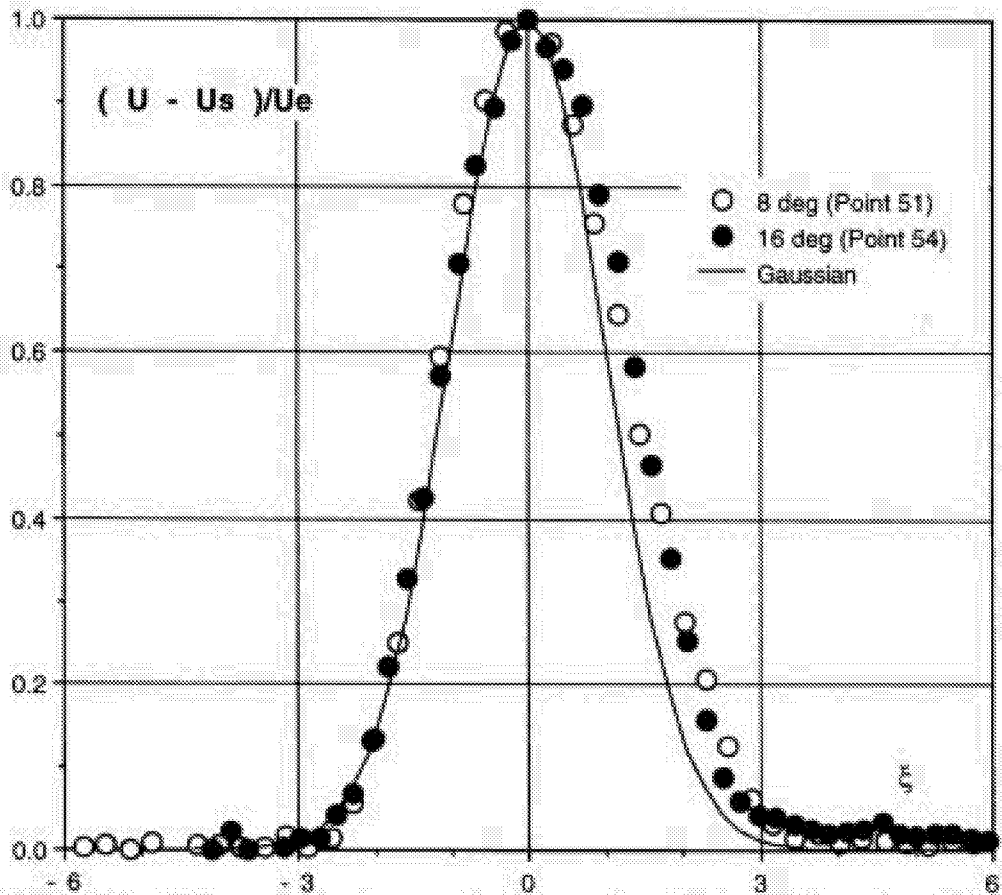


Figure 17 Wake profiles in non-dimensional velocity and length scale form. 30P/30N Mach=0.2 Re=9 million.

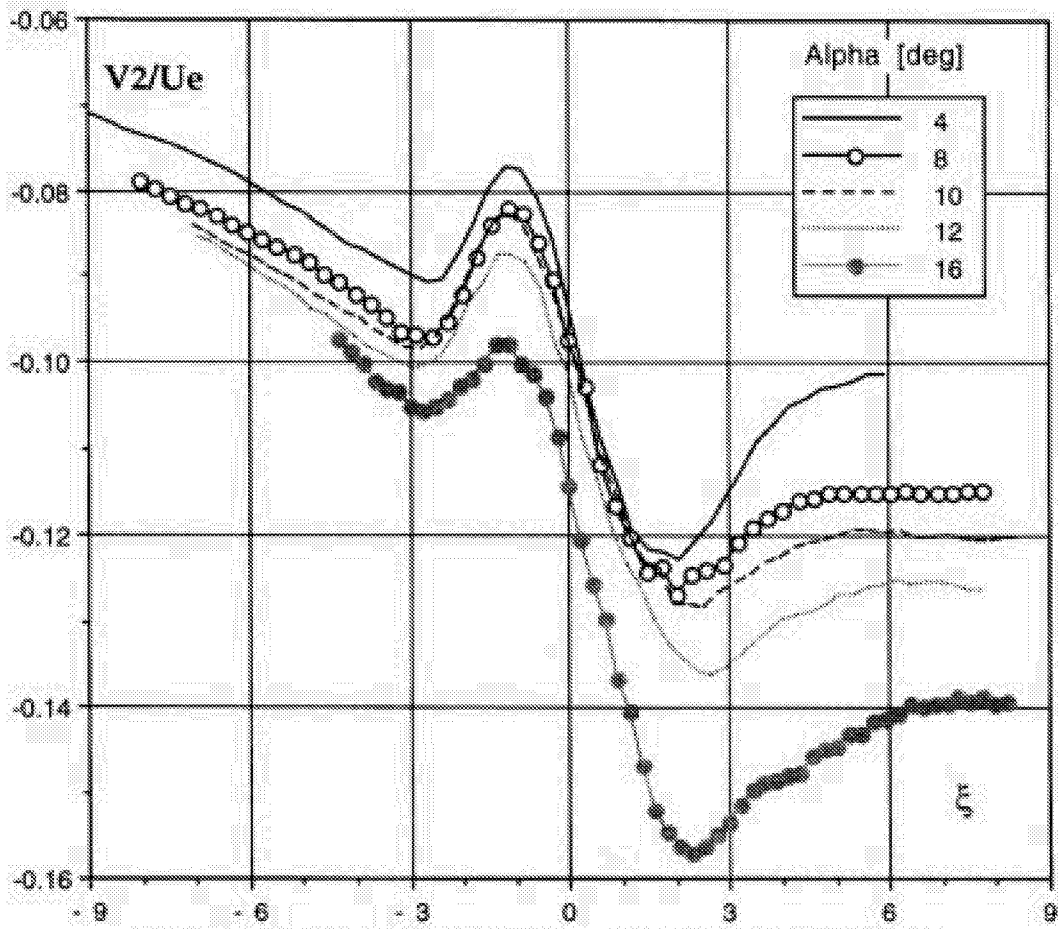


Figure 18 Wake profile sample, vertical component, $V2$, as function of non-dimensional coordinate. 30P/30N Mach=0.2 Re=9 mill.

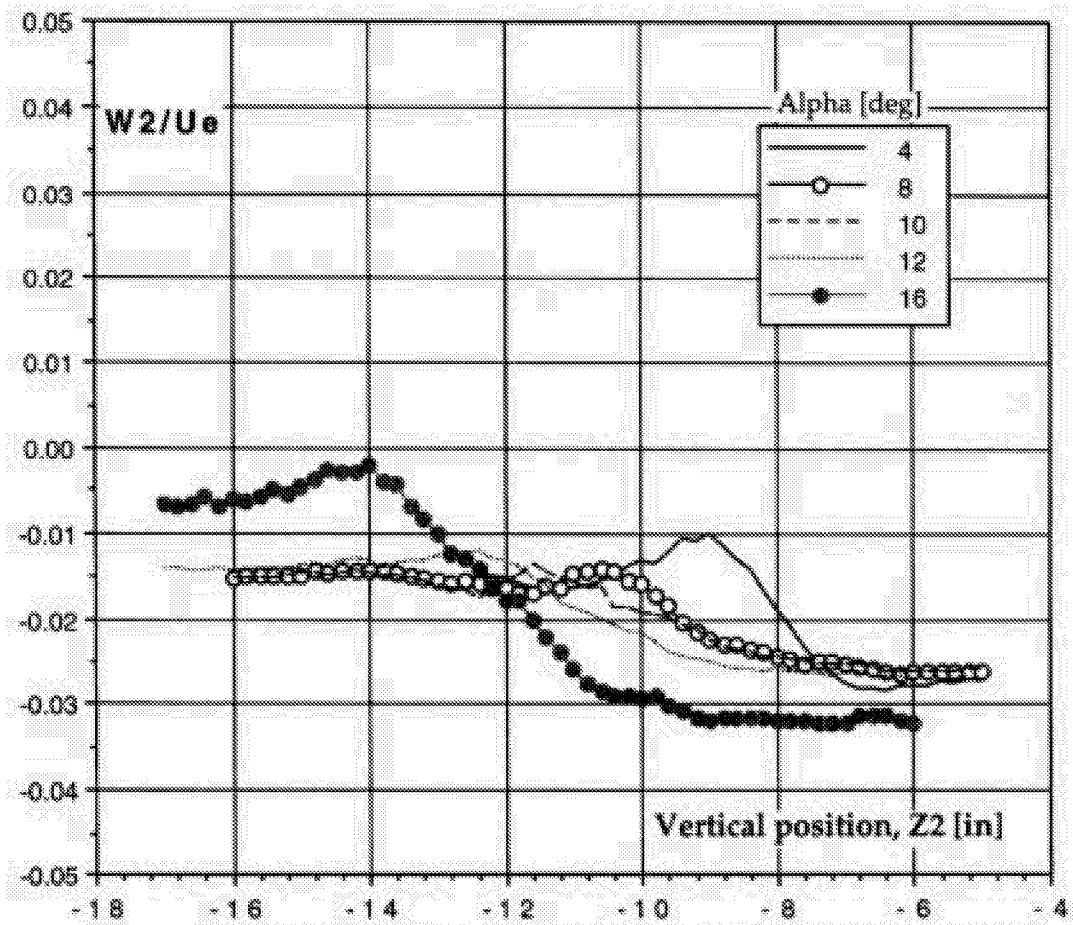


Figure 19 Wake profile sample, transverse component, W2.
 30P/30N Mach=0.2 Re=9 mill.

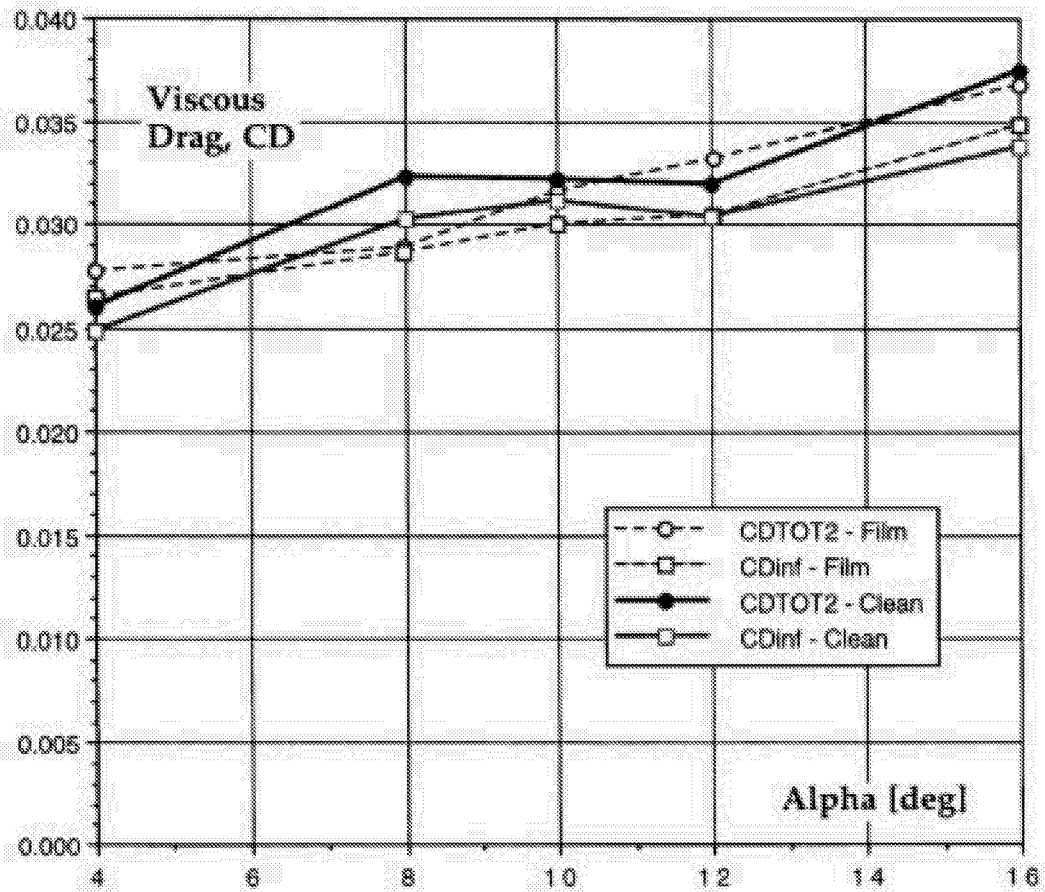


Figure 20 Viscous drag from standard integration (CDTOT2) and Squire-Young integration (CDinf). 30P/30N Mach=0.2 Re=9 mill.

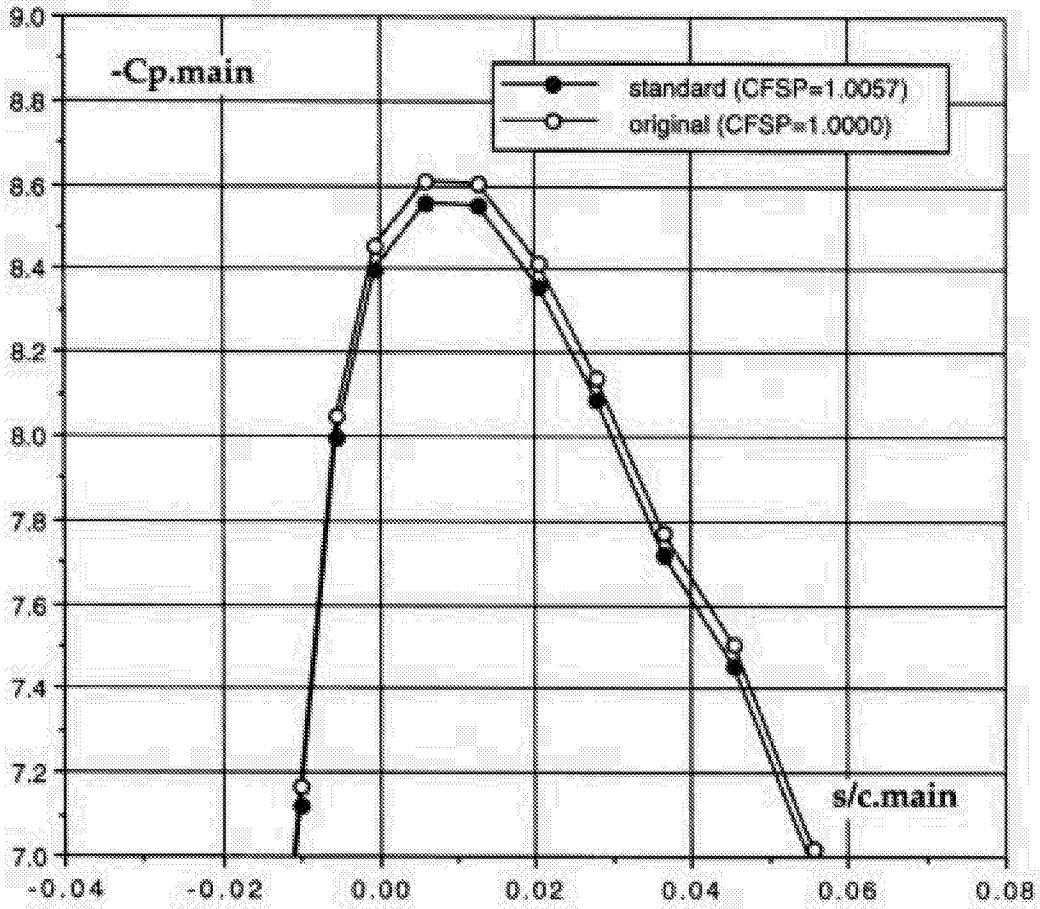


Figure 21 Sample pressure distributions showing effect of tunnel calibration factor $CFSP = 1.0057$. 30P/30N Mach=0.2 Re=9 million Alpha=16 degrees

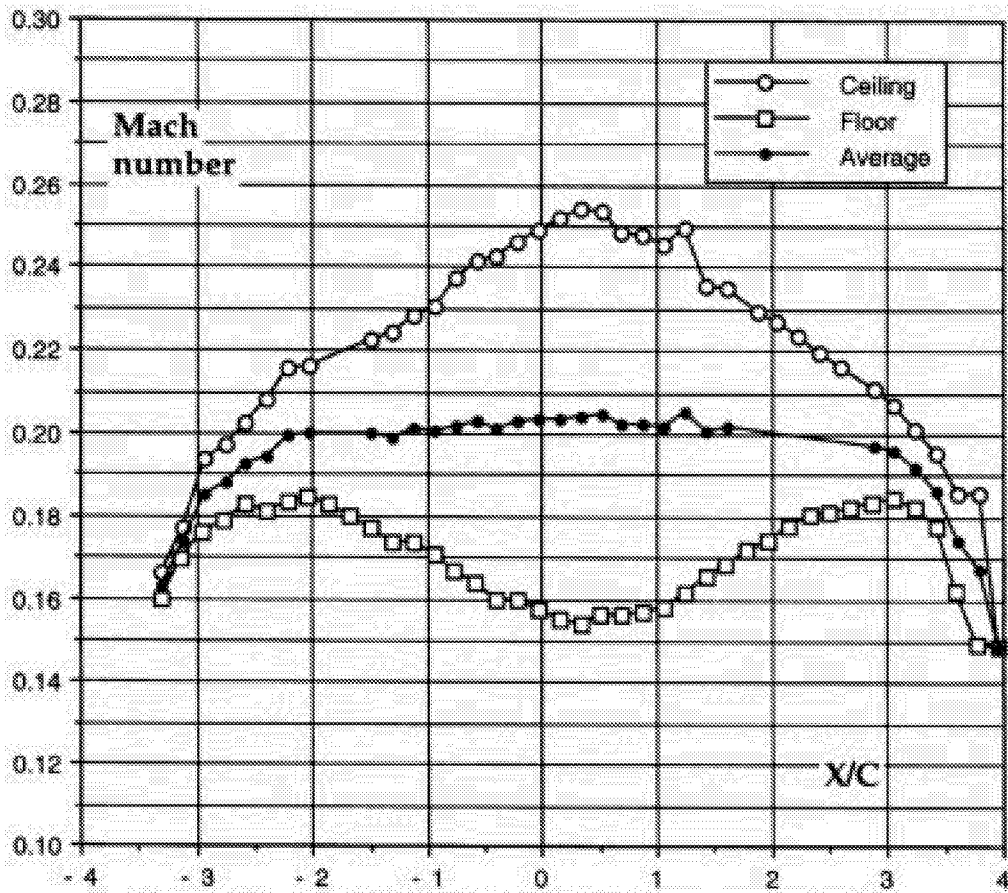


Figure 22 Mach number distributions on walls for 30P/30N, Mach=0.2, Re=9 million, Alpha=16 degrees

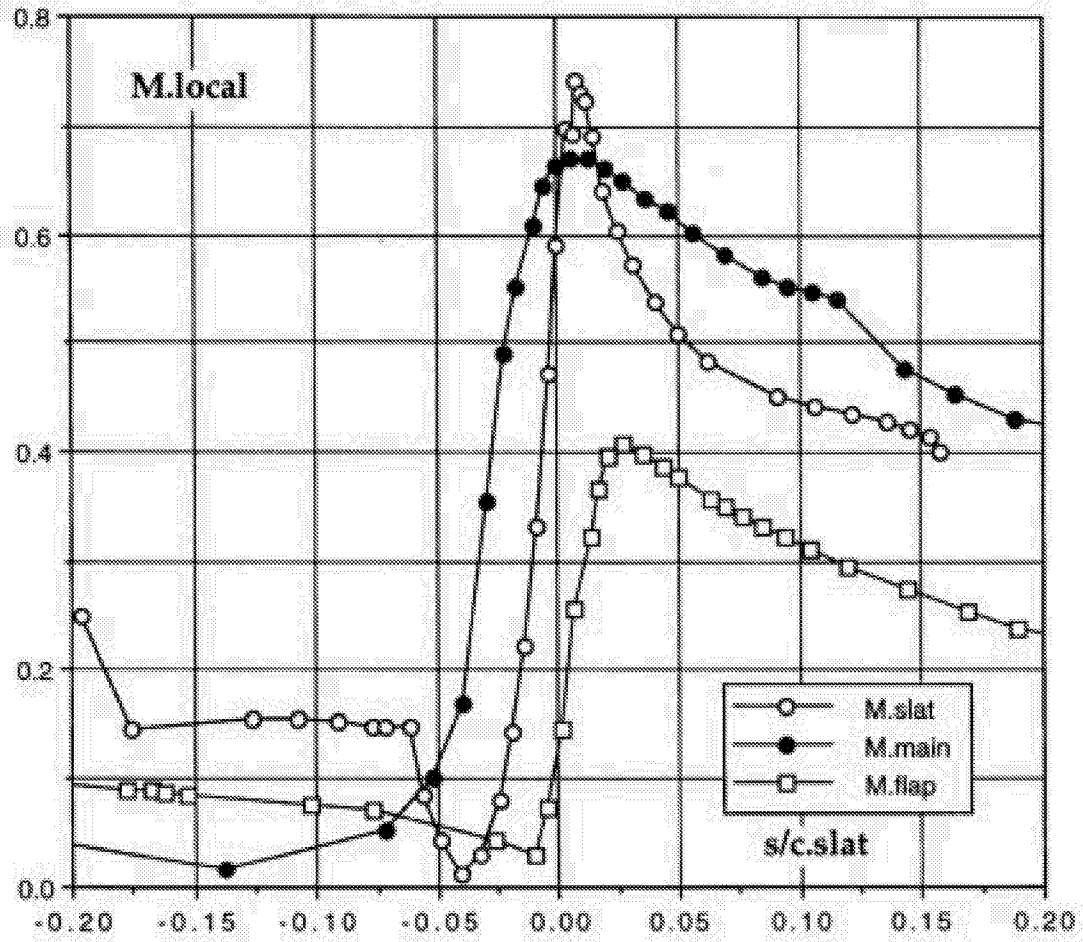


Figure 23 Mach number distributions over the three elements.
 30P/30N M=0.2 Re=9 million Alpha=16 deg

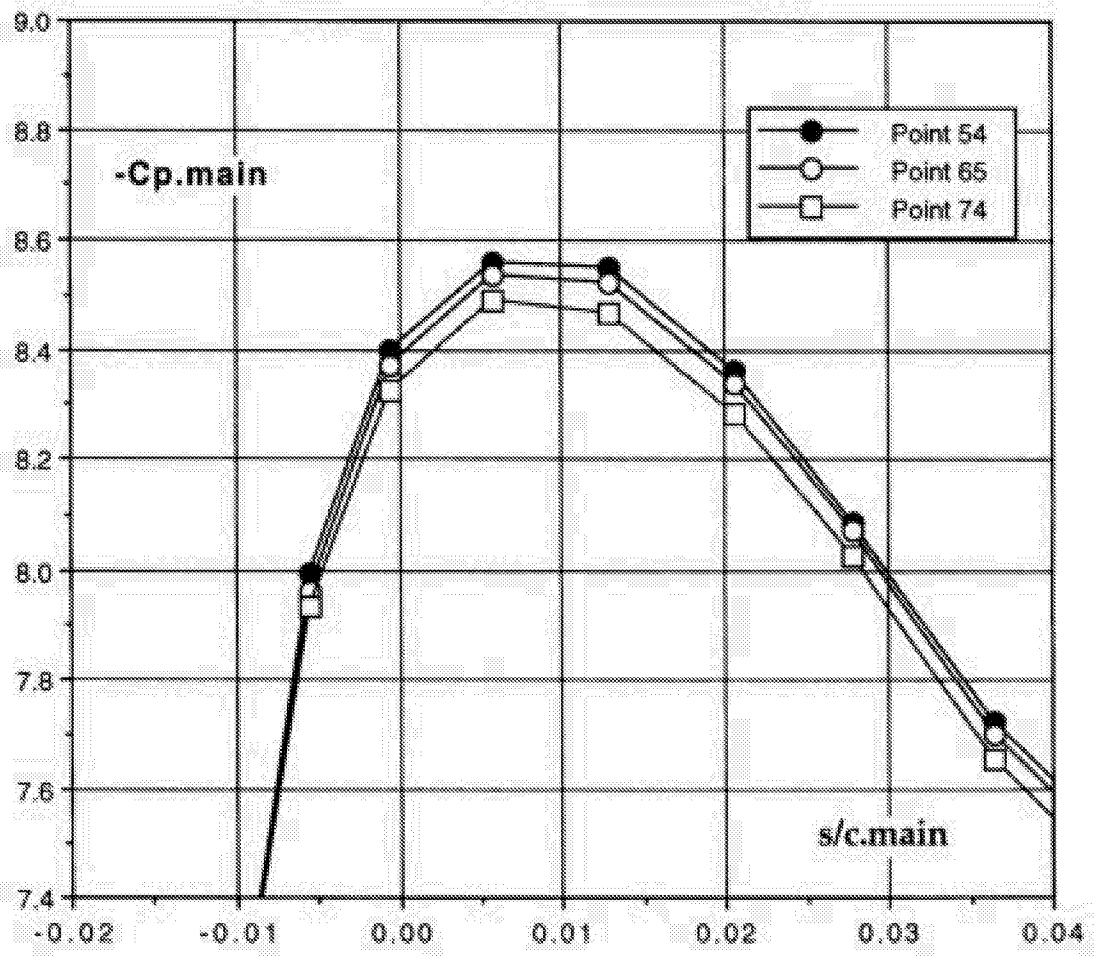


Figure 24a Repeatability in main element pressure distributions.
 30P/30N Mach=0.2 Re=9 million Alpha=16 deg.

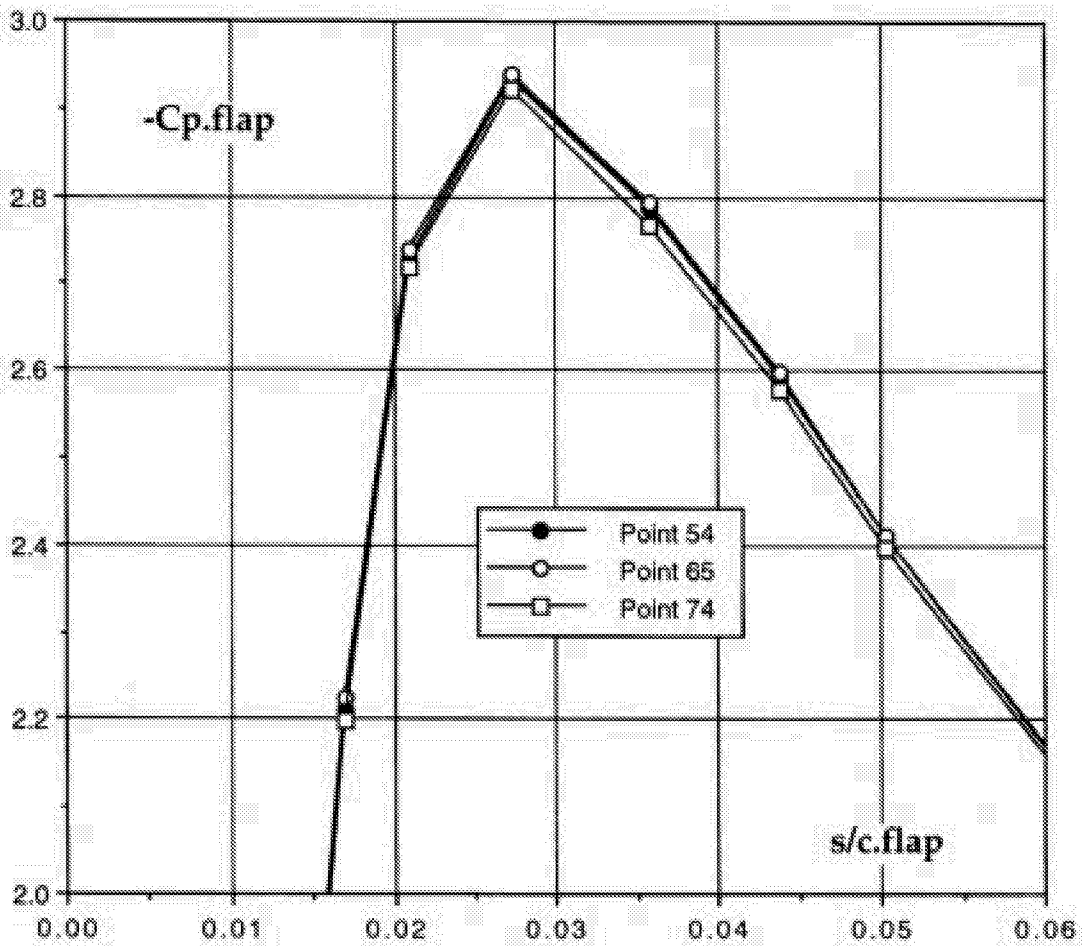


Figure 24b Repeatability in flap pressure distributions.
 30P/30N Mach=0.2 Re=9 million Alpha=16 deg.

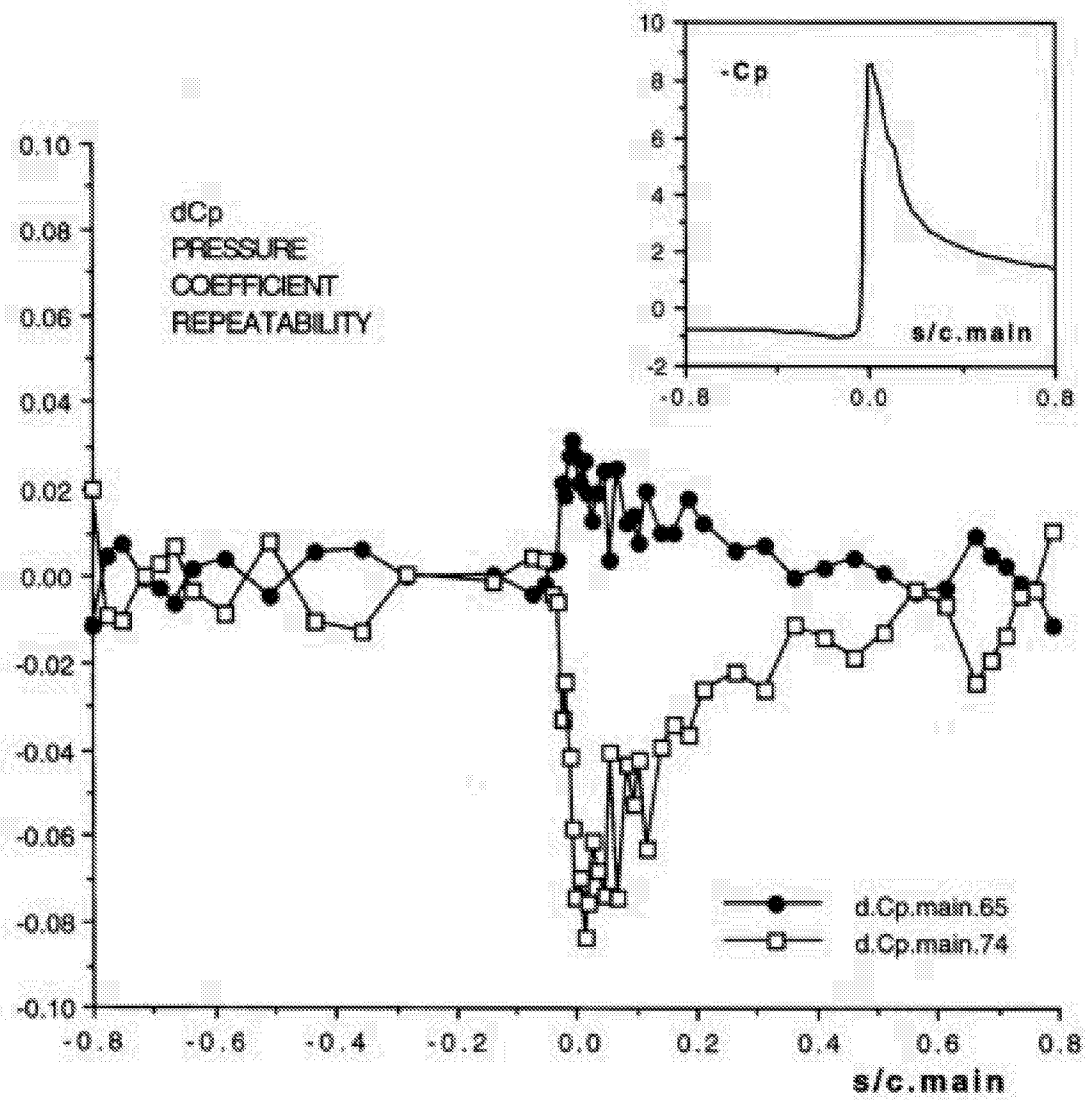


Figure 25 Pressure distribution repeatability at Alpha=16 deg.
 30P/30N Mach=0.2 Re=9 million. Points 54,65&74

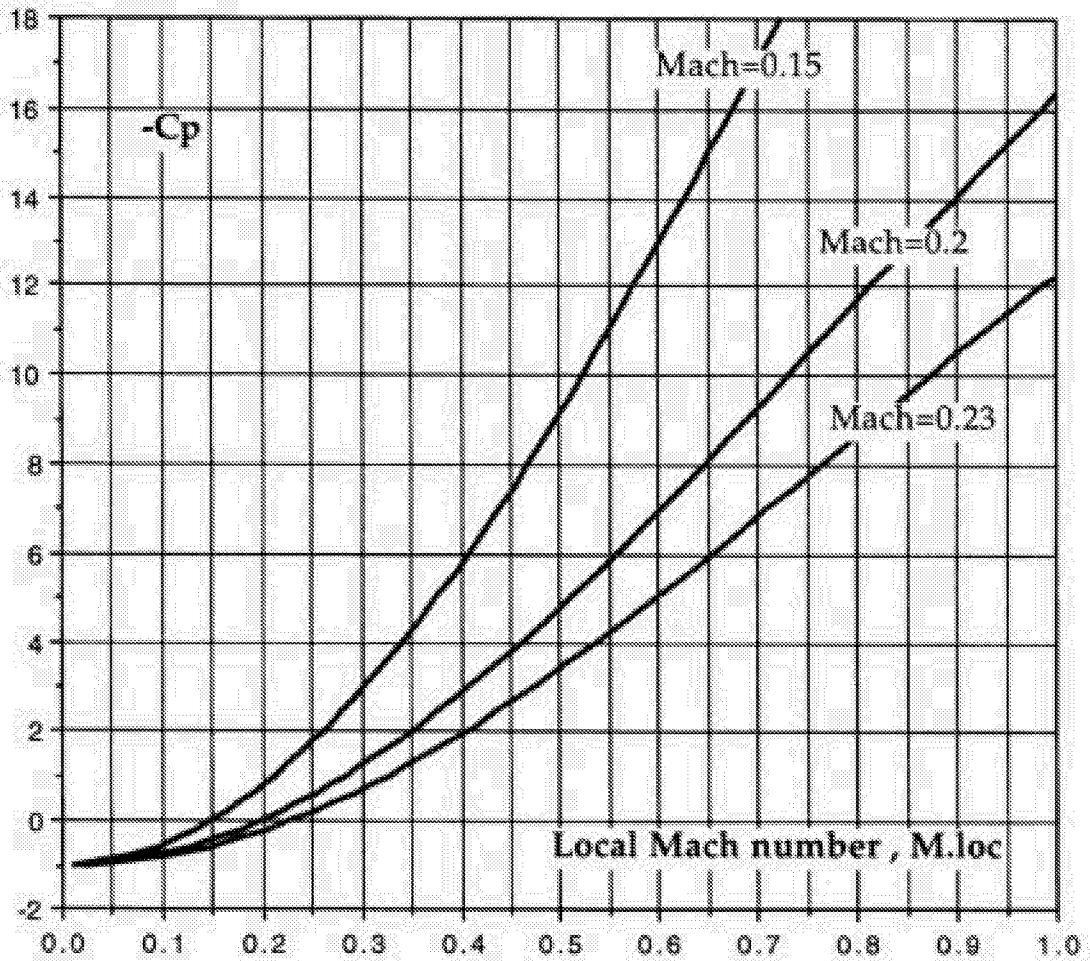


Figure 26 Relation between local Mach number and pressure coefficients for three tunnel Mach numbers.

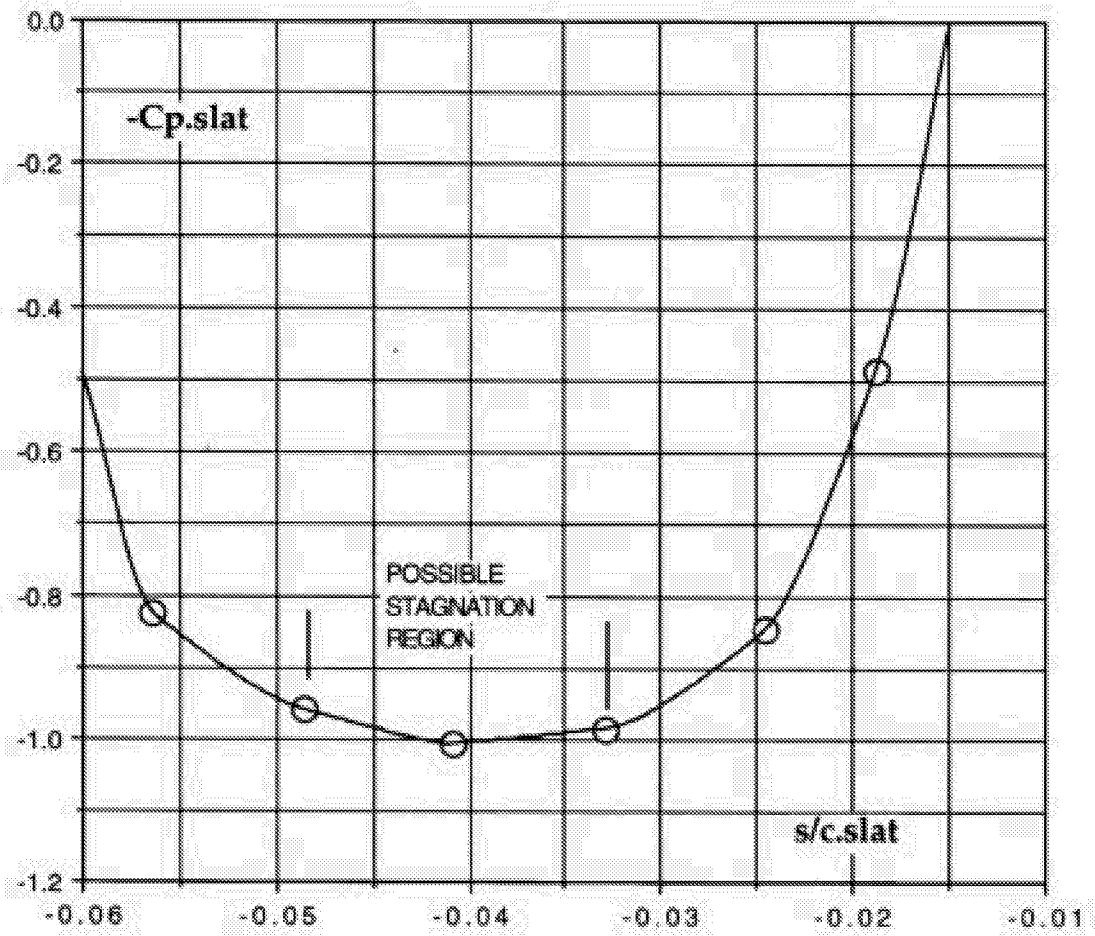


Figure 27 Pressure distribution in slat stagnation region.
 30P/30N Mach=0.2 Re=9 mill. Alpha=16 degrees (Point 54)

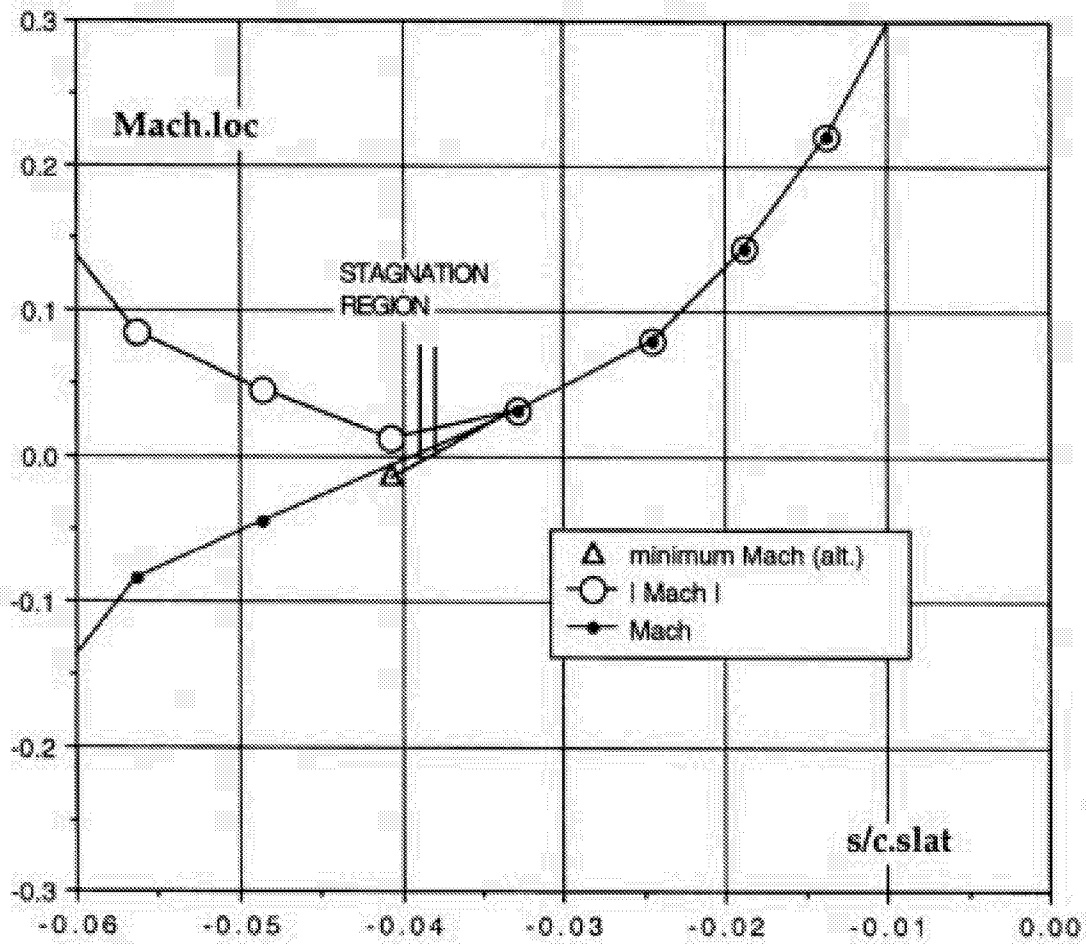


Figure 28a Stagnation region interpretation - slat.
Mach number is negative on pressure side.
30P/30N Mach=0.2 Re=9 mill Alpha=16 deg.

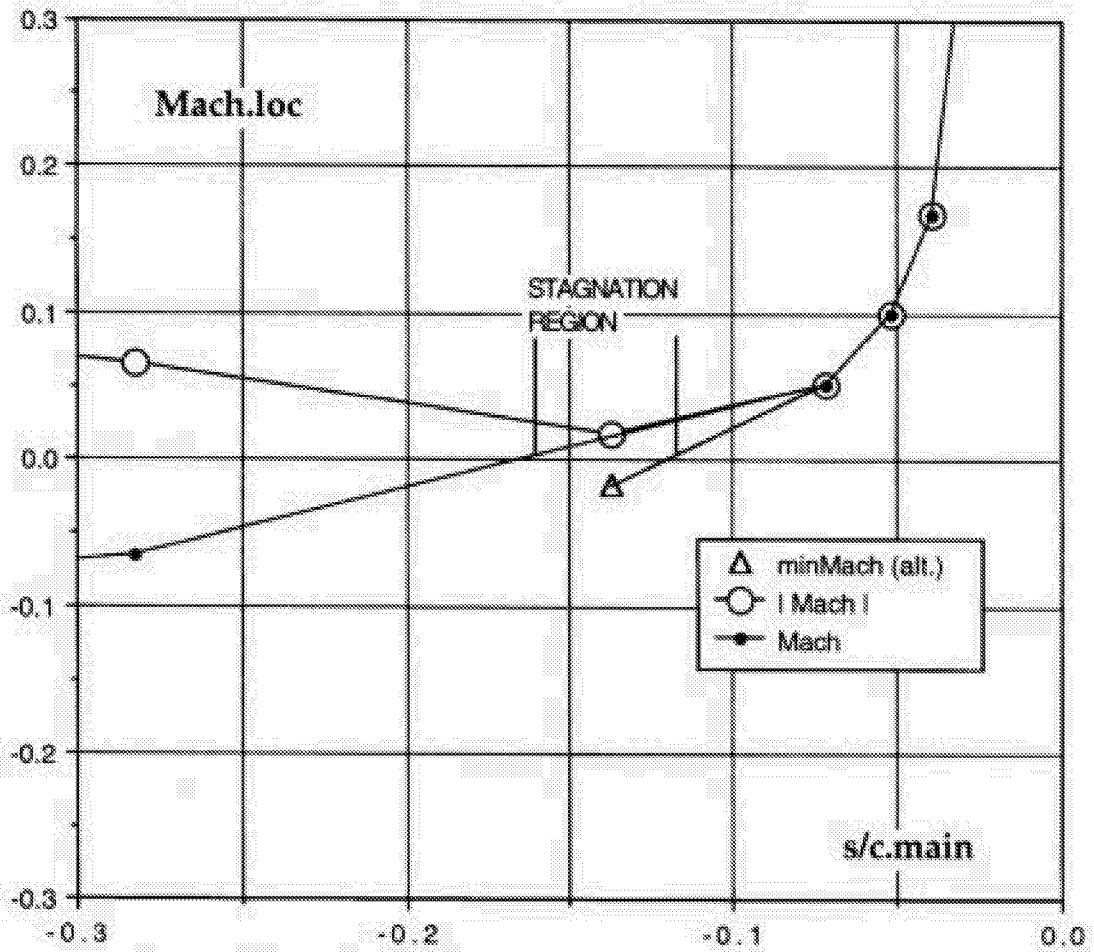


Figure 28b Stagnation region interpretation - main element.
 Mach number is negative on pressure side.
 30P/30N Mach=0.2 Re=9 mill Alpha=16 deg.

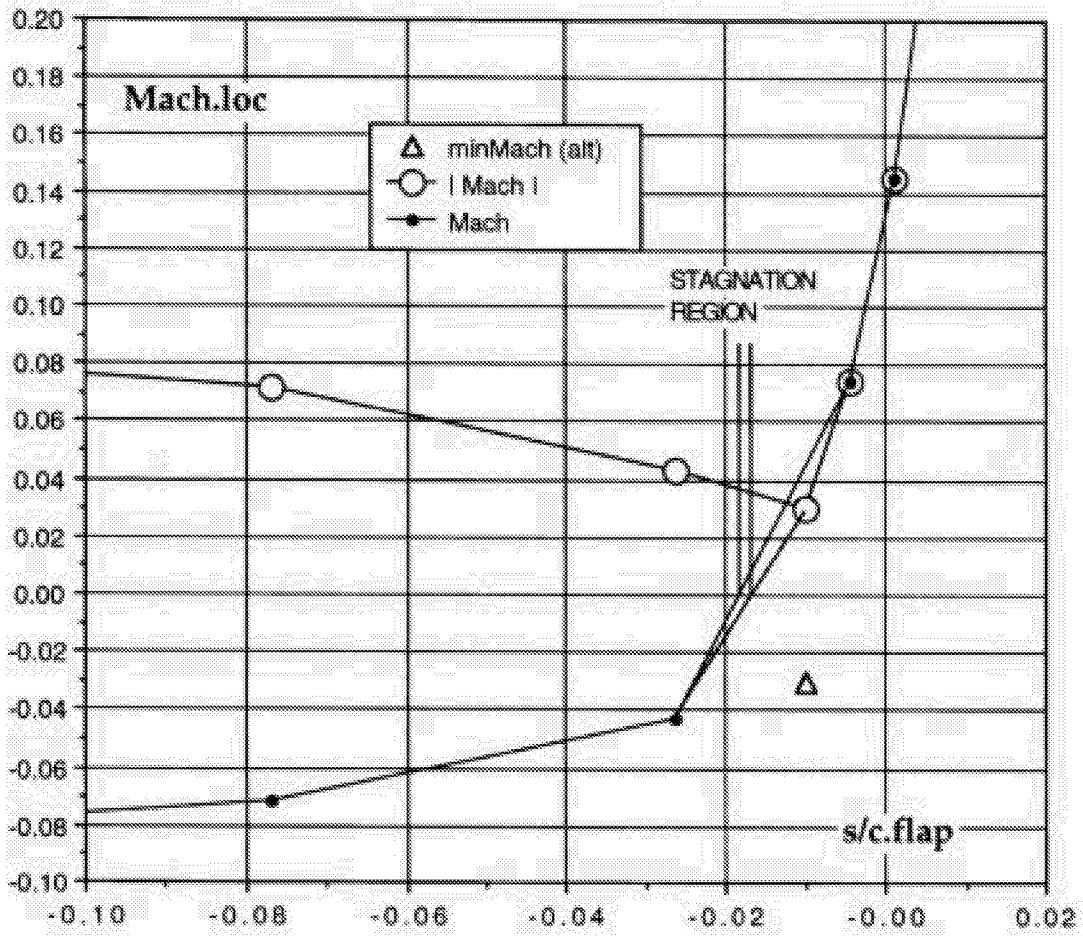


Figure 28c Stagnation region interpretation - flap.
Mach number is negative on pressure side.
30P/30N Mach=0.2 Re=9 mill Alpha=16 deg.

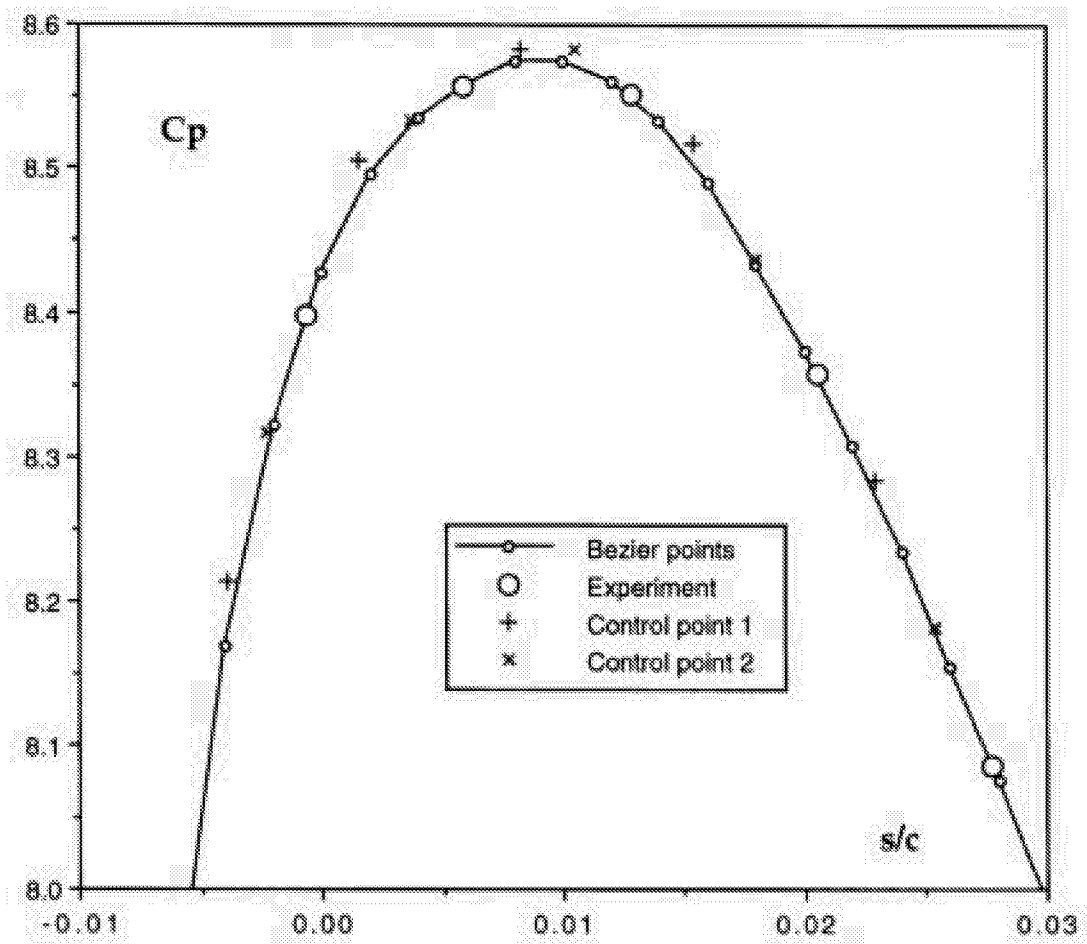


Figure 29a Suction peak region of main element.
 30P/30N Mach=0.2, Re=9 mill, Alpha = 16 deg.

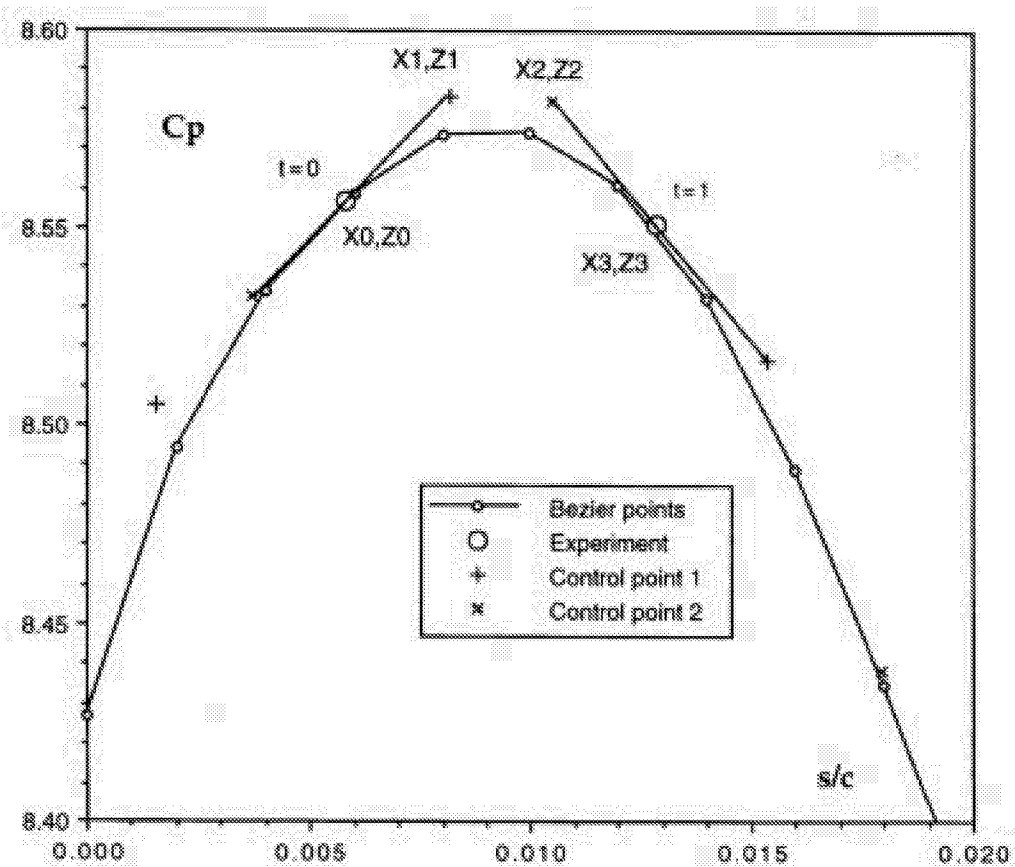


Figure 29b Suction peak region of main element with the control points indicated. 30P/30N Mach=0.2, Re=9 mill, Alpha = 16 deg.

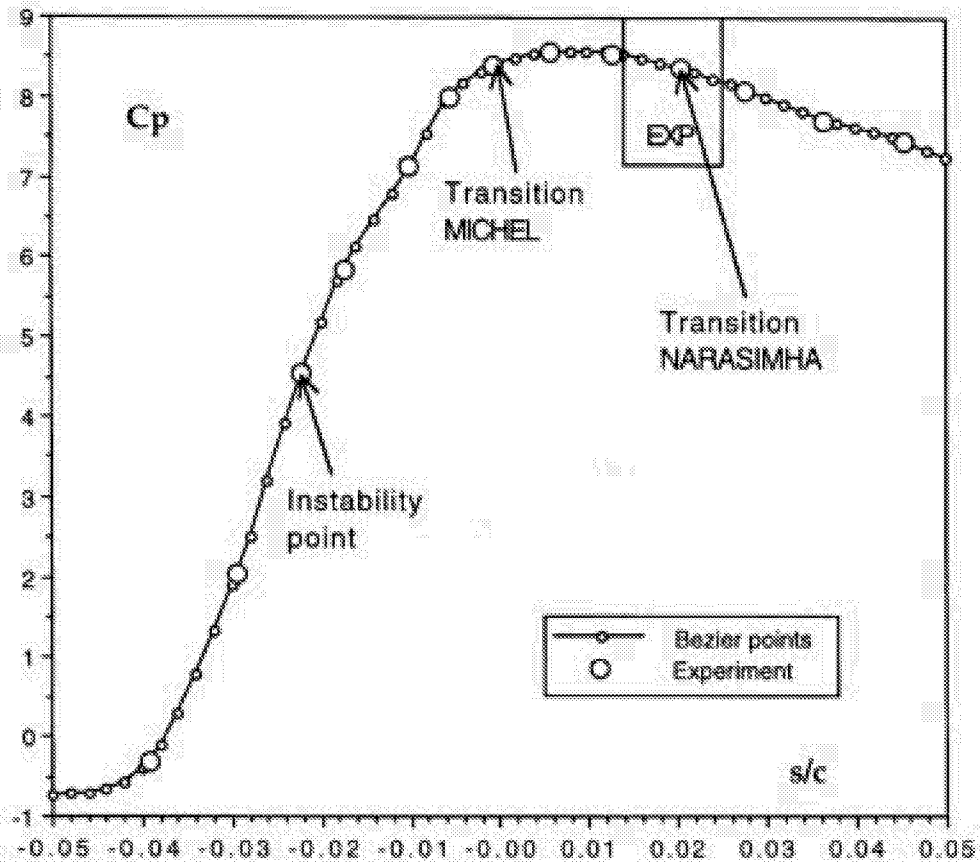


Figure 30 Suction peak region of main element. Results from engineering criteria and the hot film experiment. 30P/30N Mach=0.2, Re=9 mill, Alpha = 16 deg.

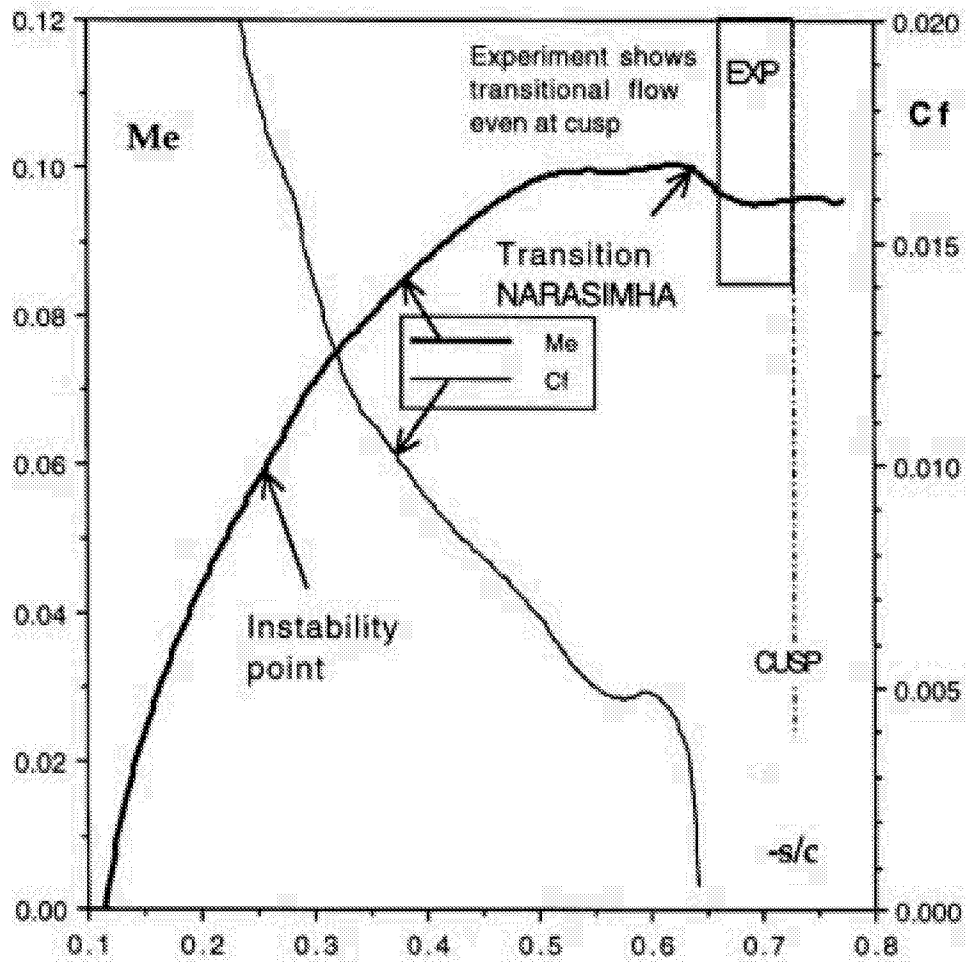


Figure 31 Mach number and computed laminar skin friction, C_f , on pressure side of main element.
 30P/30N Mach=0.2 Re=9 mill Alpha=16 deg.

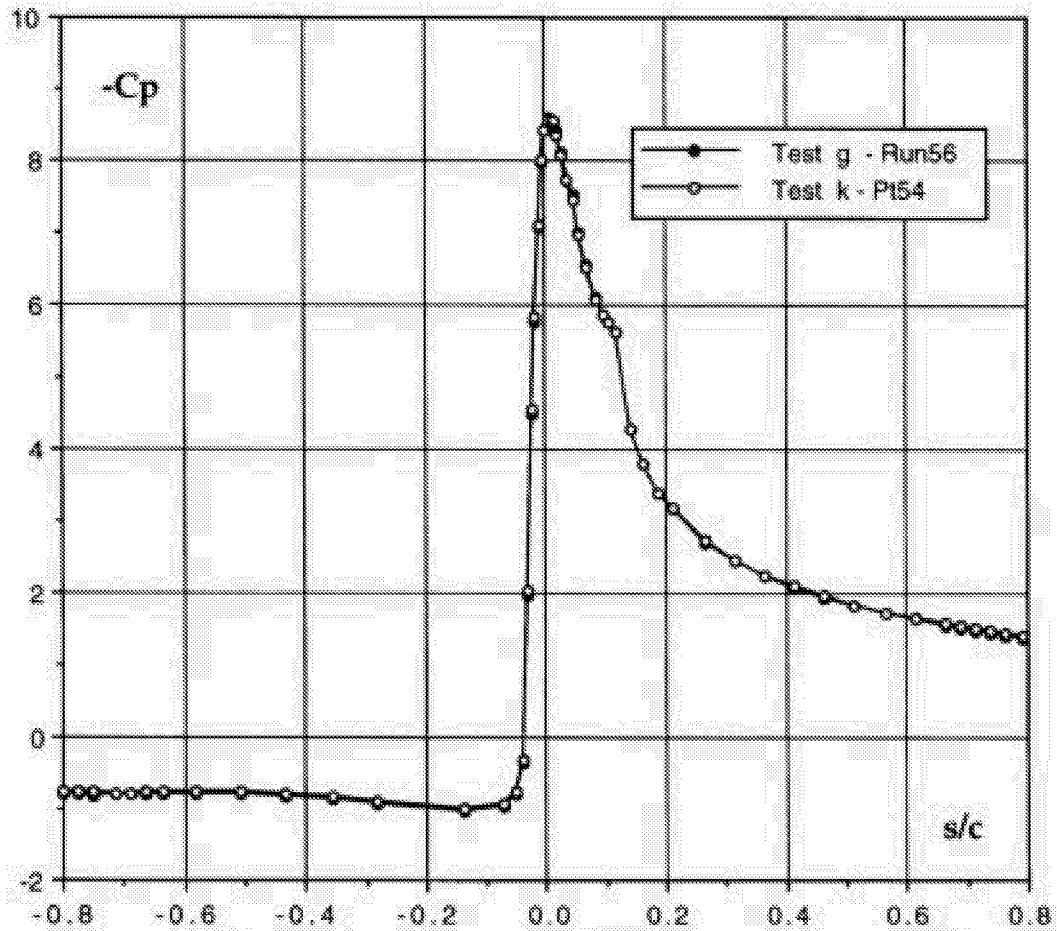


Figure 32 Comparison of pressure distributions on the main element. 30P/30N M=0.2 Re=9 mill. Alpha=16 deg. Tests g(365) and k(307)

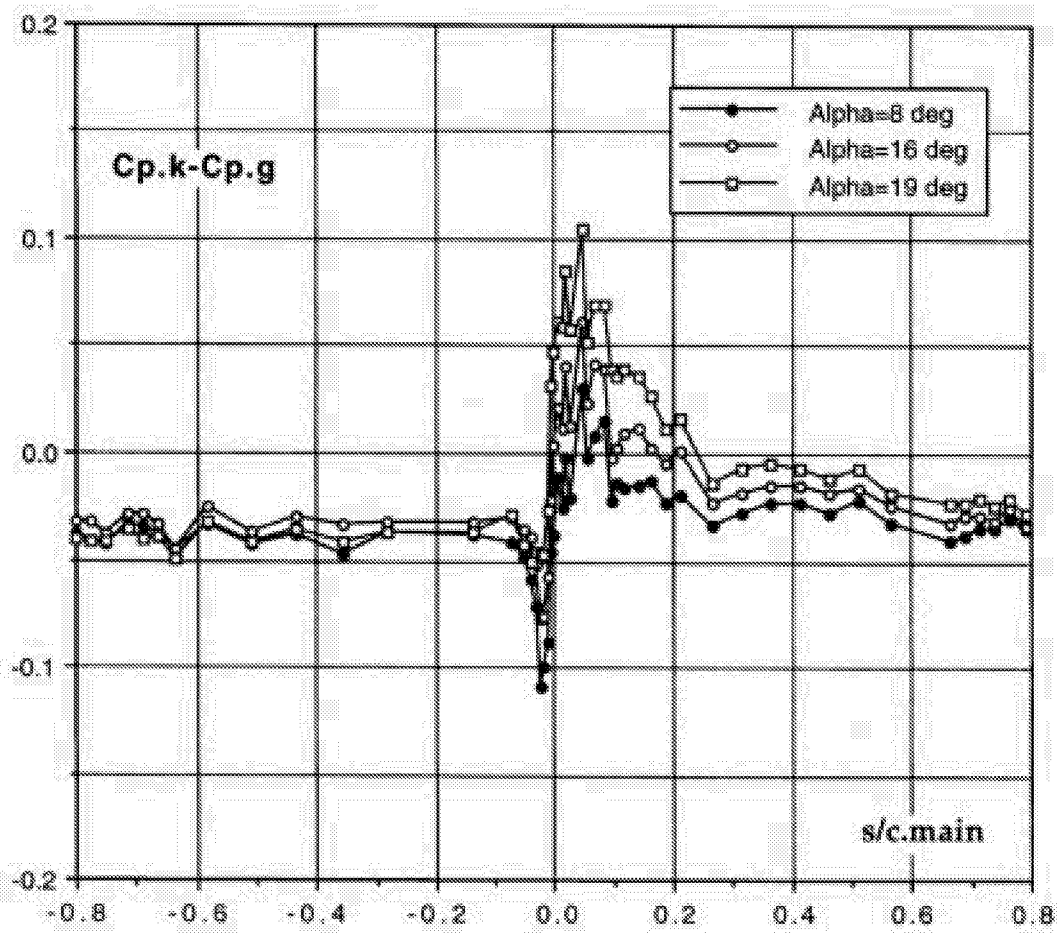


Figure 33 Difference between pressure coefficients on main element, tests g and k. Alpha=8, 16 and 19 deg.

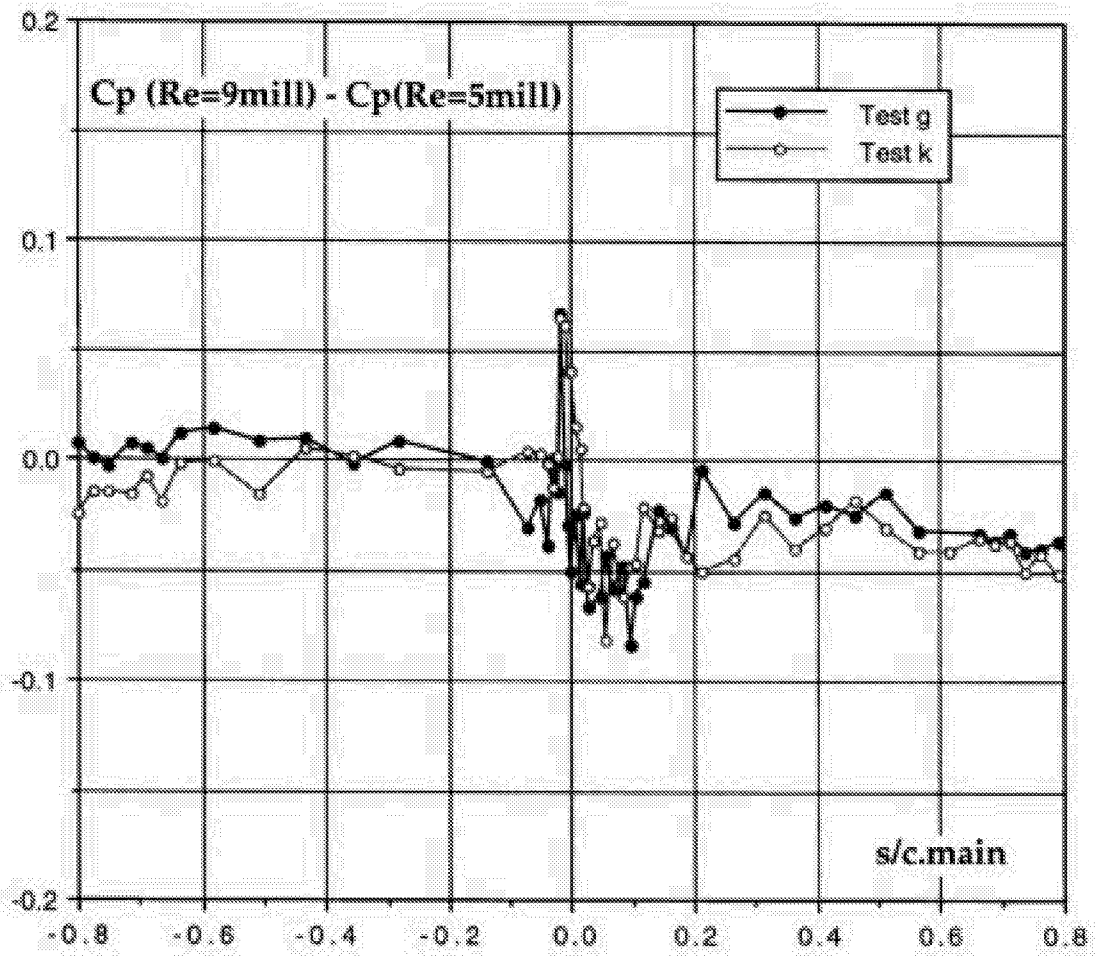


Figure 34a Reynolds number change of pressure coefficients.
 30P/30N M=0.2, Alpha=8 deg. Tests 365 (g) and 397 (k).

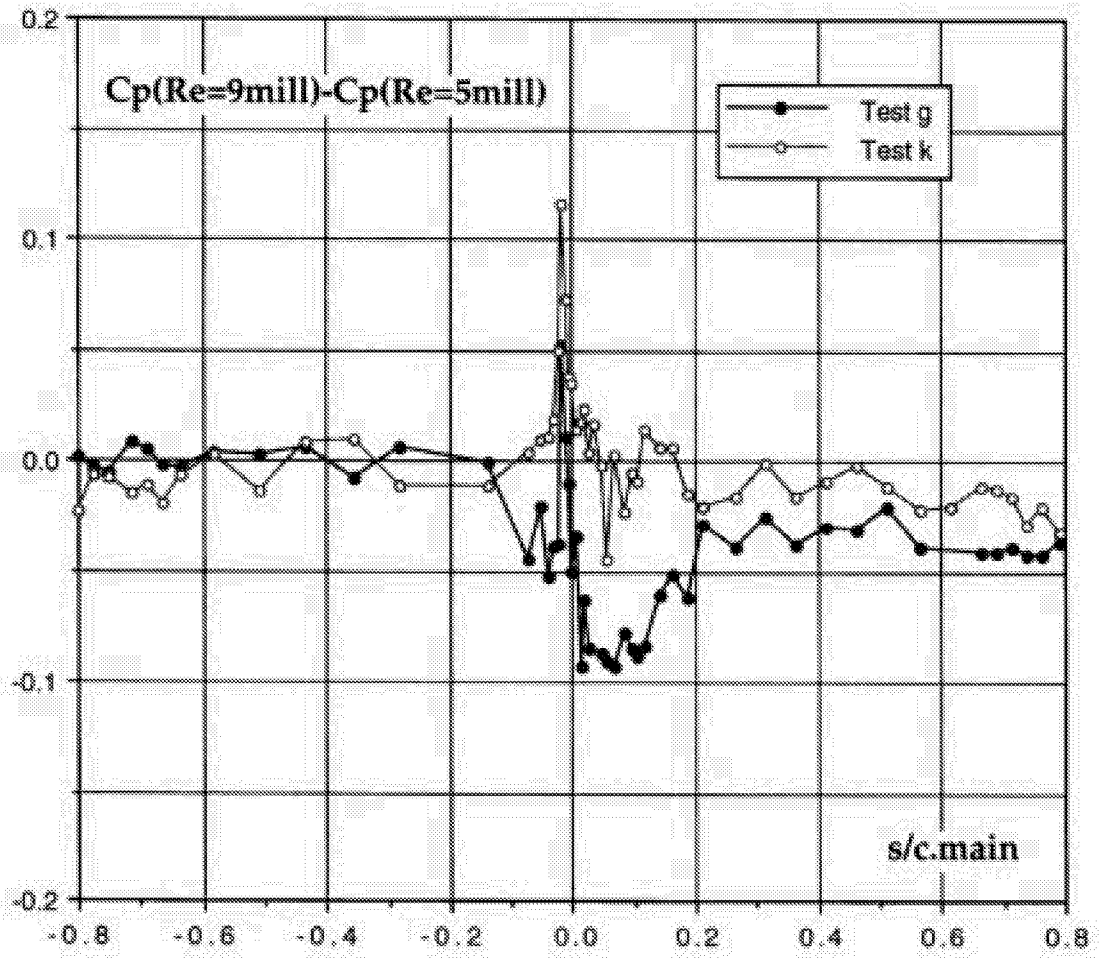


Figure 34b Reynolds number change of pressure coefficients.
 $M=0.2$, $\text{Alpha}=16$ deg. Tests 365 (g) and 397 (k).

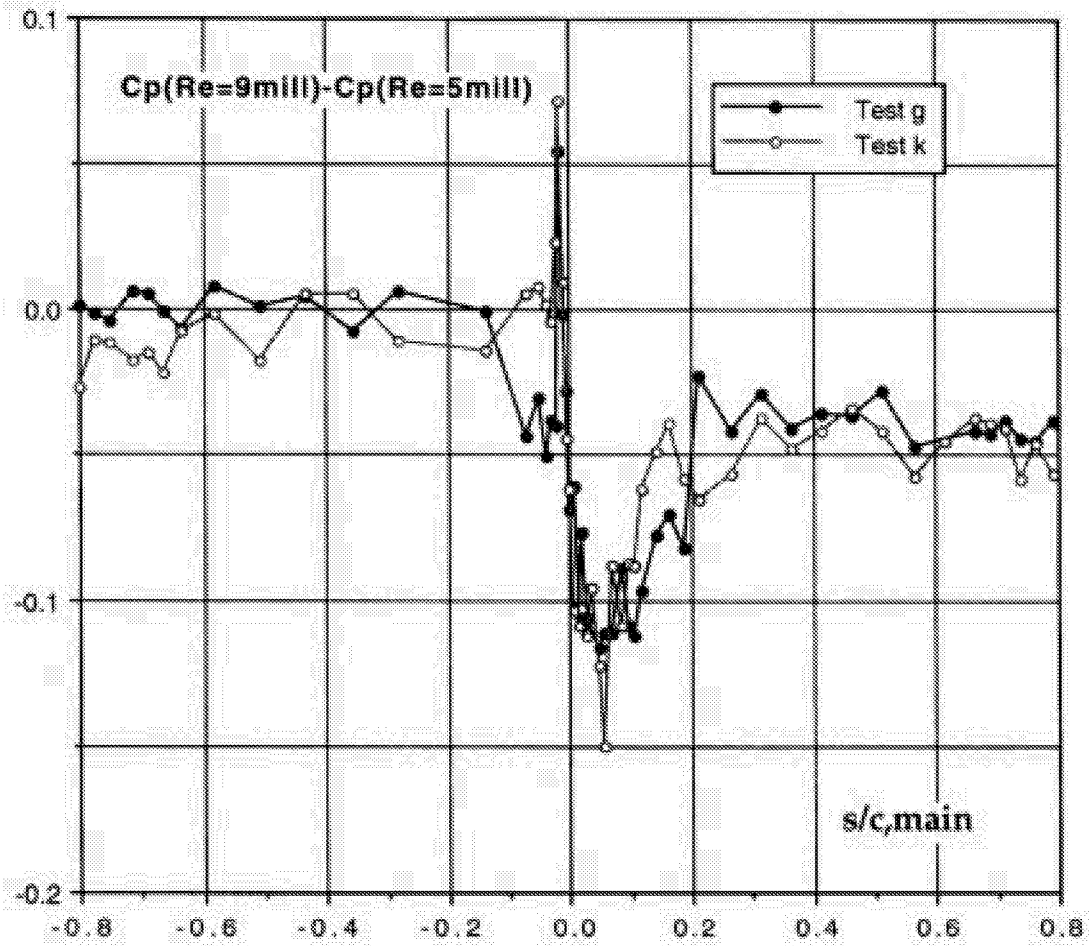


Figure 34c Reynolds number change of pressure coefficients.
 $M=0.2$, $\text{Alpha}=19$ deg. Tests 365 (g) and 397 (k).

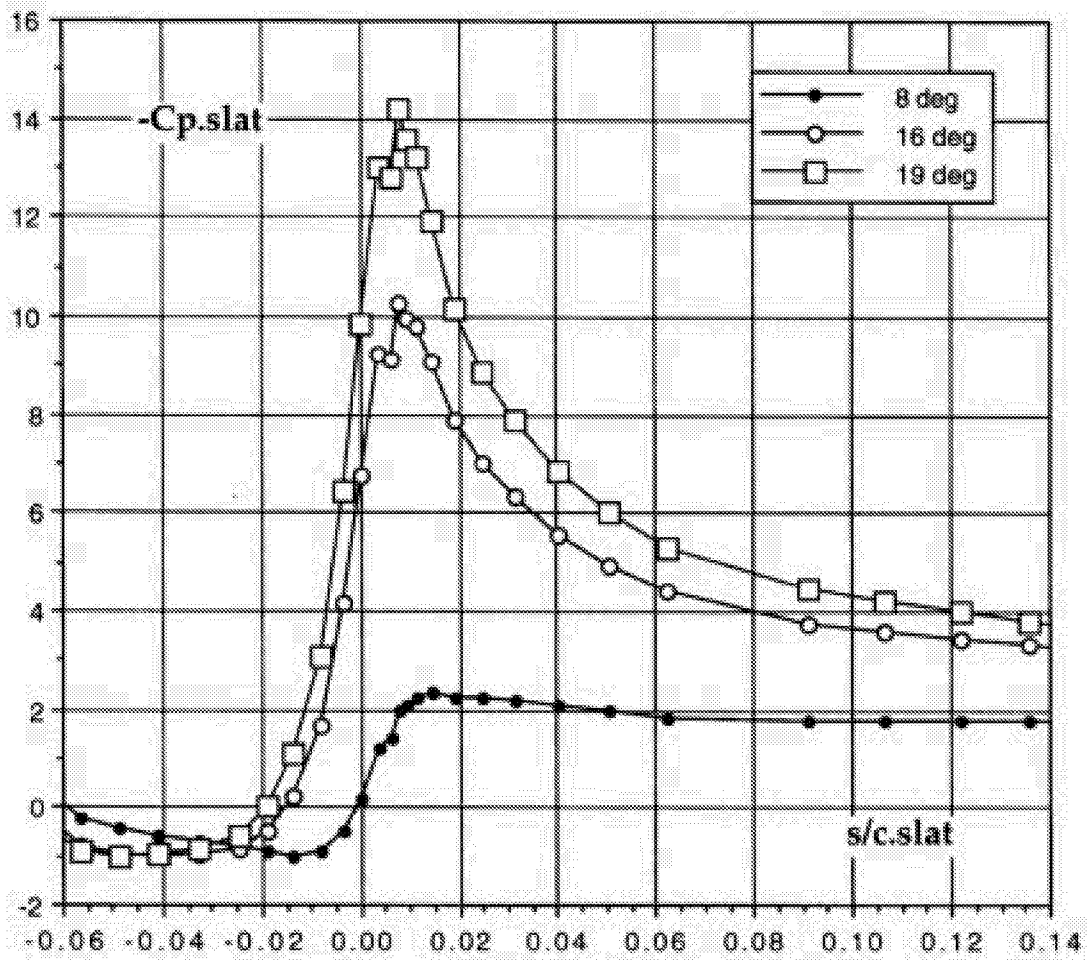


Figure 35a Pressure distributions - slat.
30P/30N Mach=0.2 Re=9 mill.

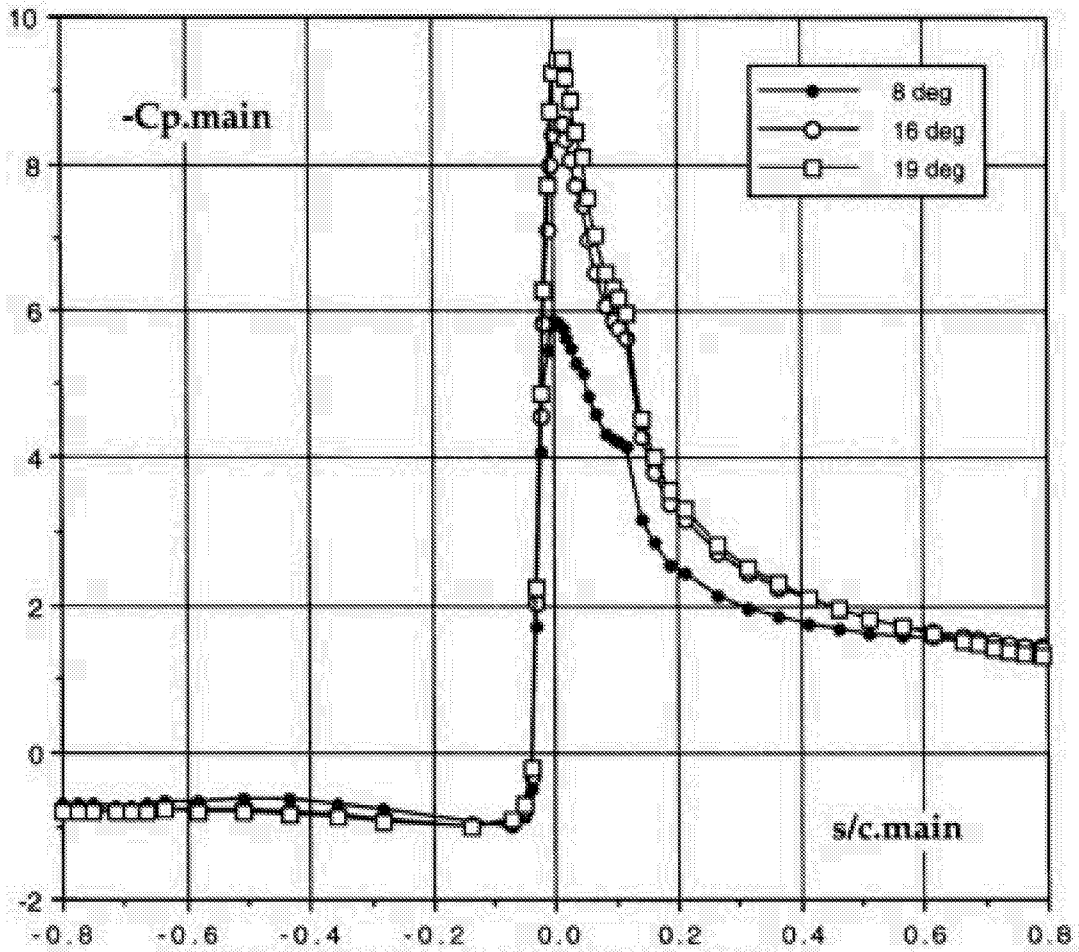


Figure 35b Pressure distributions - main.
30P/30N Mach=0.2 Re=9 mill.

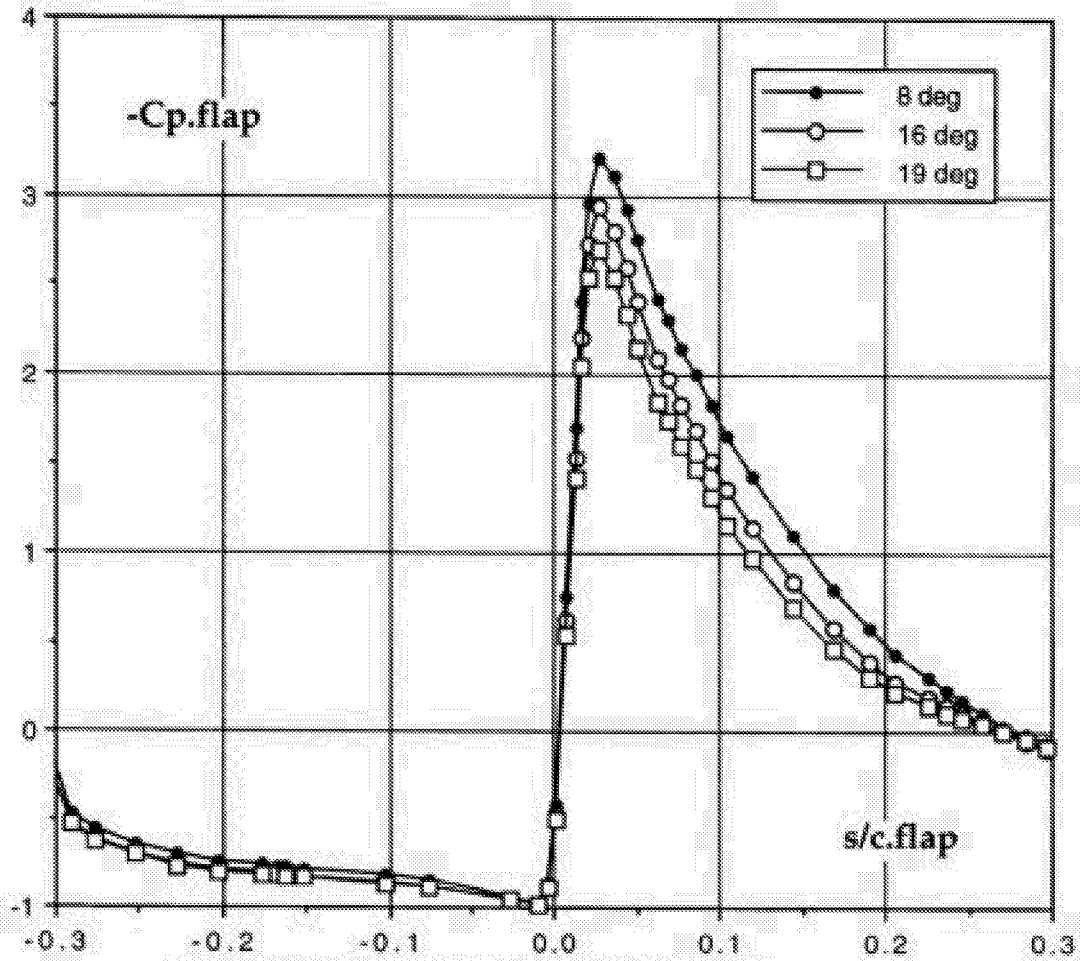


Figure 35c Pressure distributions - flap.
30P/30N Mach=0.2 Re=9 mill.

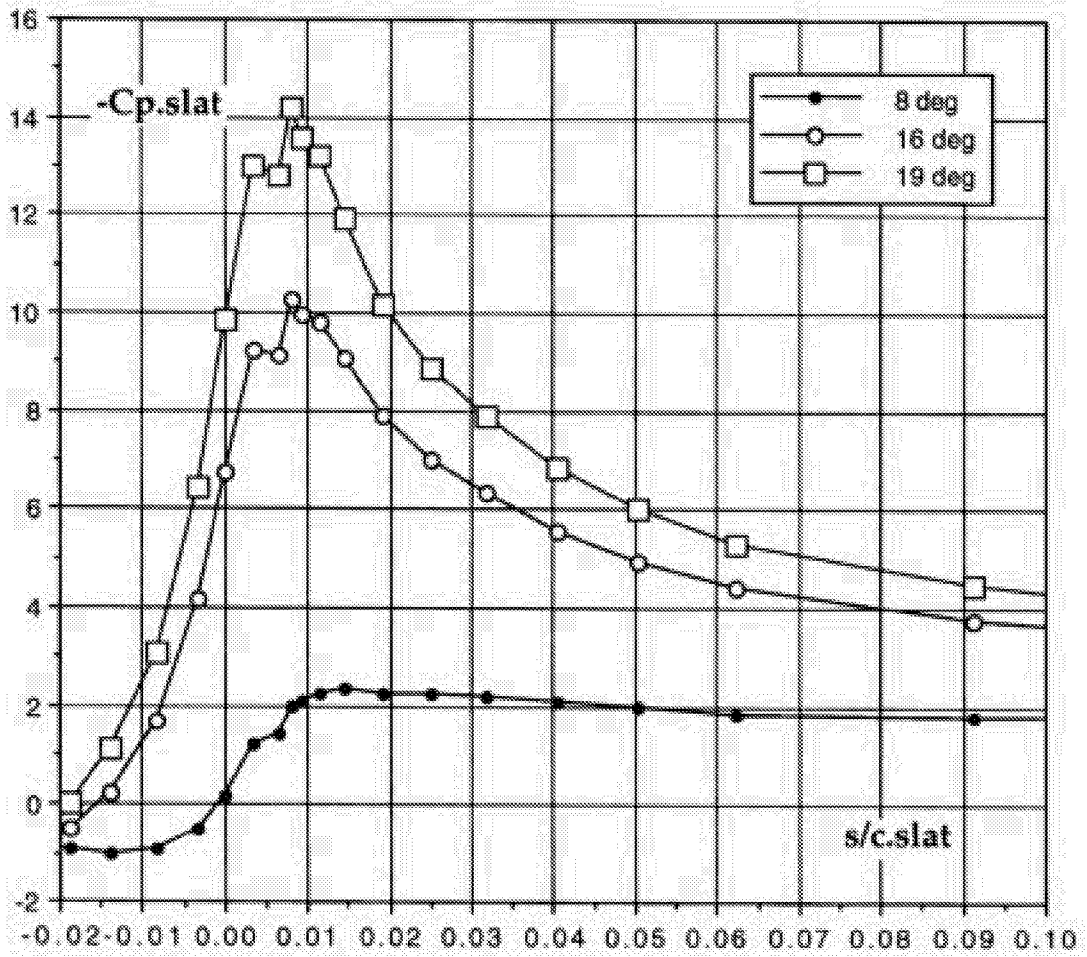


Figure 36a Pressure distributions - slat.
 30P/30N Mach=0.2 Re= 9 mill. Nose region.

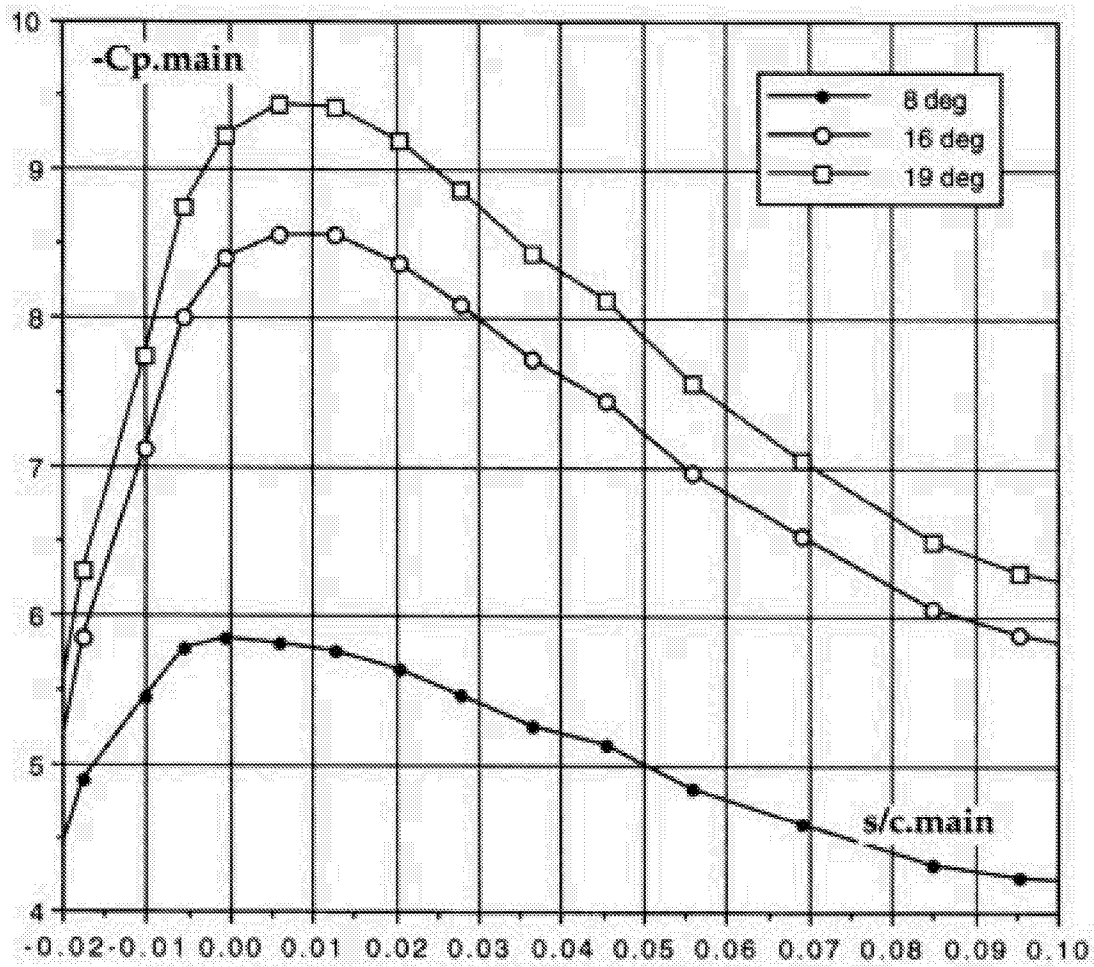


Figure 36b Pressure distributions - main.
 30P/30N Mach=0.2 Re=9 mill. Nose region.

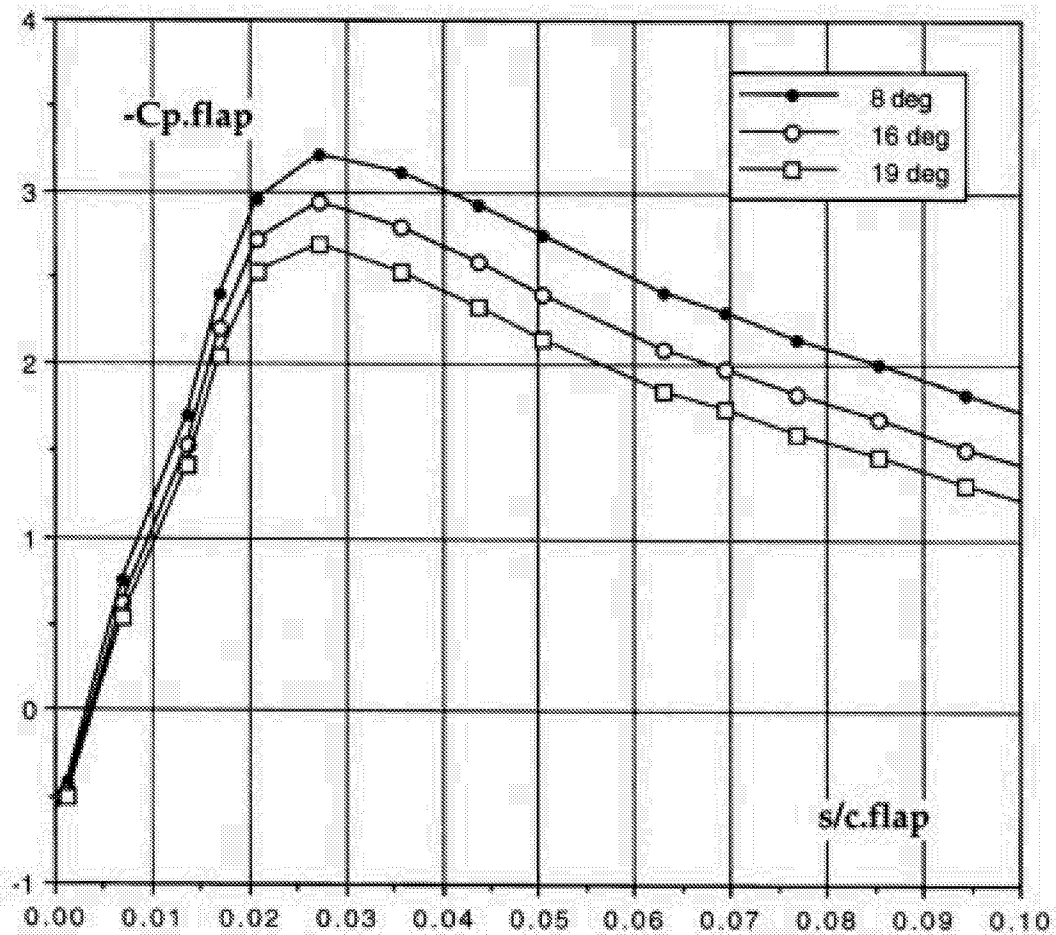


Figure 36c Pressure distributions - flap. 30P/30N Mach=0.2 Re=9 mill. Nose region.

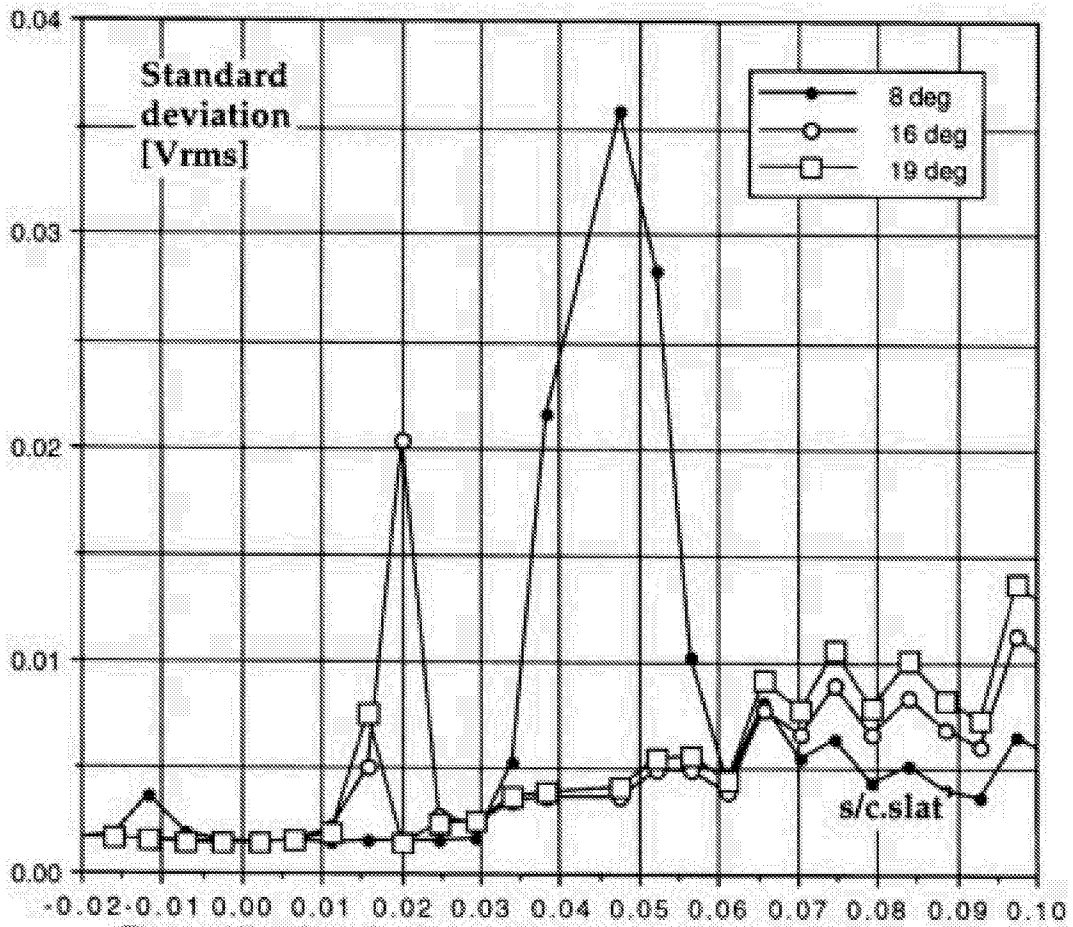


Figure 37a Standard deviation distributions - slat.
30P/30N Mach=0.2 Re=9 mill.

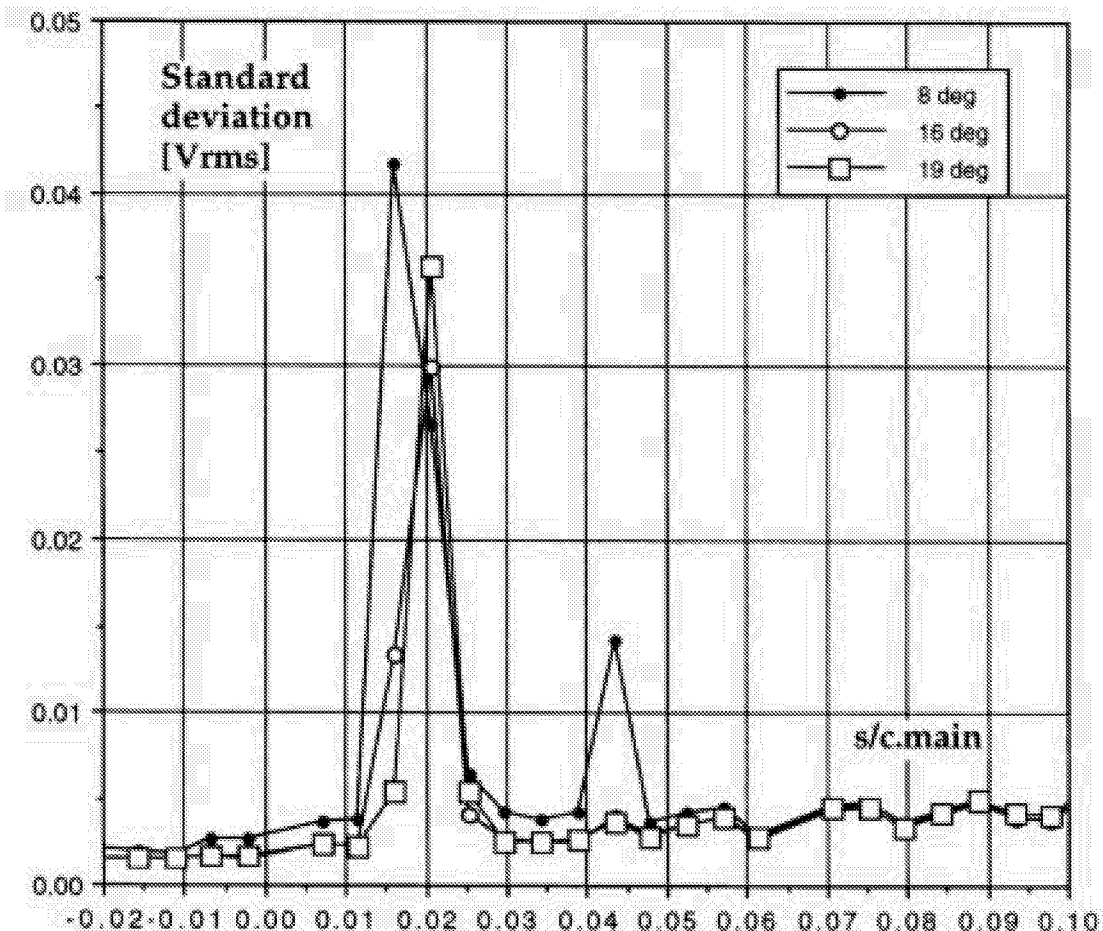


Figure 37b Standard deviation distributions - main.
 30P/30N Mach=0.2 Re=9 mill.

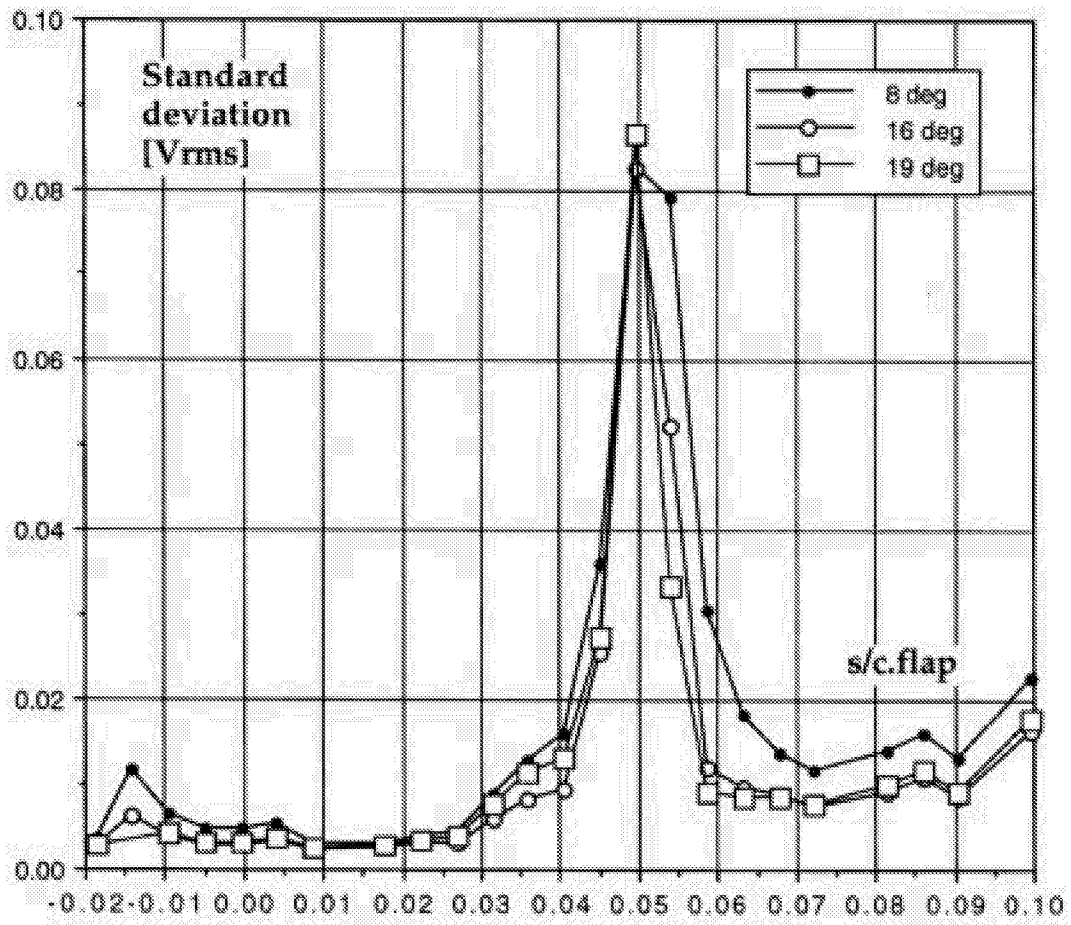


Figure 37c Standard deviation distributions - flap.
30P/30N Mach=0.2 Re=9 mill.

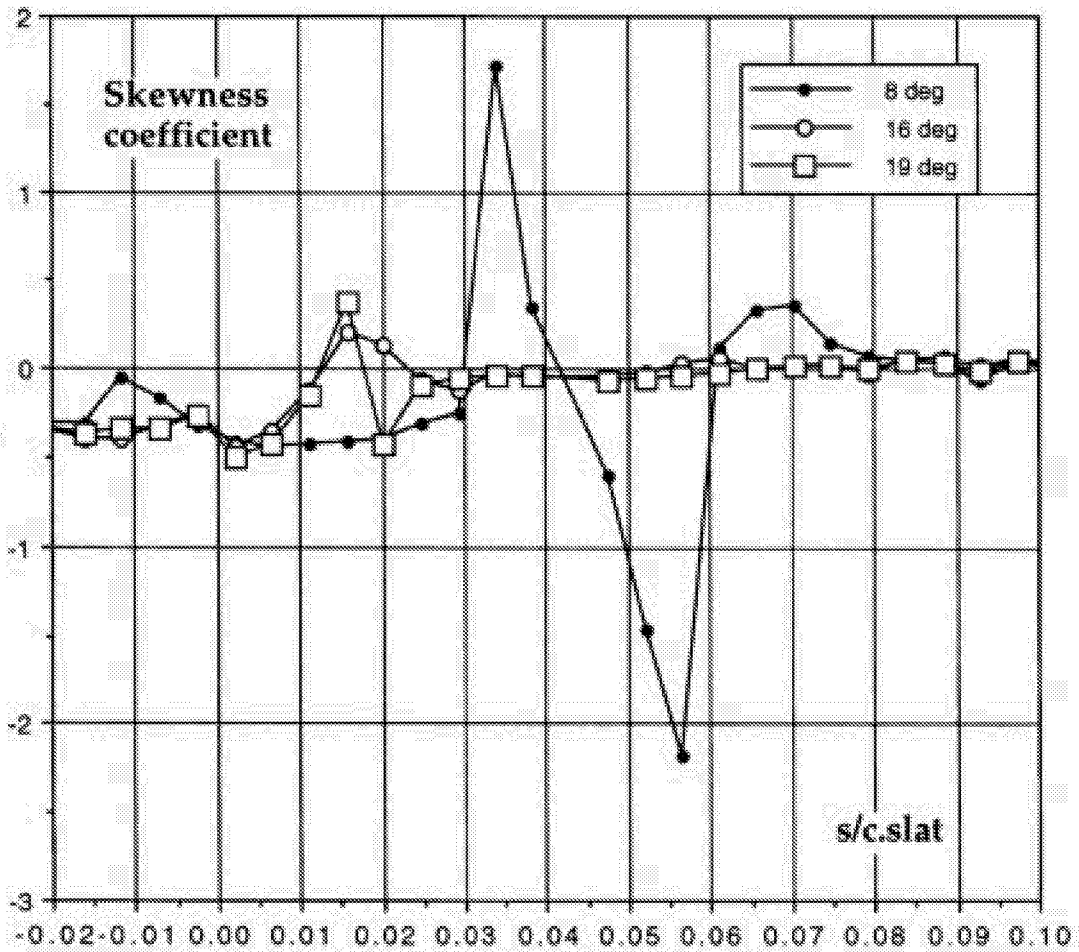


Figure 38a Skewness distributions - slat.
30P/30N Mach=0.2 Re=9 mill.

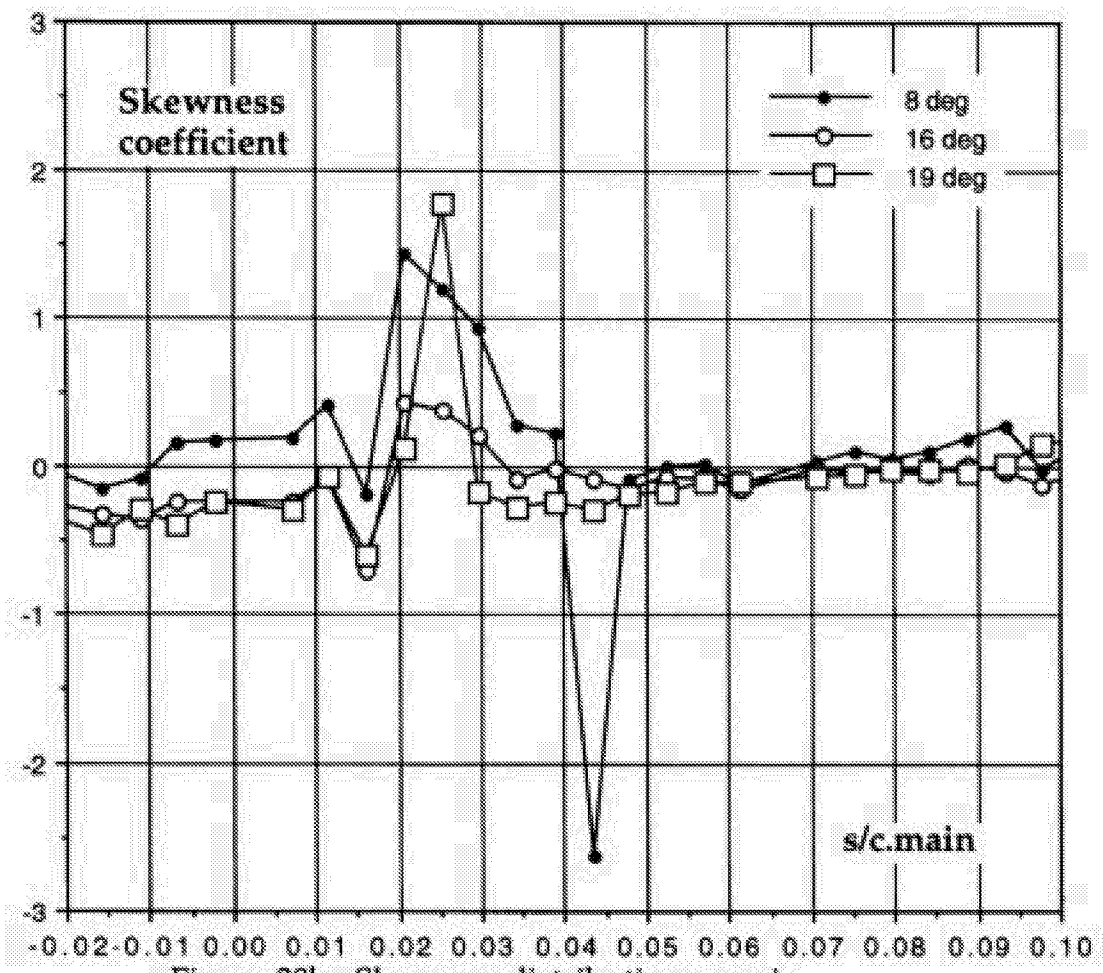


Figure 38b Skewness distributions - main.
 30P/30N Mach=0.2 Re=9 mill.

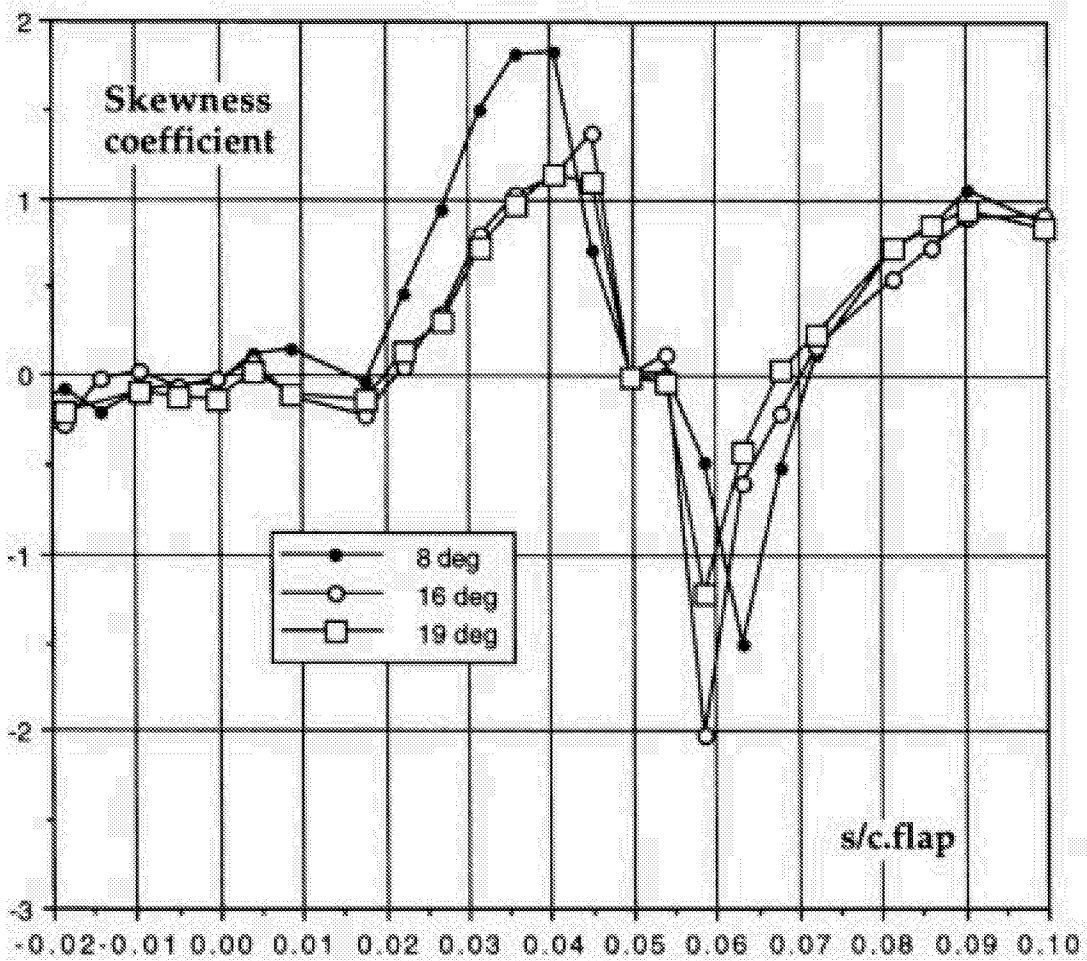


Figure 38c Skewness distributions - flap.
 30P/30N Mach=0.2 Re=9 mill.

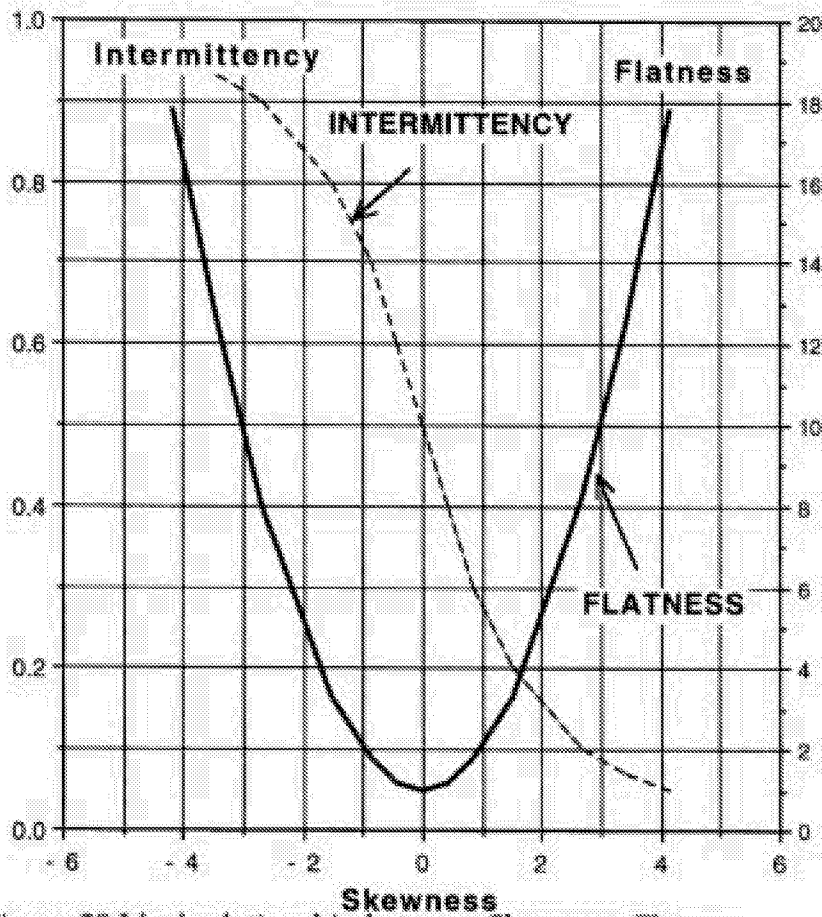


Figure 39 Ideal relationship between Skewness, Flatness and Intermittency for transitional signal (DC-coupled). Intermittency less than 0.05 and larger than 0.95 is not meaningful to consider.

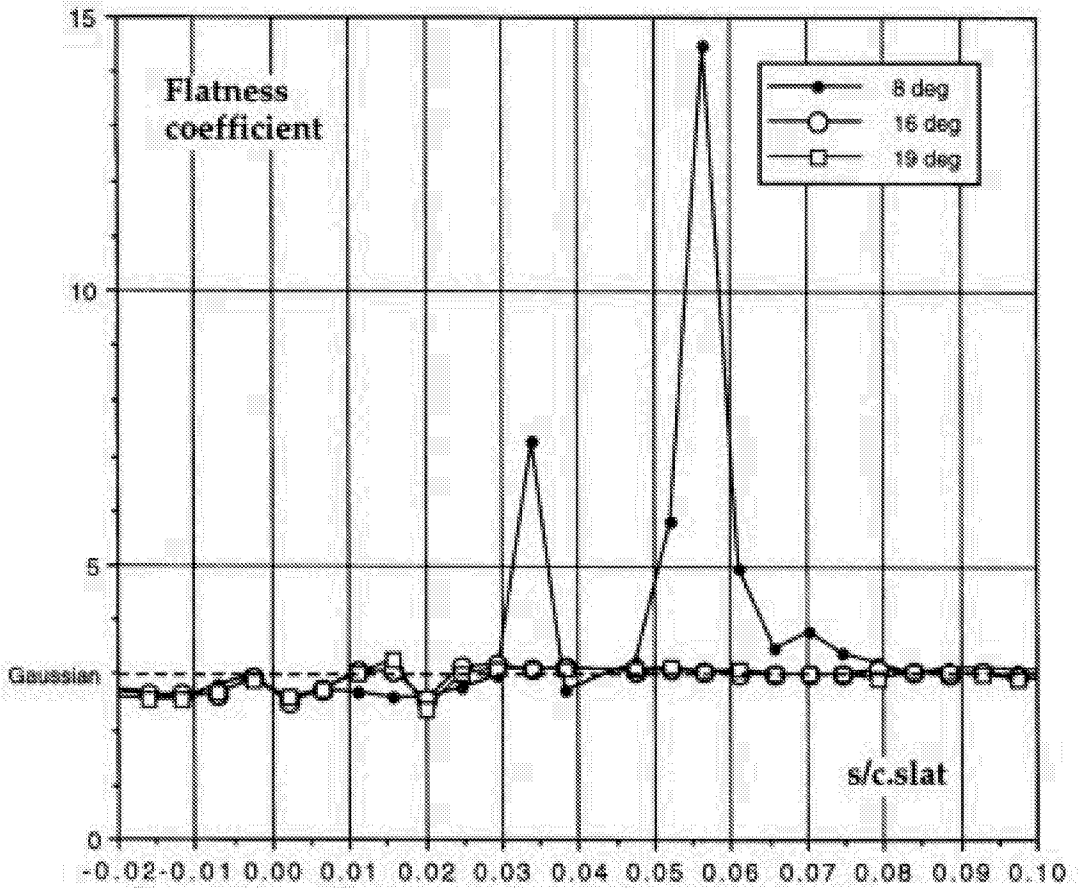


Figure 40a Flatness coefficient distributions - slat.
 30P/30N Mach=0.2 Re=9 mill.

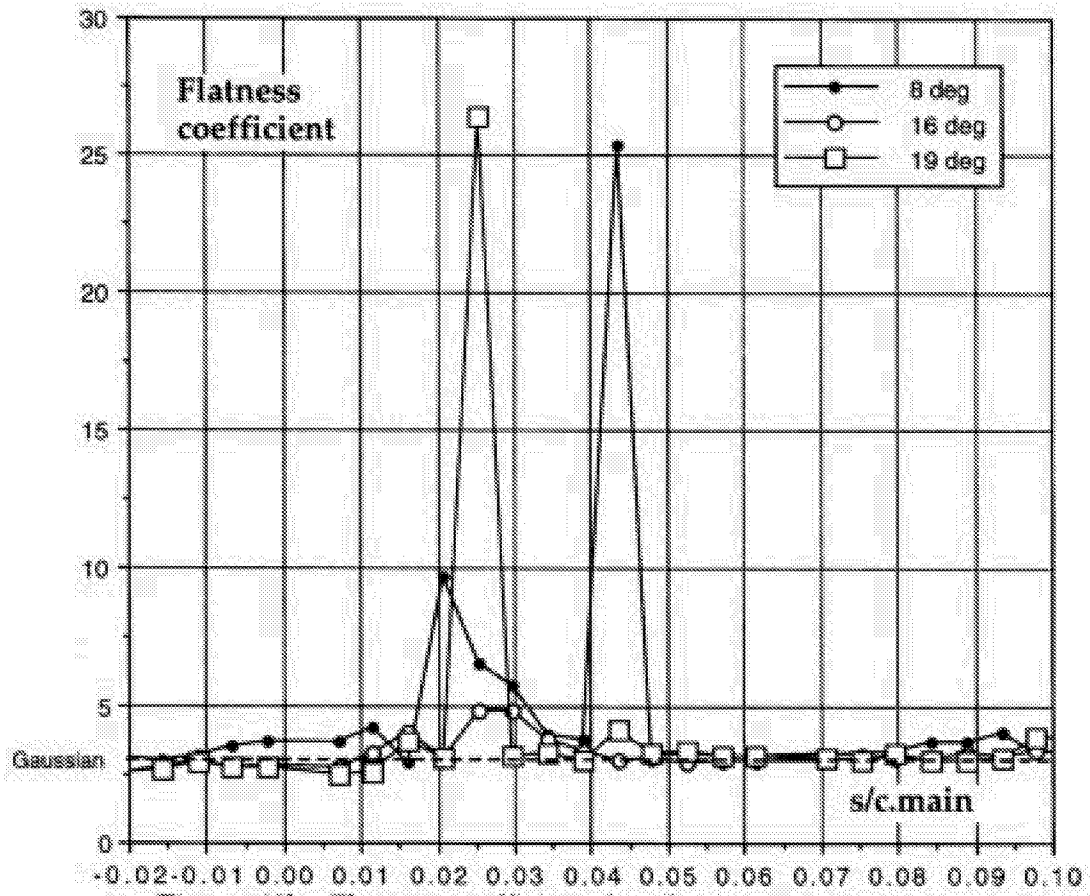


Figure 40b Flatness coefficient distributions - main.
30P/30N Mach=0.2 Re=9 mill.

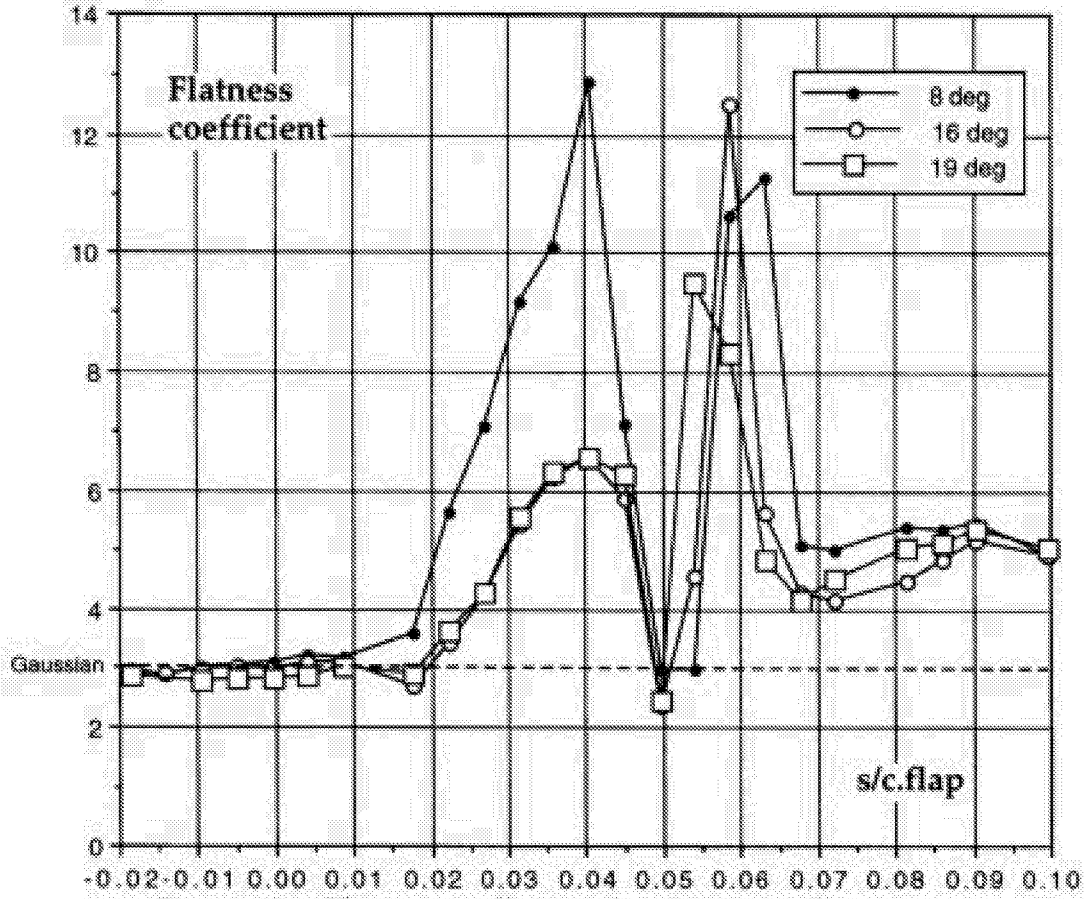


Figure 40c Flatness coefficient distributions - flap.
30P/30N Mach=0.2 Re=9 mill.

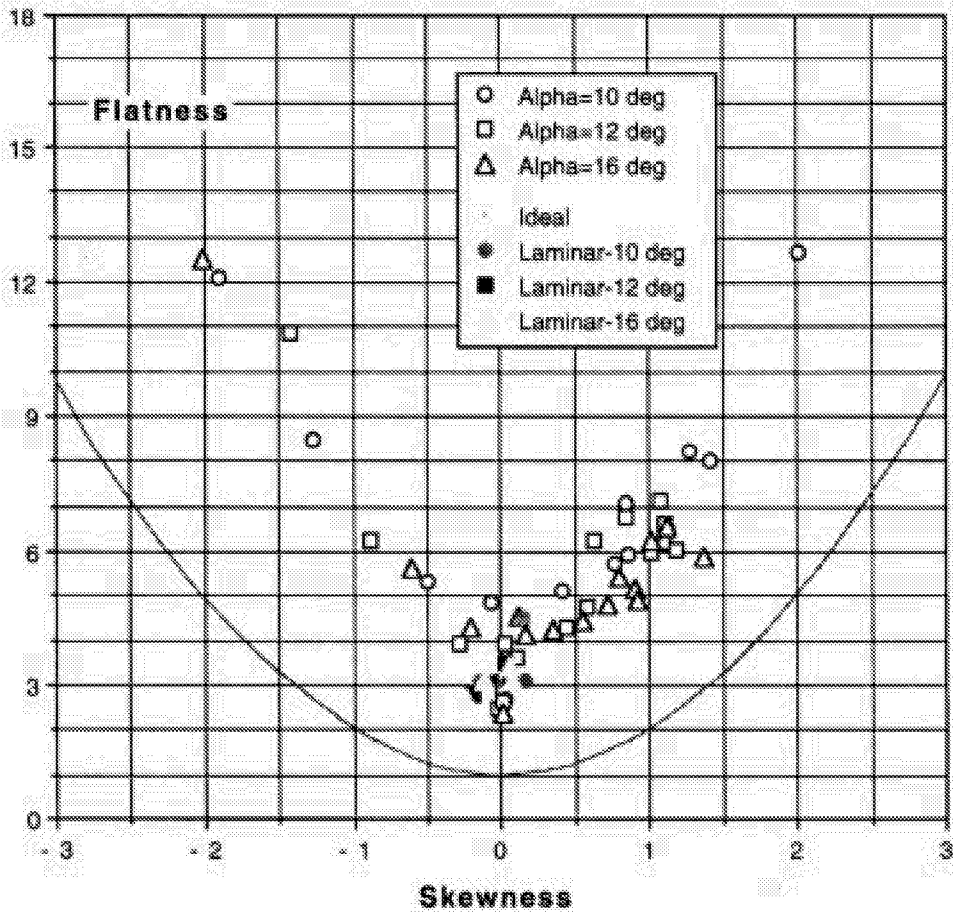


Figure 41 Flatness versus Skewness of flap sensors for Alpha = 10 to 16 degrees. Stagnation region - filled symbols. Note that the rectangular signal, with the DC component.

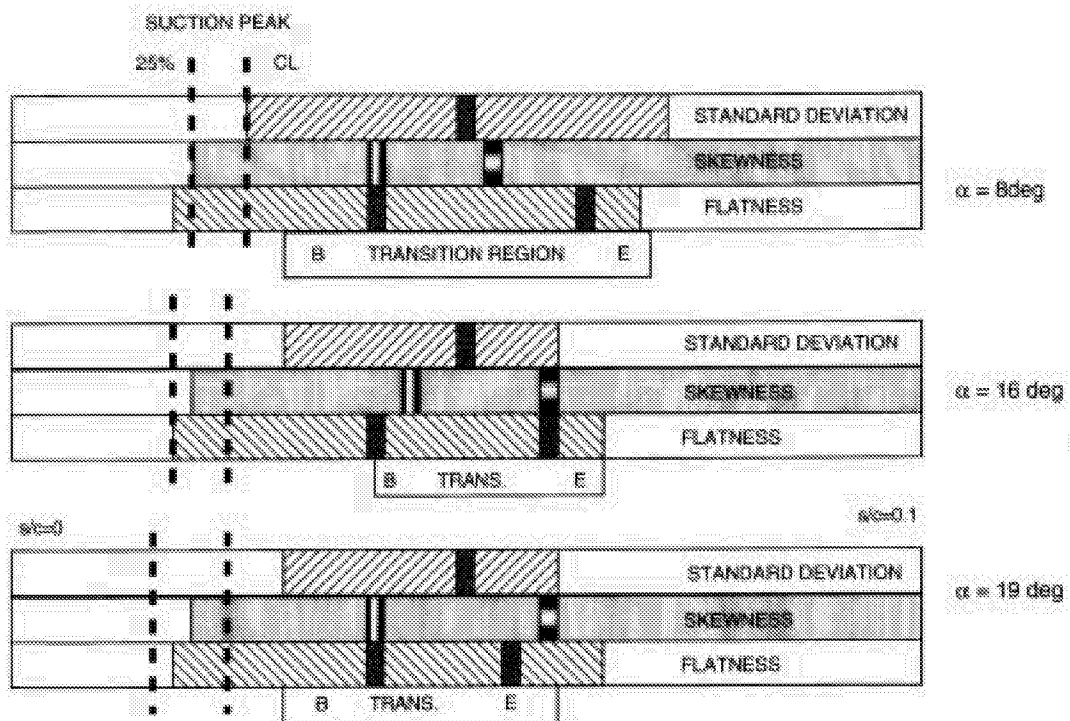


Figure 42 TRANSITION REGION CHARACTERISTICS
 30P/30N Mach=0.2 Re=9 mill FLAP - suction side

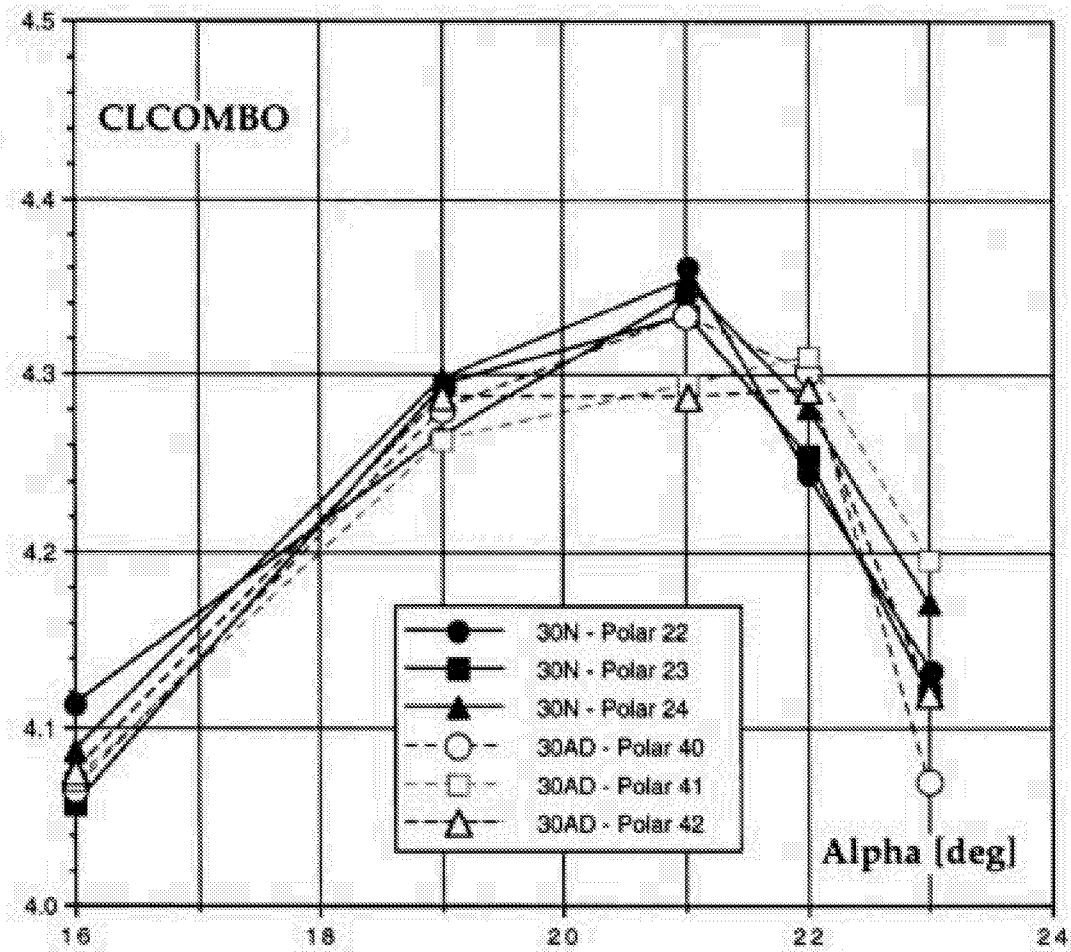


Figure 43 CLCOMBO for Mach=0.2, Re = 5 mill.
 Repeatability and comparison between 30N and 30AD.

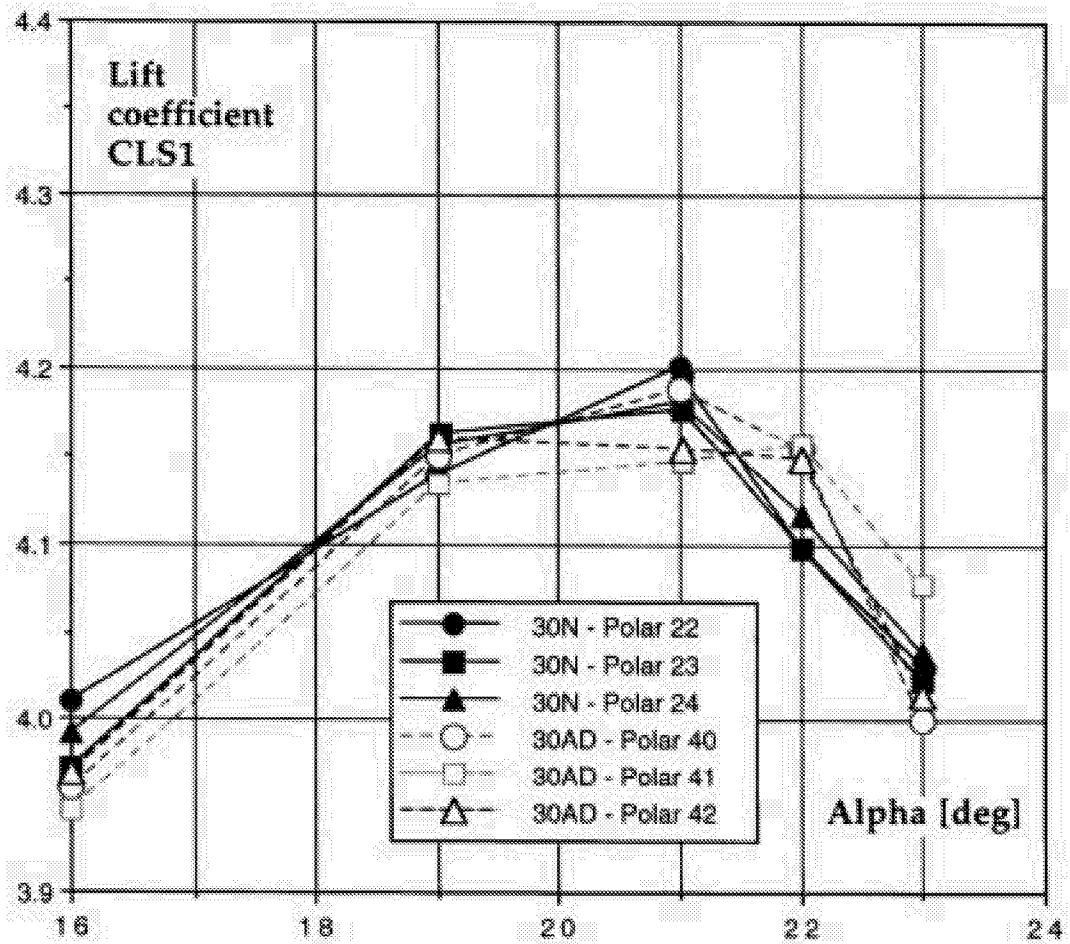


Figure 44 Lift coefficient from balance, CLS1, for Mach=0.2, Re = 5 mill. Comparison and repeatability for 30N and 30AD.

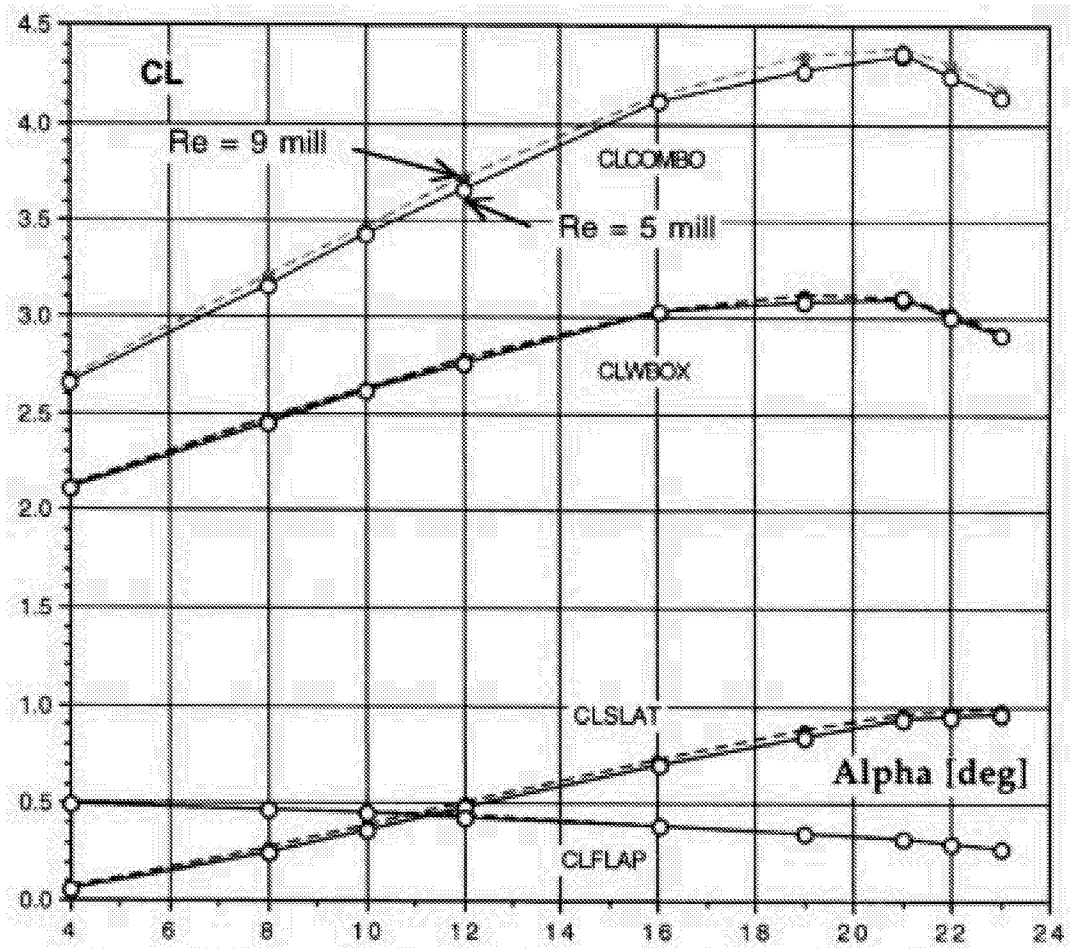


Figure 45a Reynolds number effects on loads for different elements. 30P/30N Mach=0.2 Re=5 and 9 mill.

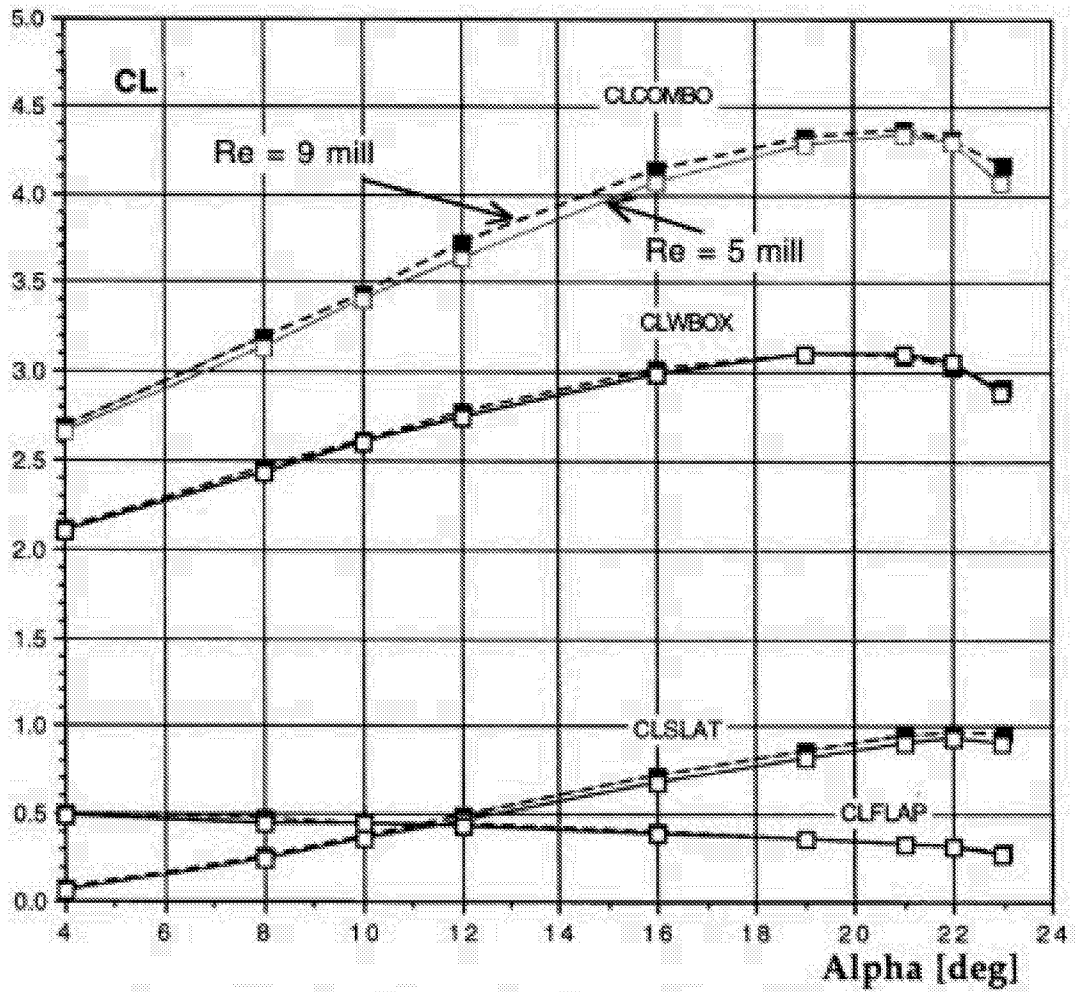


Figure 45b Reynolds number effect on lift coefficients for different elements. 30P/30AD Mach=0.2 Re=5 and 9 mill. Dashed lines denote Re=9 million.

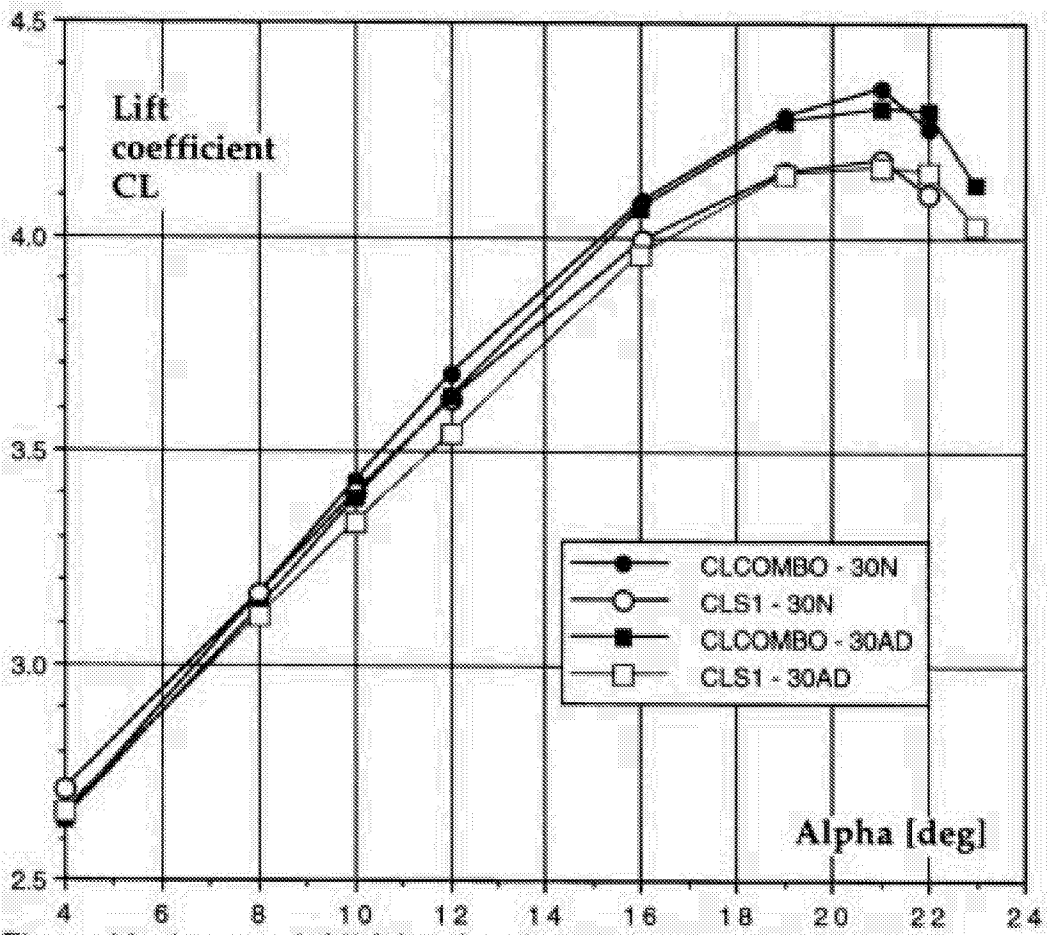
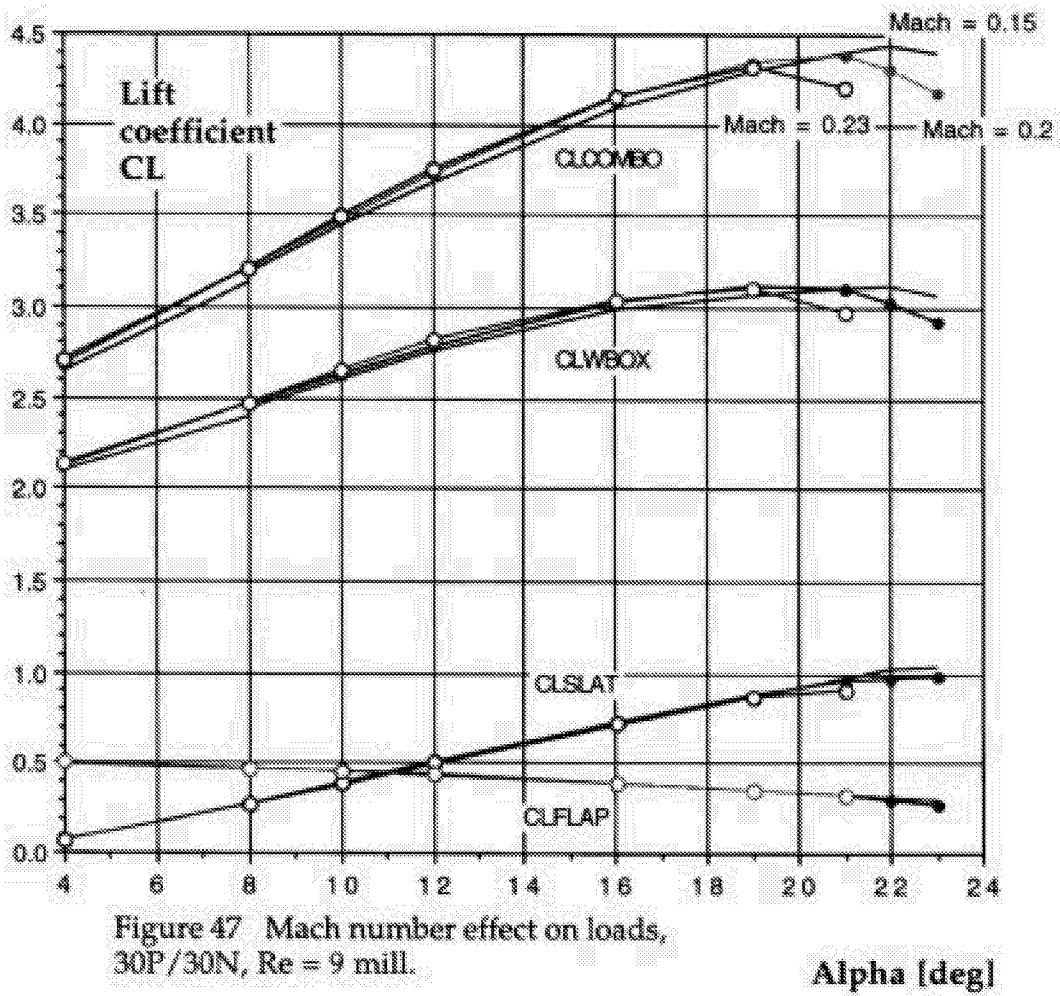


Figure 46 Average (of 3) lift polars for 30P/30N and 30P/30AD, Mach=0.2 and Re=5 mill. Comparison between pressure integration (CLCOMBO) - balance (CLS1) data.



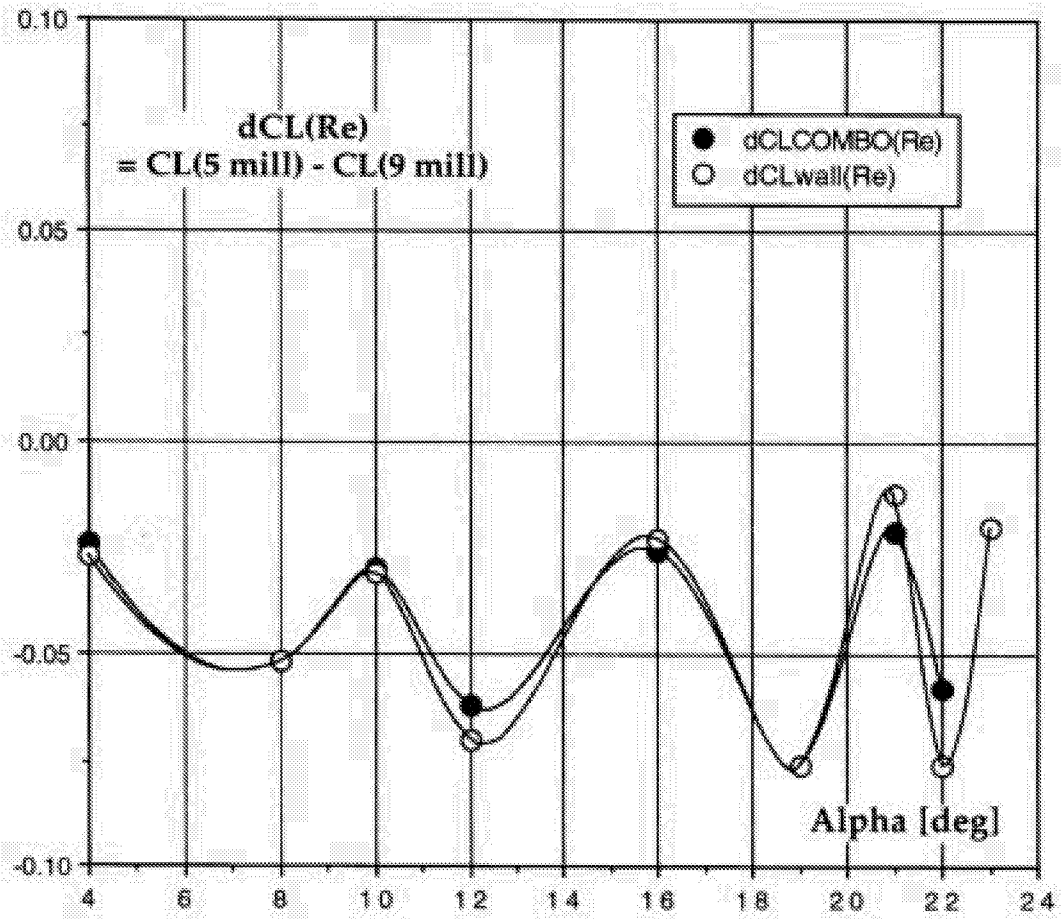


Figure 48 Reynolds number trends for 30P/30N Mach=0.2.

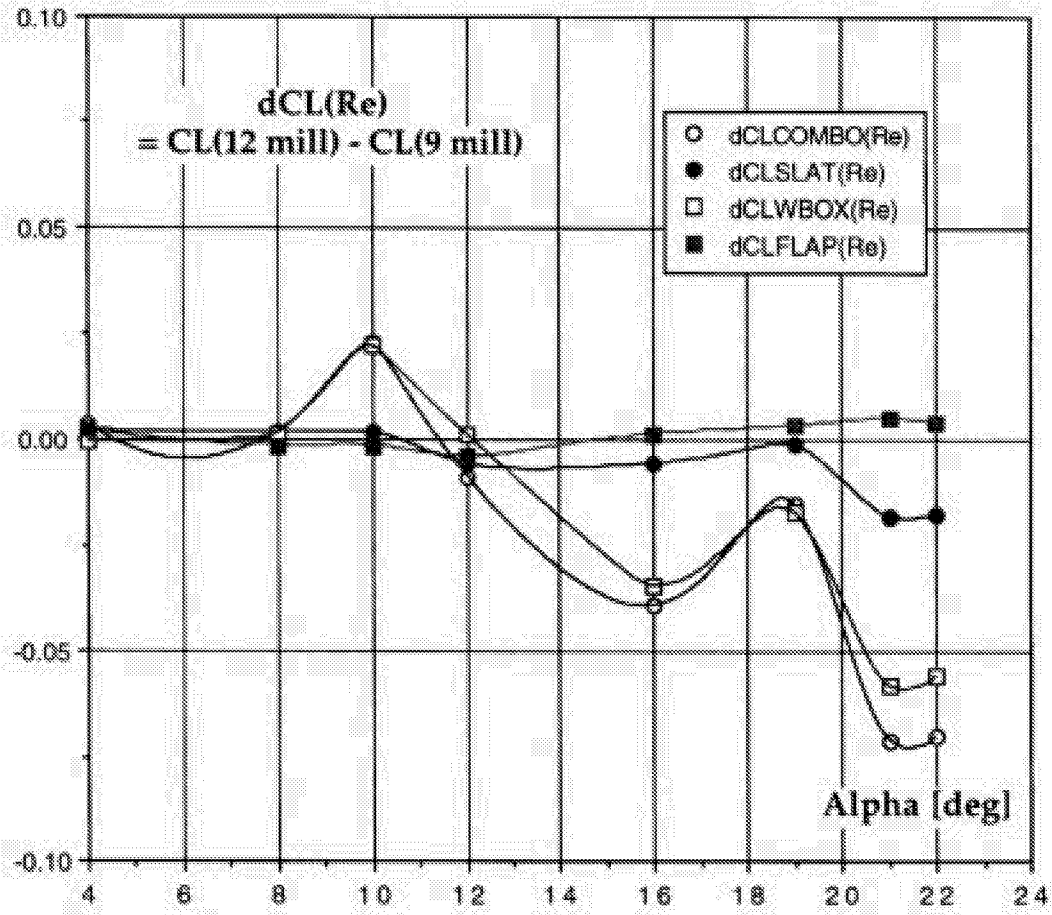


Figure 49 Lift coefficient difference dCL for different elements.
 30P/30N Mach=0.2
 dCL= CL(12 mill) -CL(9 mill)

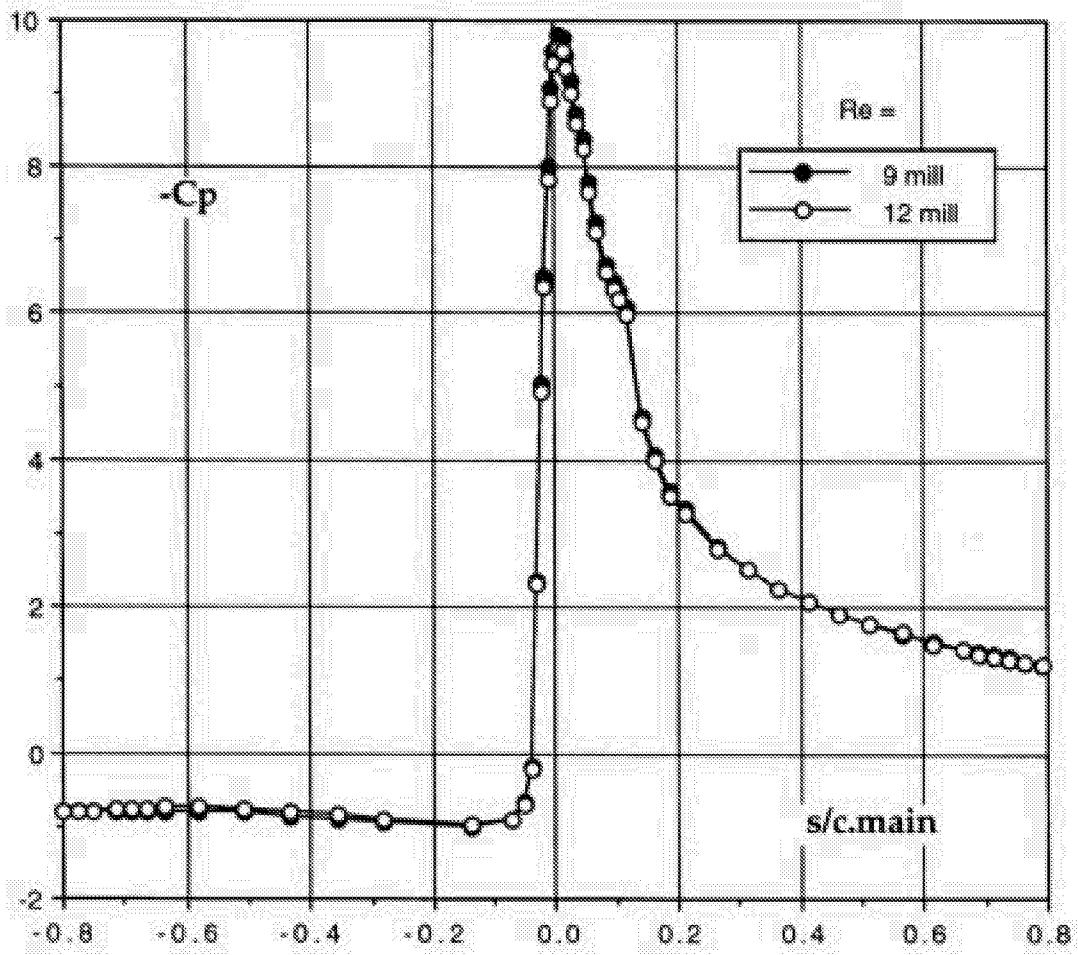


Figure 50a Pressure distribution differences between 9 and 12 million Reynolds number. 30P/30N. Mach = 0.2 Alpha=21 deg.

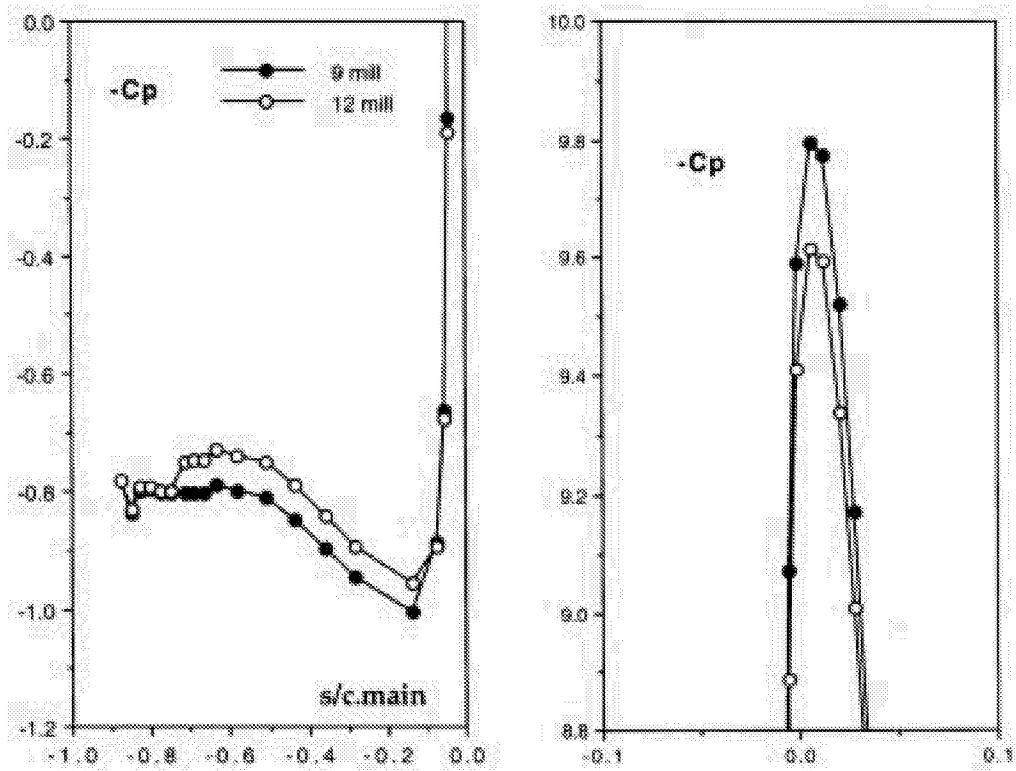


Figure 50b Pressure distribution differences between 9 and 12 million Reynolds number. 30P/30N Mach=0.2 Alpha=21 deg. Details from stagnation point and suction peak.

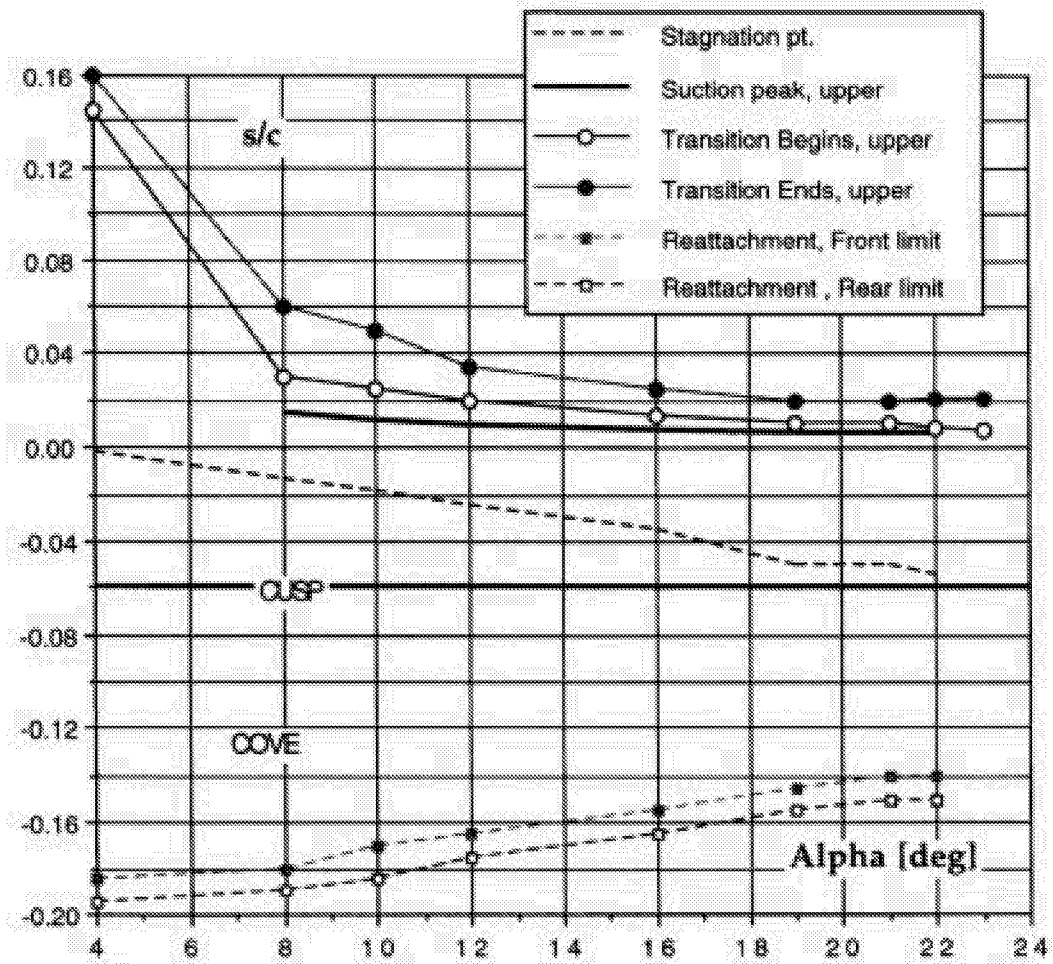


Figure 51a Transition 30P/30N M=0.2 Re=9 mill - SLAT

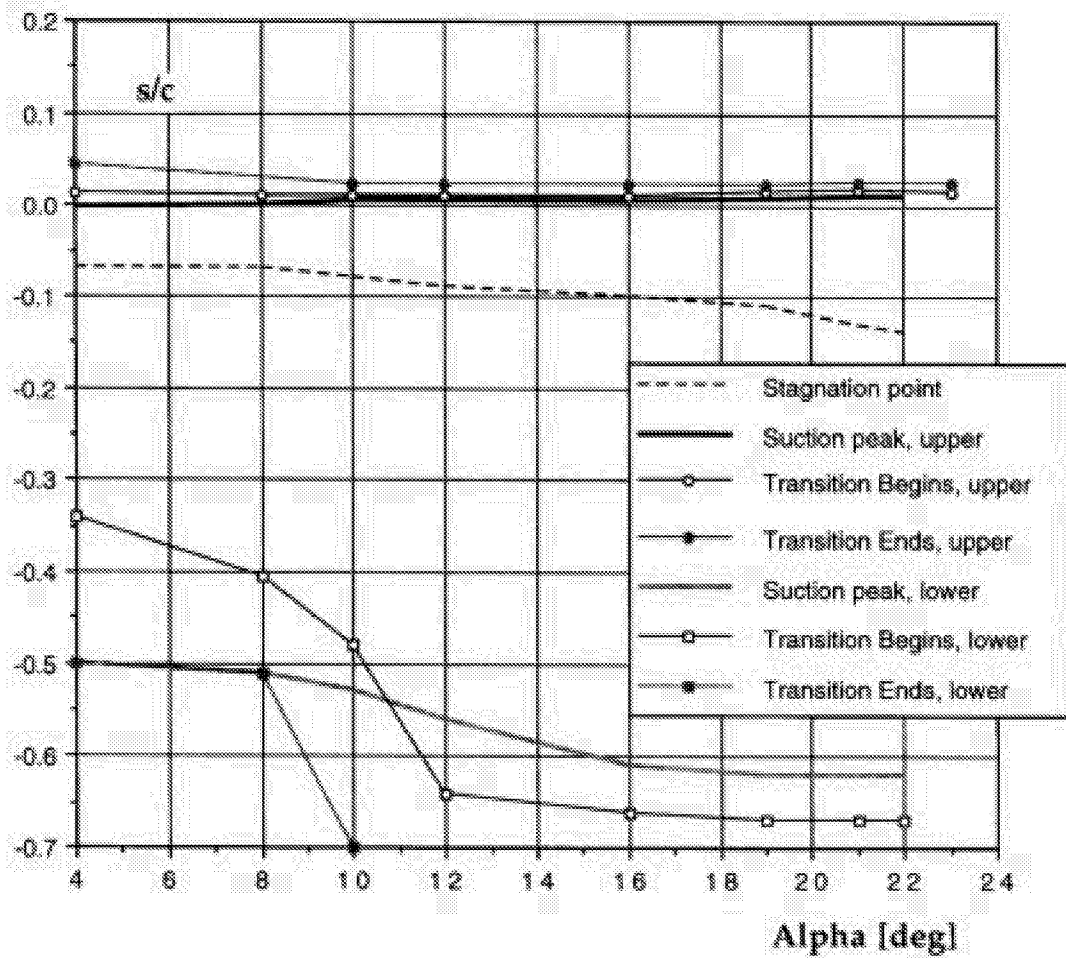


Figure 51b Transition 30P/30N M=0.2 Re=9 mill. - MAIN

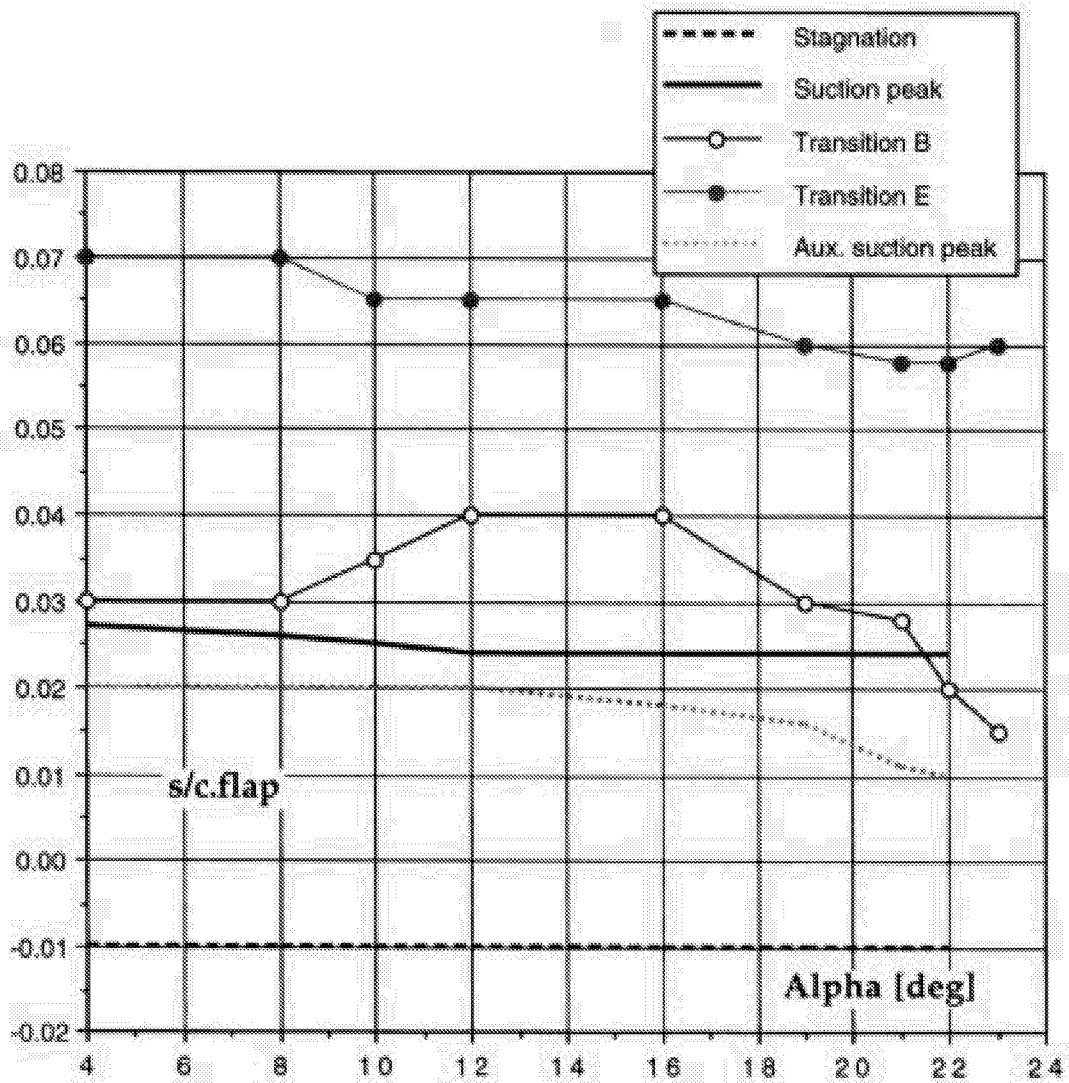


Figure 51c Transition 30P/30N M=0.2 Re=9 mill - FLAP

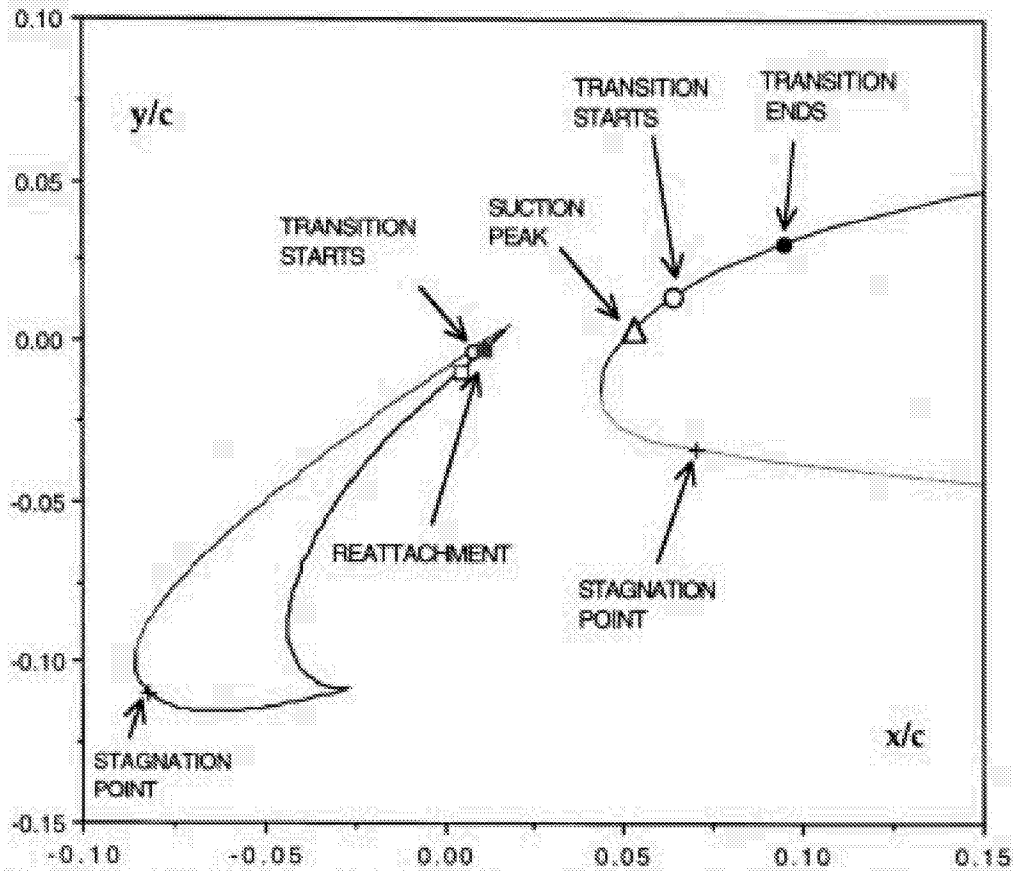


Figure 52 FLOW FEATURES 30P/30NMach=0.2 Re=9 mill Alpha = 4 deg
 Minimum pressure location on slat at trailing edge.

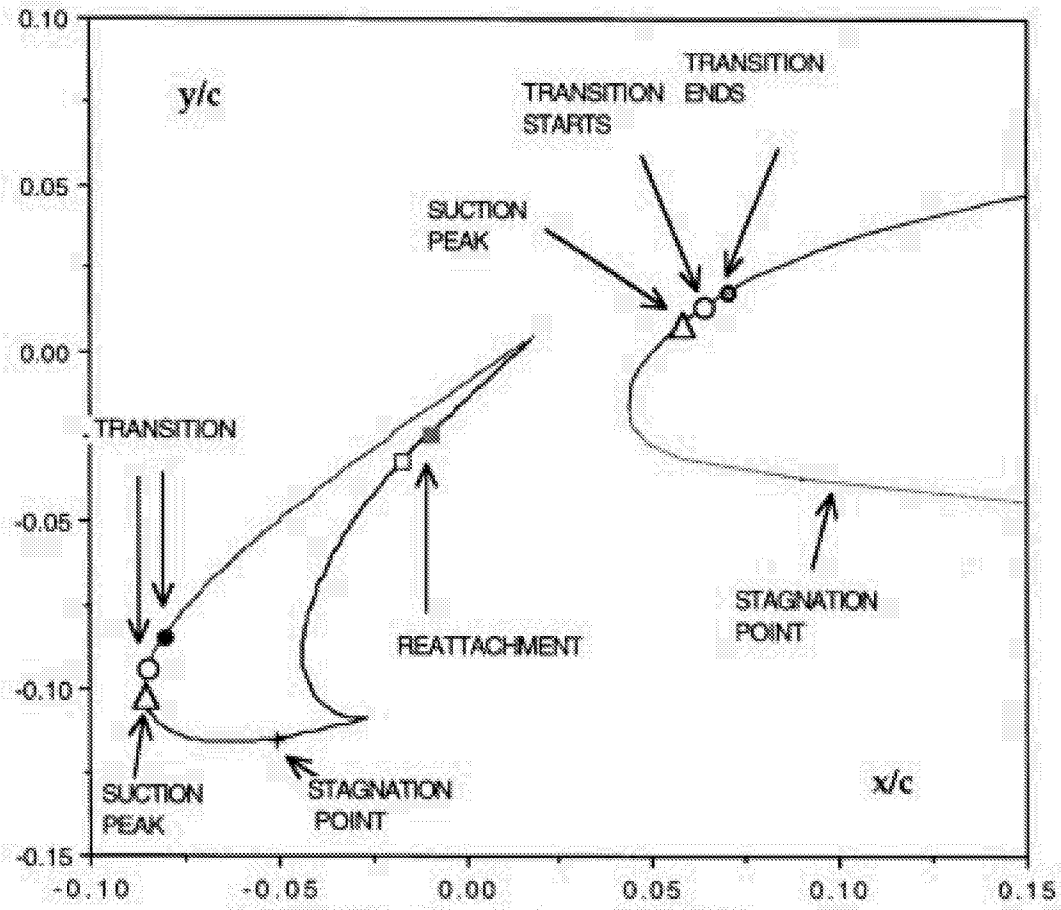


Figure 53 Flow features 30P/30N
Mach=0.2 Re=9 mill Alpha=16 deg

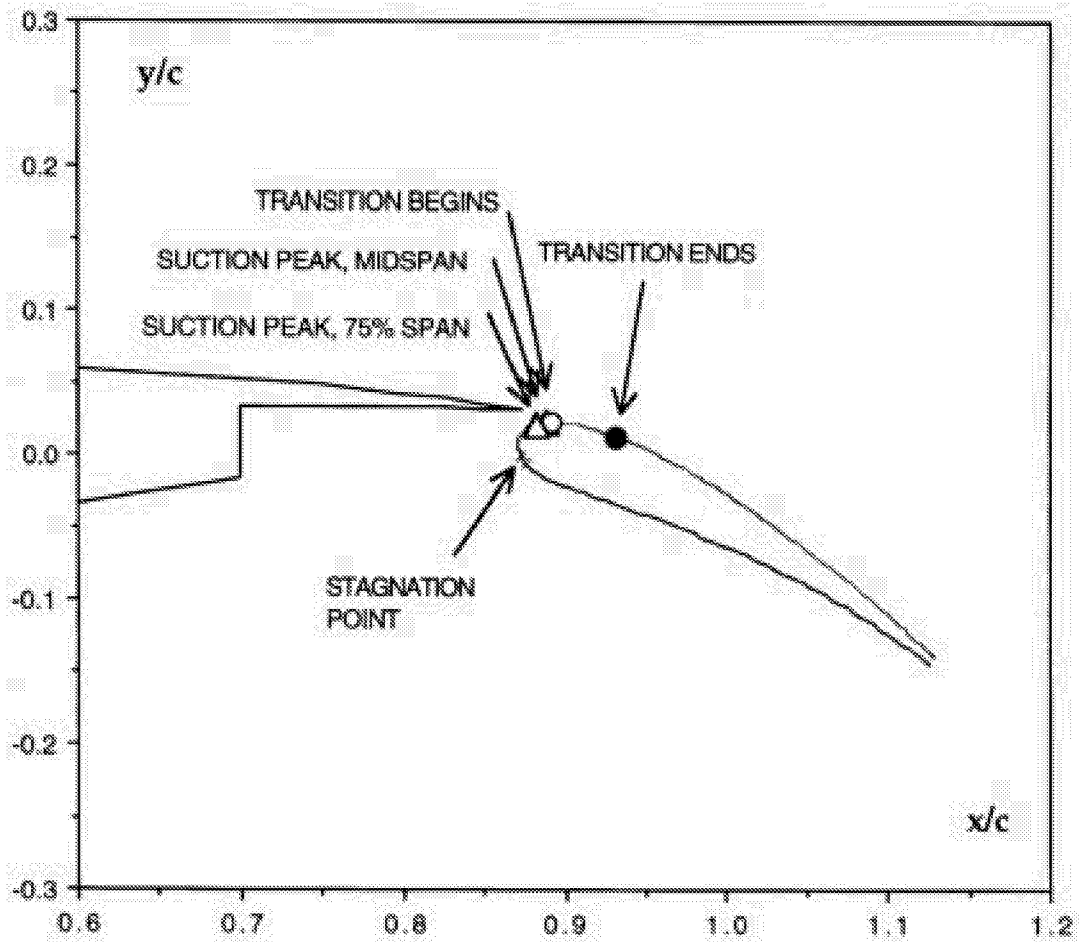


Figure 54 Flow features 30P/30N
 Mach=0.2 Re=9 million Alpha=4 deg

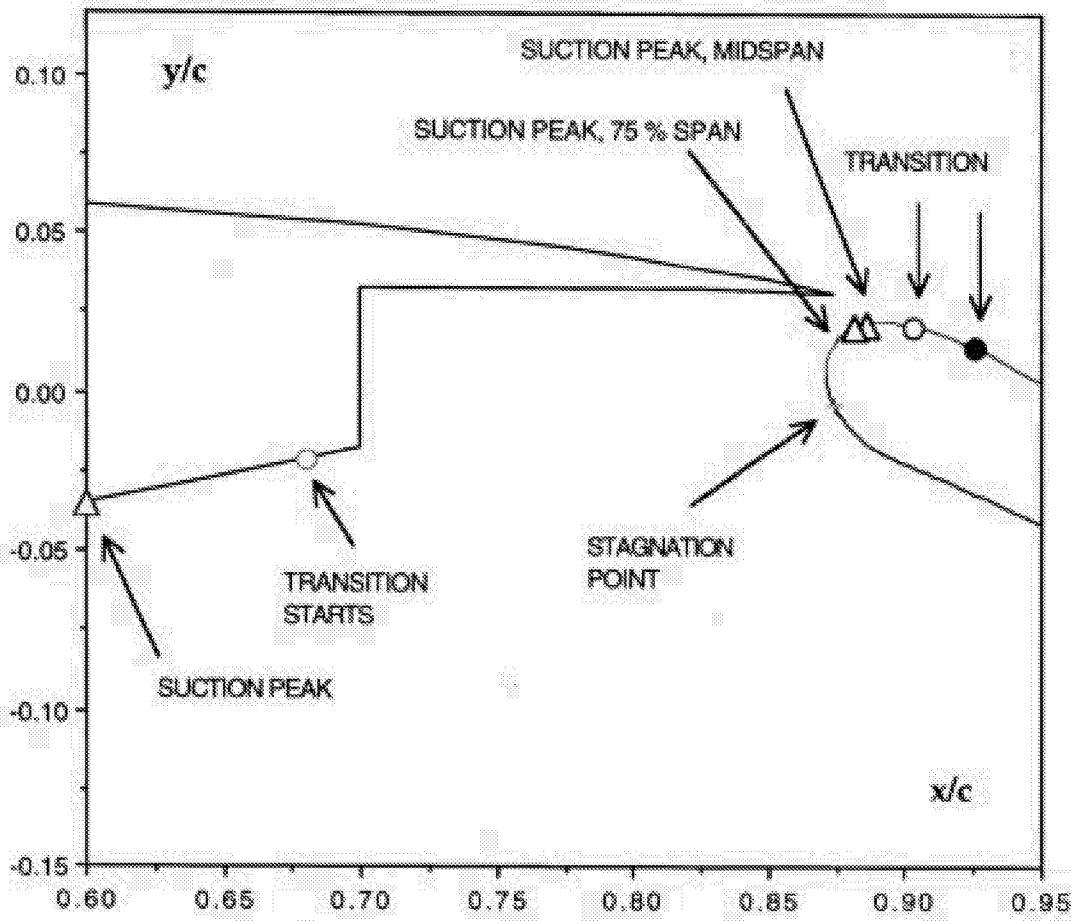


Figure 55 Flow features 30P/30N
Mach=0.2 Re=9 mill. Alpha=16 deg

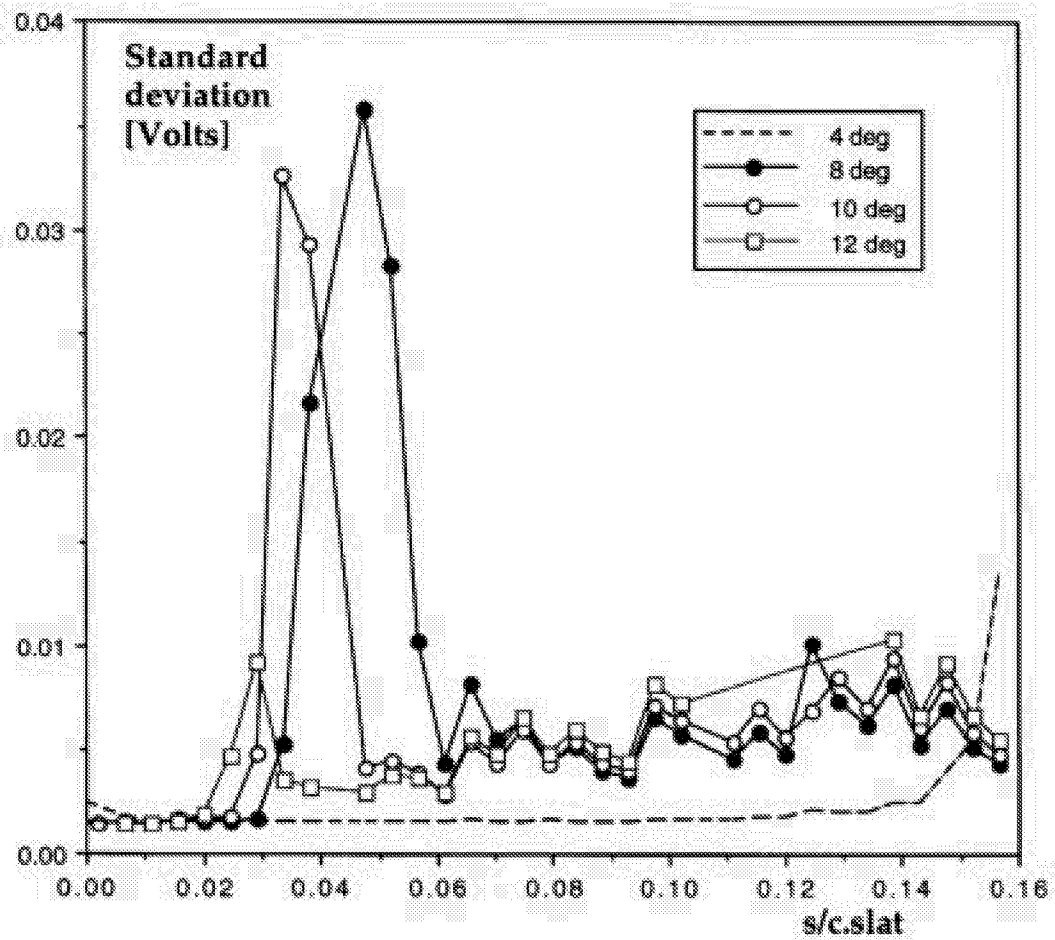


Figure 56a Standard deviation distribution on the slat for different angles of attack. 30P/30N Mach=0.2 Re= 9 mill

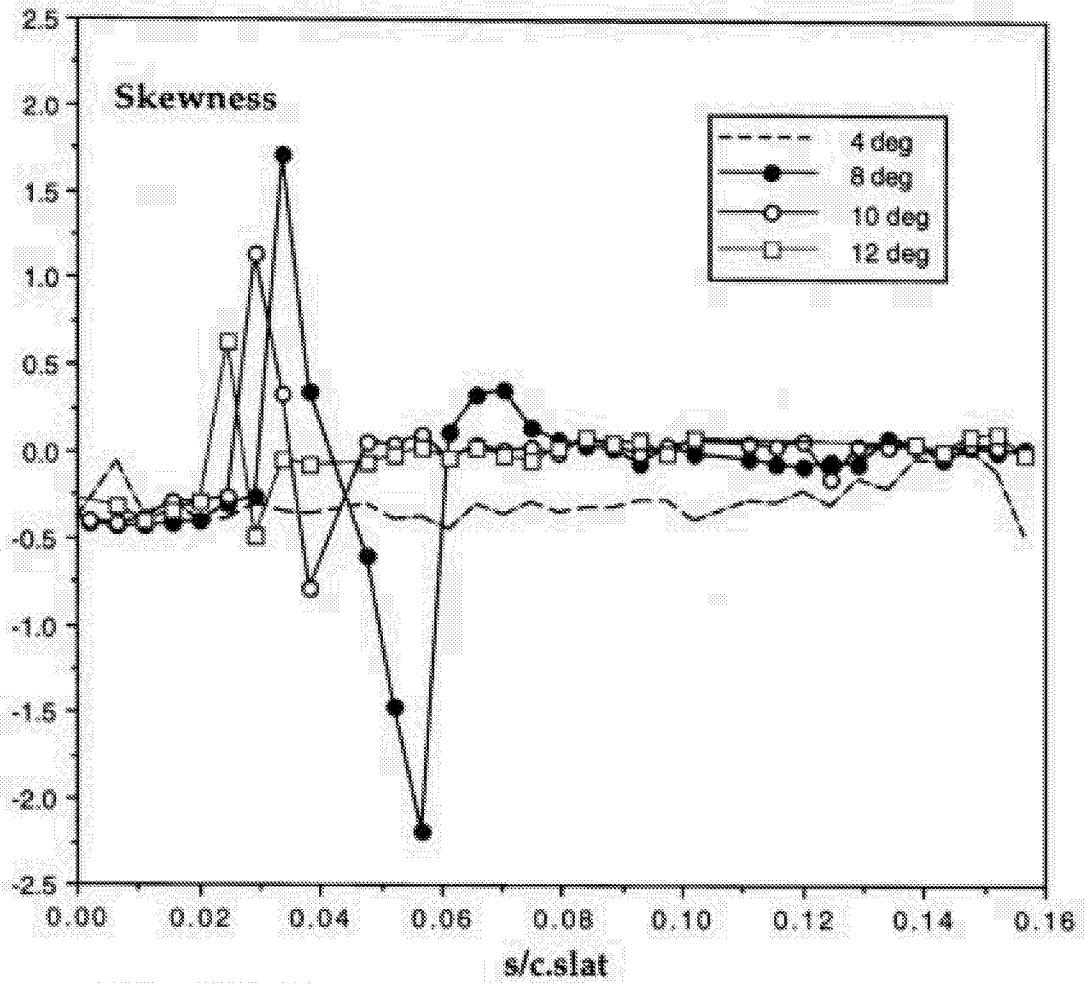


Figure 56b Skewness on the slat
for different angles of attack. 30P/30N Mach=0.2 Re= 9 mill

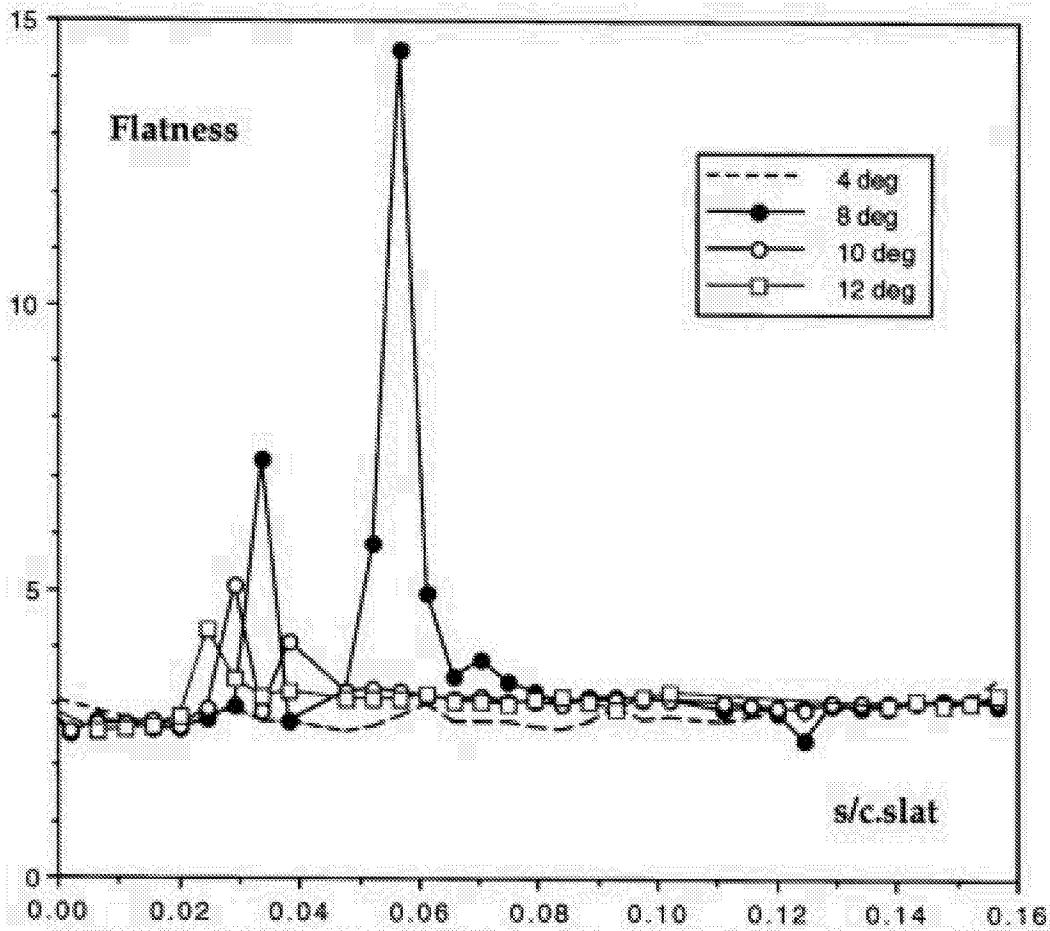


Figure 56c Flatness distribution on the slat for diferent angles of attack. 30P/30N Mach=0.2 Re=9 mill.

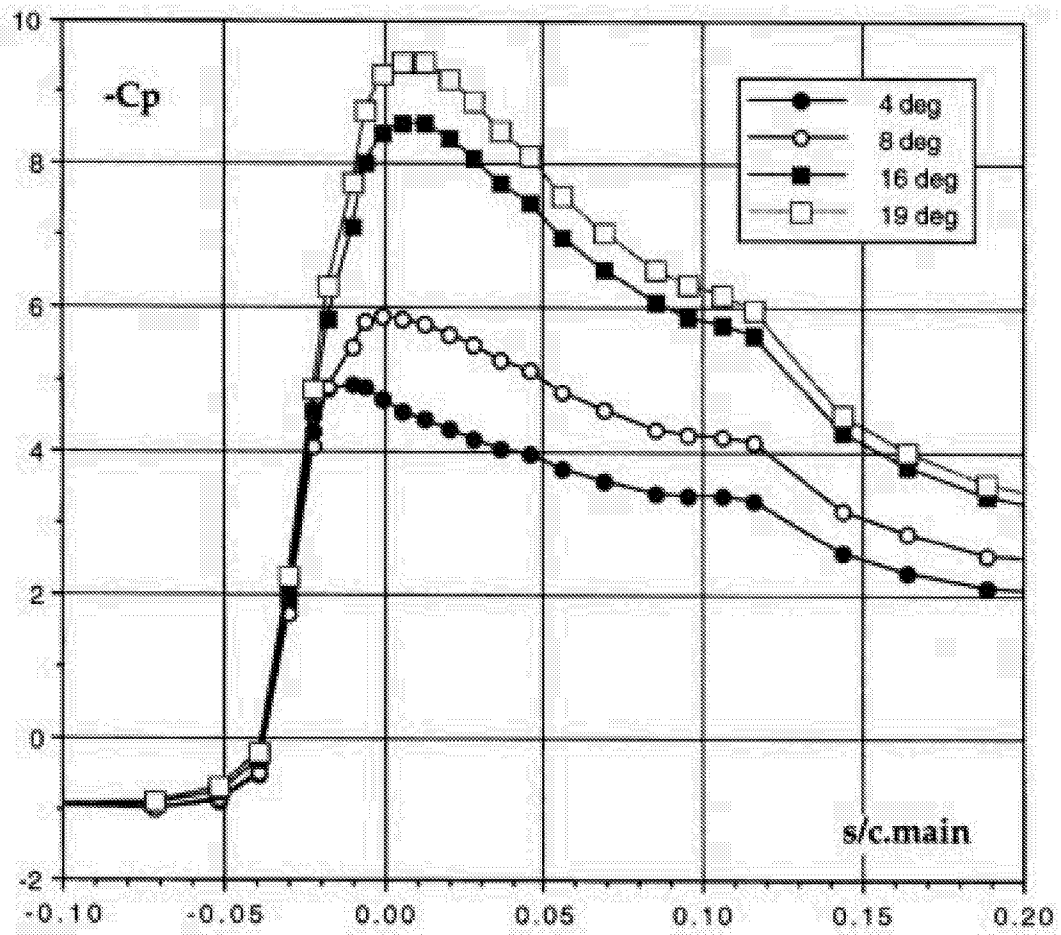


Figure 57 Pressure distribution on Main element.
 30P/30N Mach=0.2 Re=9 mill

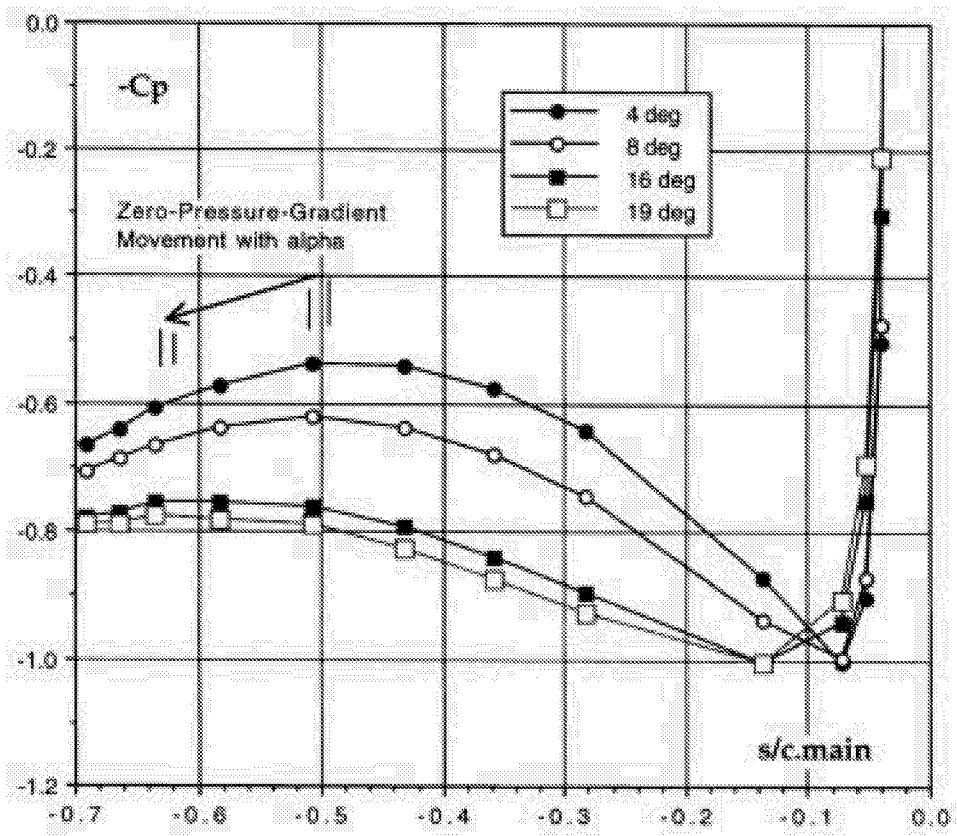


Figure 58 Pressure distribution on Main element, lower side, for different angles of attack. 30P/30N Mach=0.2 Re=9 mill

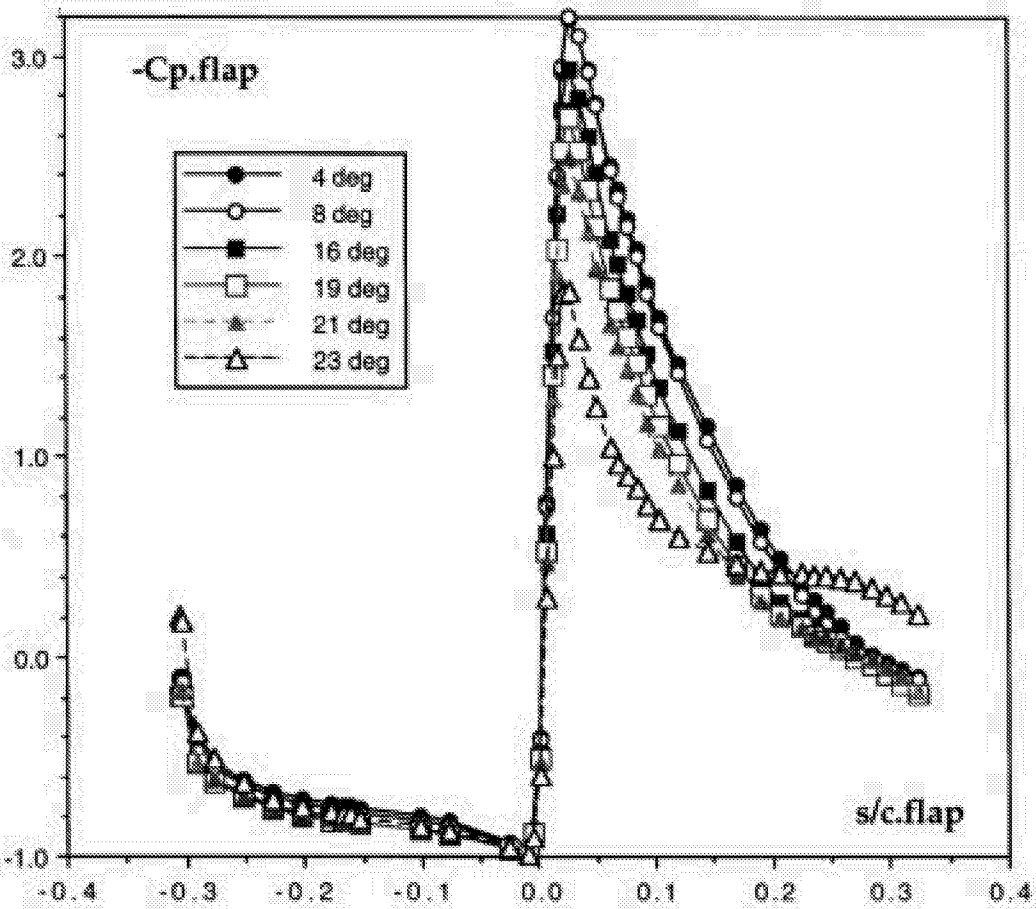


Figure 59 Flap centerline pressure distributions at different angles of attack. 30P/30N Mach=0.2 Re=9 mill.

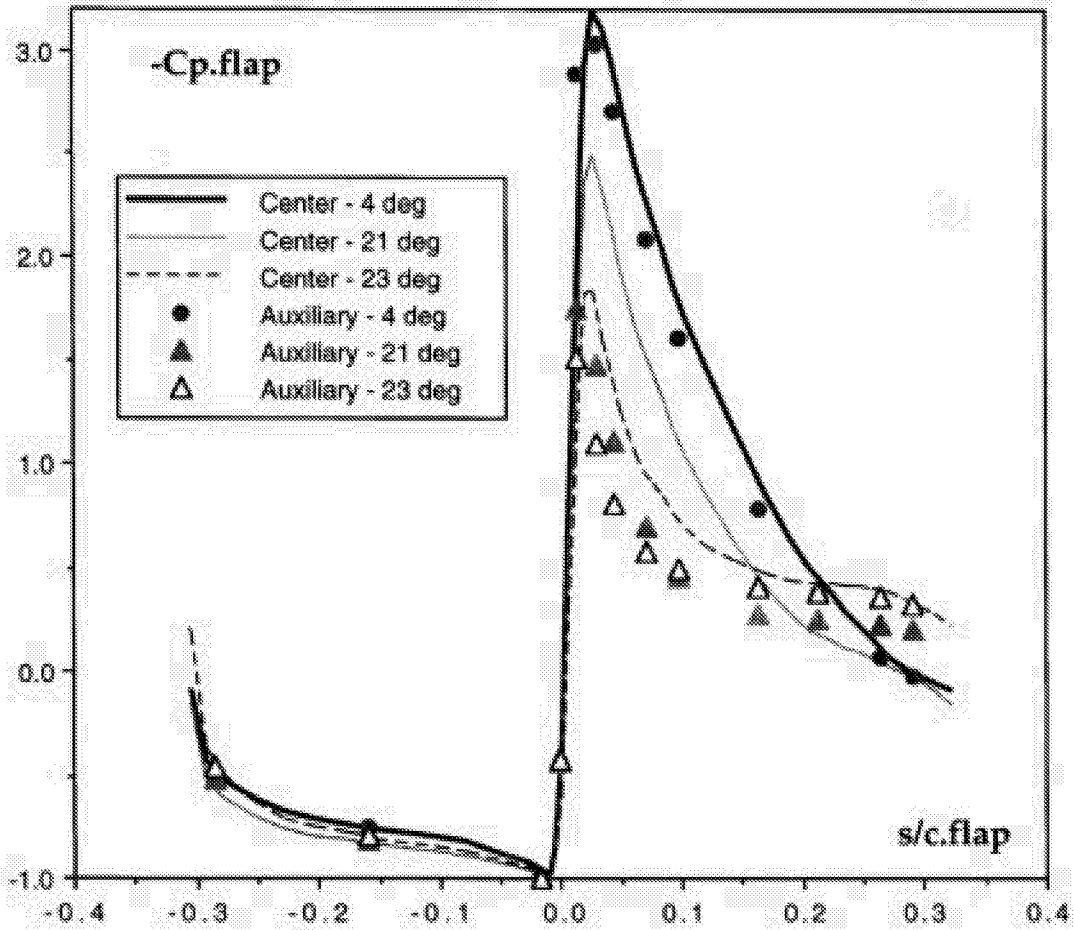


Figure 60 Flap center (50% span) and auxiliary (75% span) pressure distributions. 30P/30N Mach=0.2 Re=9 mill.

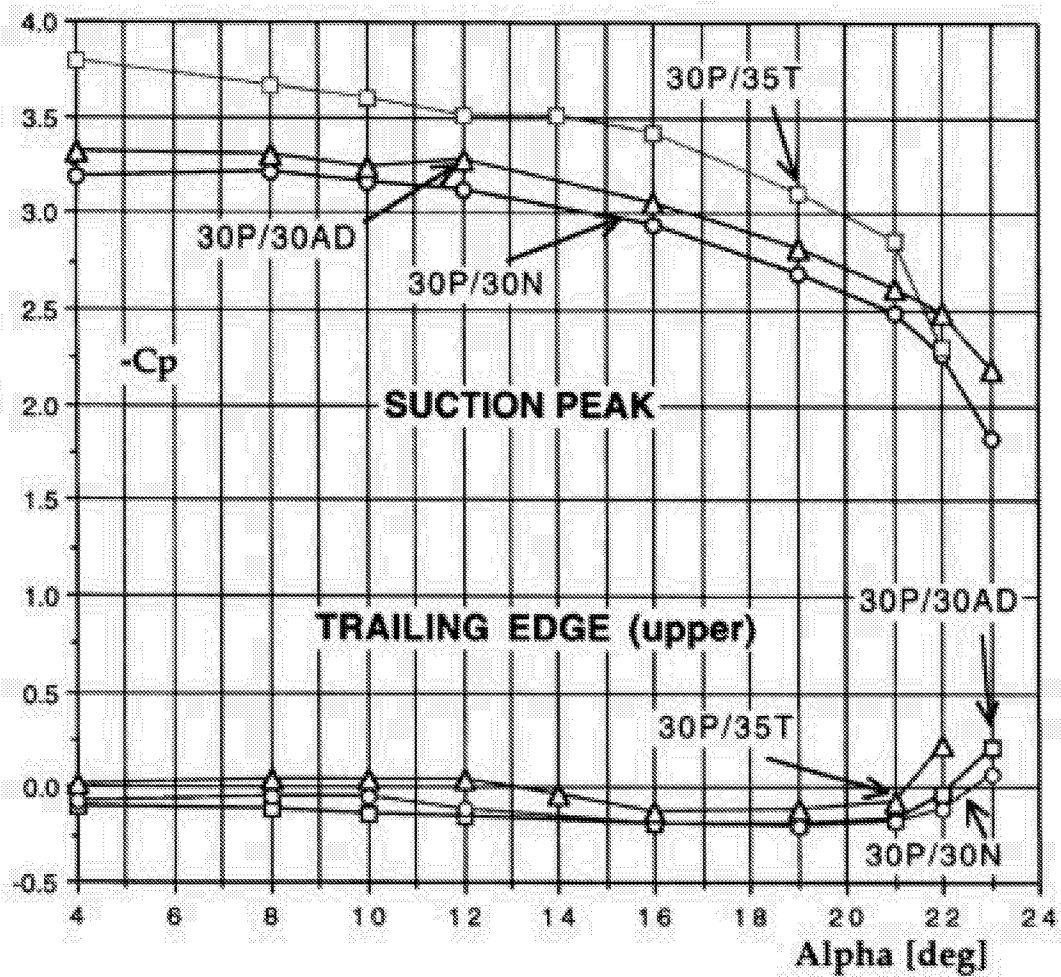


Figure 61 Flap peak and trailing edge pressure coefficients
Mach=0.2 Re=9 mill All three configurations.

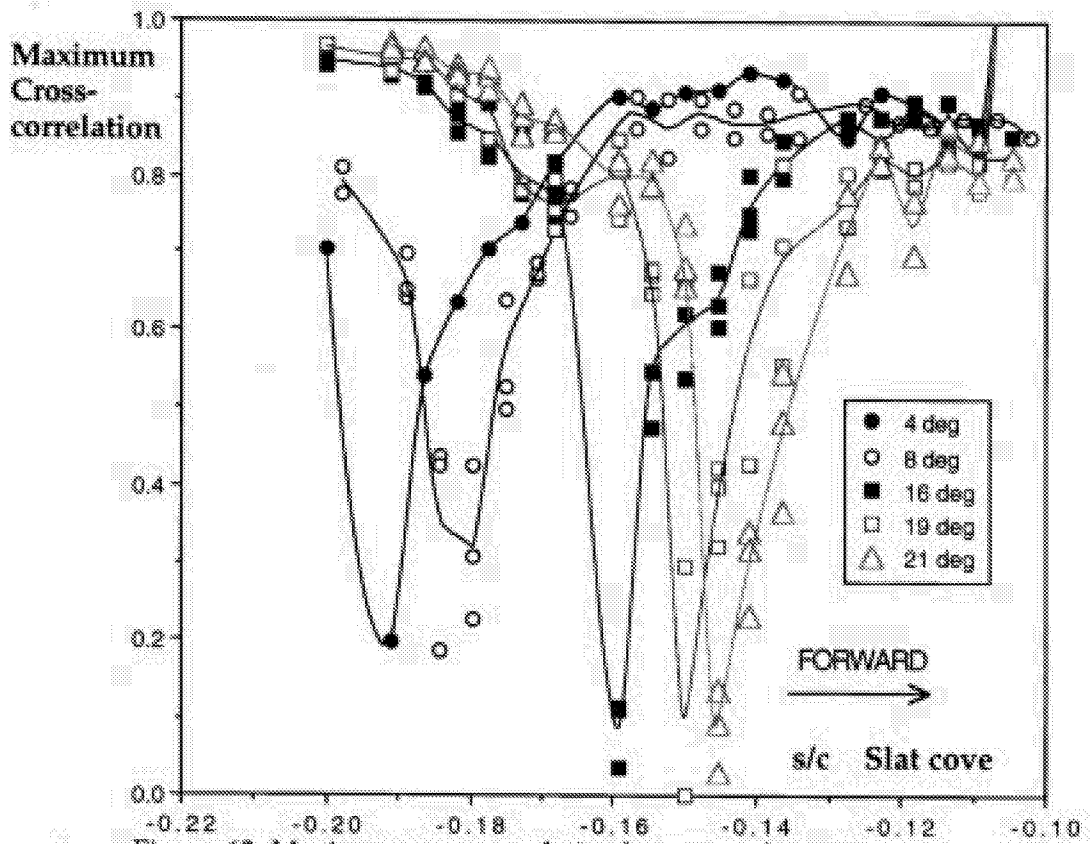


Figure 62 Maximum crosscorrelation between adjacent sensors in slat cove 30P/30N Mach=0.2 Re=9 million. Faired lines illustrate the loss of correlation where reattachment occurs.

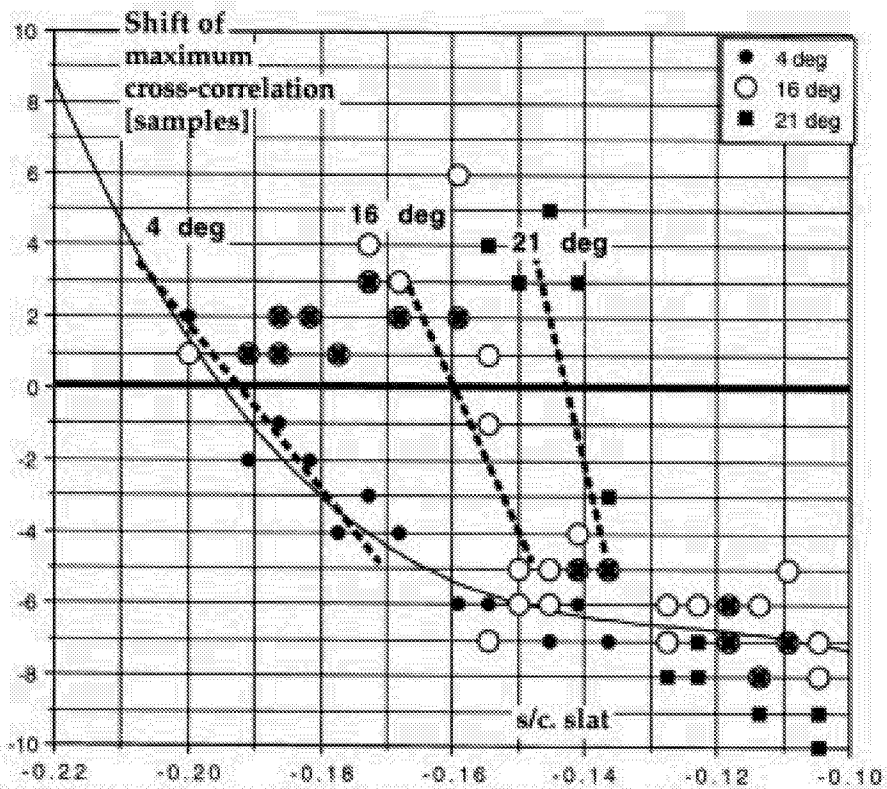


Figure 63 Time shift between the maximum correlation of adjacent sensors in the slat cove for three angles of attack. 30P/30N Mach=0.2 Re=9 million. Dashed lines crossing zero time delay-correlation corresponds to reattachment location.

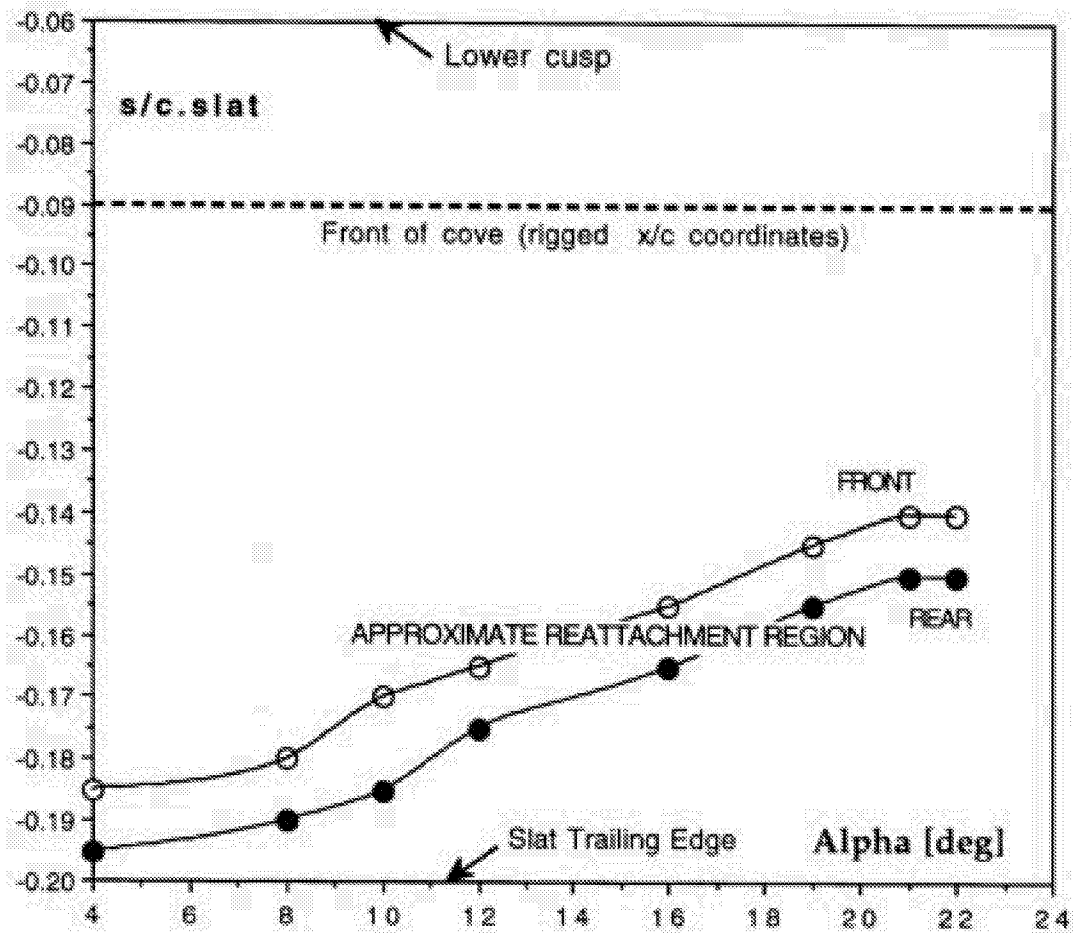


Figure 64 Cove region with approximate reattachment region as function of angle-of-attack. 30P/30N Mach=0.2 Re=9 million.

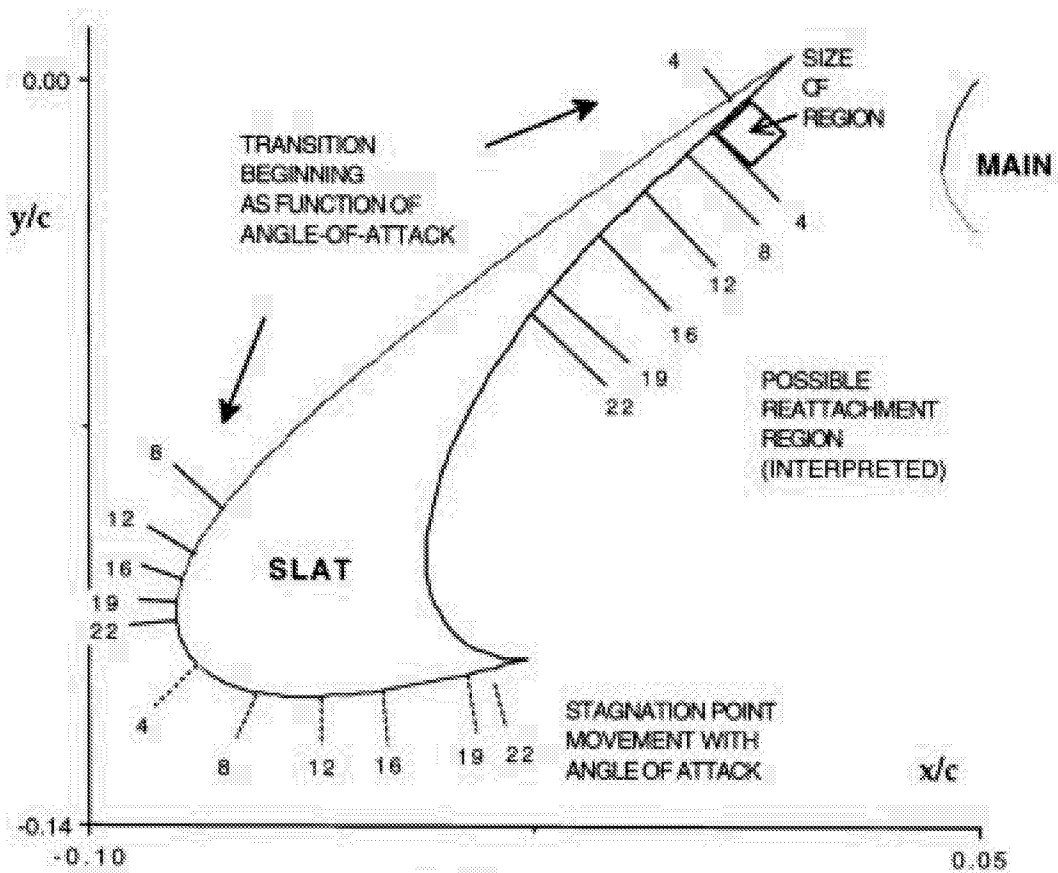


Figure 65 Slat flow features
30P/30N Mach=0.2 Re=9 million.

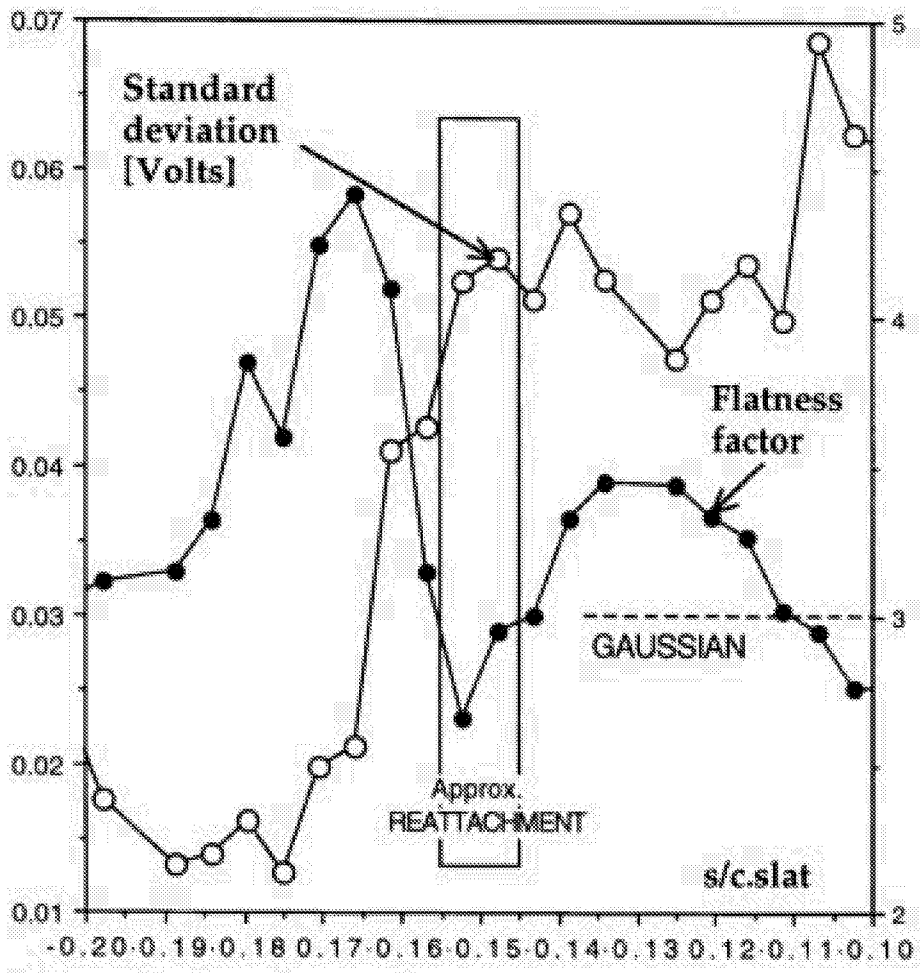


Figure 66 Distribution of statistical properties in the cove region. 30P/30N Mach=0.2 Re=9 million Alpha=19 deg.

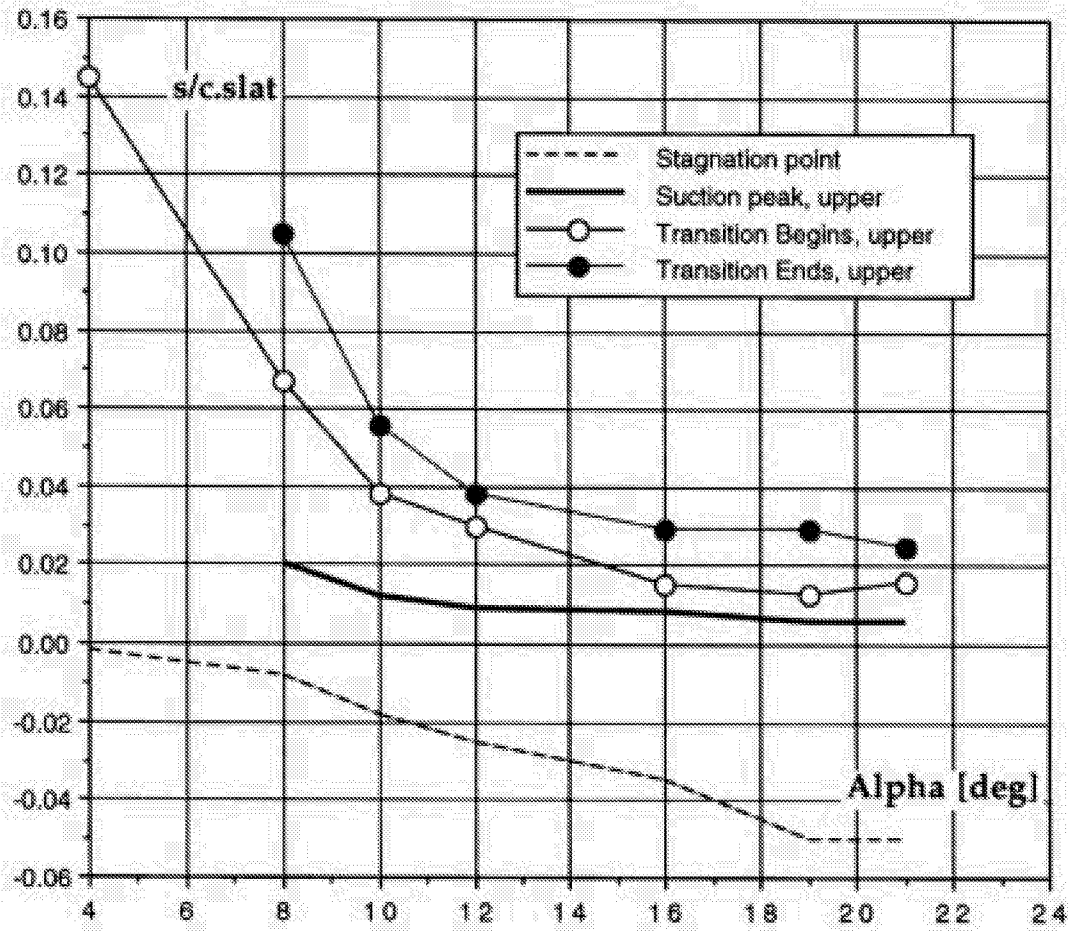


Figure 67a Transition 30P/30N M=0.2 Re=5 million - SLAT

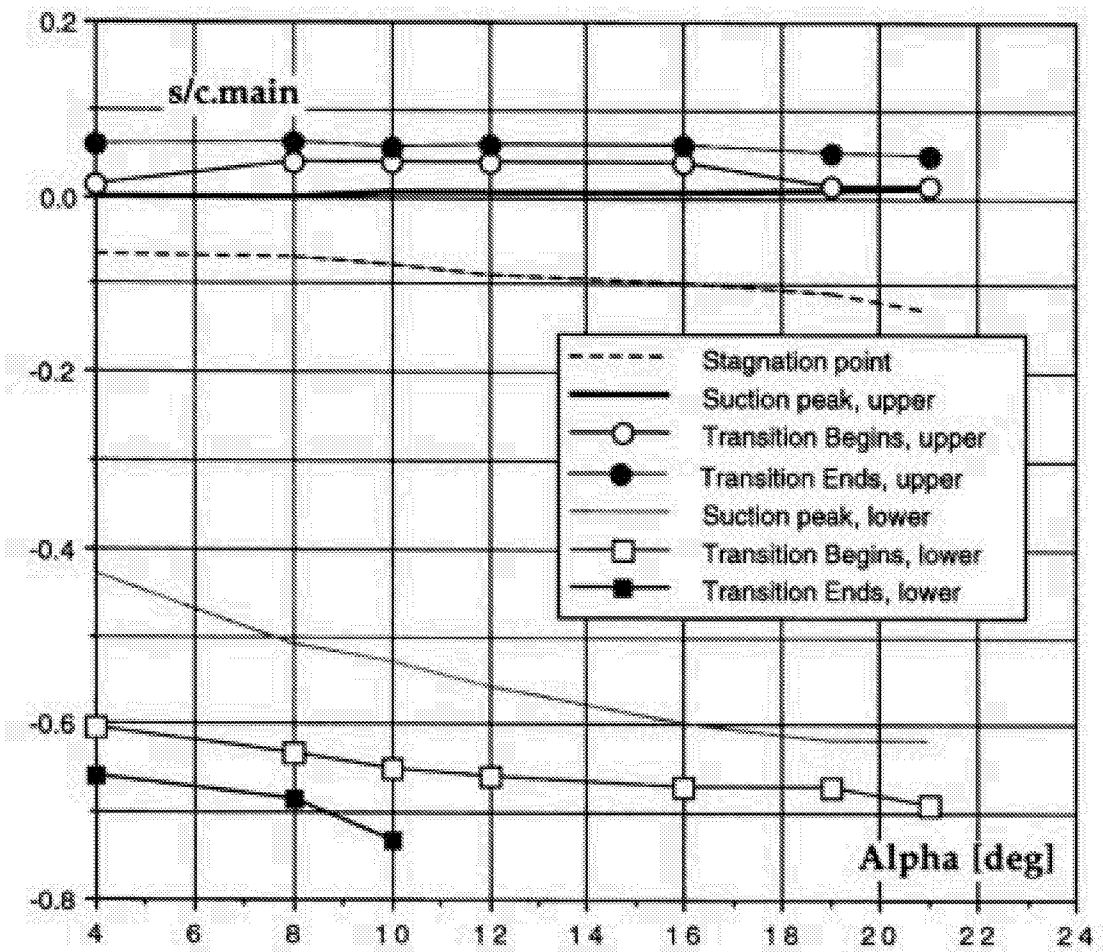


Figure 67b Transition 30P/30N M=0.2 Re=5 million - MAIN

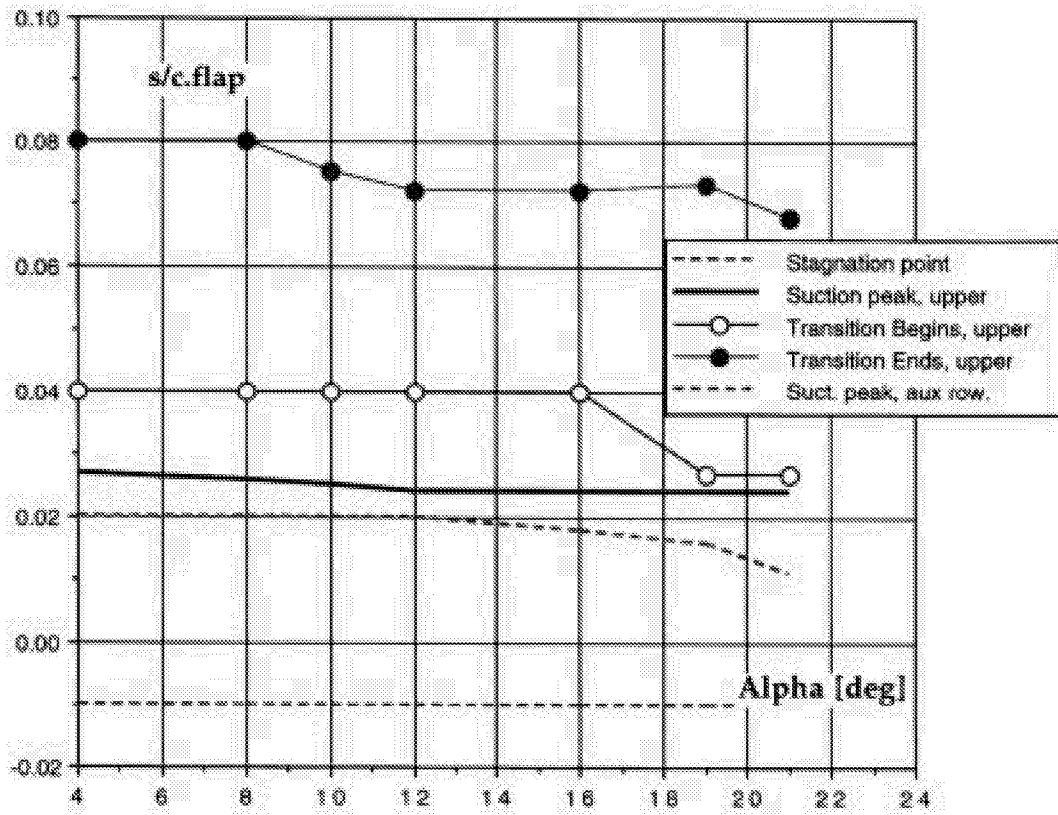


Figure 67c Transition 30P/30N M=0.2 Re=5 million - FLAP

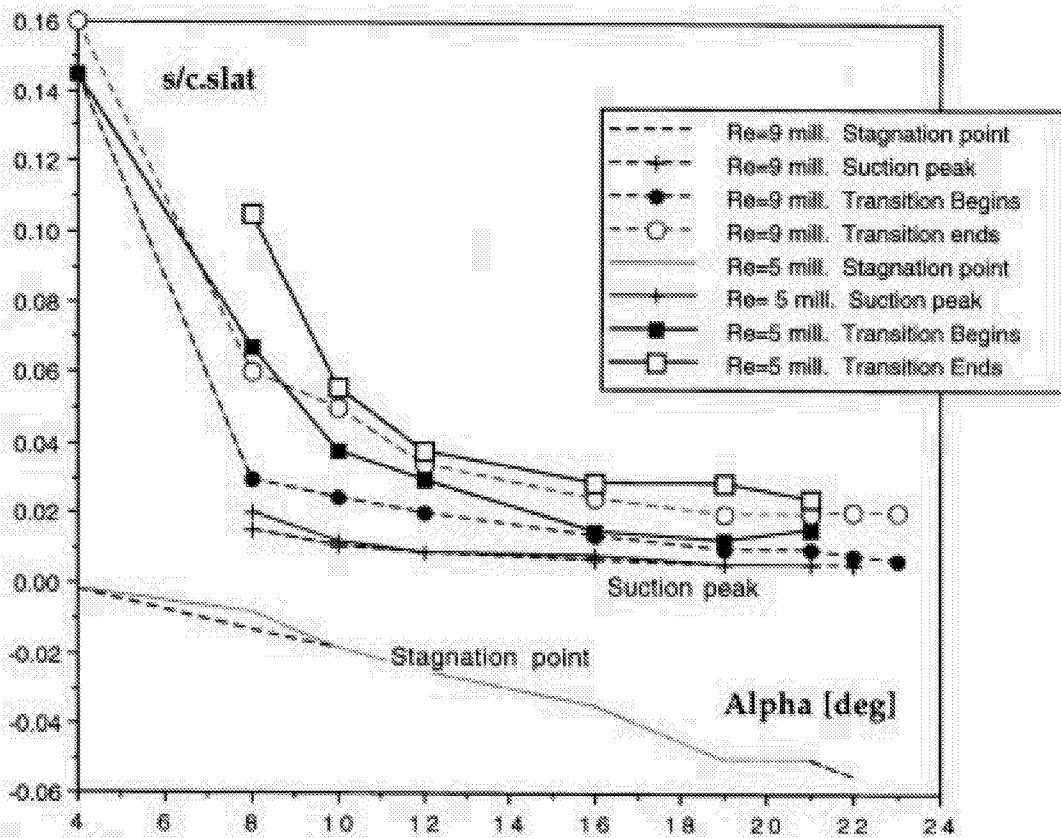


Figure 68 Reynolds number effect - SLAT
 30P/30N Mach=0.2 Re=9 million (dashed lines) Re= 5 million (full lines)

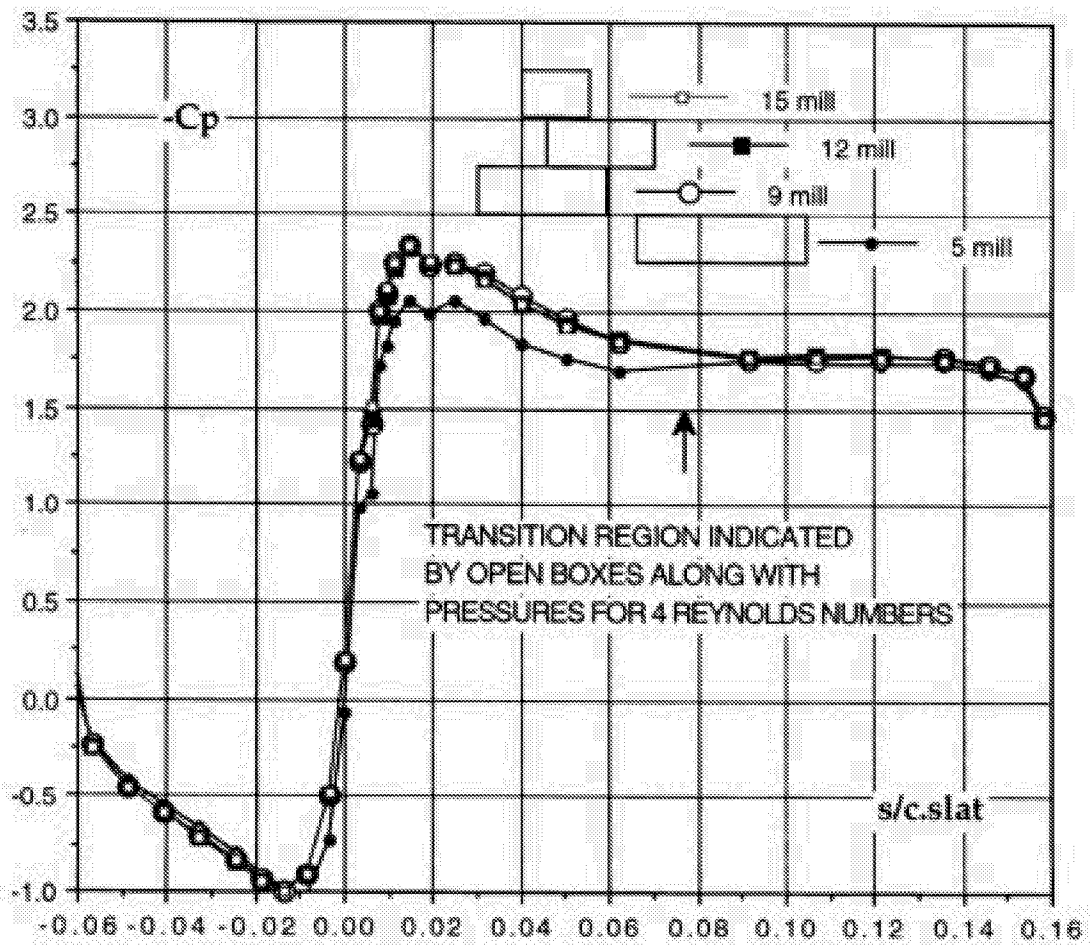


Figure 69 Reynolds number effect on pressure distribution. Slat. 30P/30N Mach=0.2 Alpha=8 deg. Data from Pts 179,51,209,234.

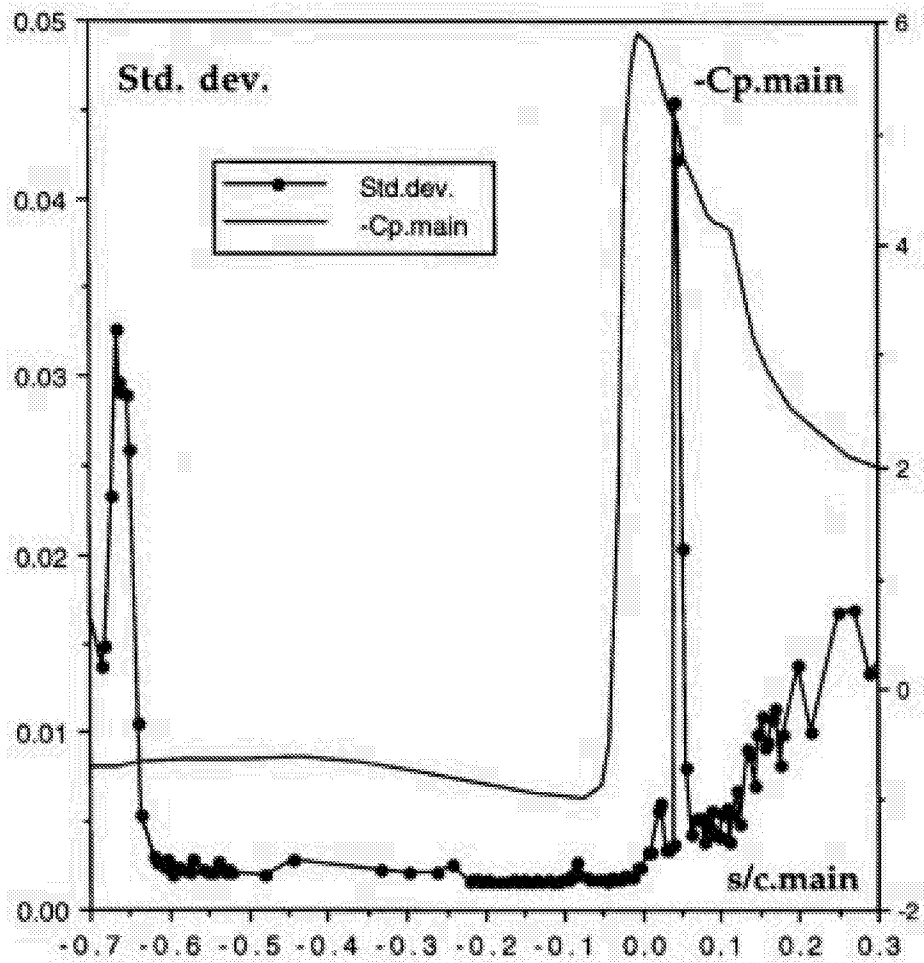


Figure 70a Pressure distribution and Standard deviation
 Main - Mach=0.2 Alpha=8 deg Re=5 million

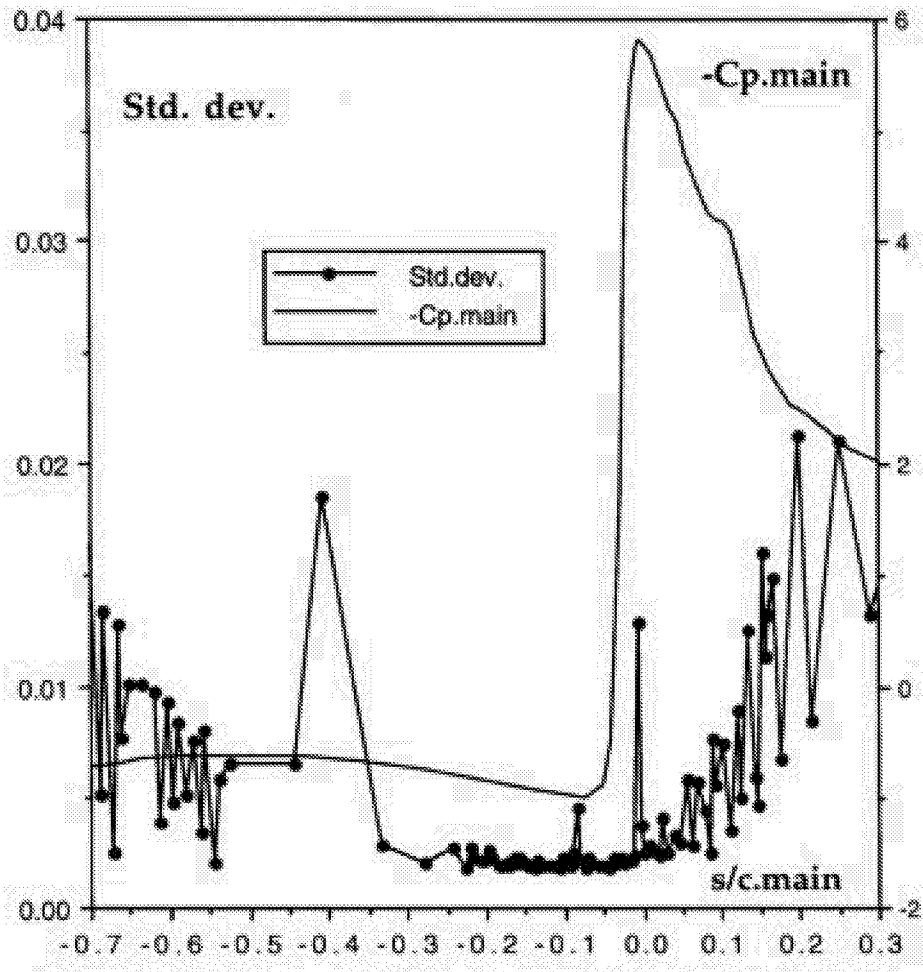


Figure 70b Pressure distribution and Standard deviation
 Main - Mach=0.2 Alpha=8 deg Re=15 mill

970604.05

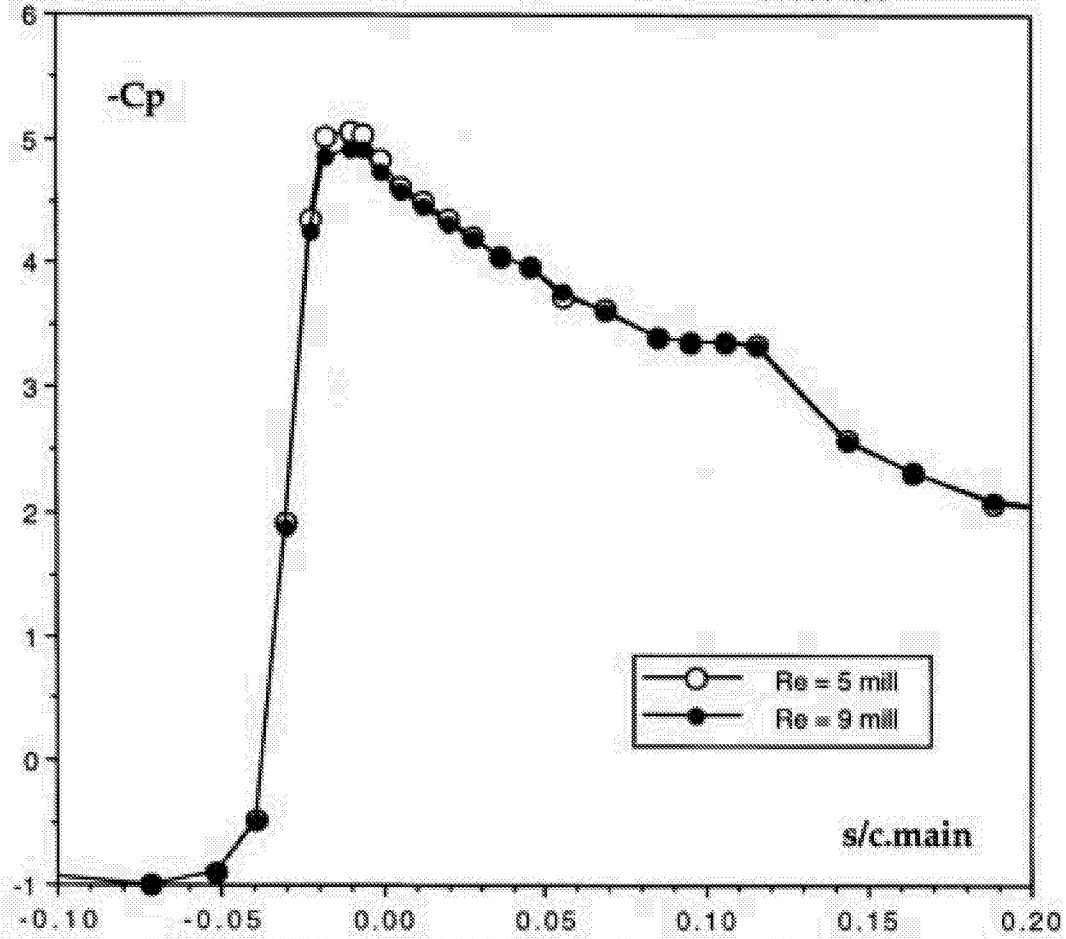


Figure 71 Pressure distribution in nose region of main.
30P/30N Mach=0.2 Alpha=4 deg Re=5 and 9 million

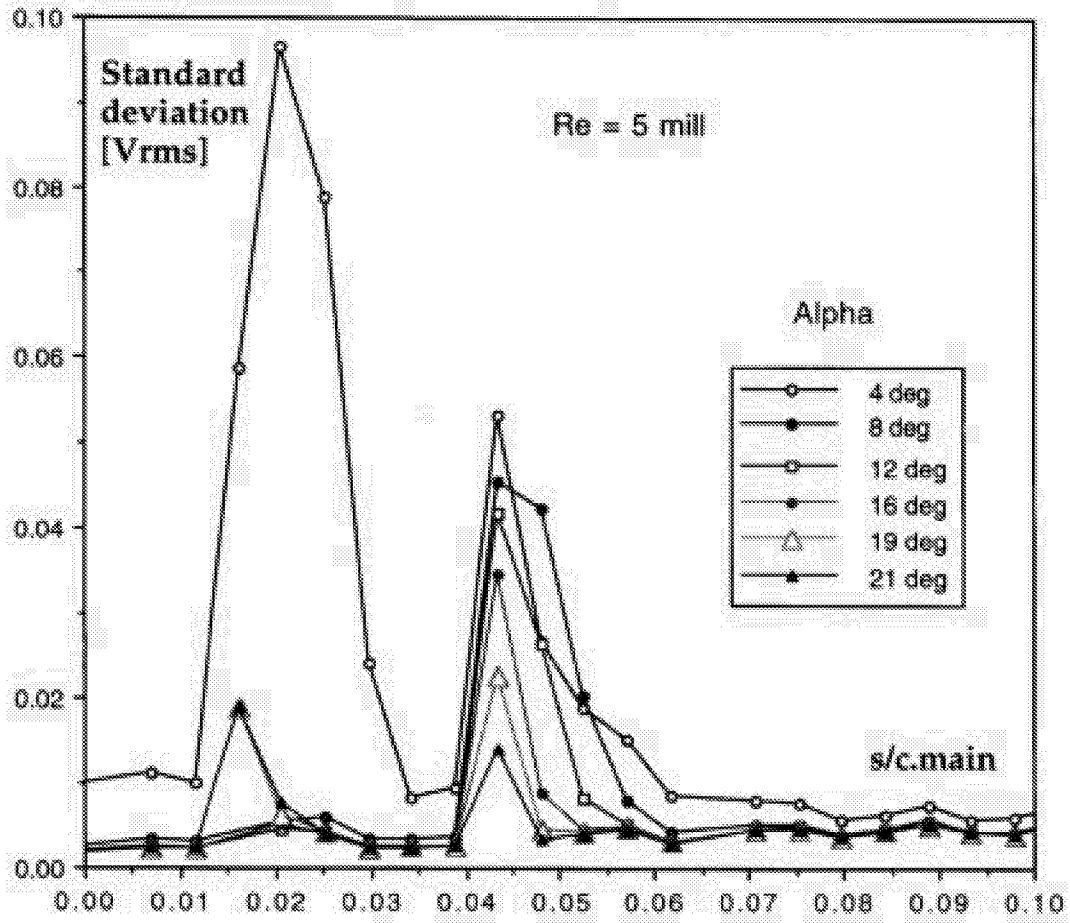


Figure 72a Distribution of standard deviation on main element for several angles of attack. 30P/30N Mach=0.2

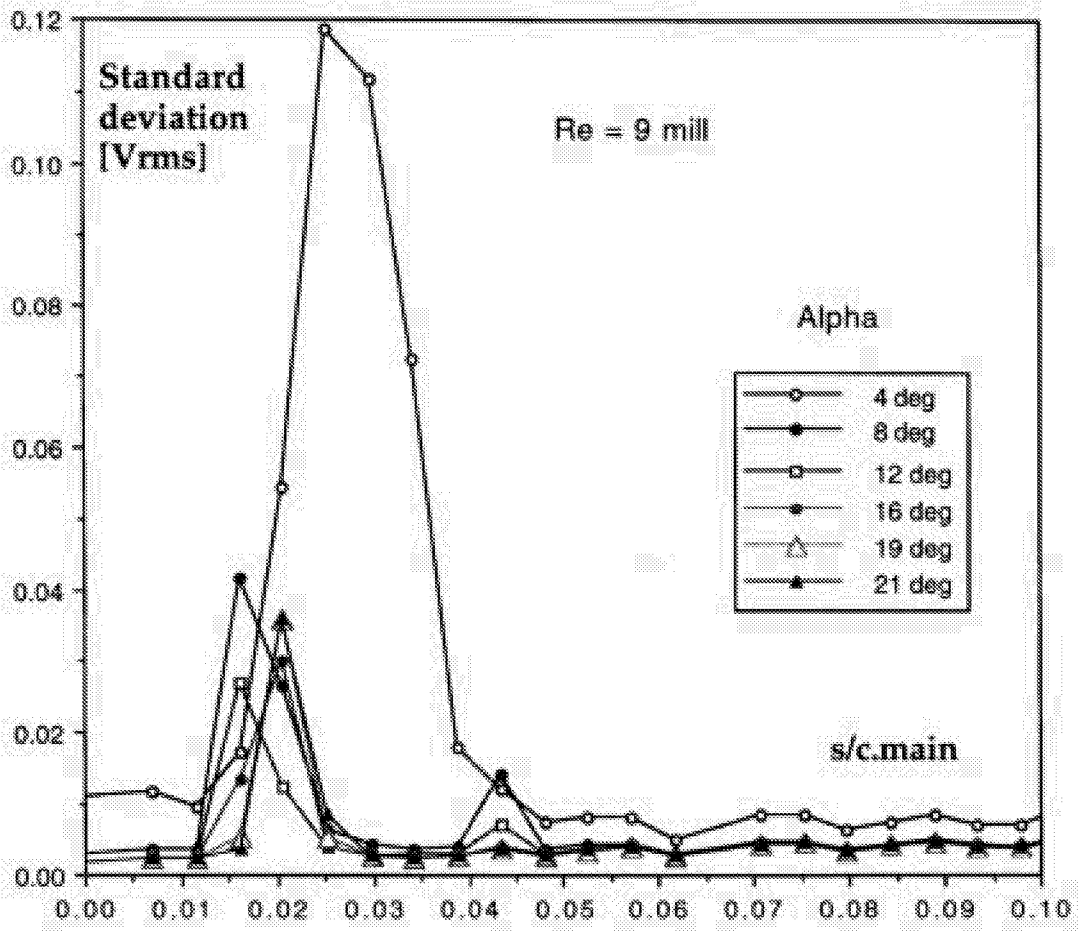


Figure 72b Distribution of standard deviation on main element for several angles of attack. 30P/30N Mach=0.2

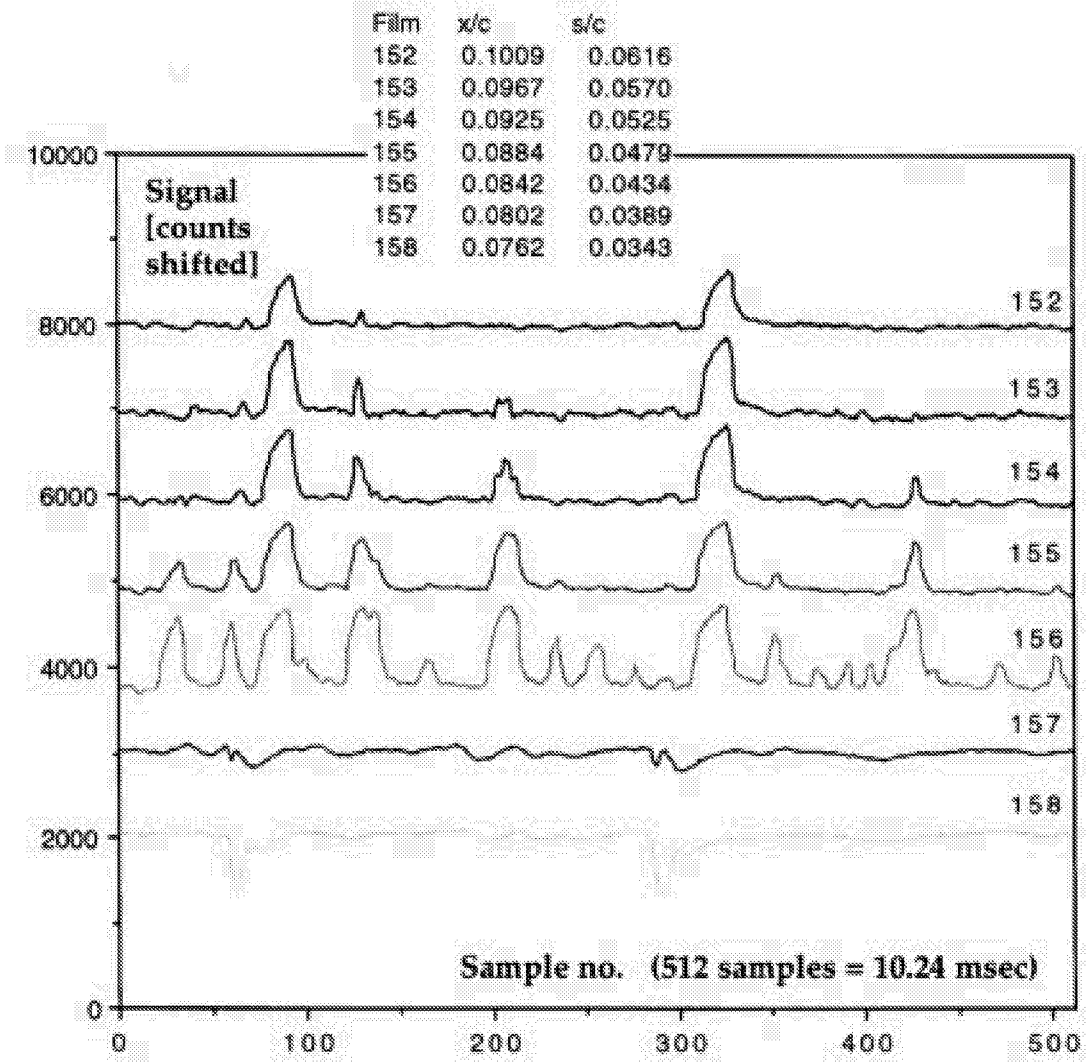


Figure 73 Signal traces (zero-shifted) corresponding to Figure 74. 30P/30N M=0.2 Re=5 mill. Alpha = 4 deg.

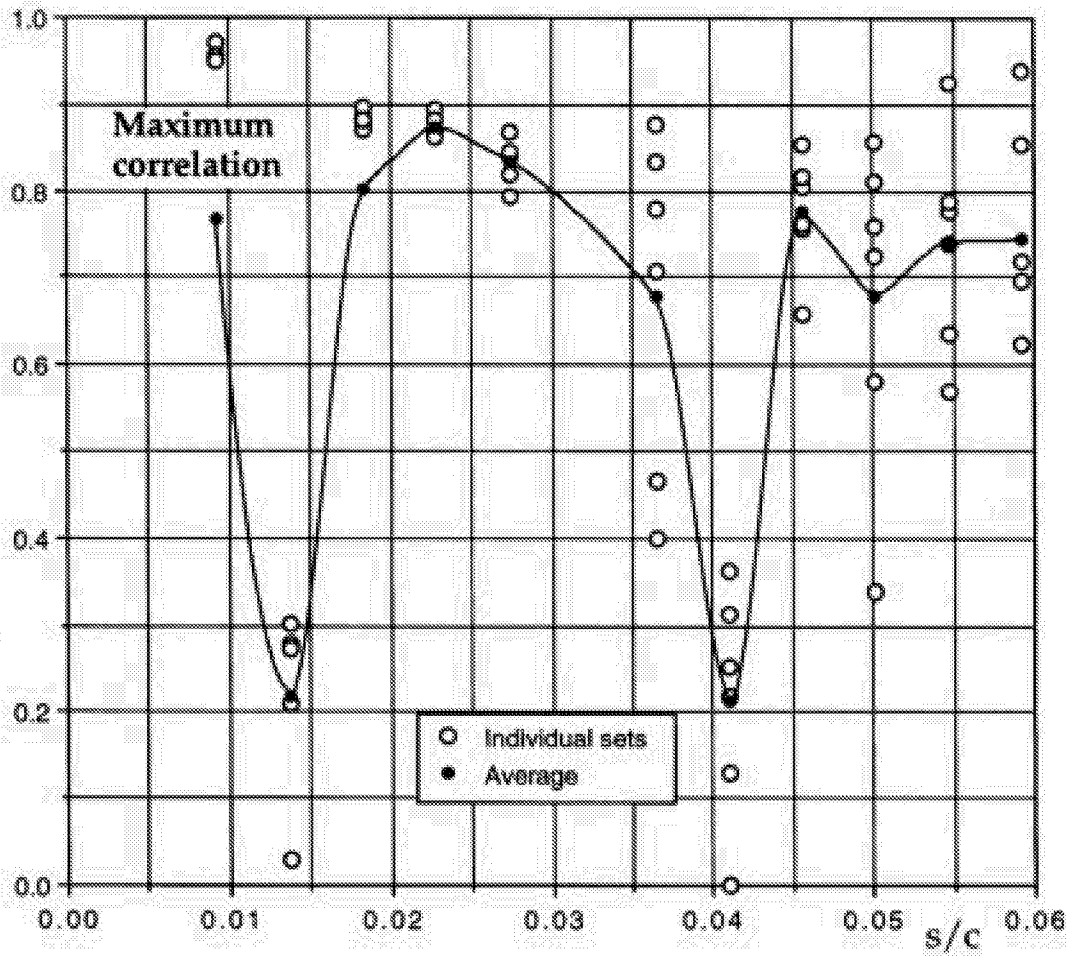


Figure 74 Maximum crosscorrelation on main nose.
30P/30N, Mach=0.2, Re=5 mill. Alpha=4 deg

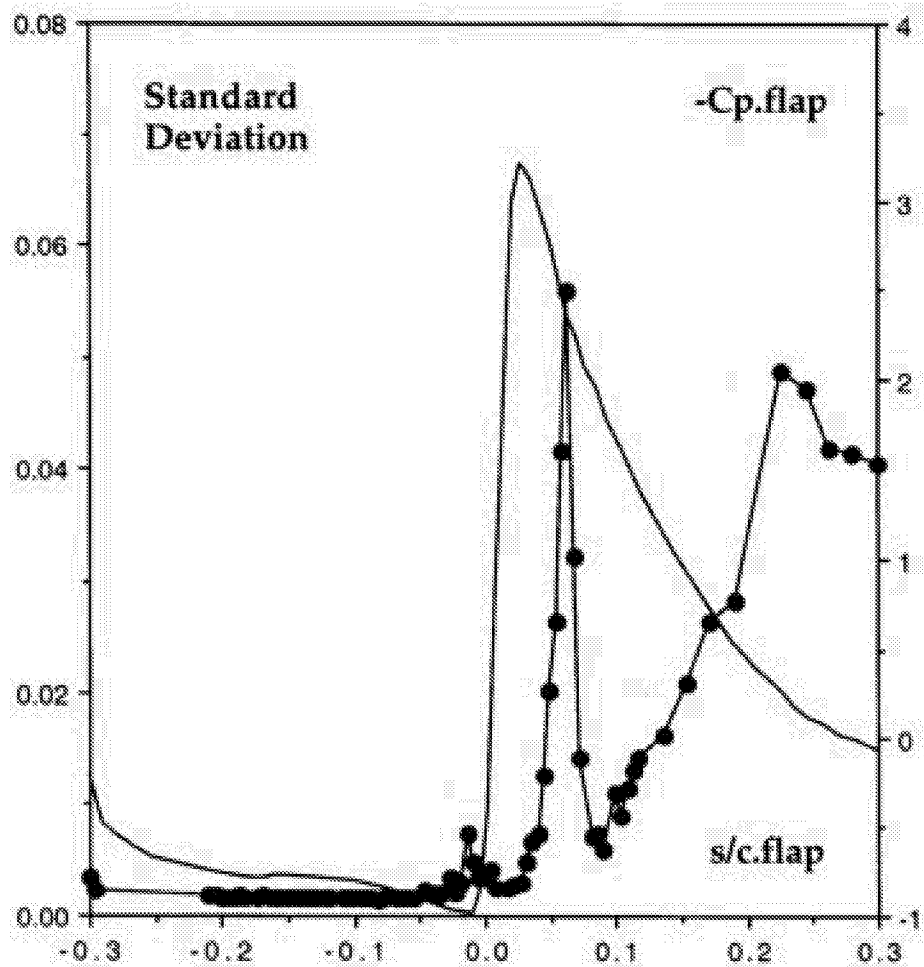


Figure 75 Pressure distribution and Standard deviation on the flap 30P/30N Mach=0.2 Re=5 mill Alpha=8 deg

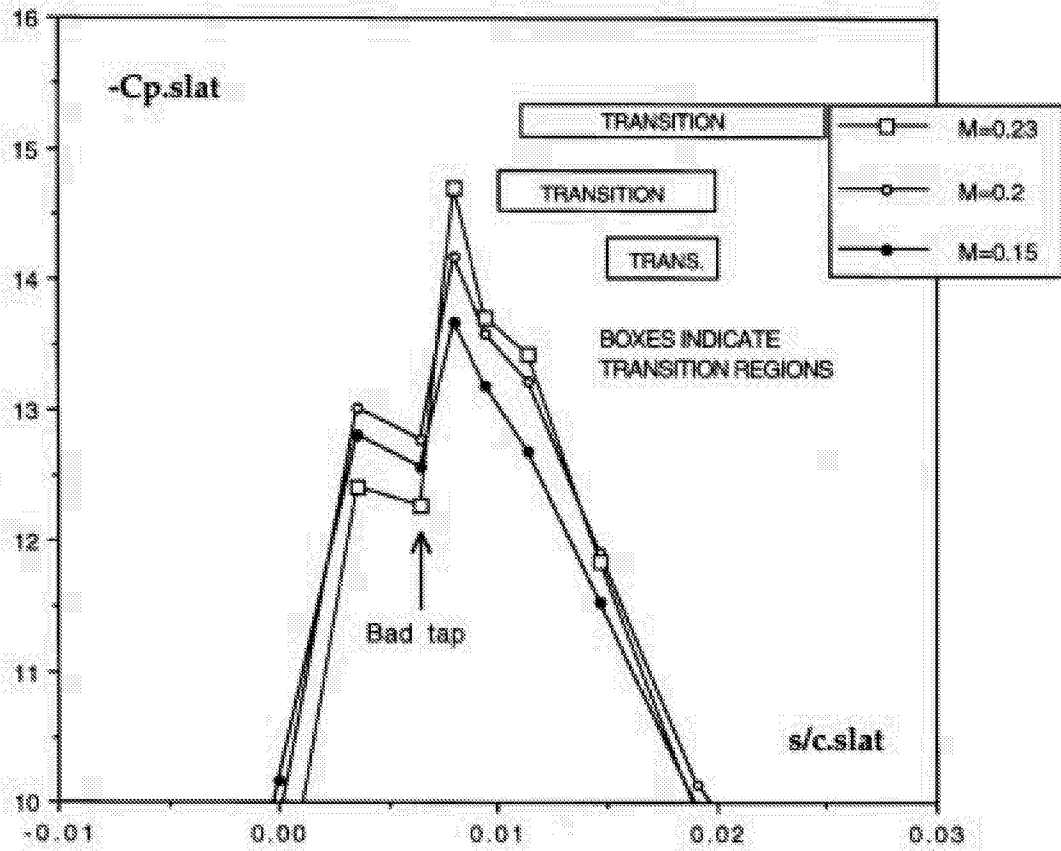


Figure 76 Mach number effect on Slat pressure distribution.
 30P/30N Re=9 mill Alpha=19 deg.

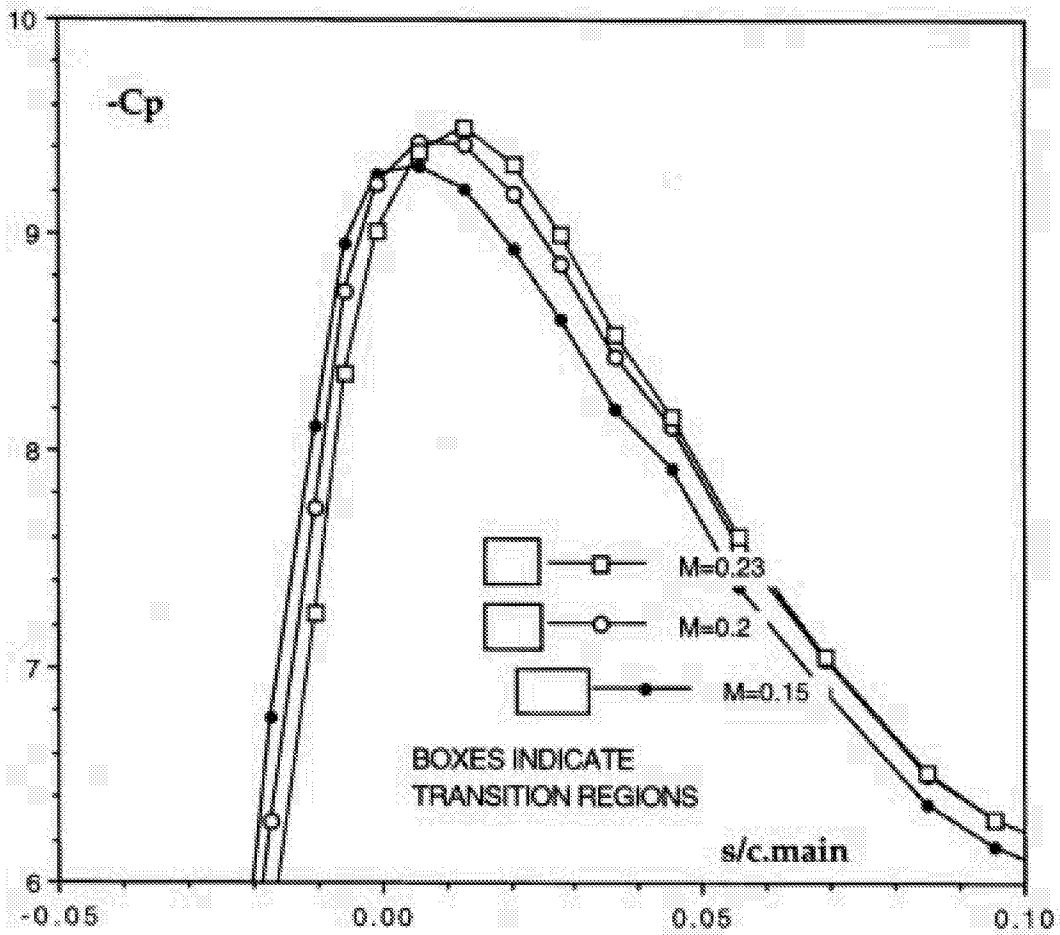


Figure 77 Mach number effect on Main.
 30P/30N Re=9 mill Alpha=19 deg.

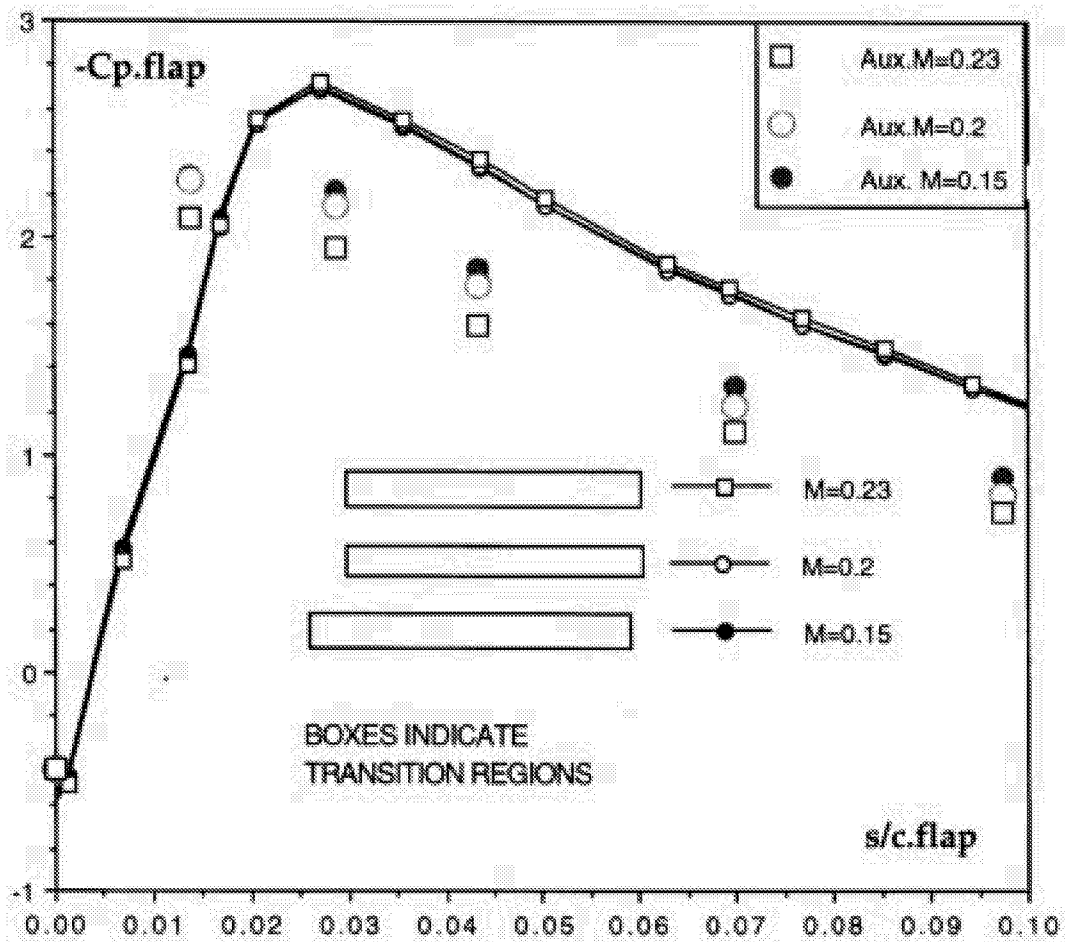


Figure 78 Mach number effect on Flap.
 30P/30N Re=9 mill Alpha=19 deg.

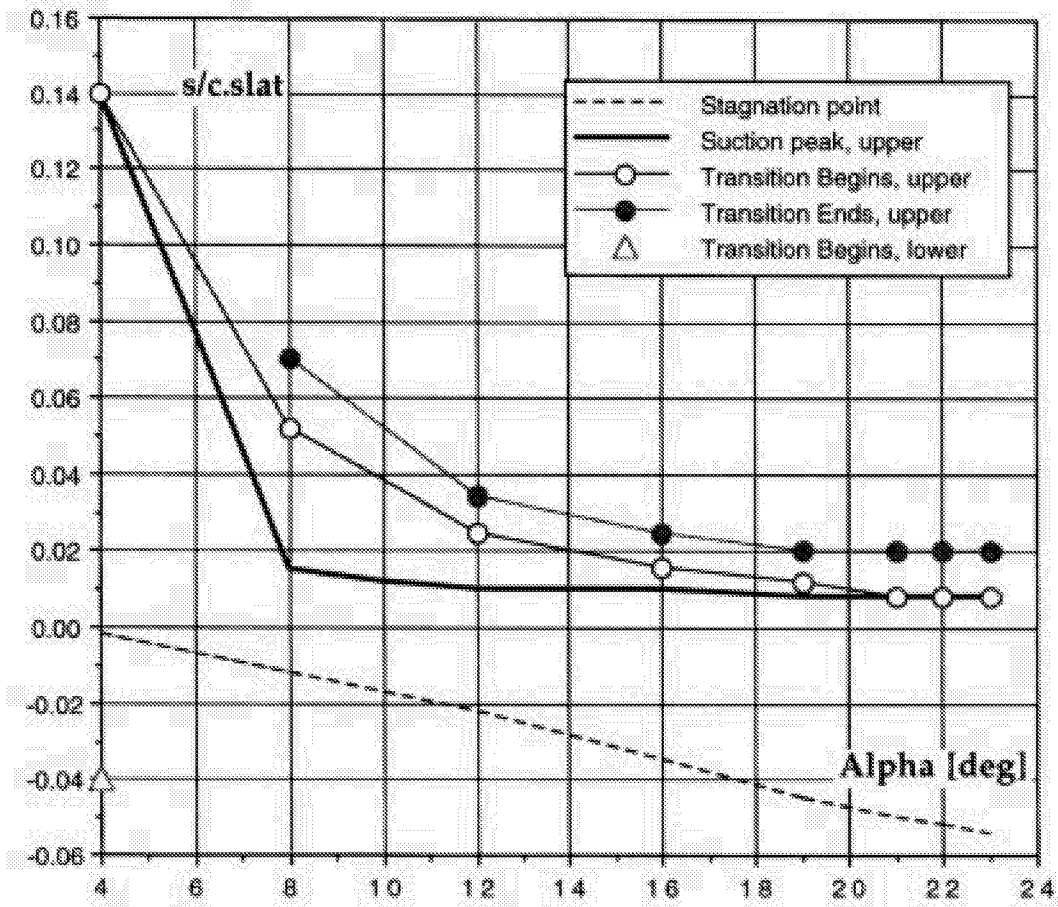


Figure 79a Transition 30P/30AD Mach=0.2 Re=9 mill - SLAT

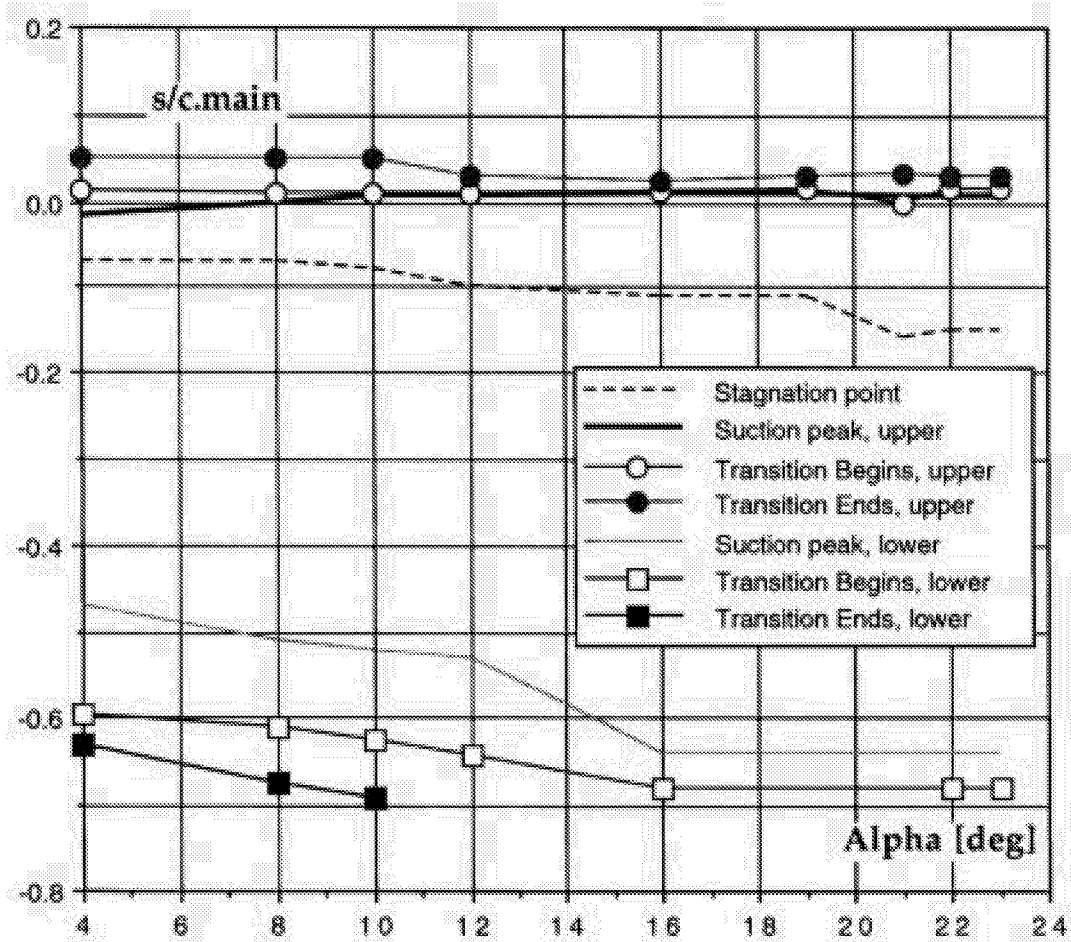


Figure 79b Transition 30P/30AD M=0.2 Re=9 mill - MAIN

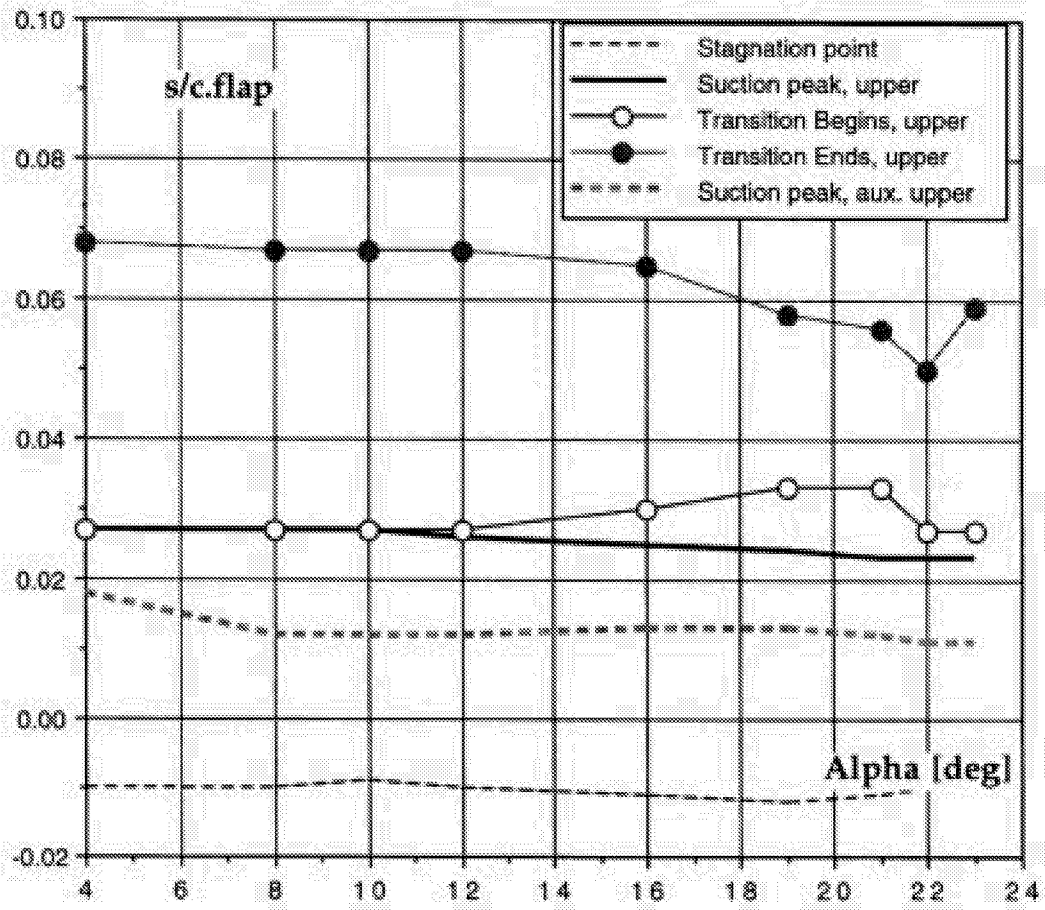


Figure 79c Transition 30P/30AD Mach=0.2 Re=9 mill - FLAP

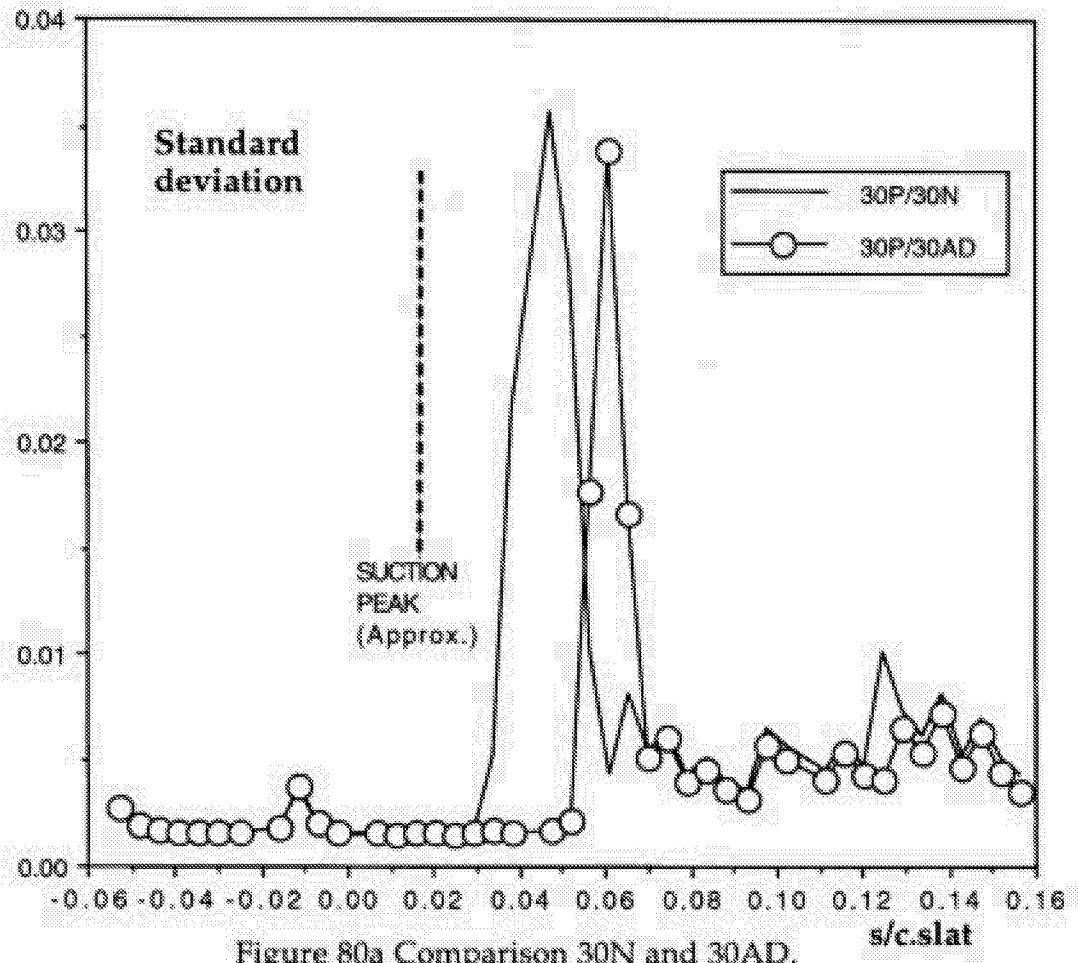


Figure 80a Comparison 30N and 30AD,
Mach=0.2 Re=9 mill Alpha=8deg

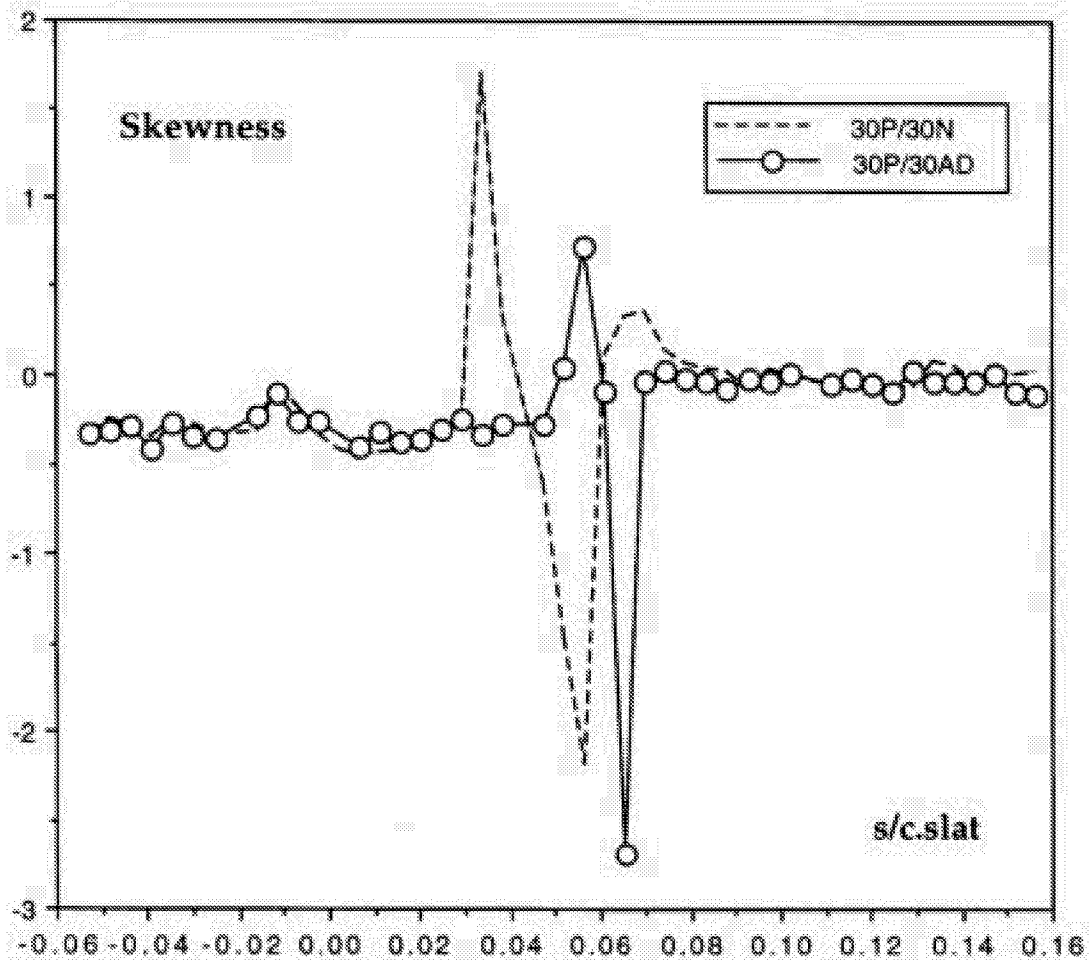


Figure 80b Comparison 30N and 30AD, Skewness.
Mach=0.2 Re=9 mill Alpha=8 deg.

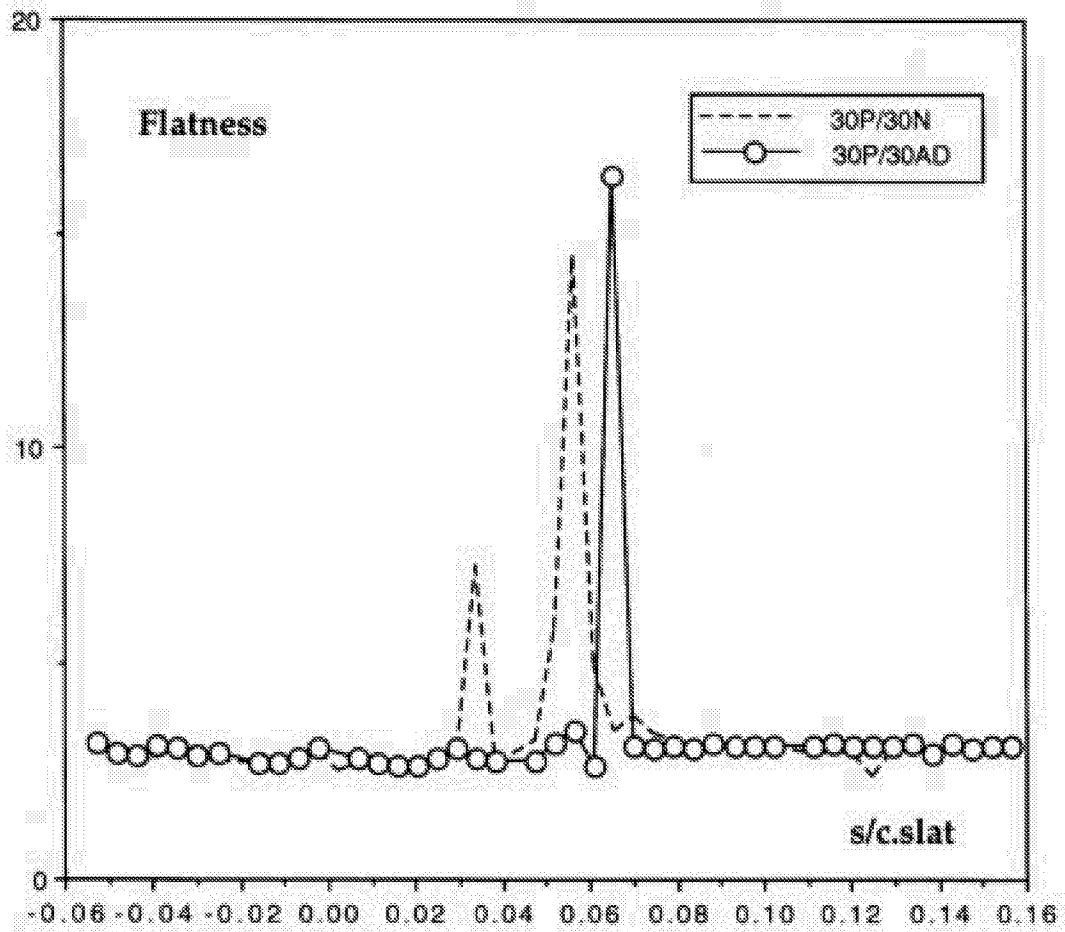


Figure 80c Comparison 30N and 30AD, Flatness.
Mach=0.2 Re=9 mill Alpha=8 deg.

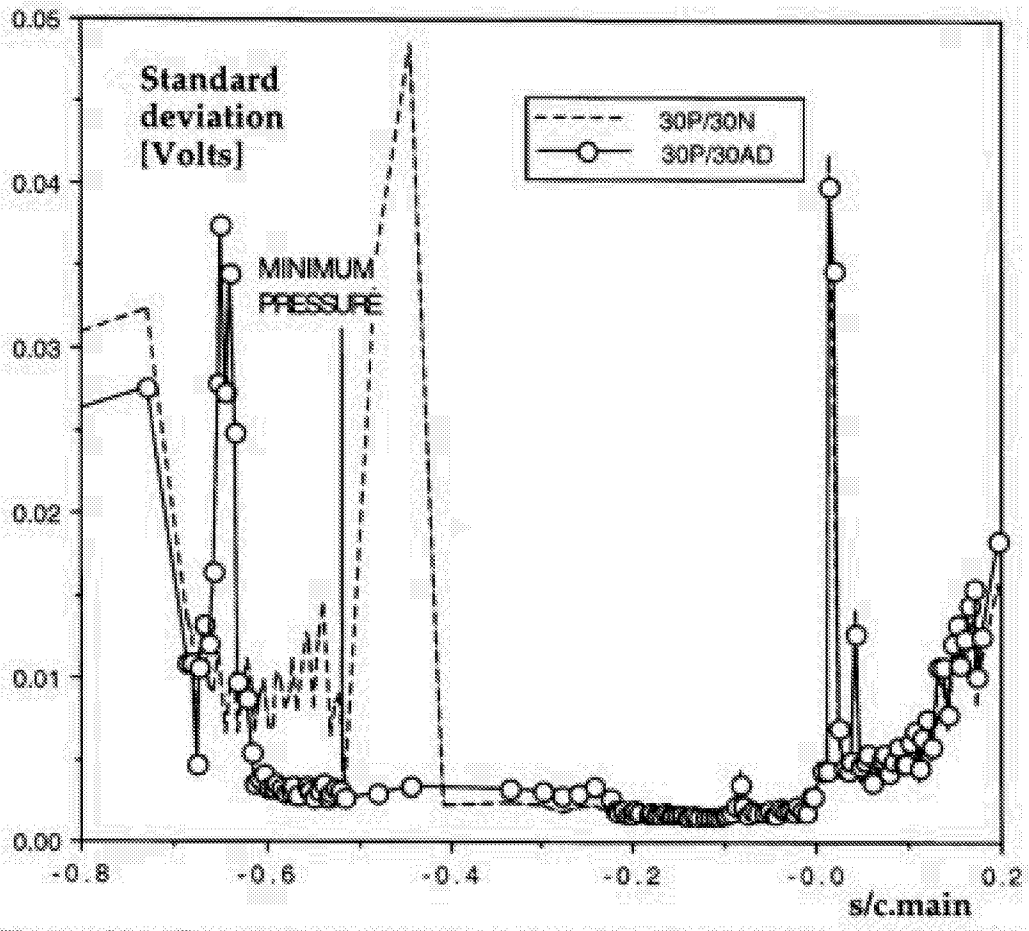


Figure 81a Comparison 30N and 30AD, Standard deviation. Main wing. Mach=0.2 Re=9 mill Alpha=8 deg.

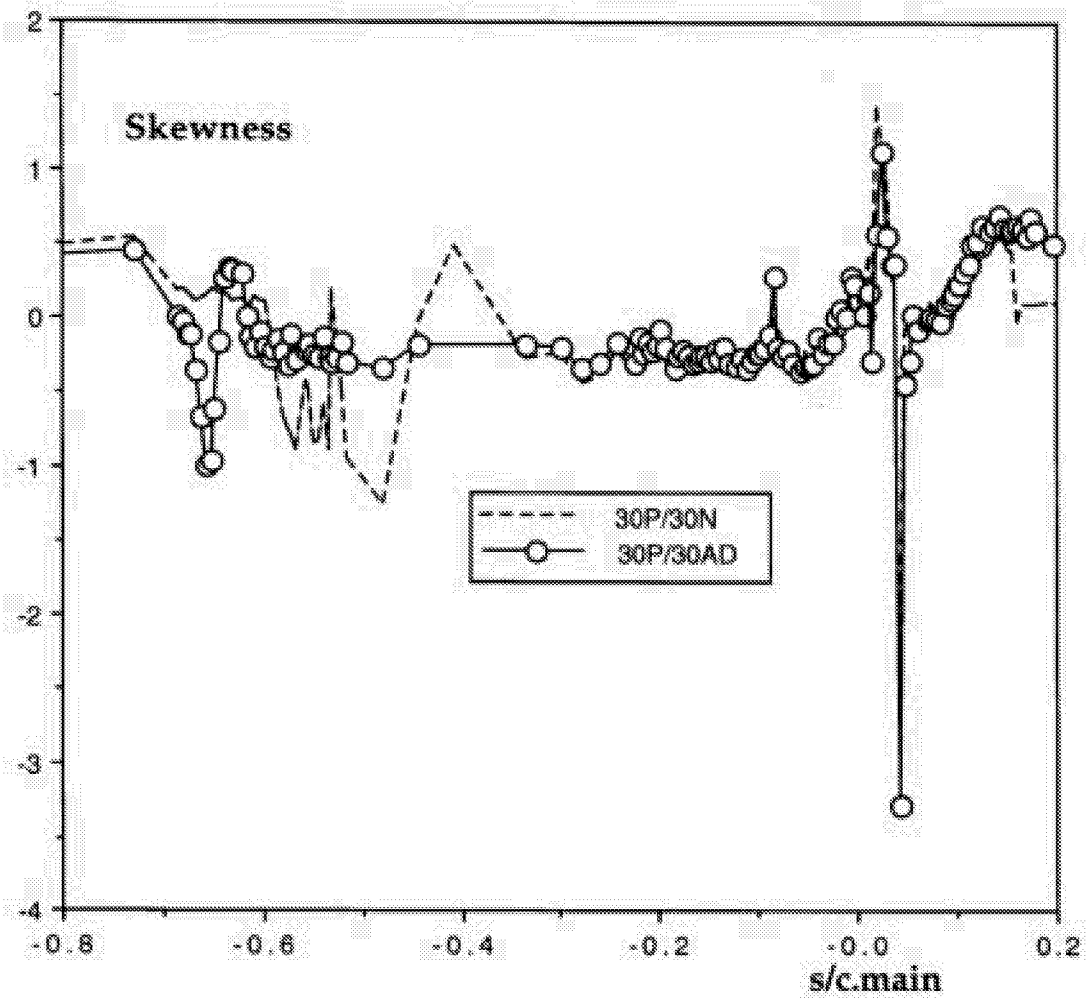


Figure 81b Comparison 30N and 30AD, Skewness. Main element.
Mach=0.2 Re=9 mill Alpha=8 deg.

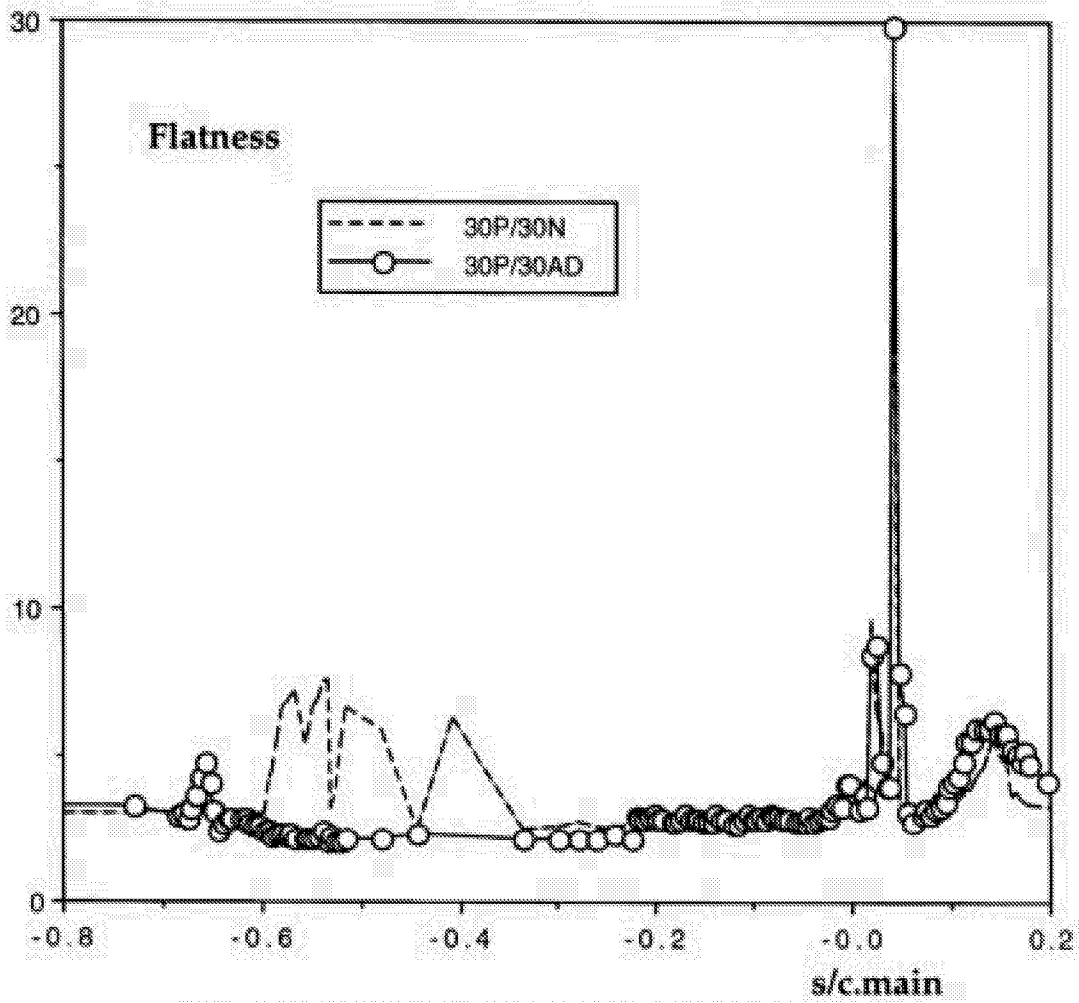


Figure 81c Comparison 30N and 30AD, Flatness.
Mach=0.2 Re=9 mill Alpha=8 deg.

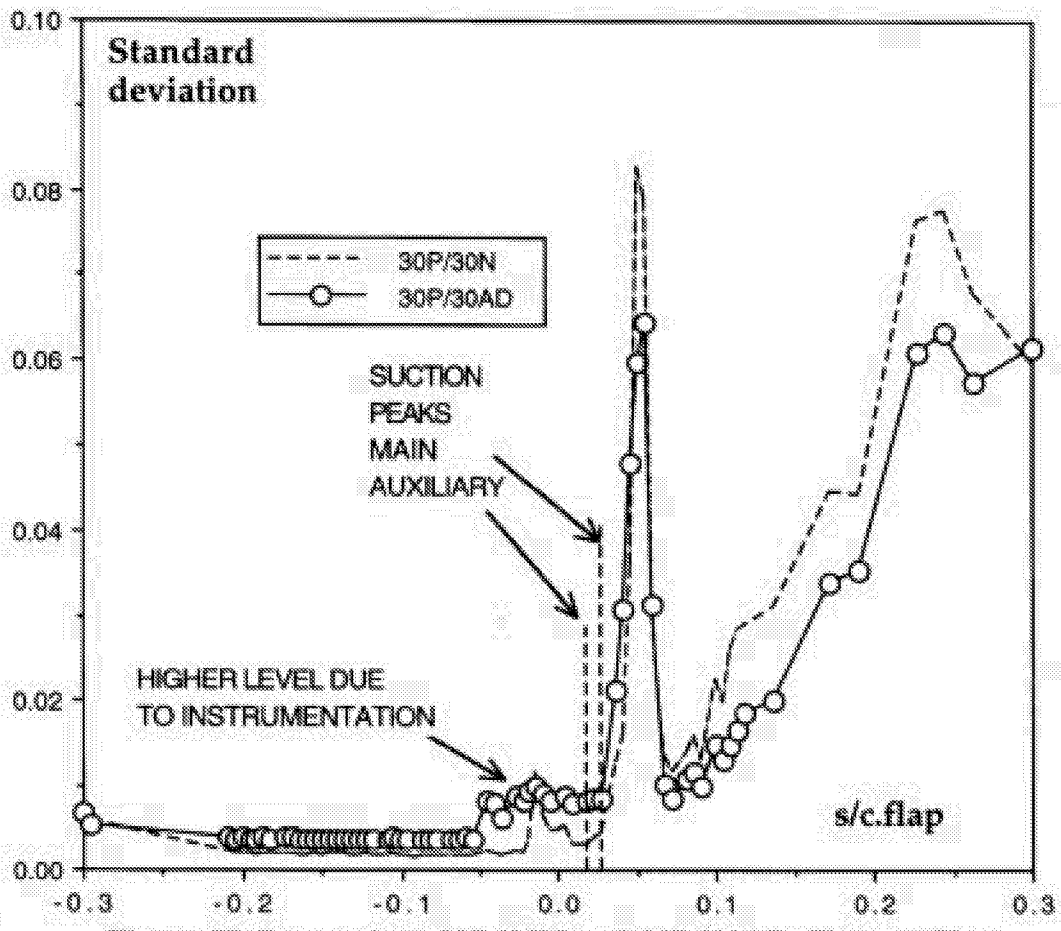


Figure 82 Comparison 30P/30N and 30P/30AD, Flatness Flap. Mach=0.2 Re=9 mill Alpha=8 deg.

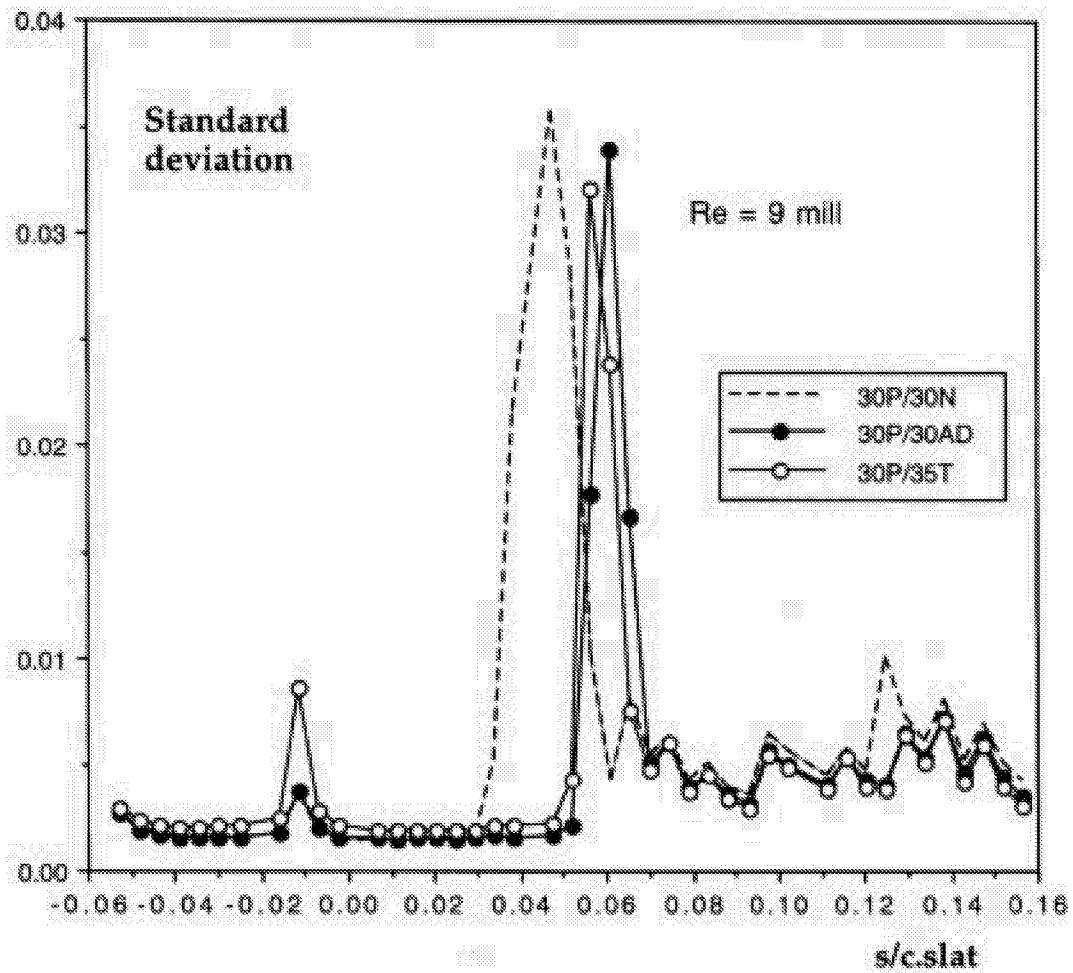


Figure 83a Comparison M=0.2, Re=9 mill. Alpha=8 deg. All three configurations. Slat.

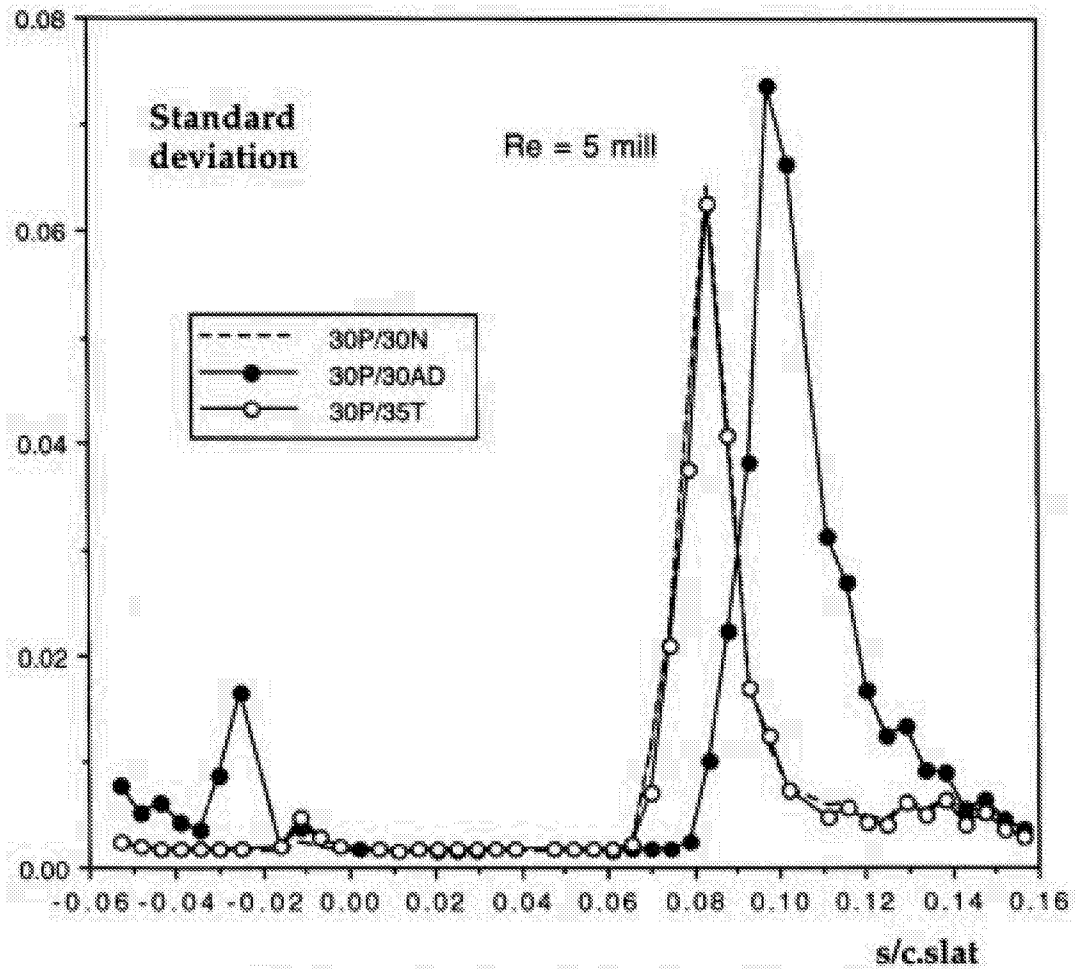


Figure 83b Comparison M=0.2, Re=5 mill. Alpha=8 deg. All three configurations. Slat.

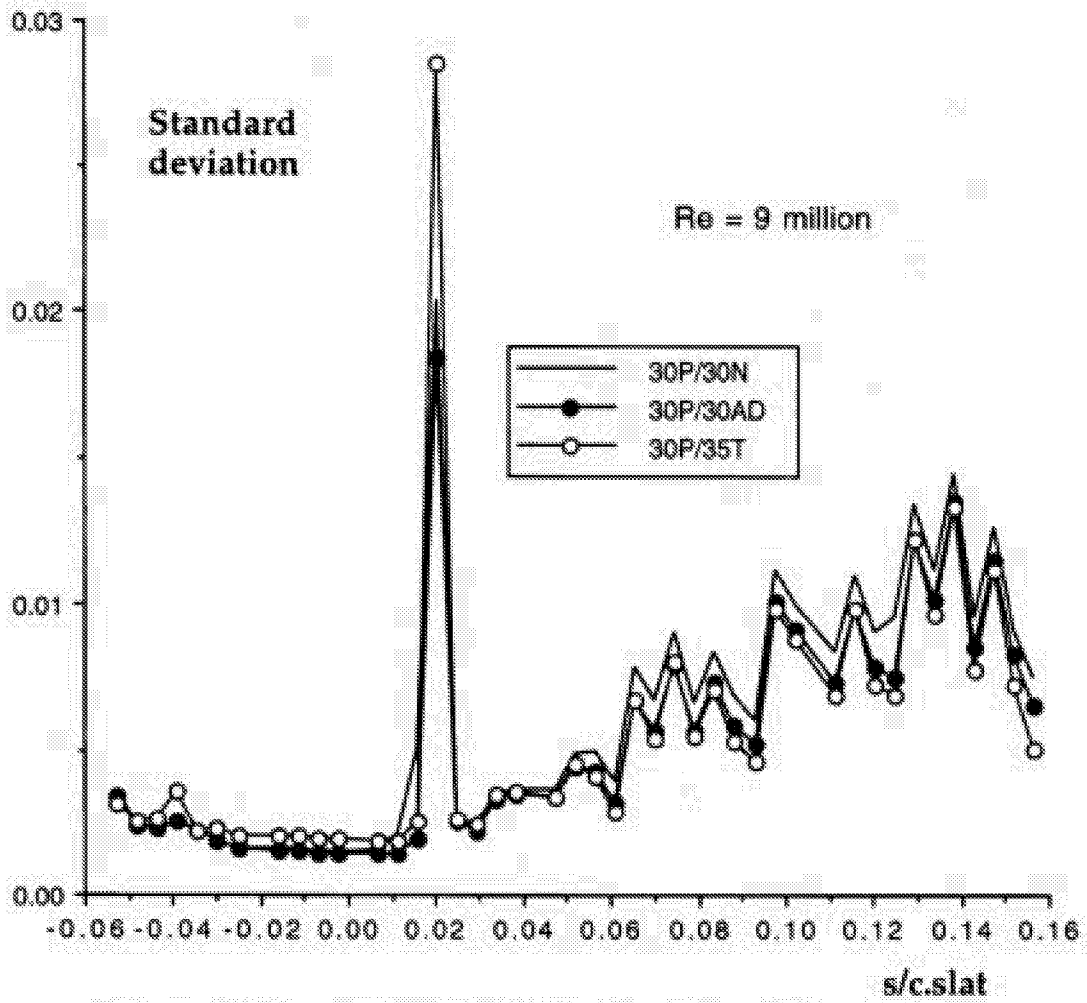


Figure 84 Comparison $M=0.2$, $Re=9 \text{ million}$ $\text{Alpha}=16 \text{ deg}$. All three configurations. Slat.

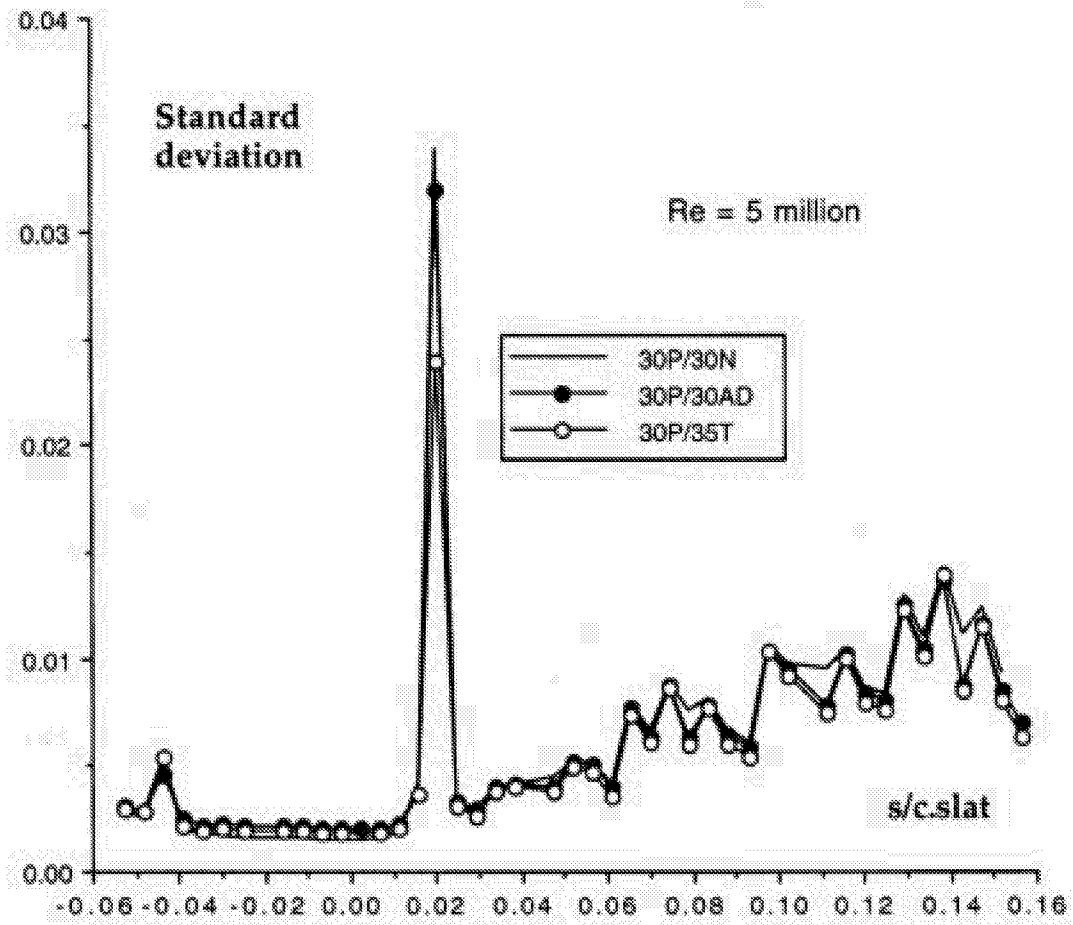


Figure 85 Comparison M=0.2, Re=5 million Alpha=19 deg. All three configurations. Slat.

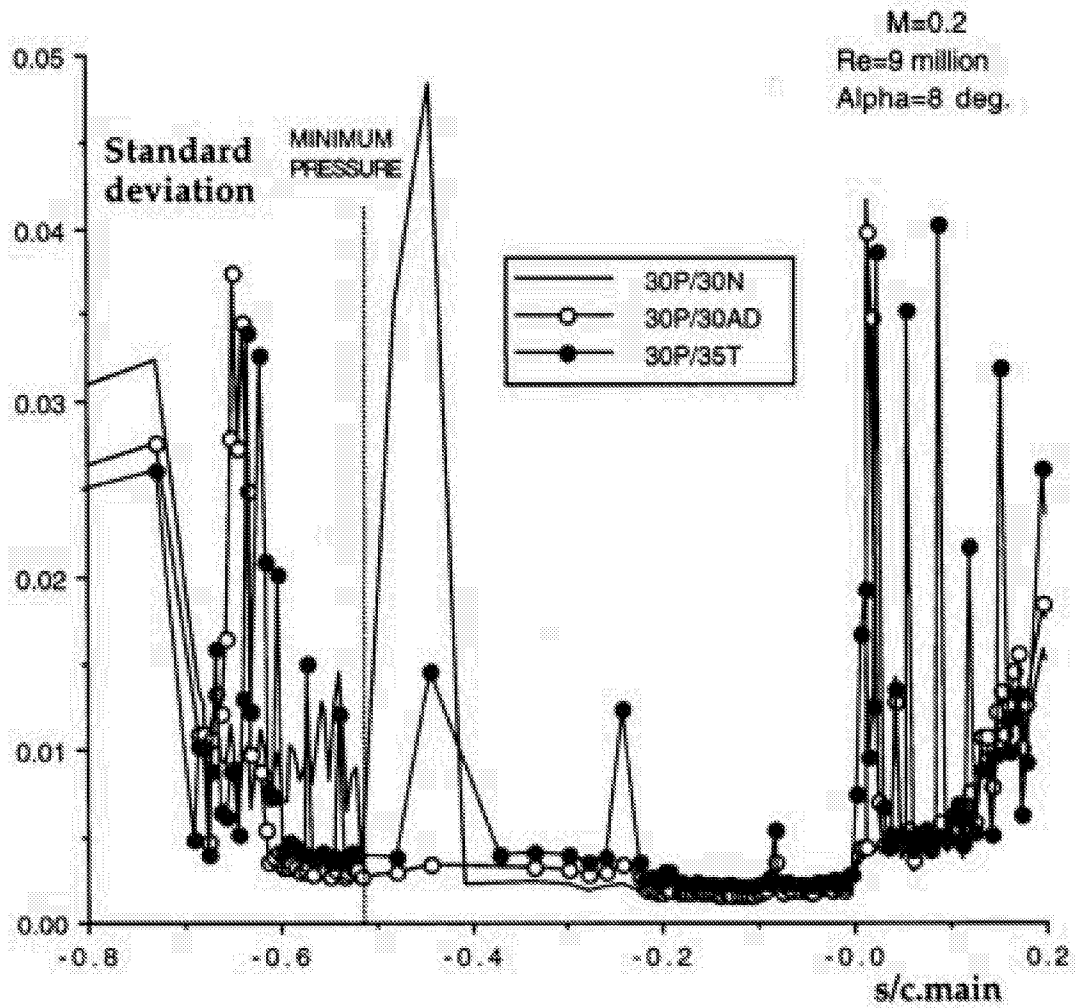


Figure 86 Standard deviation on main element. Notice instrumentation disturbances for one anemometer channel on one system on upper side and rear lower side for 30P/35T data.

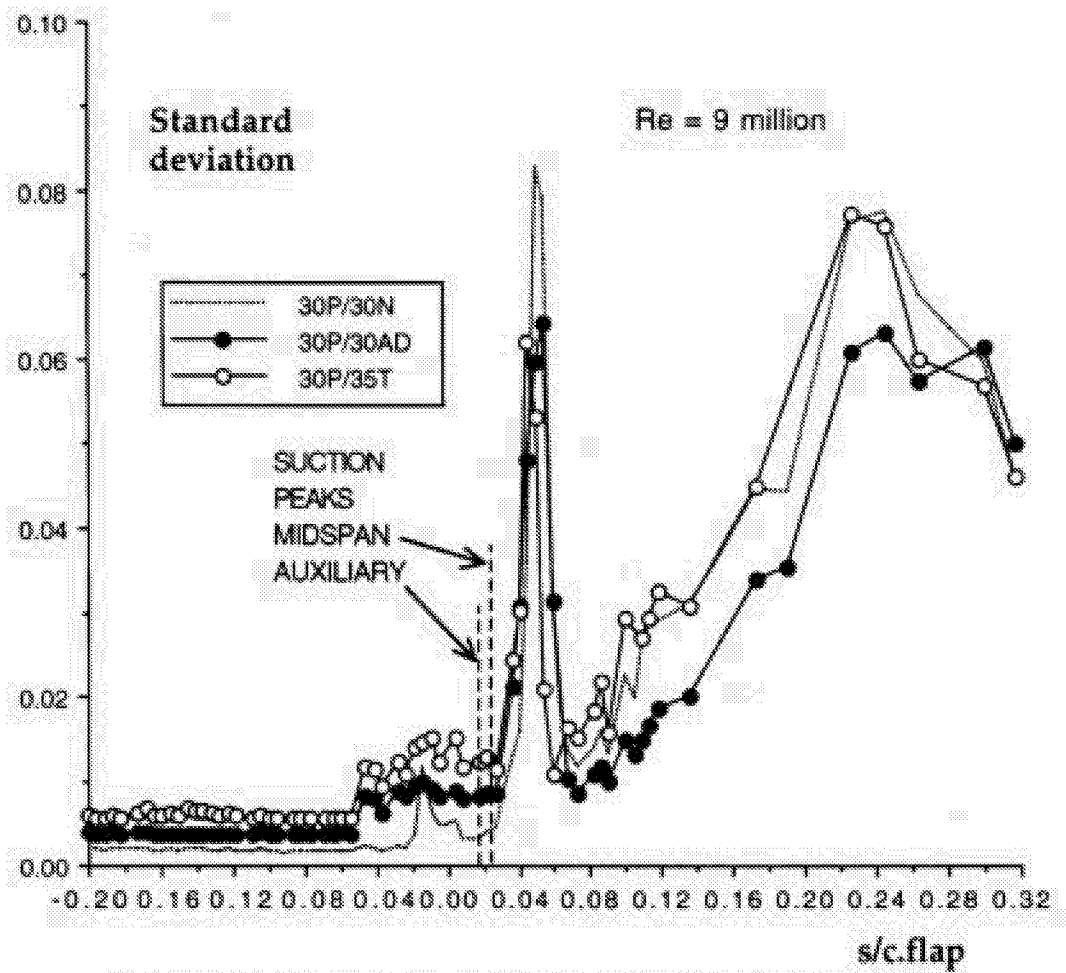


Figure 87a Comparison M=0.2, Re=9 million Alpha=8 deg. Three configurations. Flap.

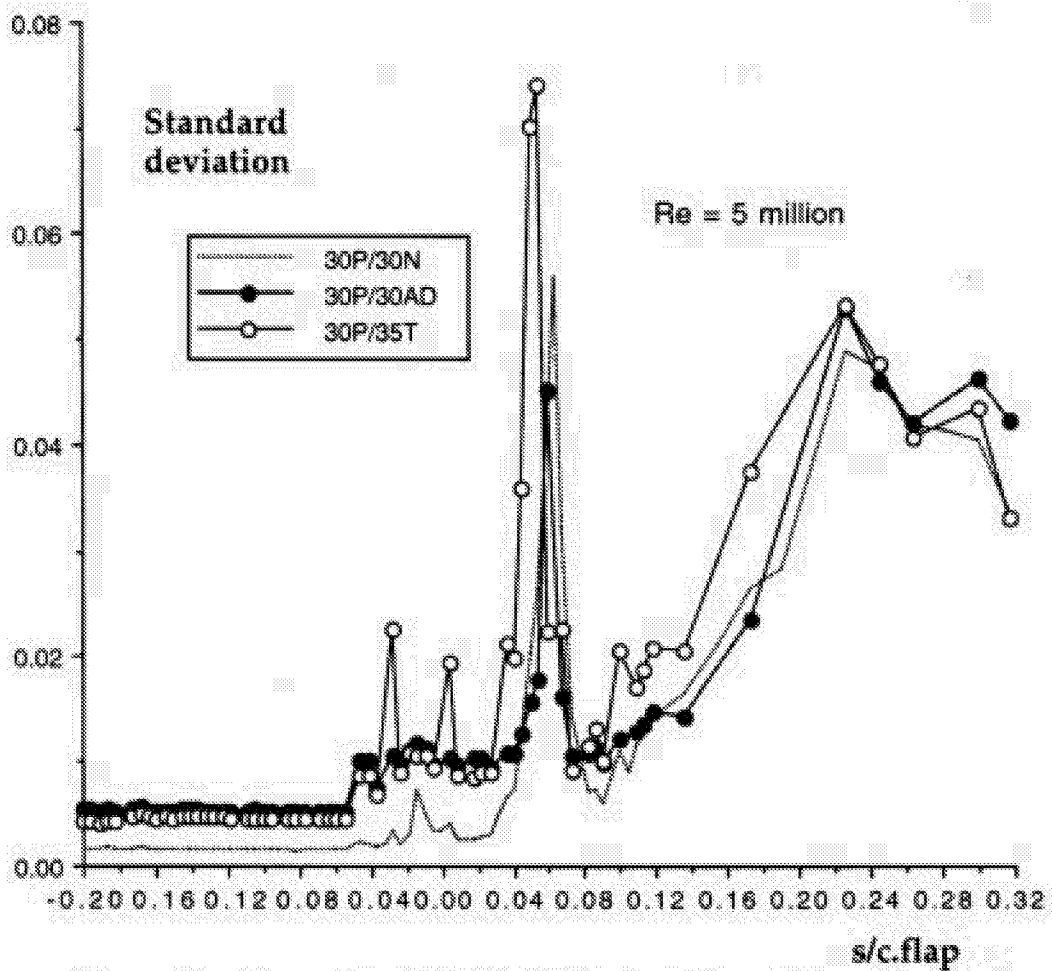


Figure 87b Comparison Mach=0.2, Re=5 million Alpha=8 deg. Three configurations. Flap.

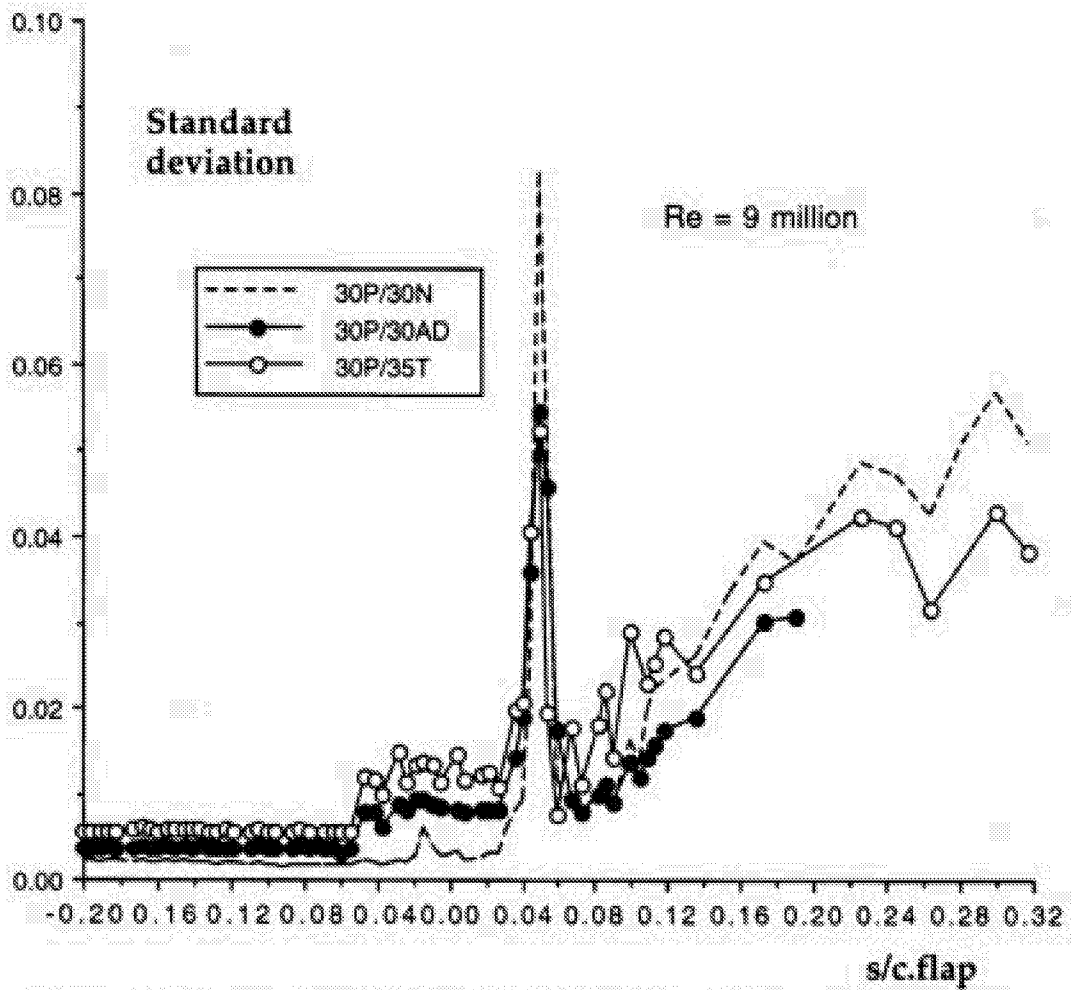


Figure 88 Comparison Mach=0.2, Re=9 million. Three configurations. Alpha=16 deg. Flap.

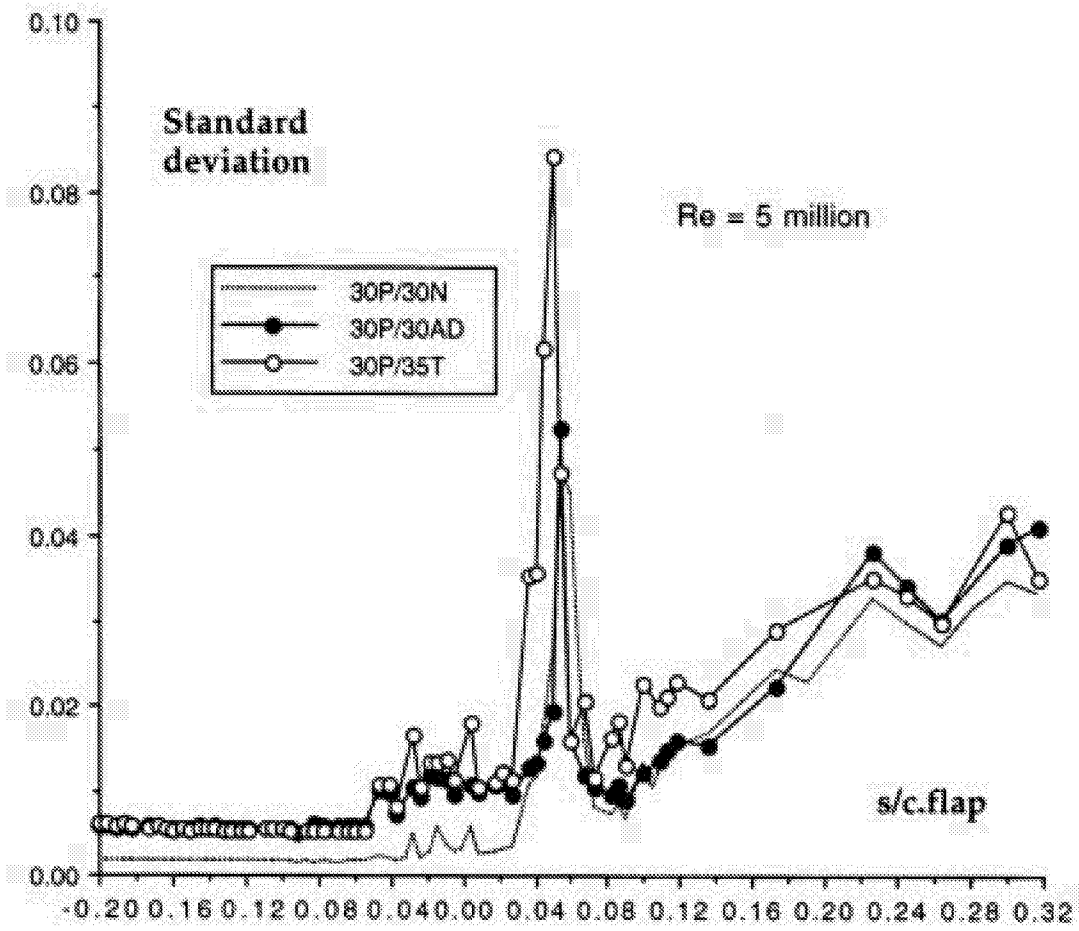


Figure 89 Comparison Mach=0.2, Re=5 million. Three configurations. Alpha=19 deg. Flap.

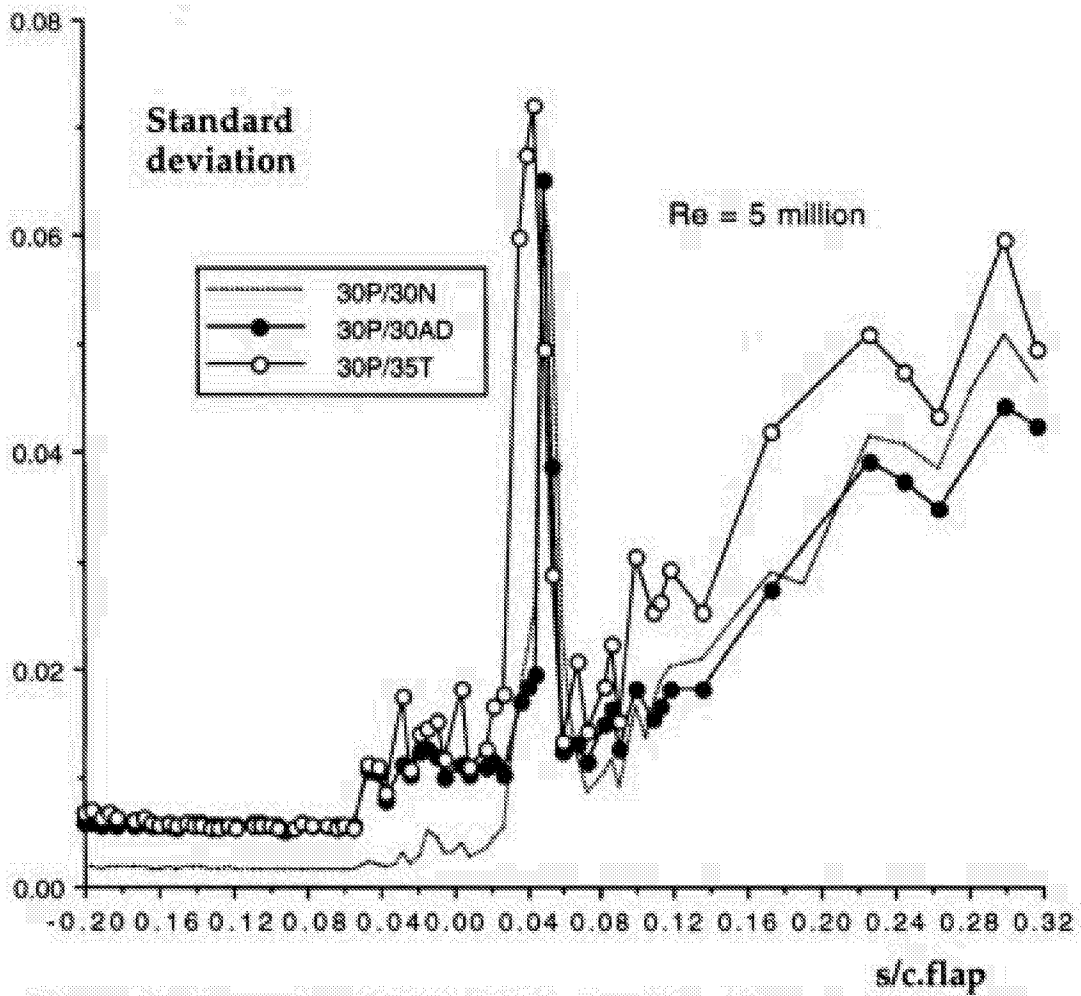


Figure 90 Comparison Mach=0.2, Re=5 million. Three configurations. Alpha=21 deg. Flap.

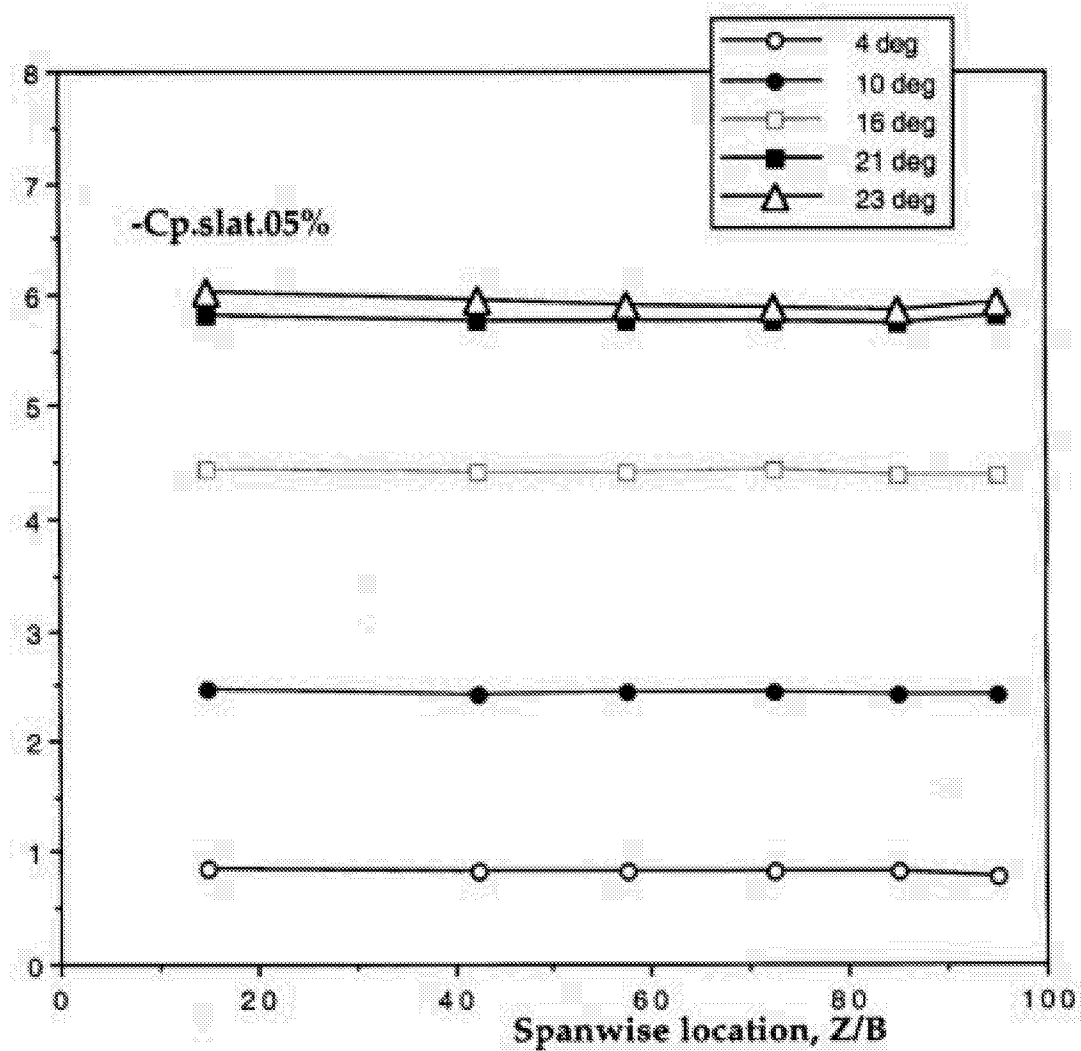


Figure 91a Spanwise pressure distribution - Slat
30P/30N Mach=0.2, Re = 9 million

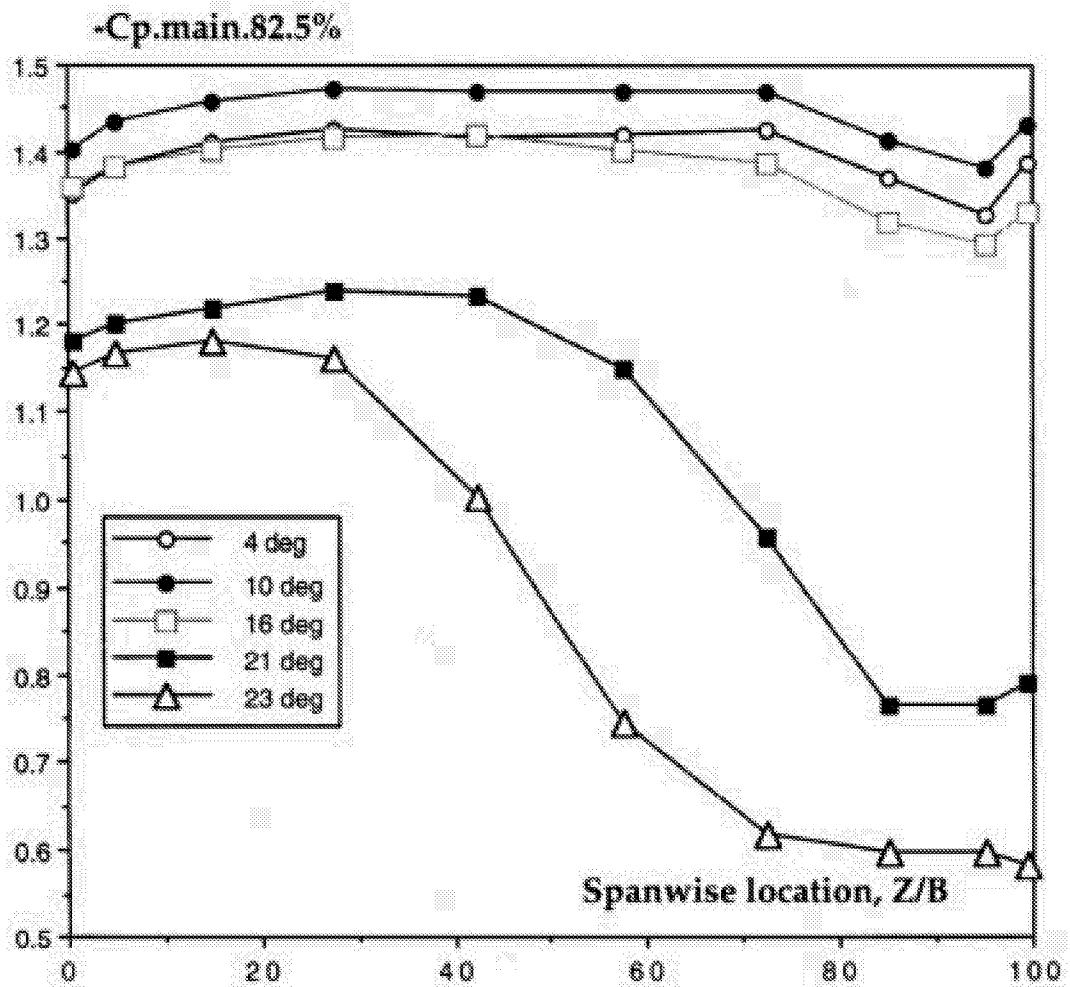


Figure 91b Spanwise pressure distribution - MAIN (82.5% stowed chord)
 30P/30N Mach=0.2, Re = 9 million

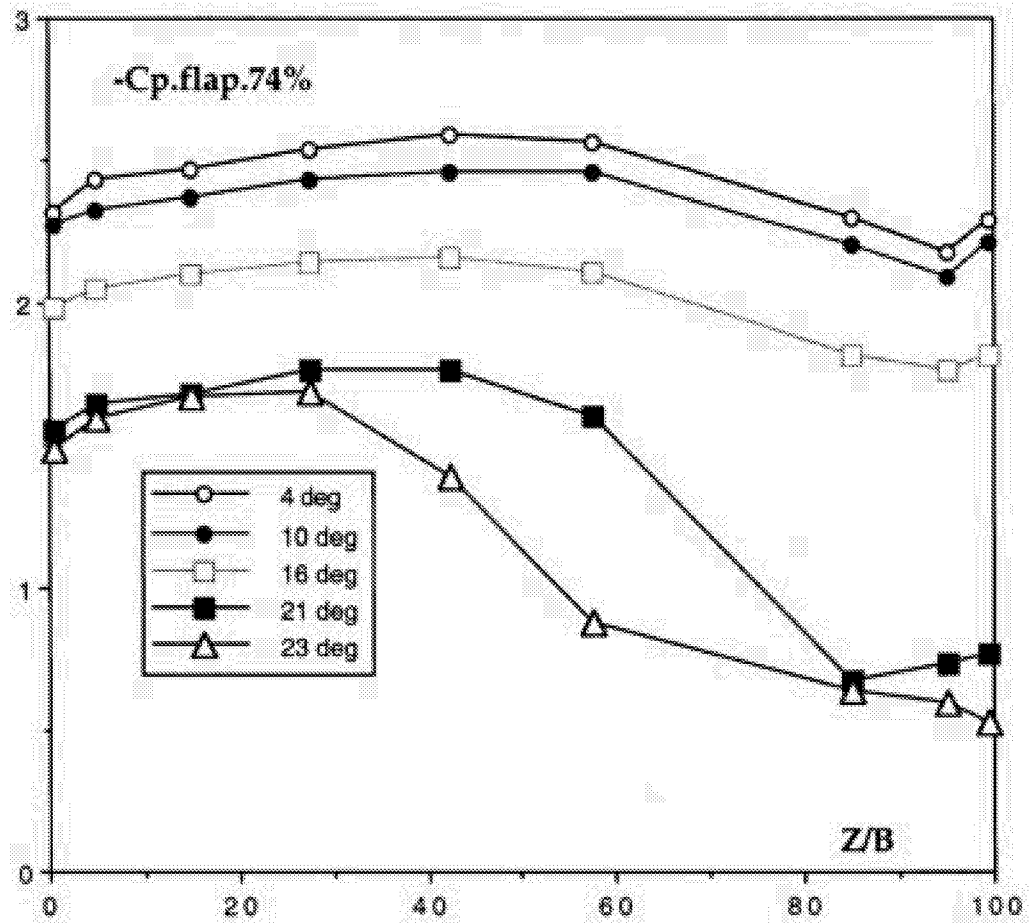


Figure 91c Spanwise pressure distribution -FLAP (74 % stowed coordinate)
 30P/30N Mach=0.2, Re = 9 mill

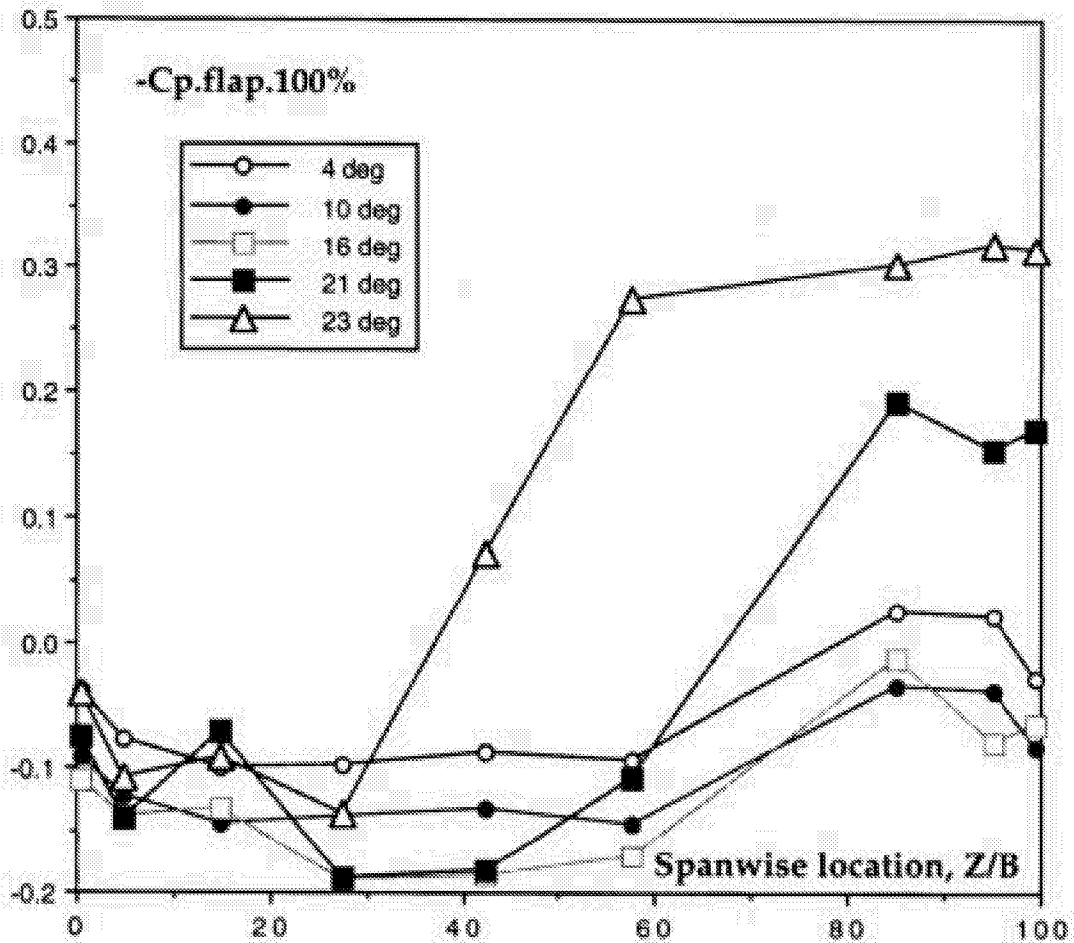


Figure 91d Spanwise pressure distribution - FLAP (Trailing edge)
 30P/30N Mach=0.2, Re = 9 million

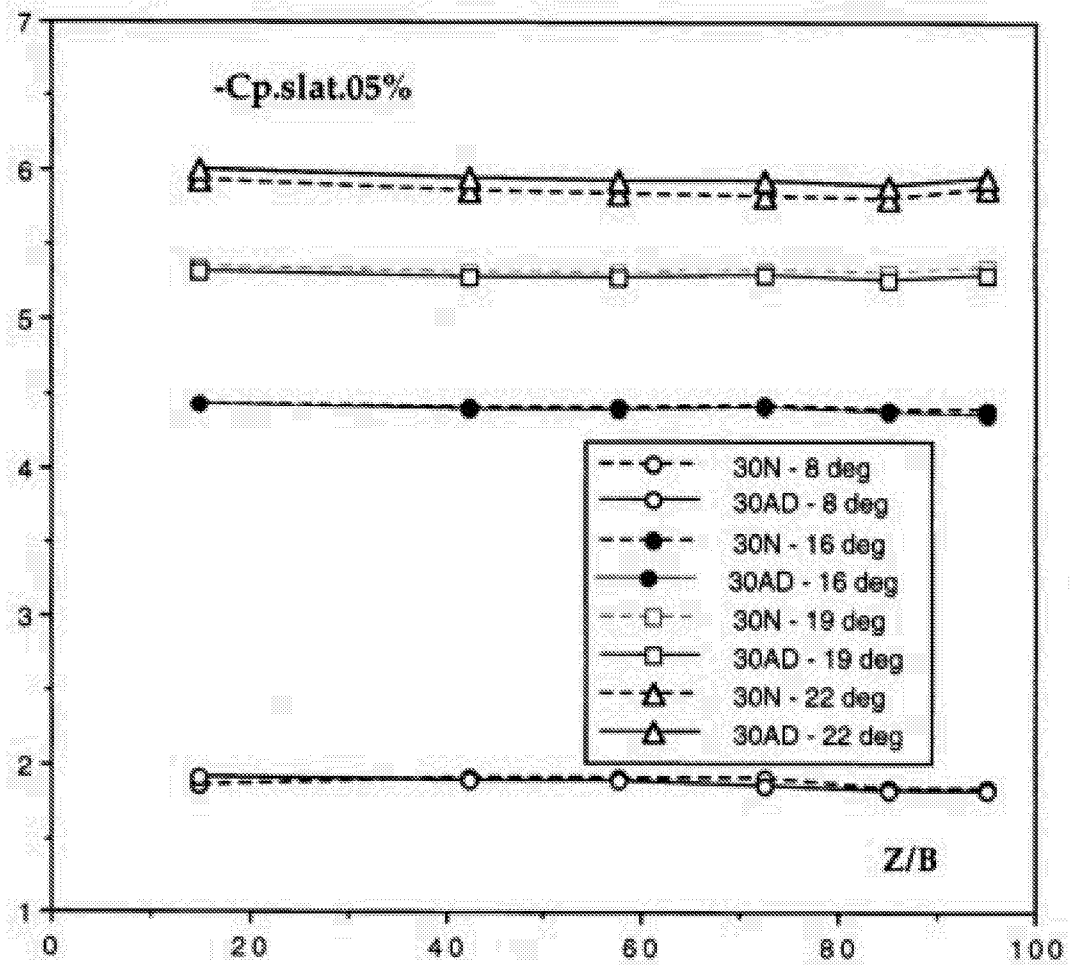


Figure 92a Spanwise pressure distribution
 30P/30AD compared with 30P/30N
 Mach=0.2 Re =9 million

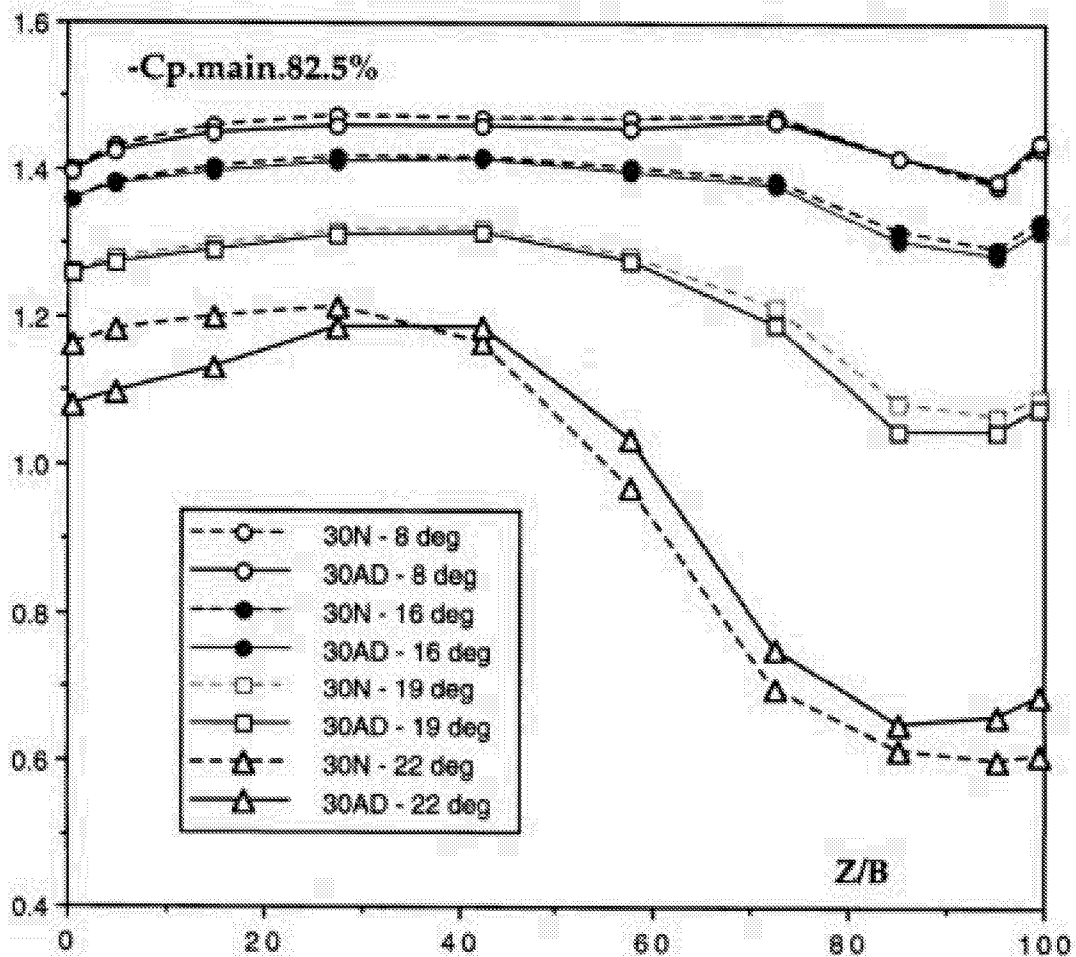


Figure 92b Spanwise pressure distribution
 30P/30AD compared with 30P/30N
 Mach=0.2 Re =9 million

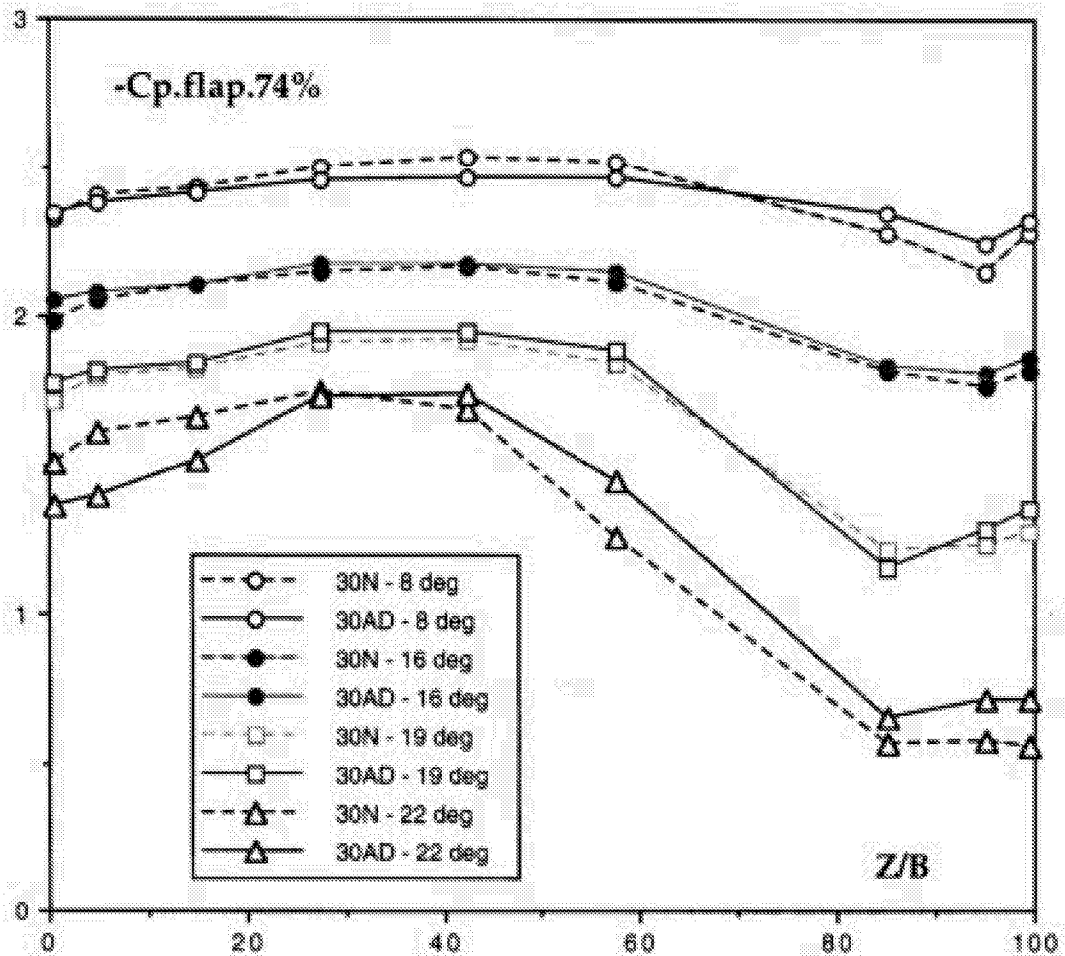


Figure 92c Spanwise pressure distribution
 30P/30AD compared with 30P/30N
 Mach=0.2 Re =9 million

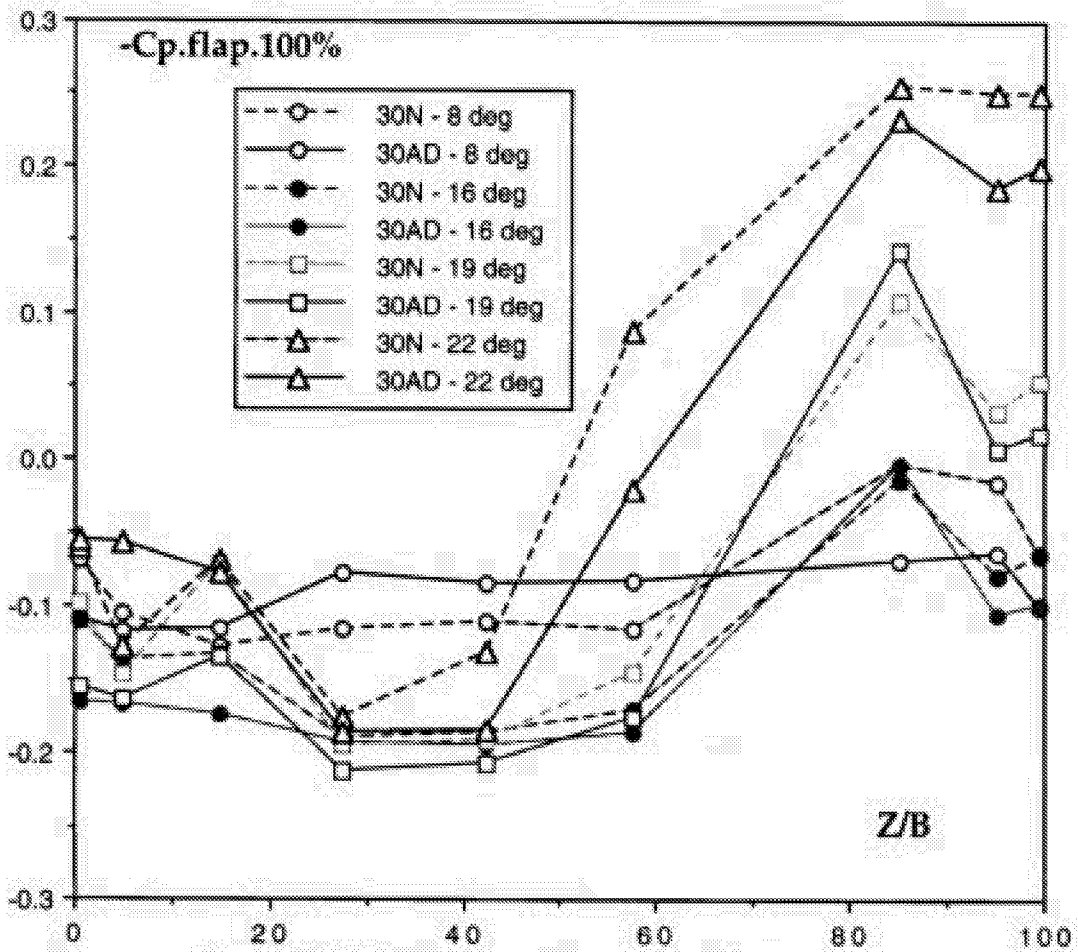


Figure 92d Spanwise pressure distribution
 30P/30AD compared with 30P/30N
 Mach=0.2 Re =9 million

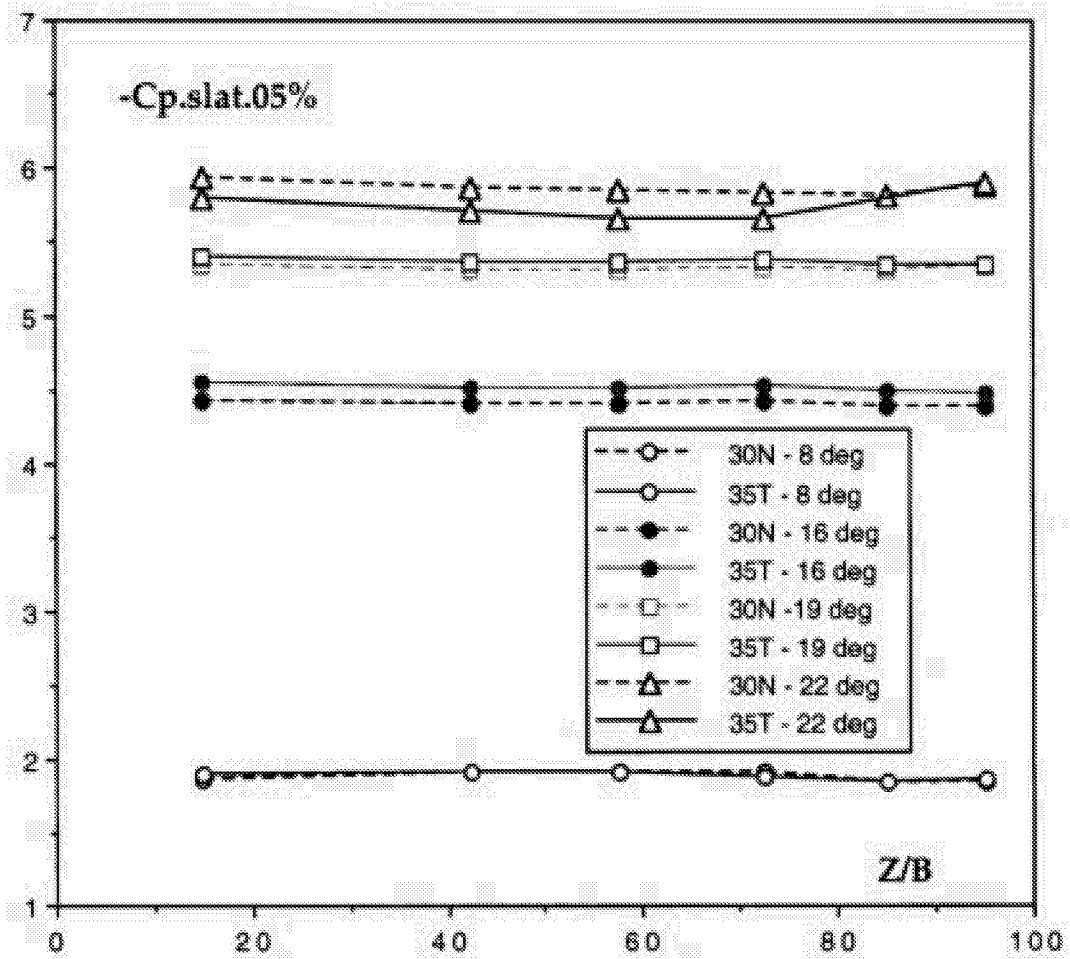


Figure 93a Spanwise pressure distribution
30P/35T Mach=0.2 Re=9 million

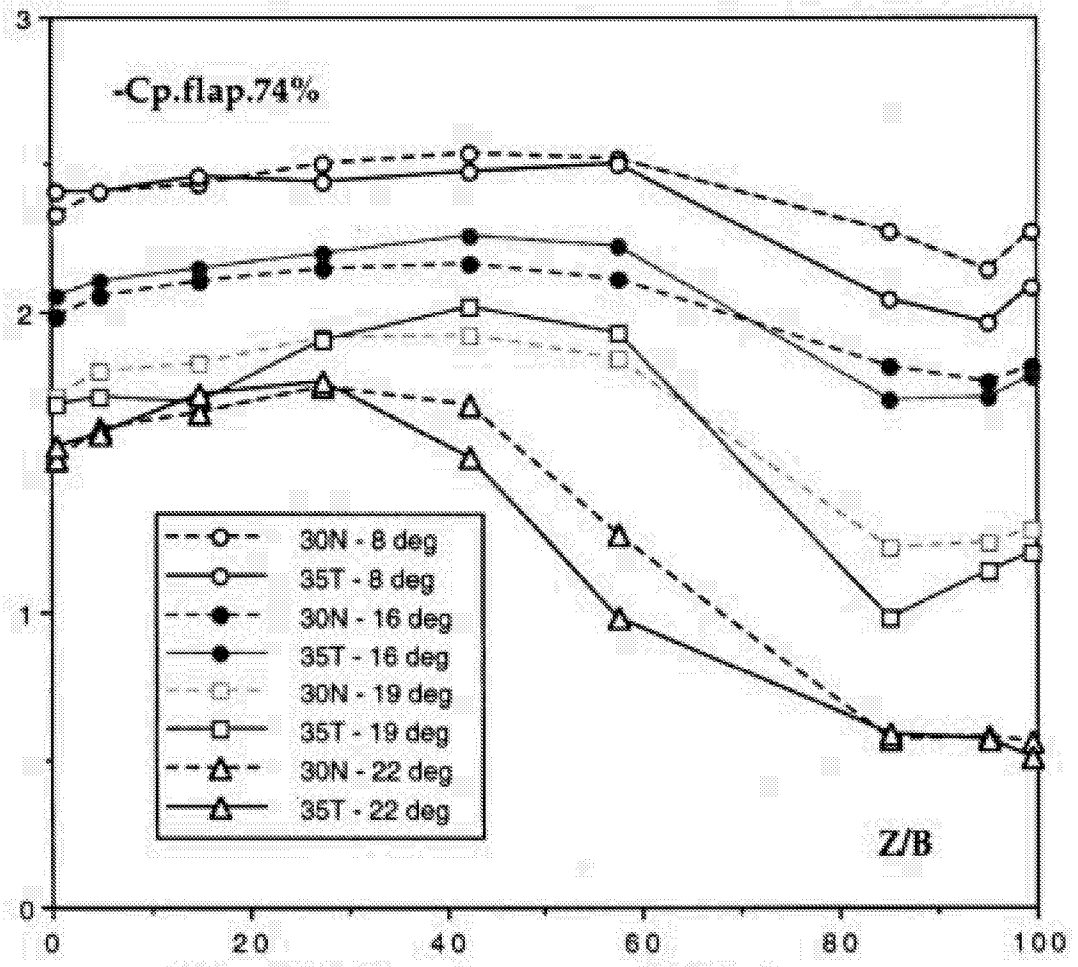


Figure 93b Spanwise pressure distribution
30P/35T Mach=0.2 Re=9 million

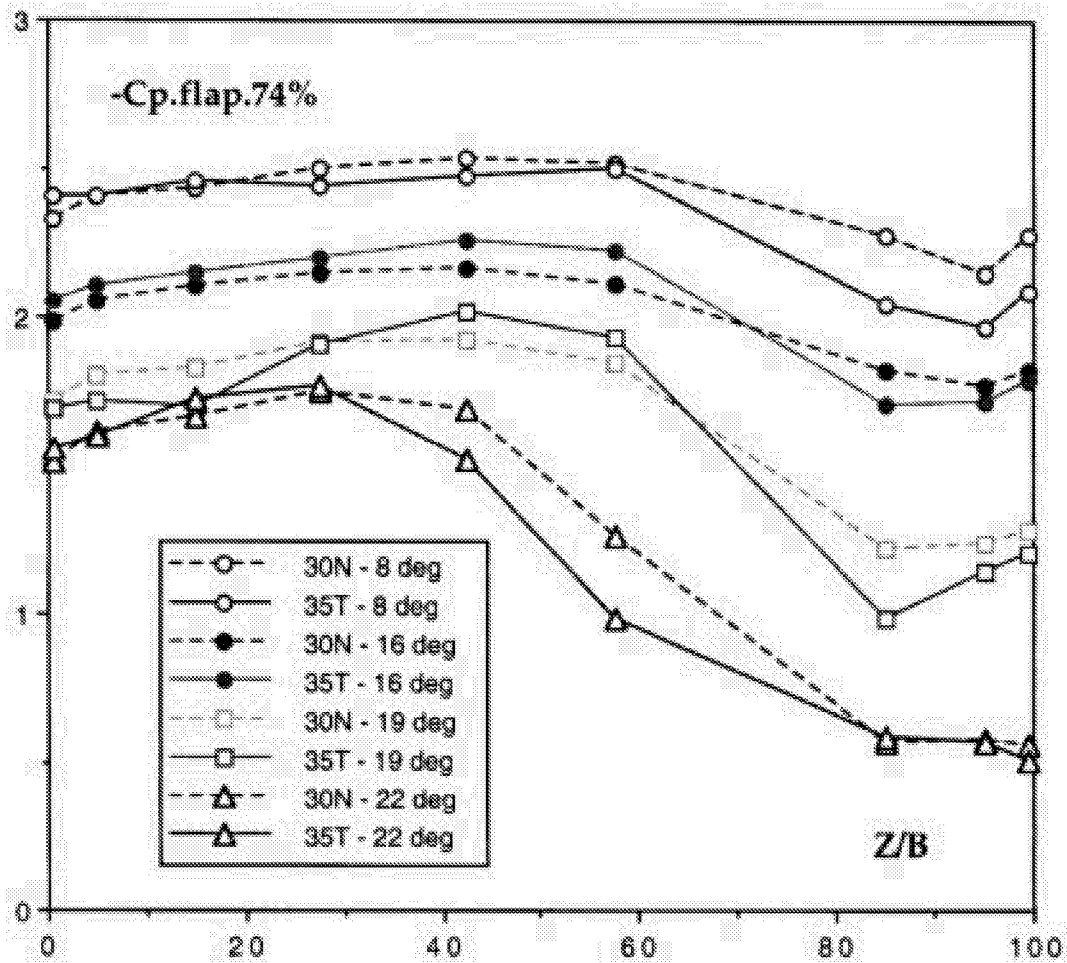


Figure 93c Spanwise pressure distribution
30P/35T Mach=0.2 Re=9 million

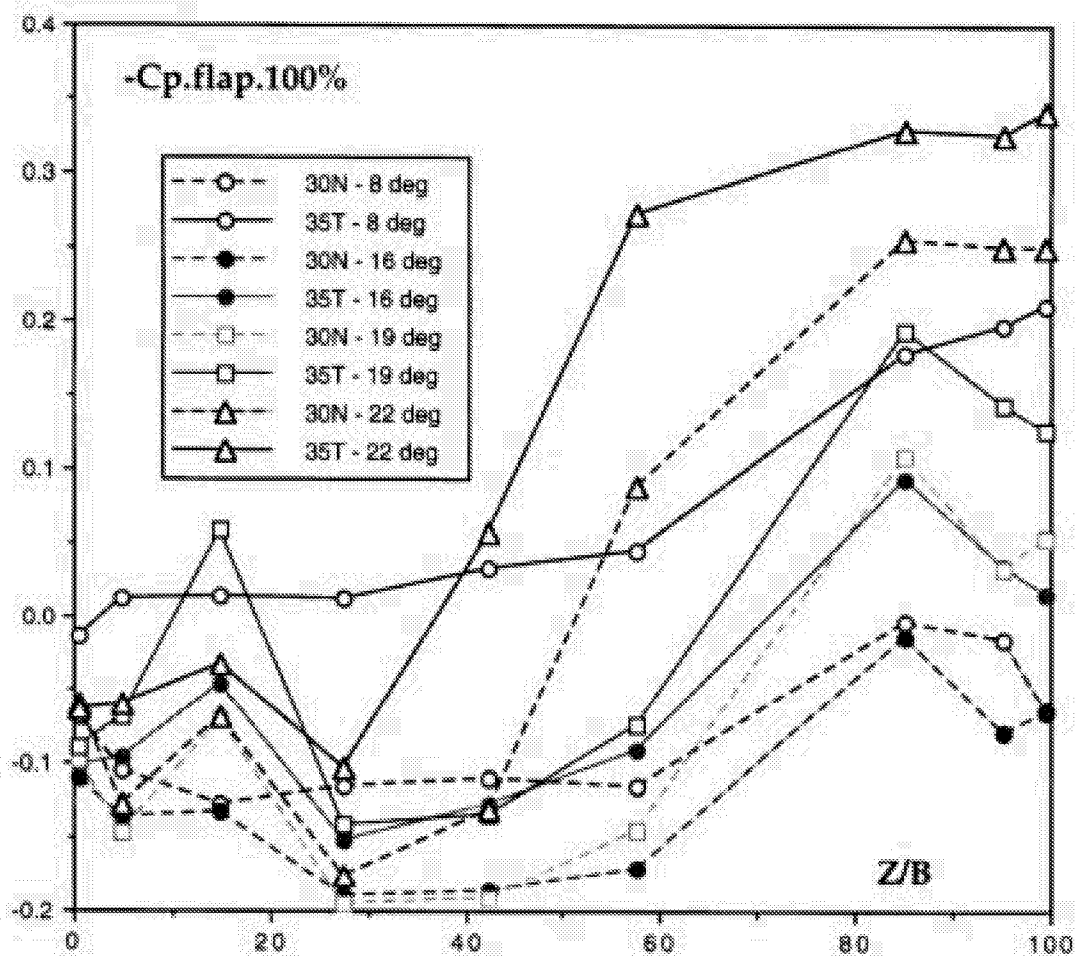


Figure 93d Spanwise pressure distribution
30P/35T Mach=0.2 Re=9 million

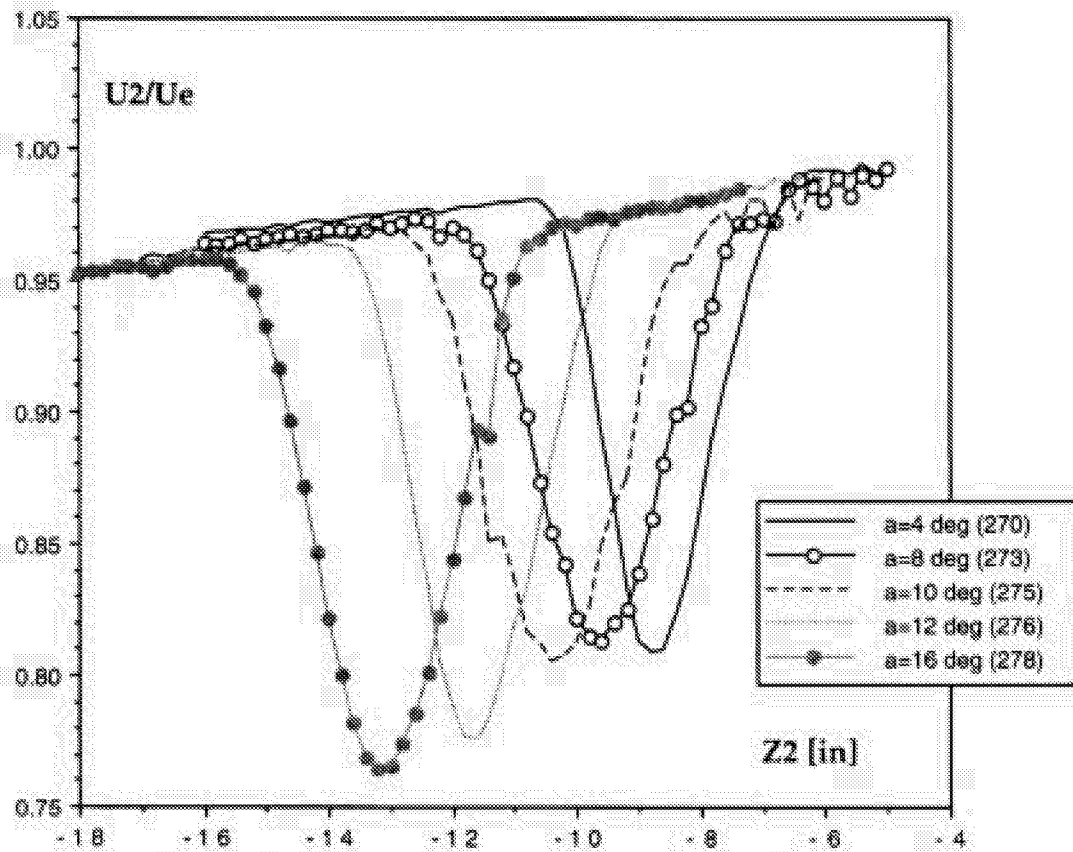


Figure 94a Wake profiles as function of angle-of-attack.
 30P/30AD Mach=0.2 Re=9 million

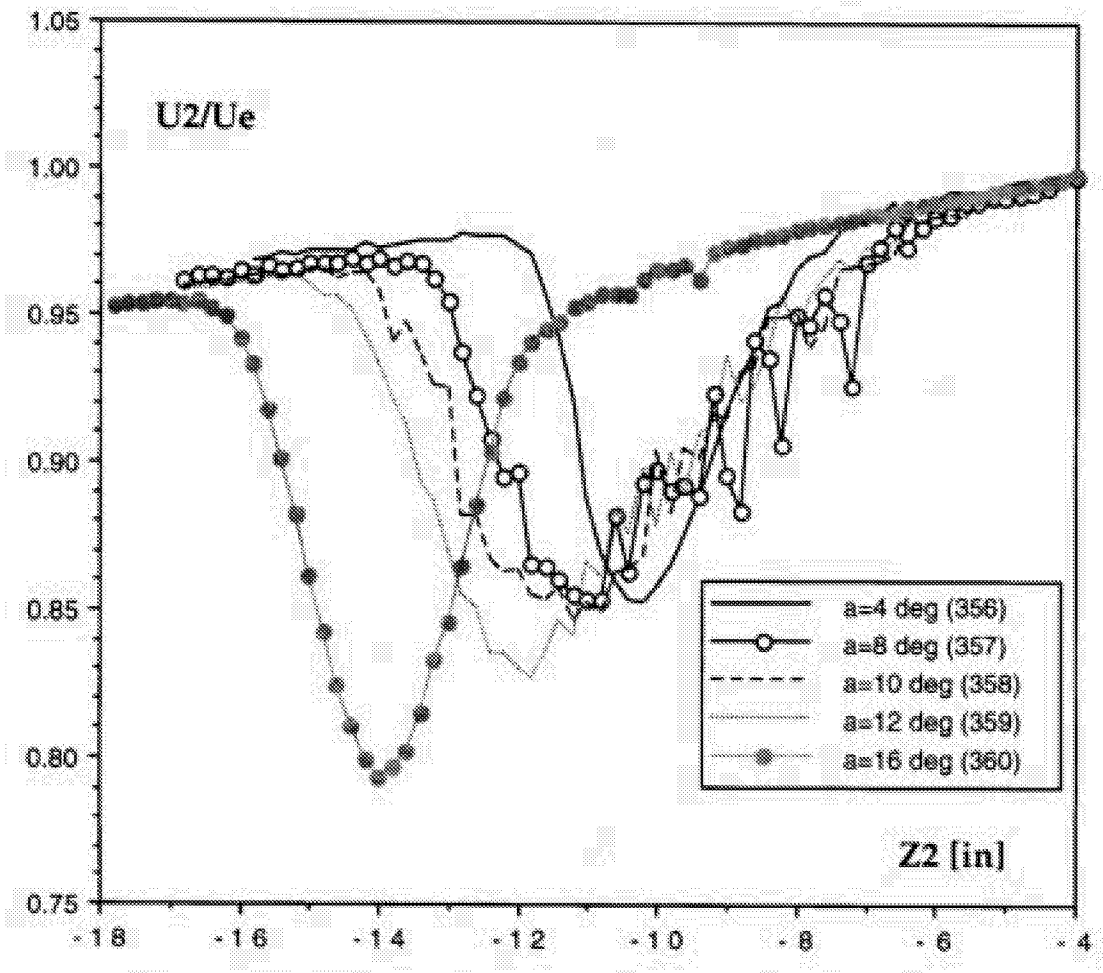


Figure 94b Wake profiles as function of angle-of-attack.
 30P/35T Mach=0.2 Re=9 million

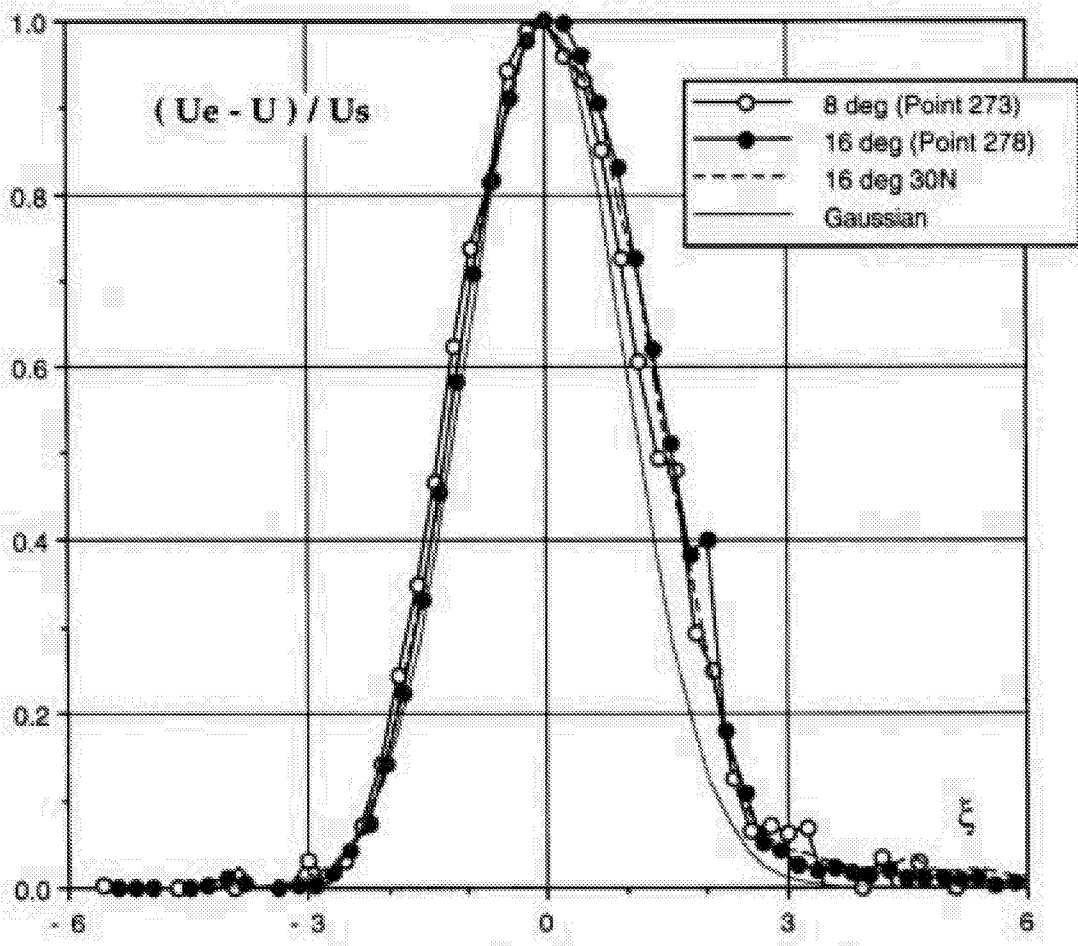


Figure 95a Non-dimensional wake profiles for 30P/30AD
 Comparison with 30P/30N and Gaussian. Mach=0.2 Re=9 million

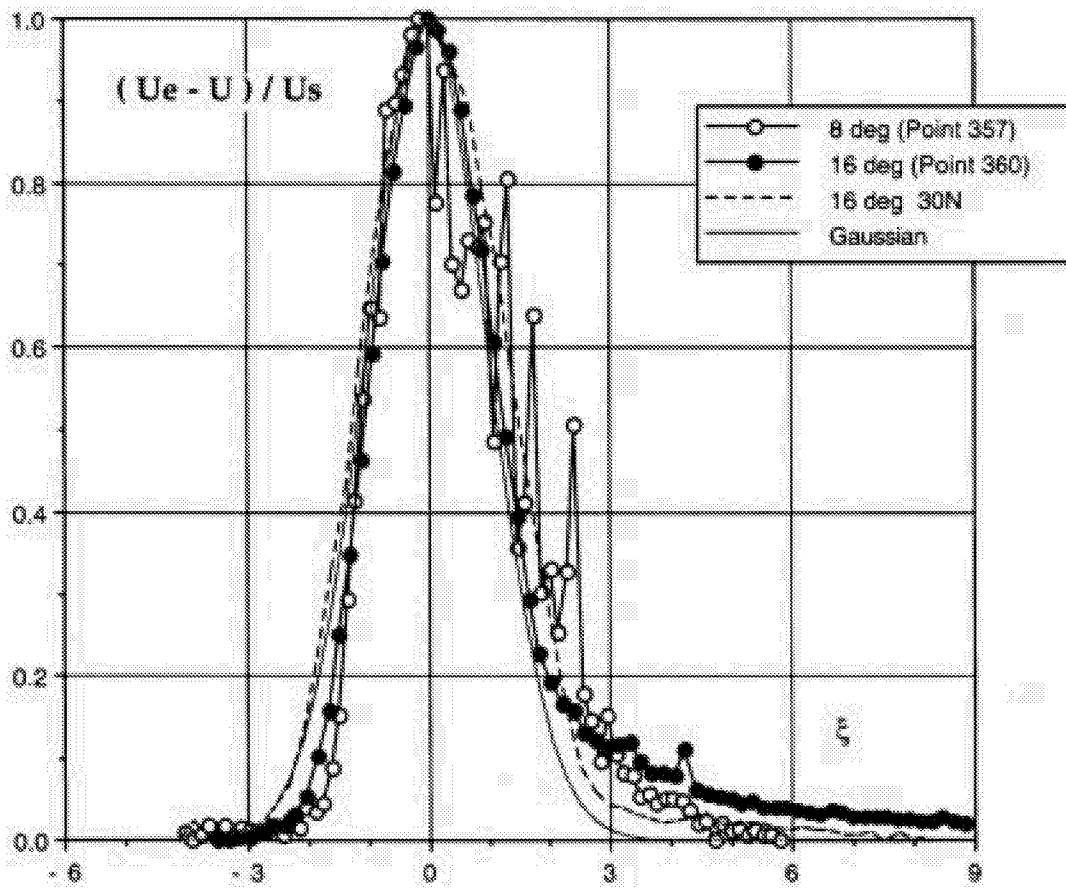


Figure 95b Non-dimensional wake profiles for 30P/35T
 Comparison with 30P/30N and gaussian. Mach=0.2 Re=9 million

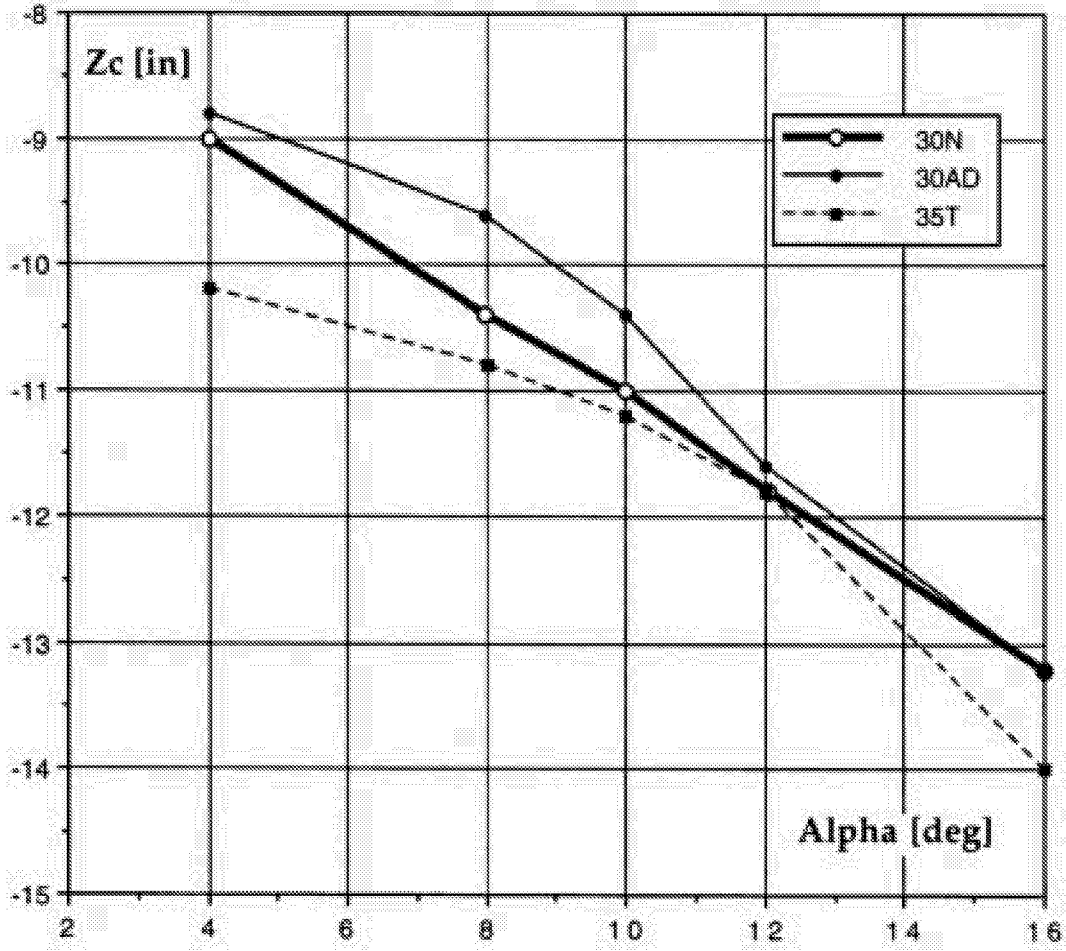


Figure 96 Vertical location (Z_c) of maximum velocity defect (U_s) for all three configurations. Mach=0.2 Re=9 million

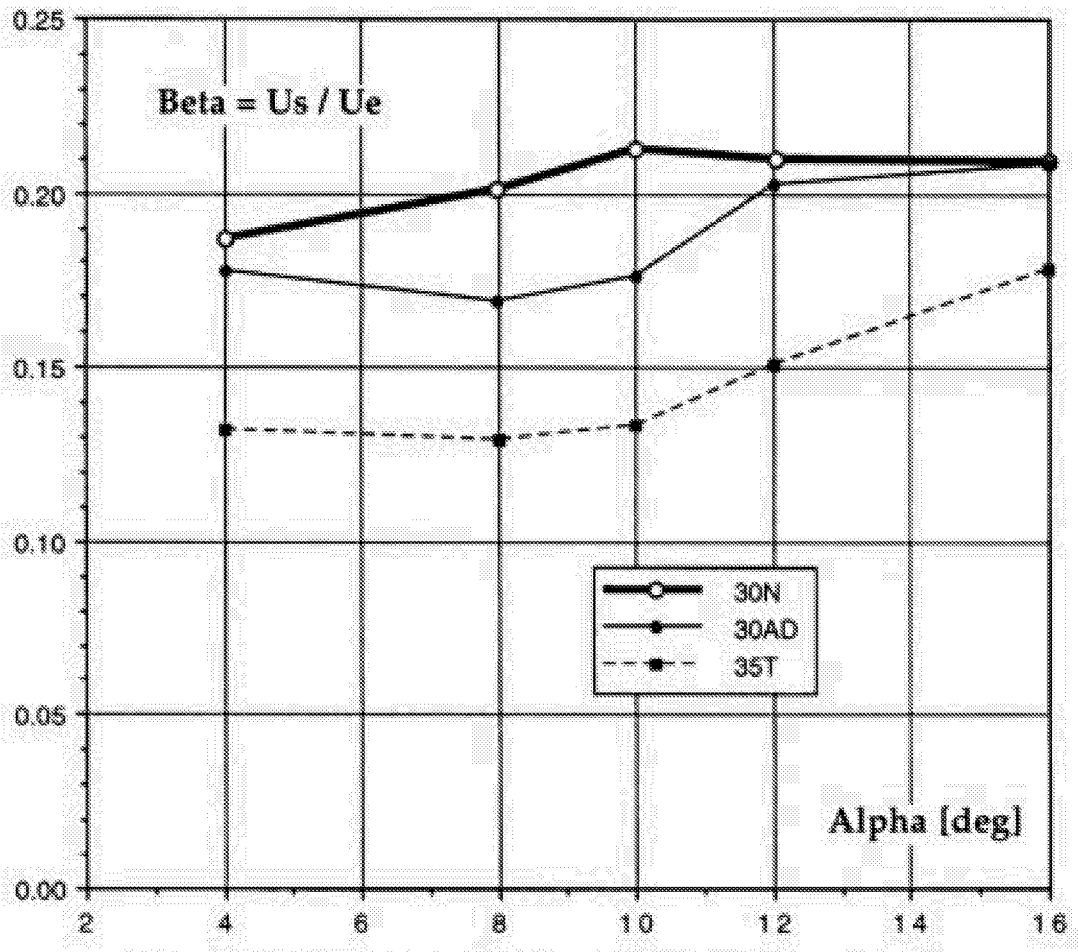


Figure 97 Maximum non-dimensional velocity defect:
 $Beta = (U_{e,c} - U_c) / U_{e,c}$ Mach=0.2 Re=9 million

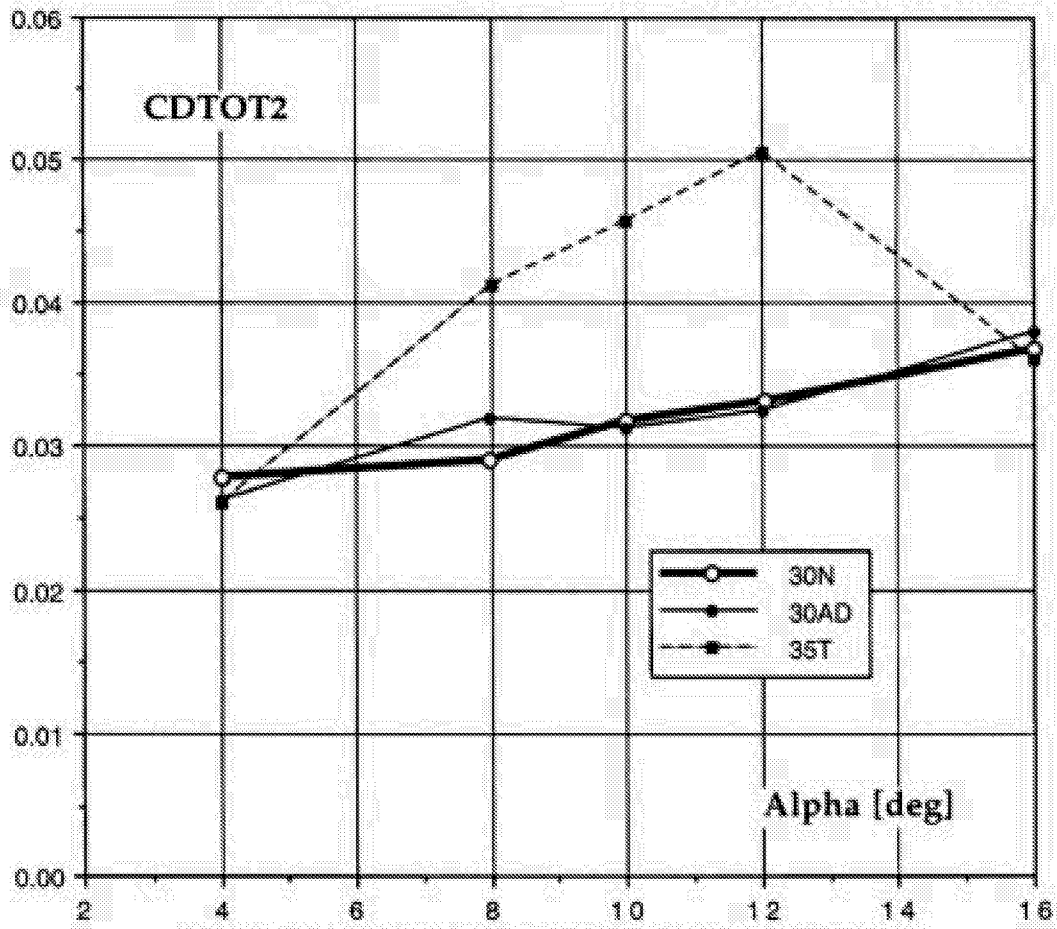


Figure 98 Viscous drag for the three configurations.
Mach=0.2 Re=9 million

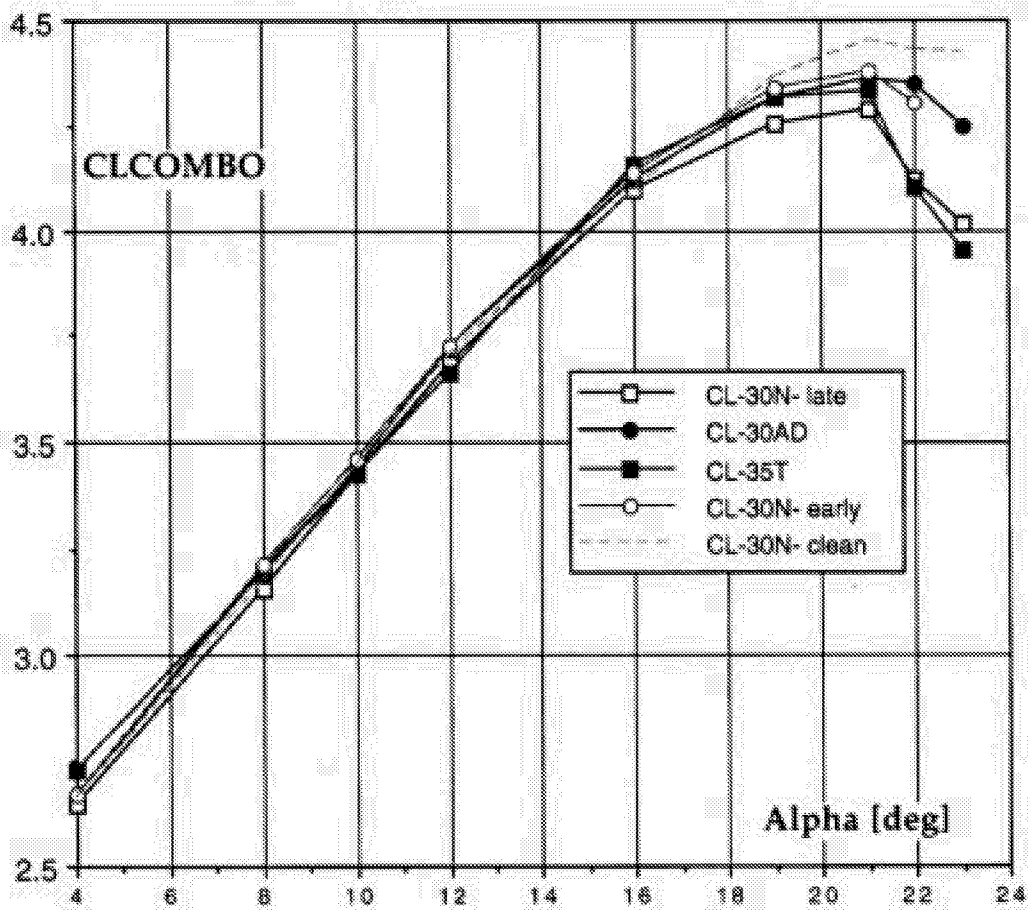


Figure A3.1 Integrated pressure load CLCOMBO for 30P/30N with film and clean as well as the 30AD and 35T configurations. Mach=0.2 Re=9 million

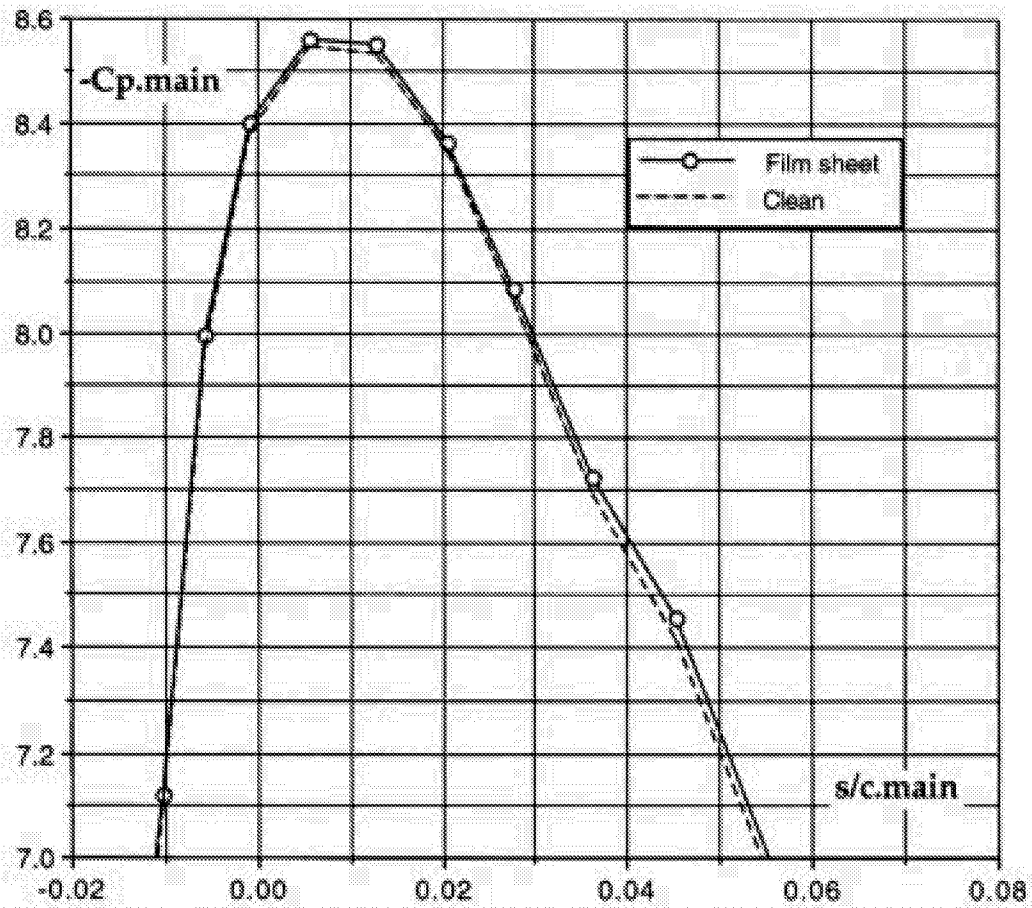


Figure A3.2 Main element pressure distributions, with film sheet and clean. 30P/30N Mach=0.6 Re=9 million. Alpha=16 deg.

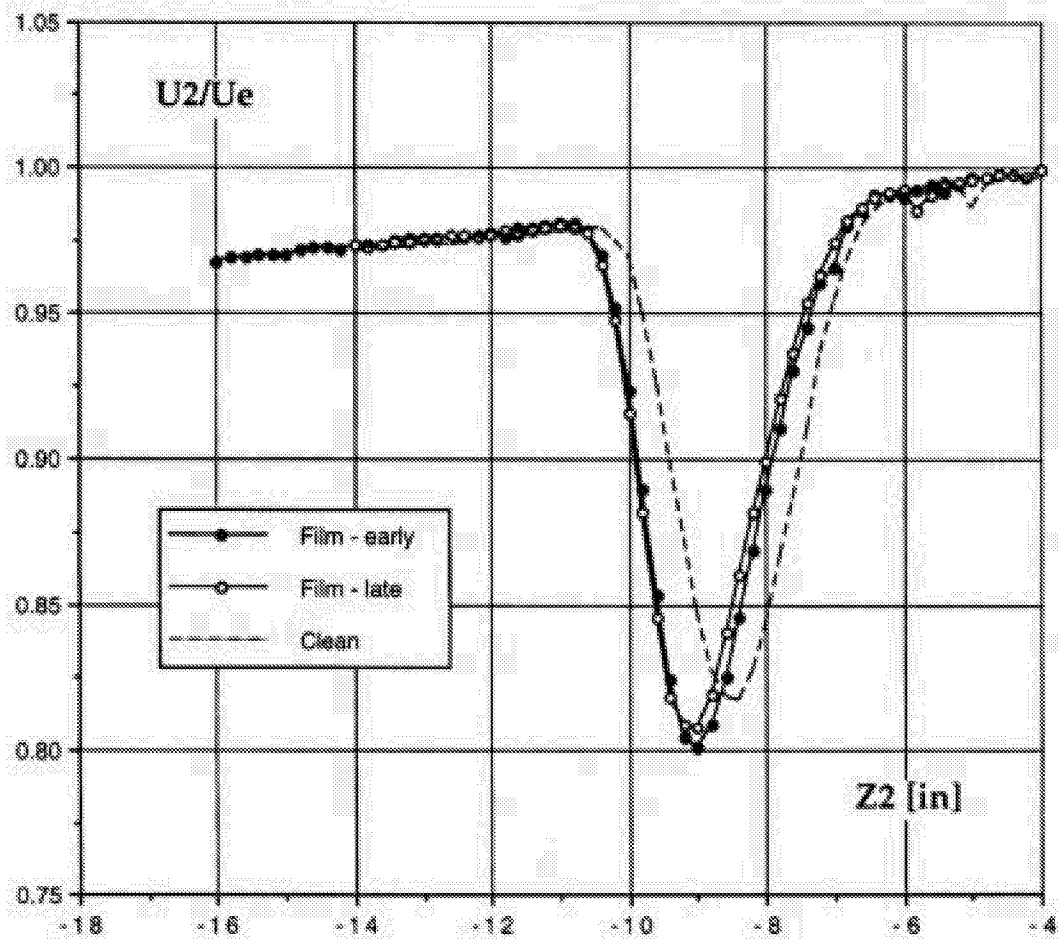


Figure A3.3a Wake profiles. 30P/30N Mach=0.2
 Re=9 million Alpha=4 deg.

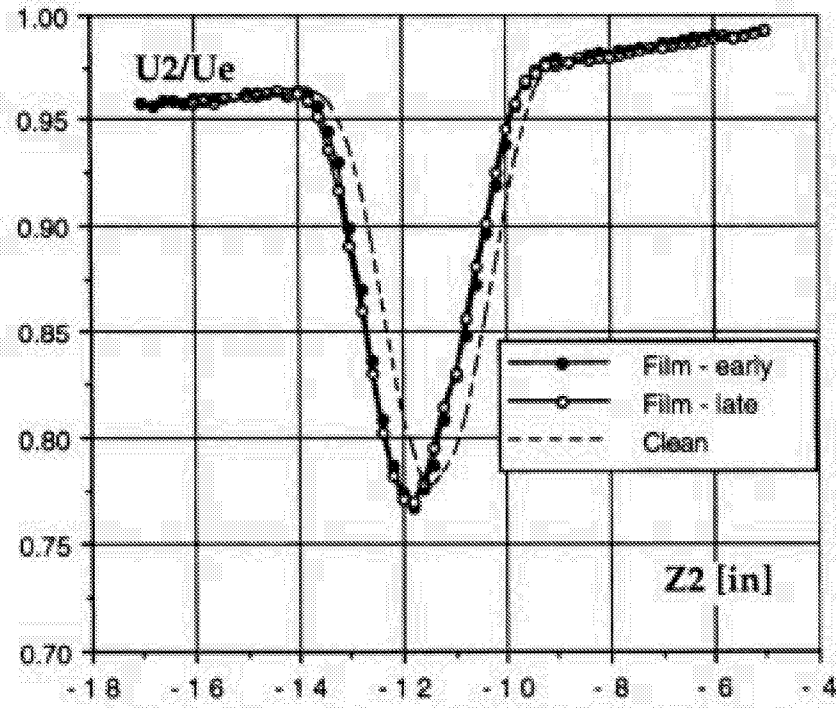


Figure A3.3b Wake profiles. 30P/30N Mach=0.2 Re=9 million. Alpha=12 deg.

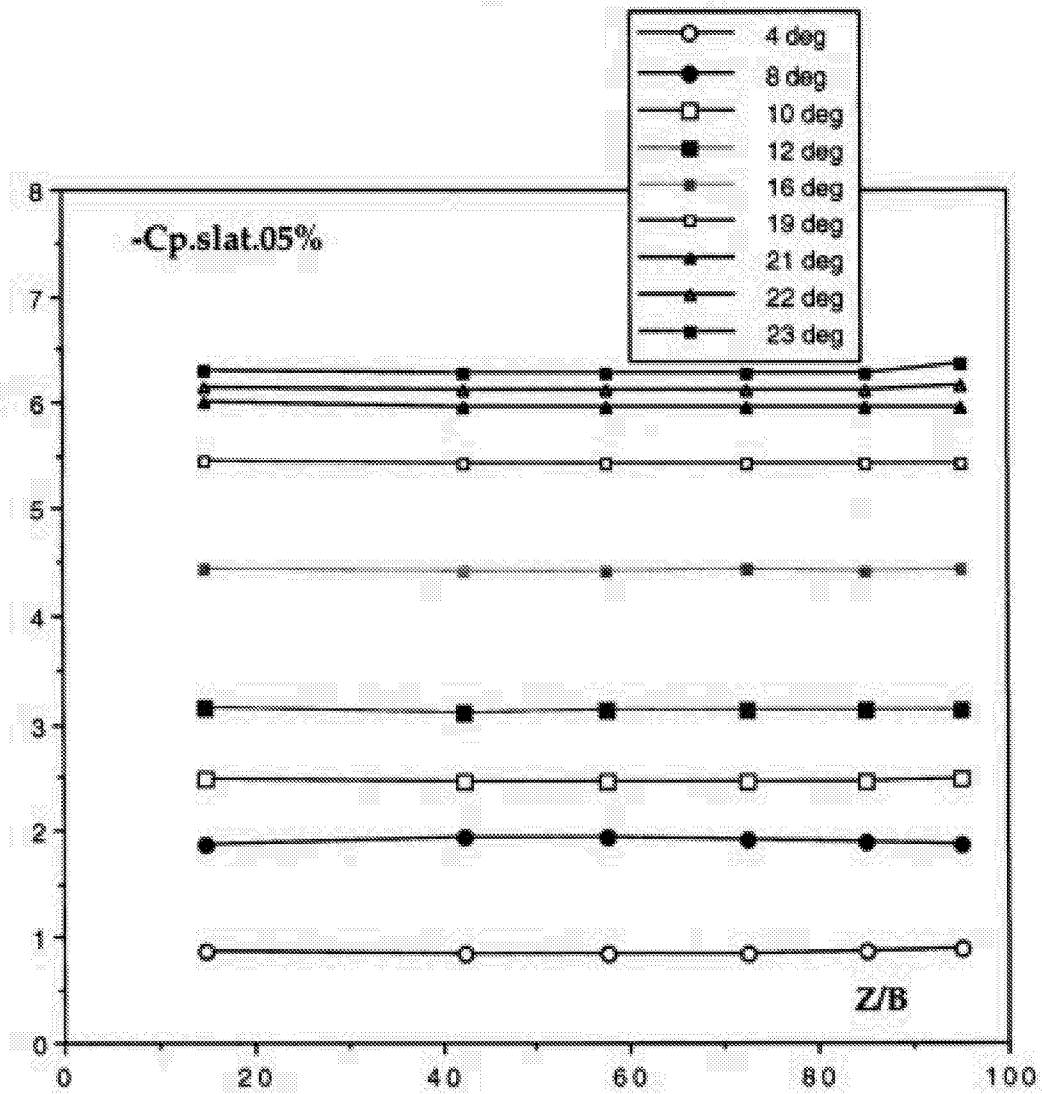


Figure A.3.4a Spanwise pressure distribution - SLAT (CLEAN Polar 71) 30P/30N Mach=0.2, Re = 9 million

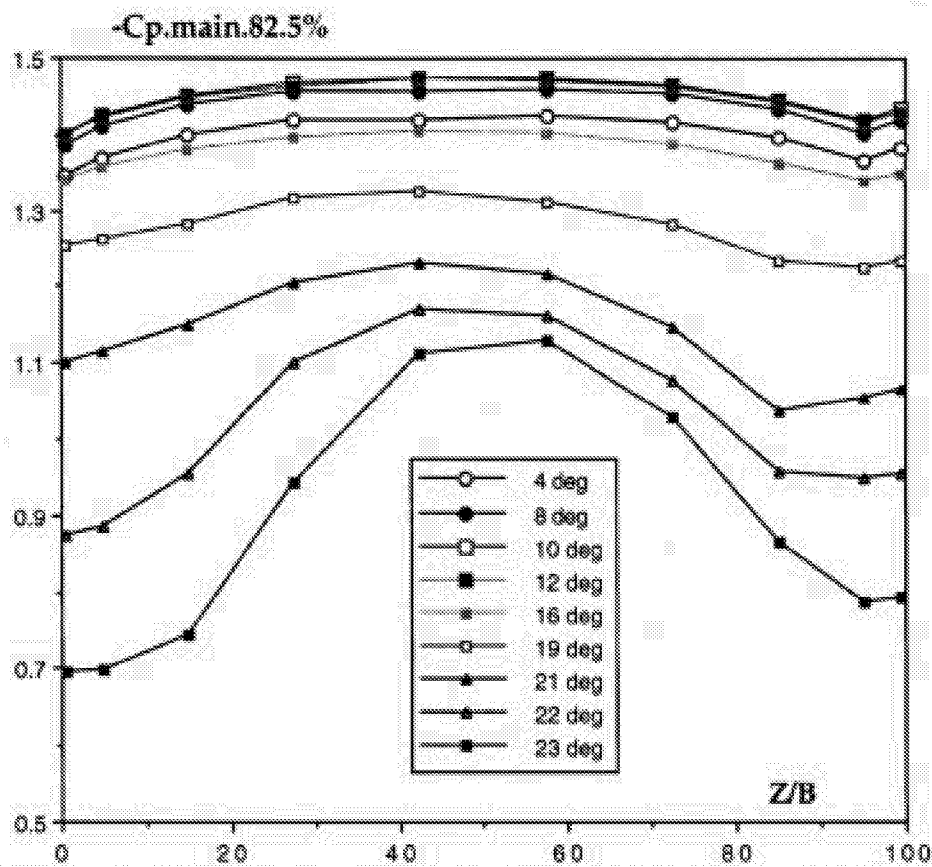


Figure A.3.4b Spanwise pressure distribution - MAIN (82.5%) - CLEAN (Polar 71) 30P/30N Mach=0.2, Re = 9 million

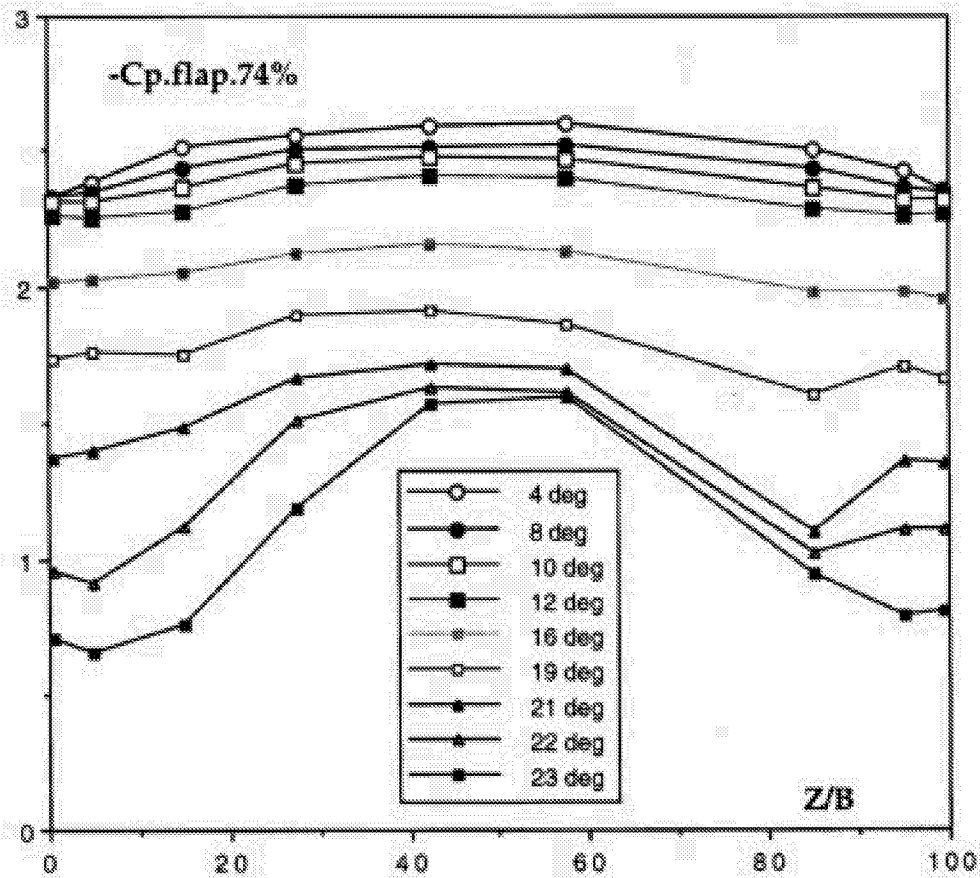


Figure A3.4c Spanwise pressure distribution - FLAP (74%) CLEAN - Polar 71 30P/30N Mach=0.2, Re = 9 million

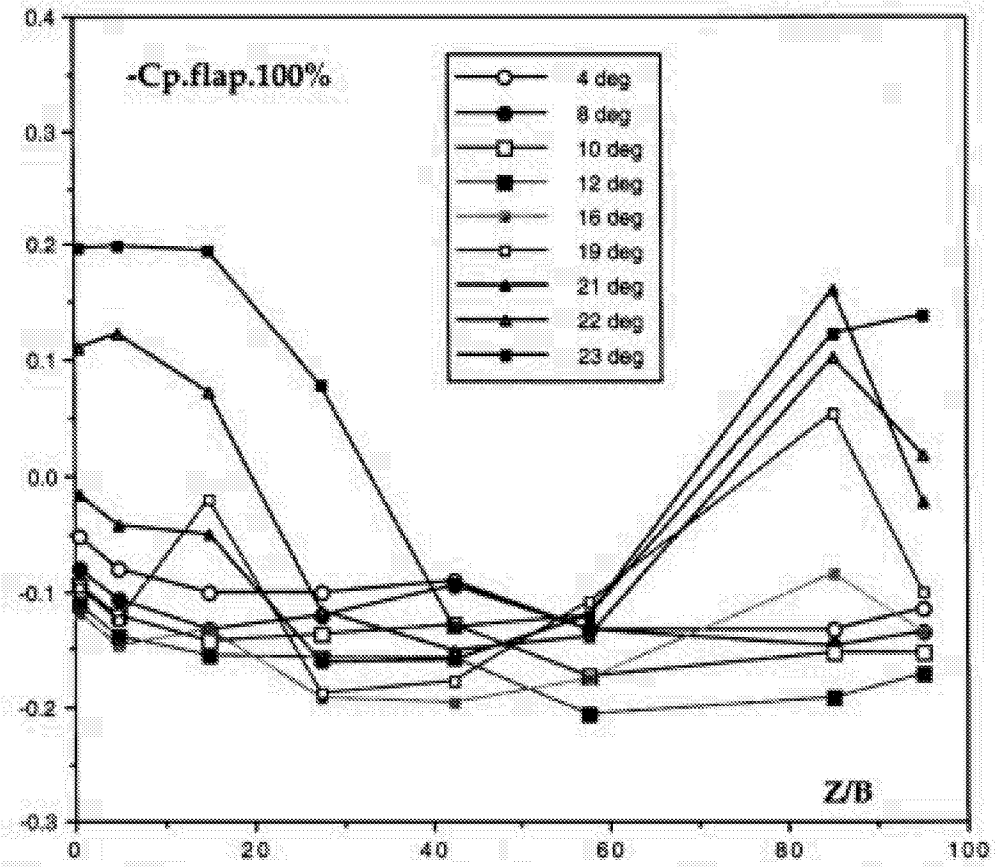


Figure A3.4d Spanwise pressure distribution - FLAP 100% - CLEAN (Polar 71) 30P/30N Mach=0.2, Re = 9 million

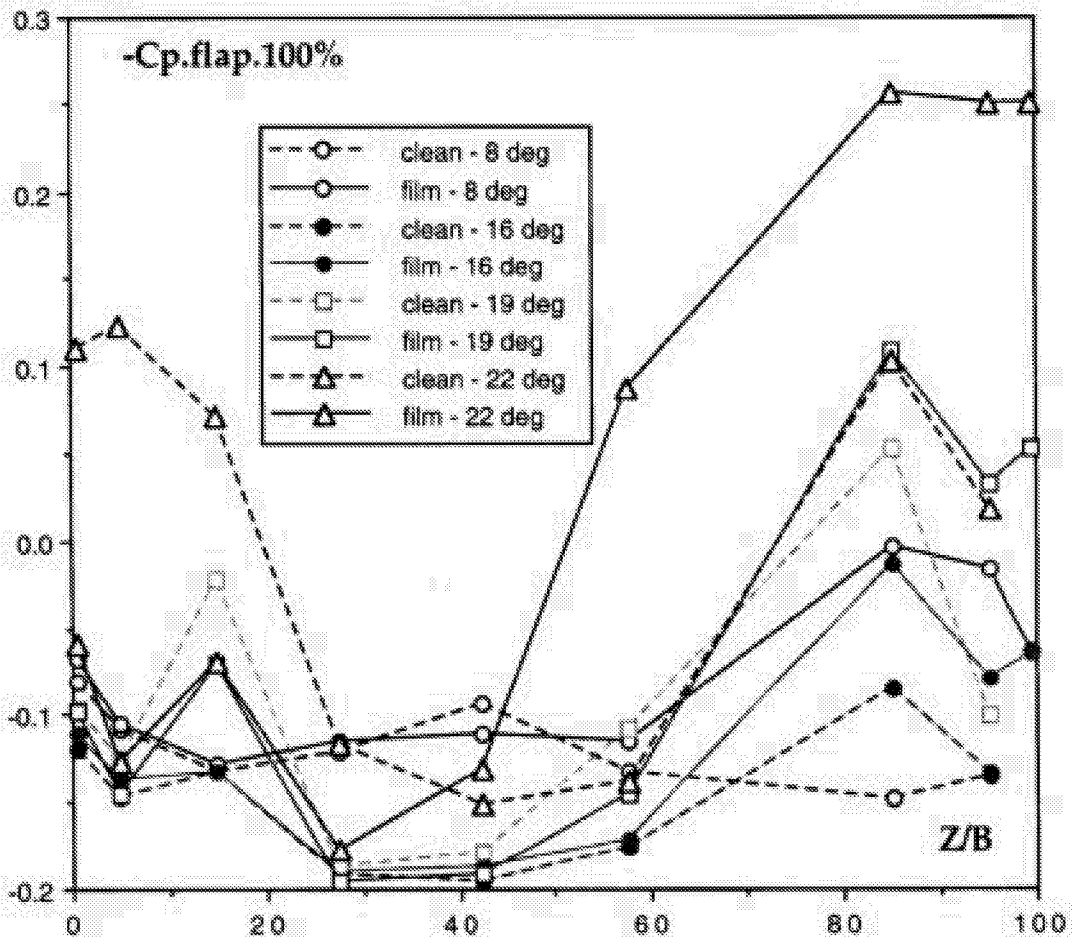


Figure A3.5a 30P/30N Spanwise pressure distributions with hot film sheet and clean. Mach=0.2 Re=9 million

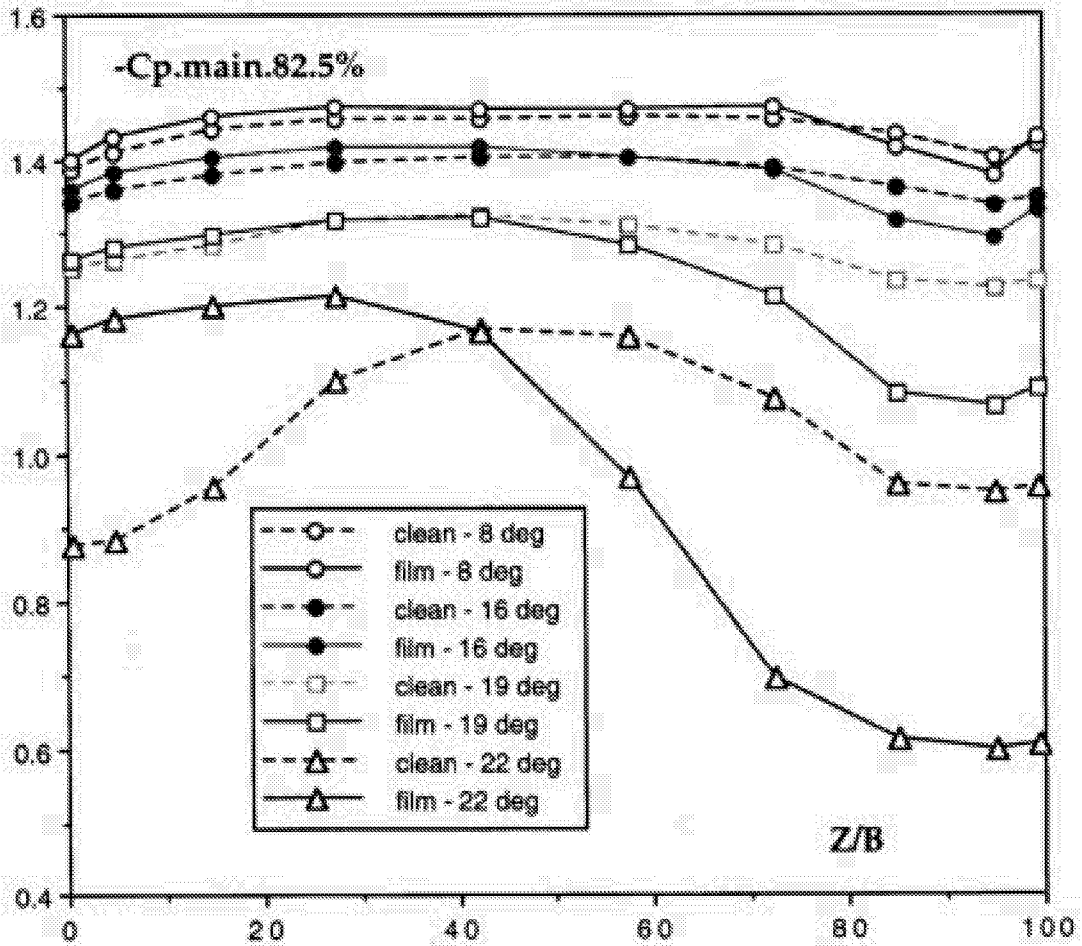


Figure A3.5b 30P/30N Spanwise pressure distributions with hot film sheet and clean. Mach=0.2 Re=9 million

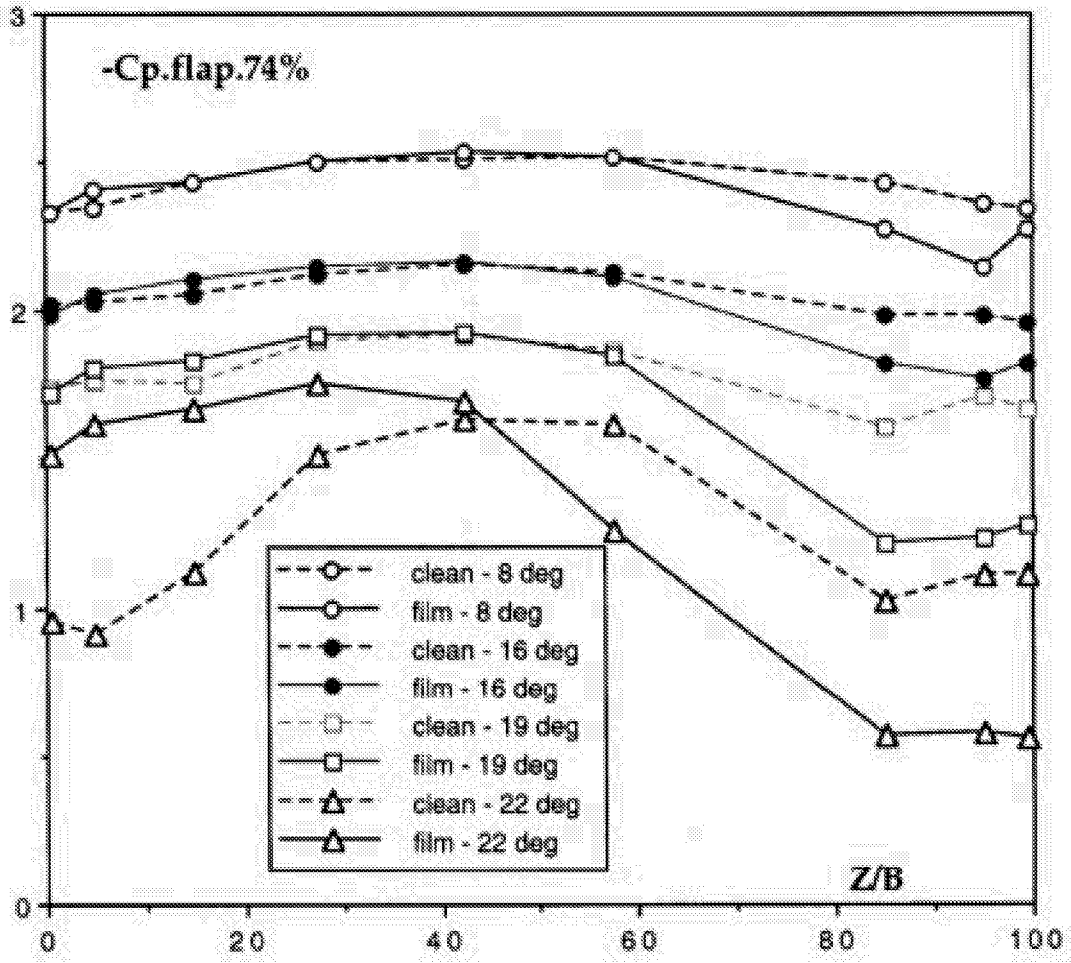


Figure A3.5c 30P/30N Spanwise pressure distributions with hot film sheet and clean. Mach=0.2 Re=9 million

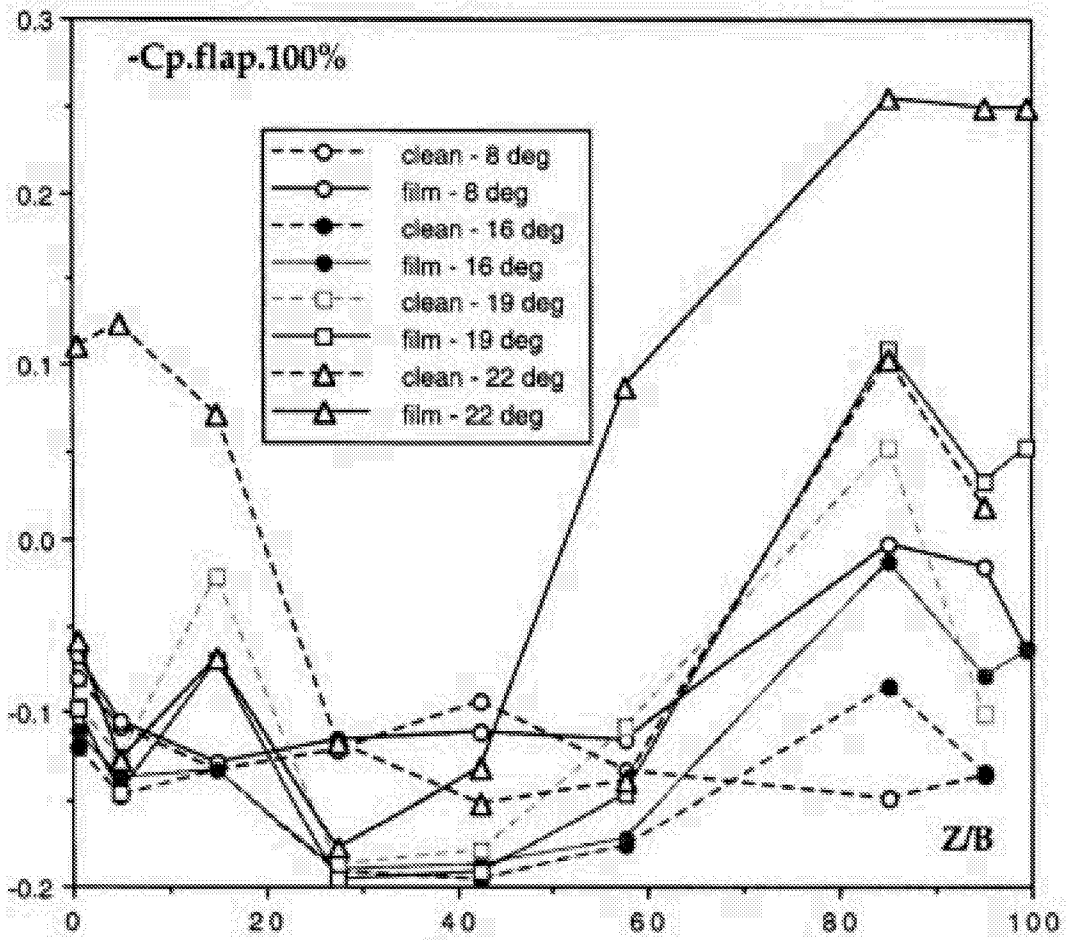


Figure A3.5d 30P/30N Spanwise pressure distributions with hot film sheet and clean. Mach=0.2 Re=9 million

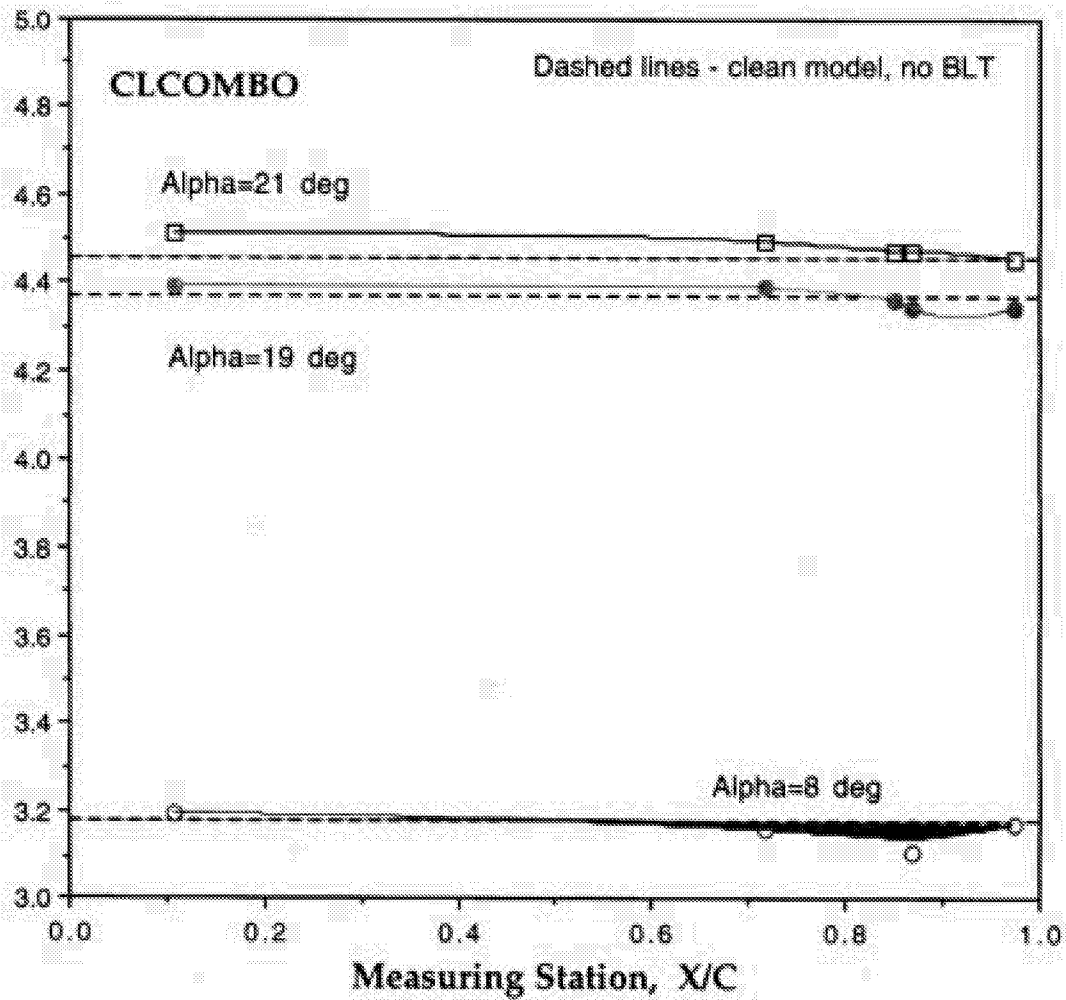


Figure A3.6 Effect of BLT (Boundary Layer Traverse) mechanism on integrated midspan pressure, CLCOMBO

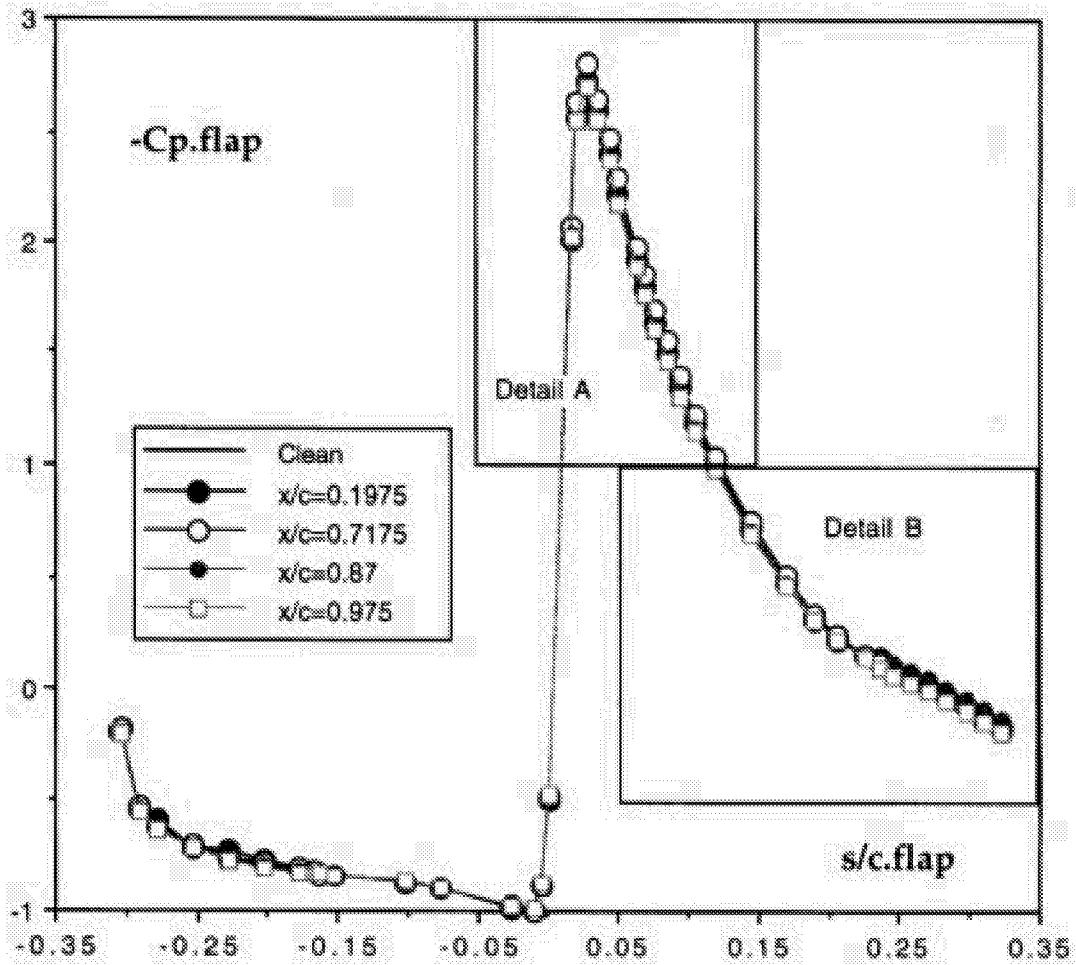


Figure A3.7 Effect of BLT on pressure distributions
 30P/30N Mach=0.2 Re=9 mill Alpha=19 degrees

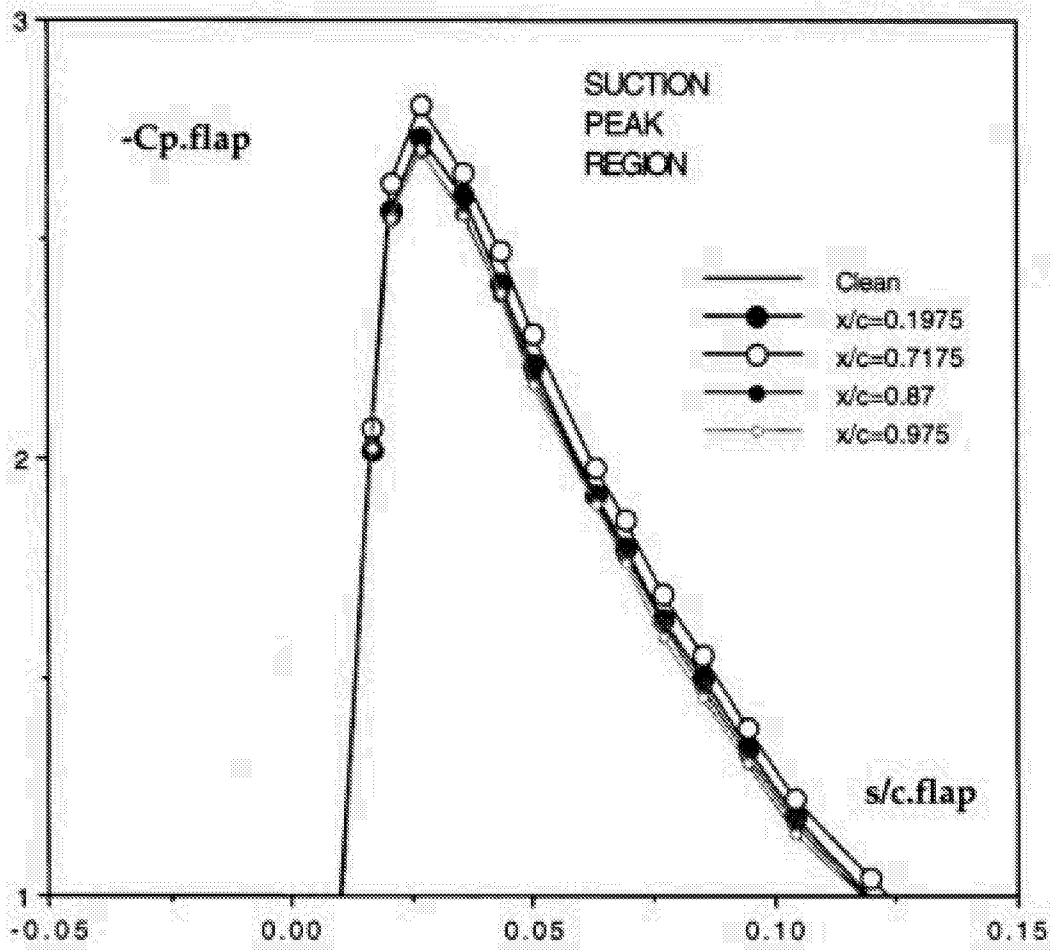


Figure A3.8a Effect of BLT on pressure distributions
 30P/30N Mach=0.2 Re=9 mill Alpha=19 degrees

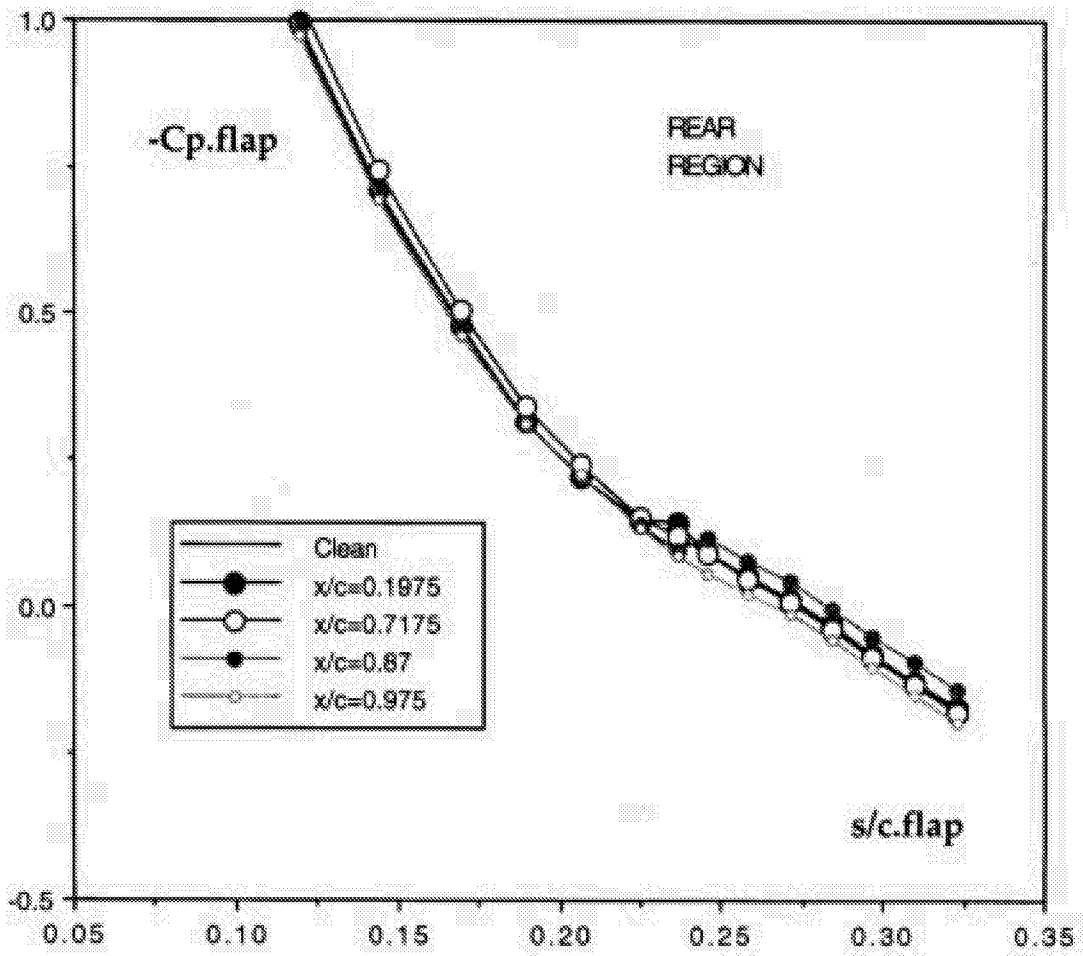


Figure A3.8b Effect of BLT on pressure distributions
 30P/30N Mach=0.2 Re=9 mill Alpha=19 degrees

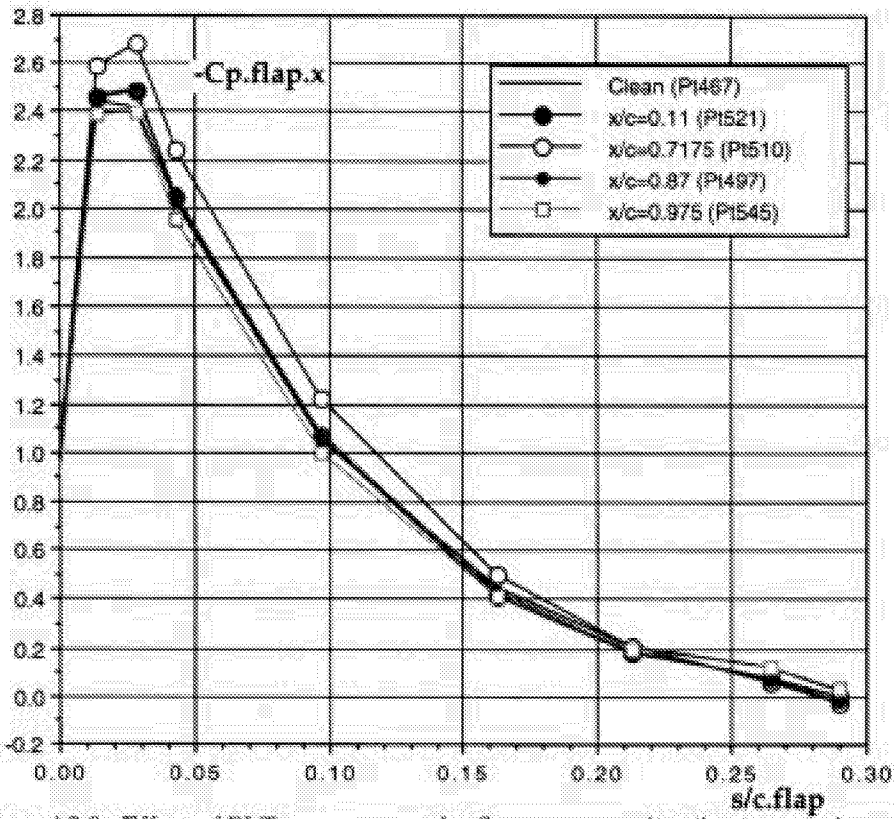


Figure A3.9 Effect of BLT presence on the flap pressure distributions at the auxiliary row, for various positions, x/c , of the BLT. 30P/30N Mach=0.2 Re=9 mill. Alpha=19 deg. x/c denotes chordwise location of BLT.

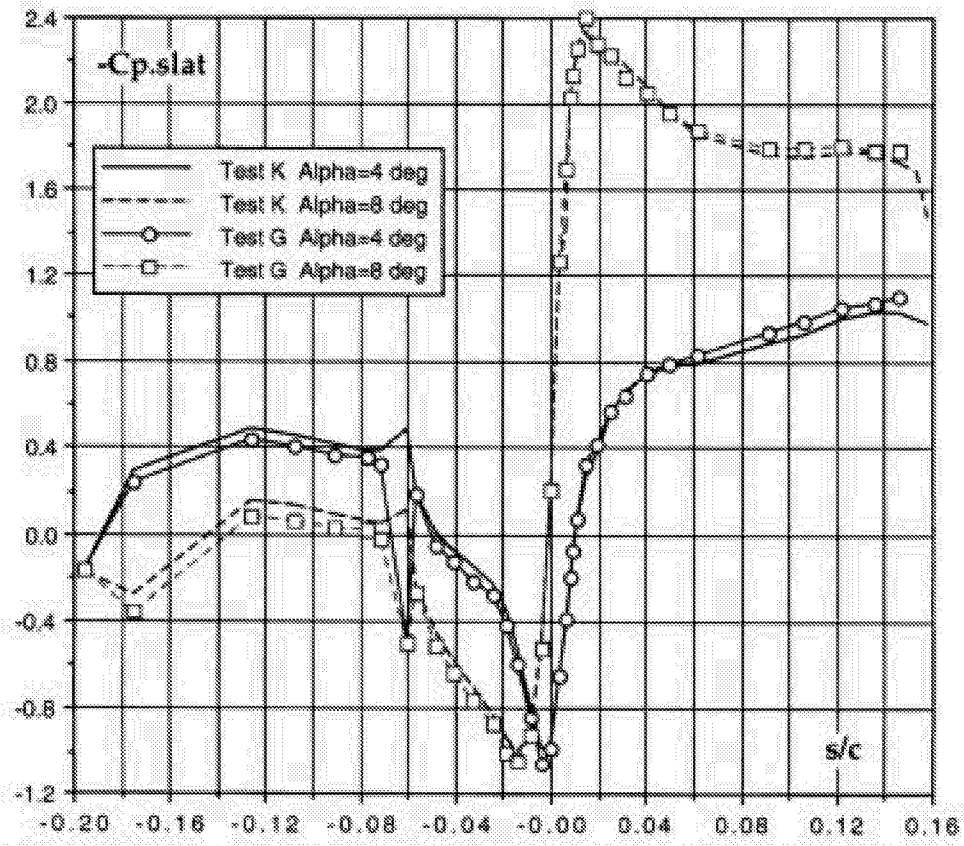


Figure A3.10 Comparison of slat pressure distributions, Test G and Test K (current). 30P/30N Mach=0.2 Re=9 mill.

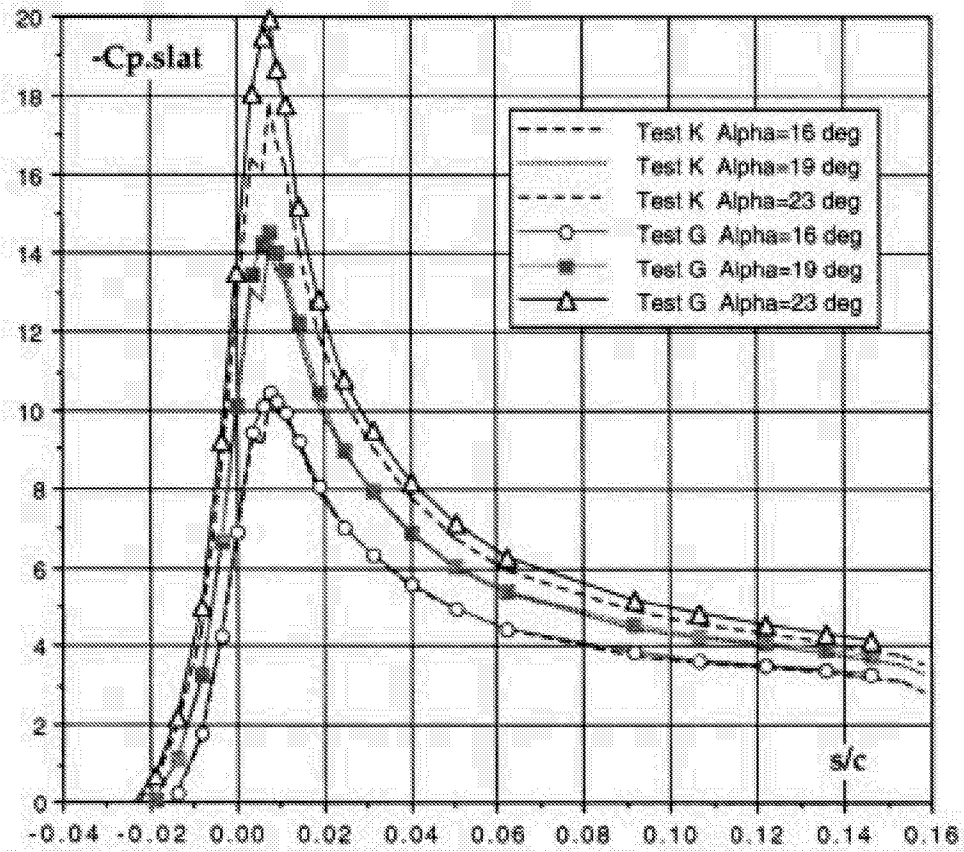


Figure A3.11 Comparison of slat pressure distributions, Test G and Test K (current). 30P/30N Mach=0.2 Re=9 mill. High Alpha.

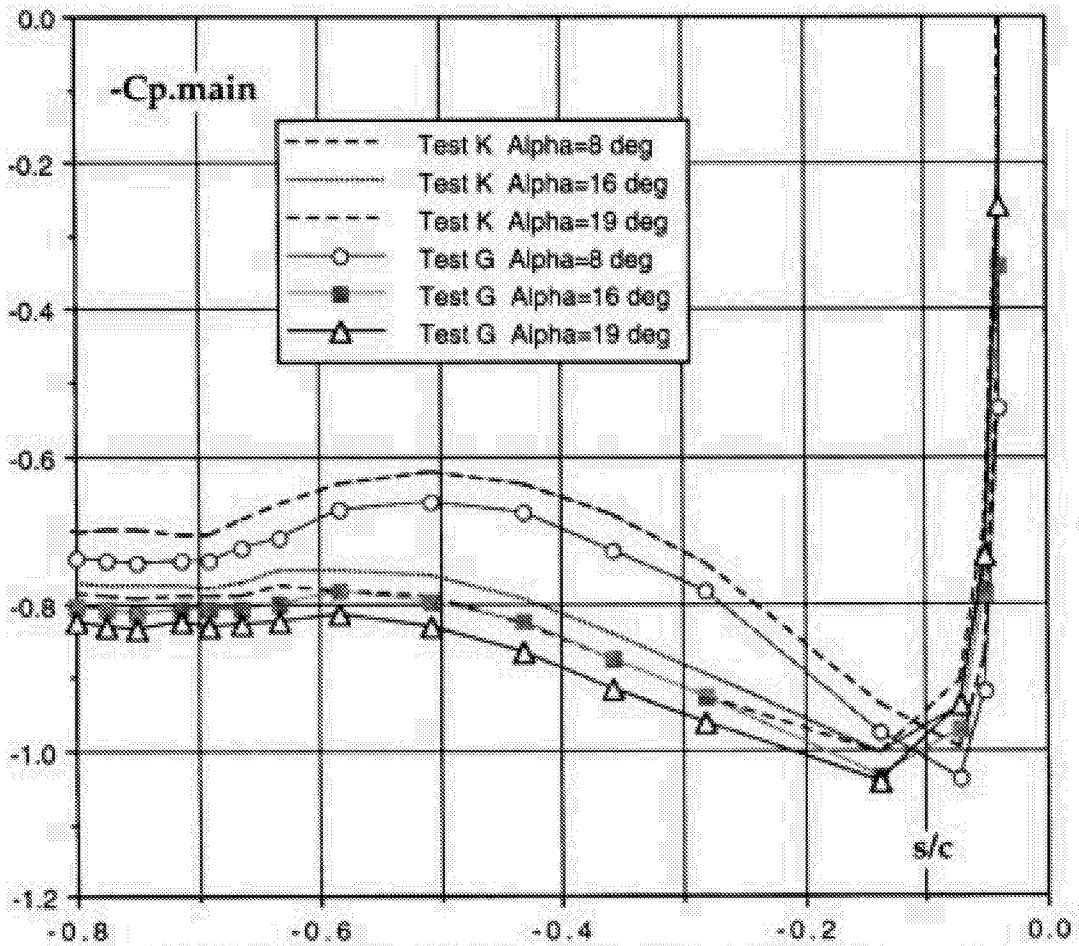


Figure A3.12a Pressure distributions on main element, lower side, Tests G and K (current). 30P/30N mach=0.2 Re=9 mill.

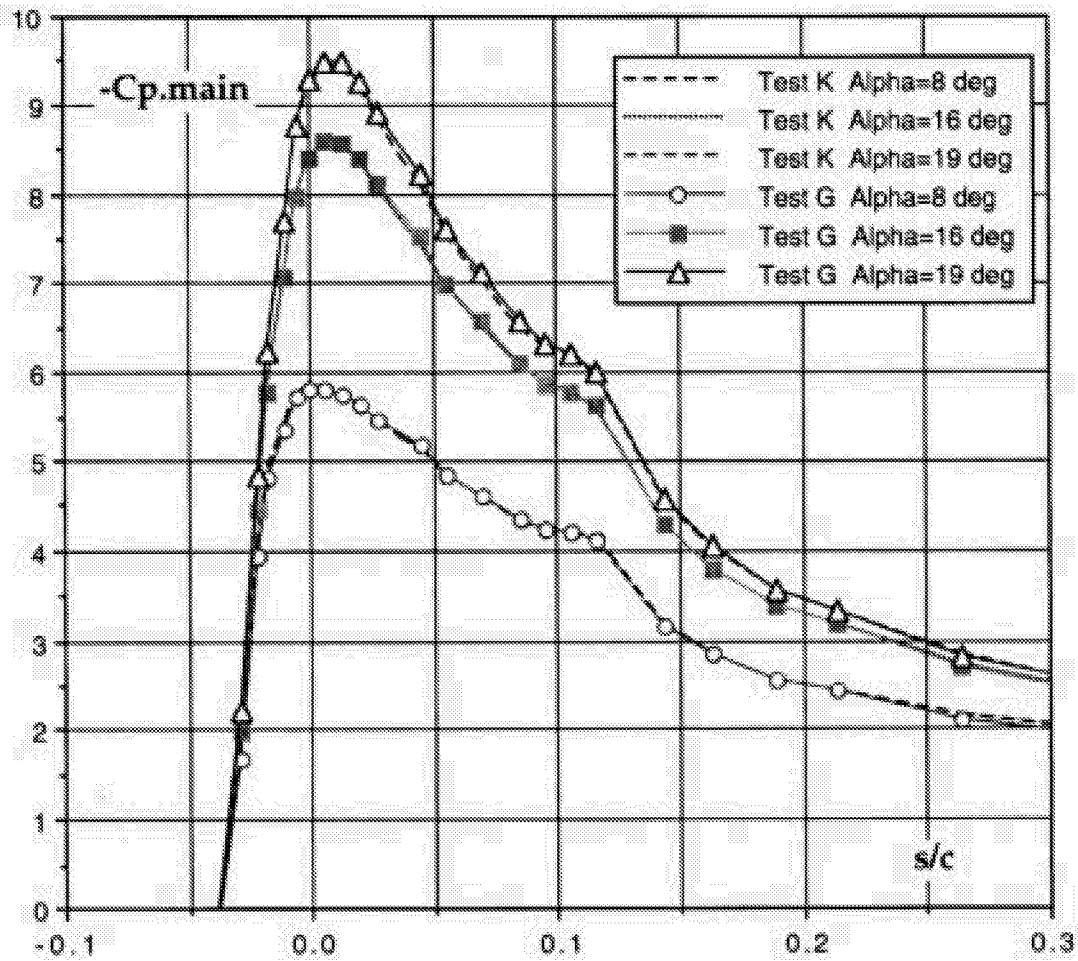


Figure A3.12b Pressure distributions on main element, suction peak, Tests G and K (current). 30P/30N Mach=0.2 Re=9 mill.

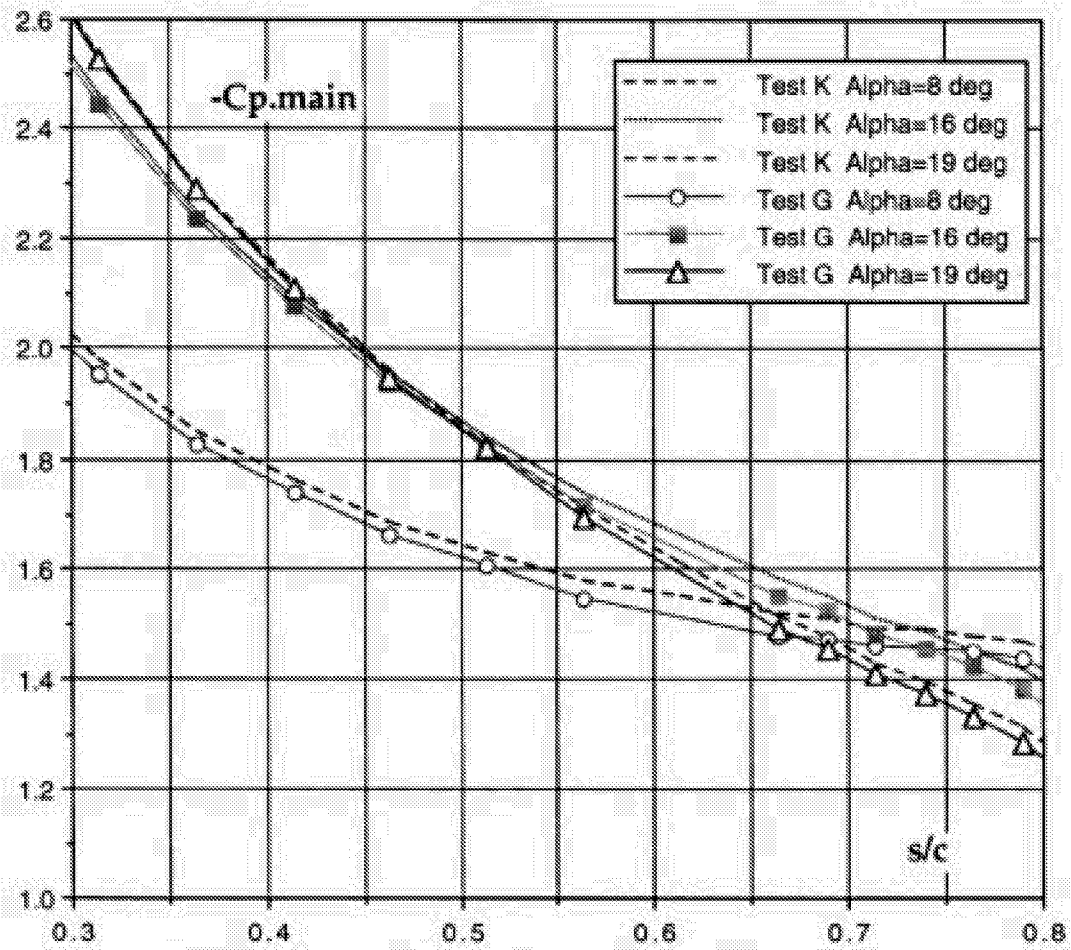


Figure A3.12c Pressure distributions on main element, rear upper, Tests G and K (current). 30P/30N Mach=0.2 Re=9 mill.

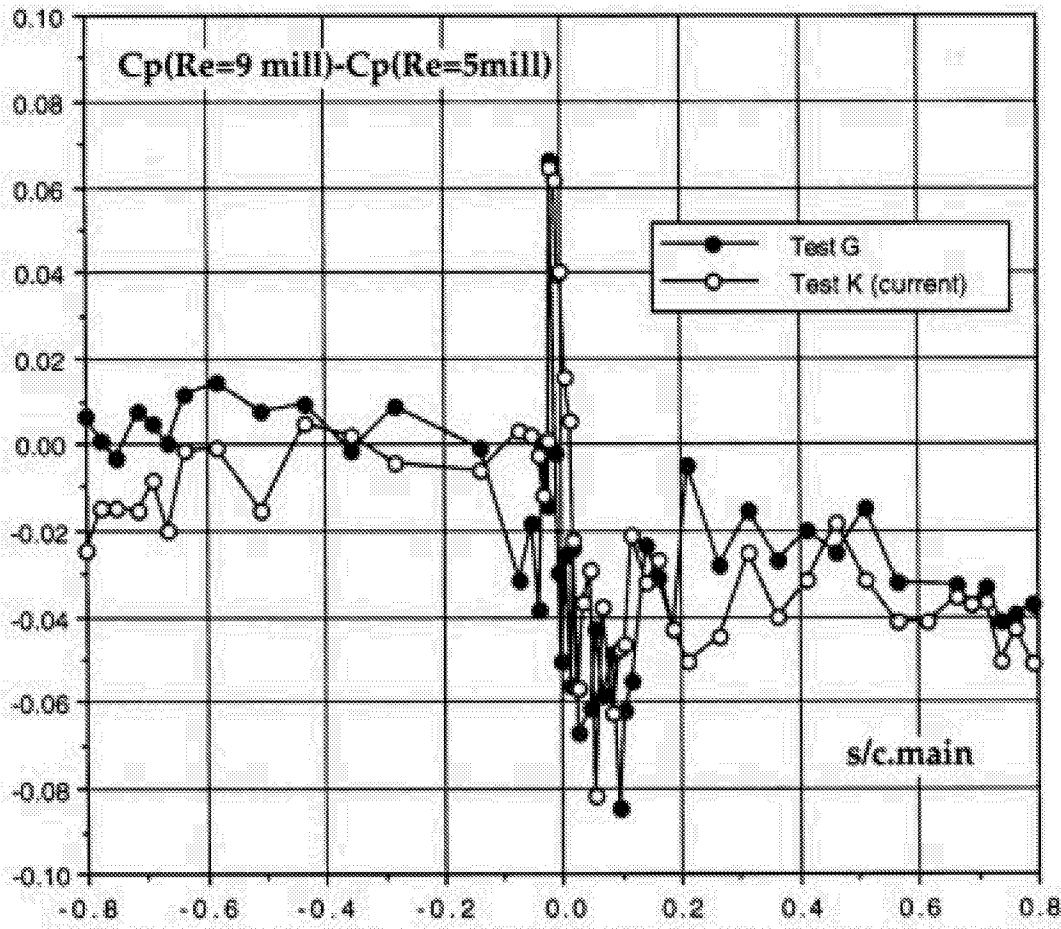


Figure A3.13a Pressure distribution difference between Re=9 and 5 mill. for tests G and K. 30P/30N Mach=0.2 Alpha=8 deg.

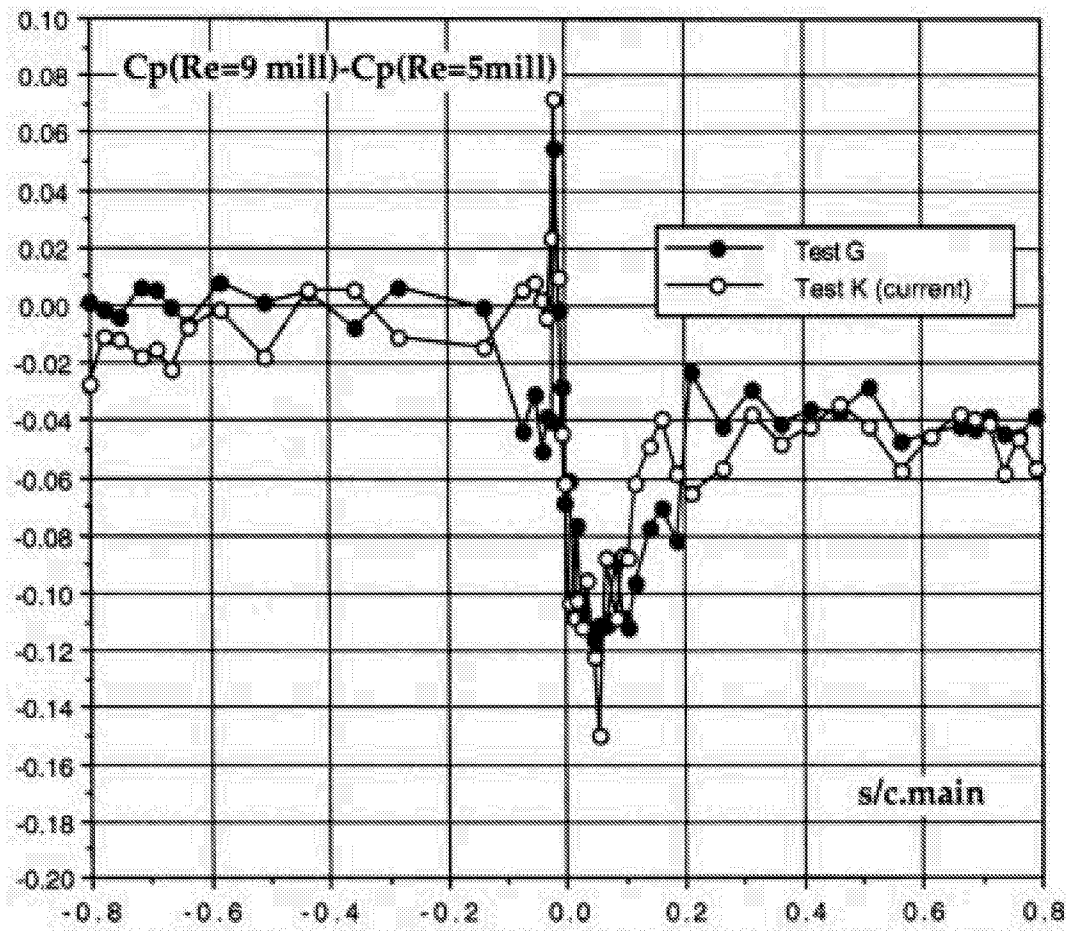


Figure A3.13b Pressure distribution difference between Re=9 and 5 mill. for tests G and K. 30P/30N Mach=0.2 Alpha=19 deg.

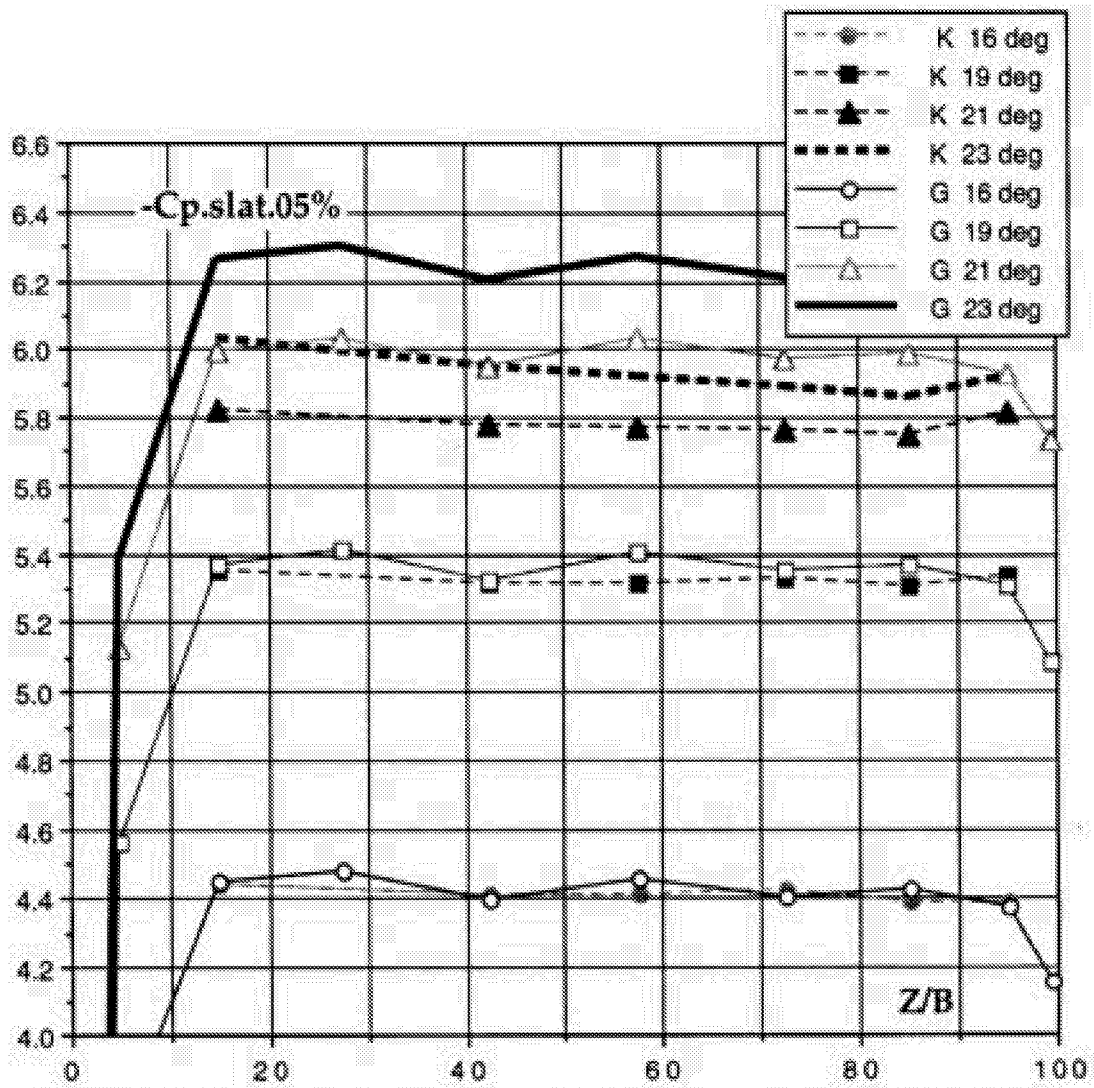


Figure A3.14a Spanwise pressure distributions, tests G and K - SLAT 30P/30N Mach=0.2, Re = 9 million

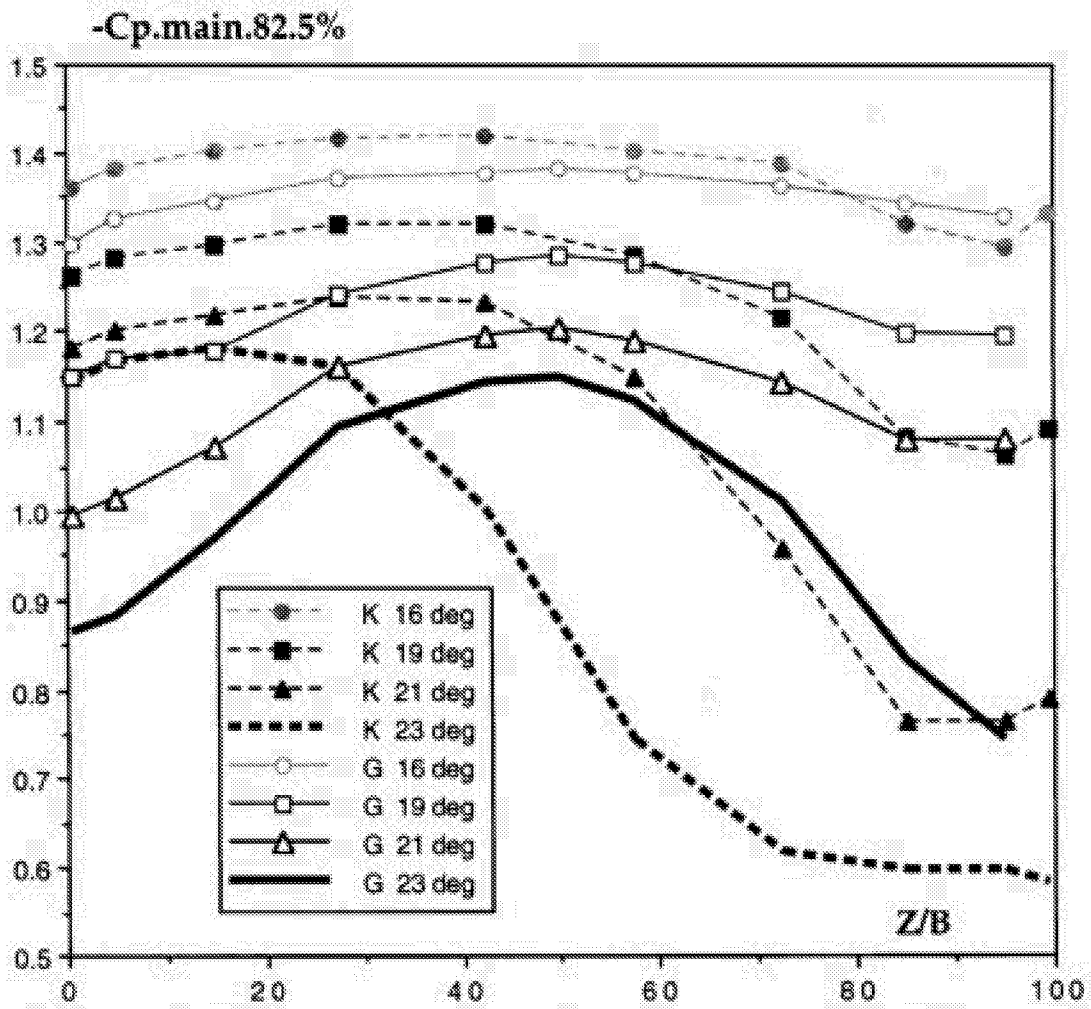


Figure A3.14b Spanwise pressure distribution, tests G and K - MAIN (82.5% stowed chord) 30P/30N Mach=0.2, Re = 9 million

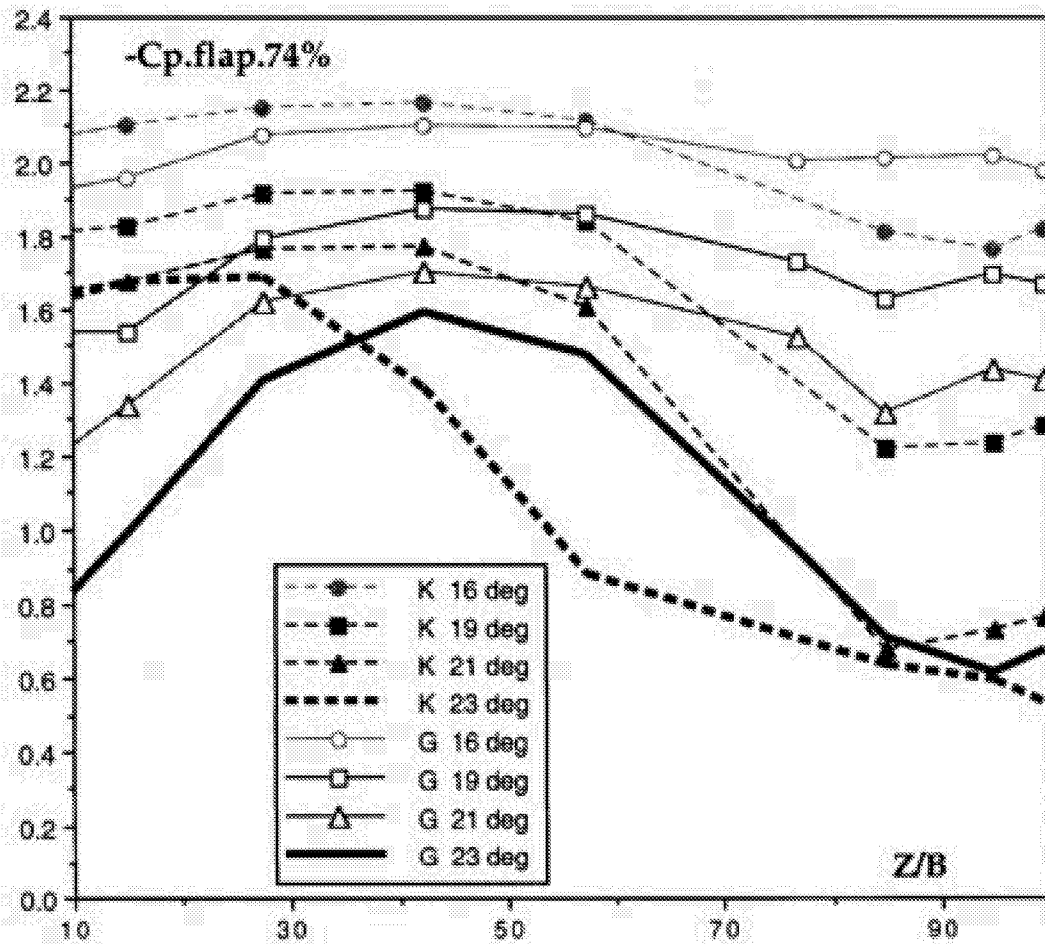


Figure A3.14c Spanwise pressure distribution, tests G and K -FLAP (74 % stowed coordinate) 30P/30N Mach=0.2, Re = 9 million

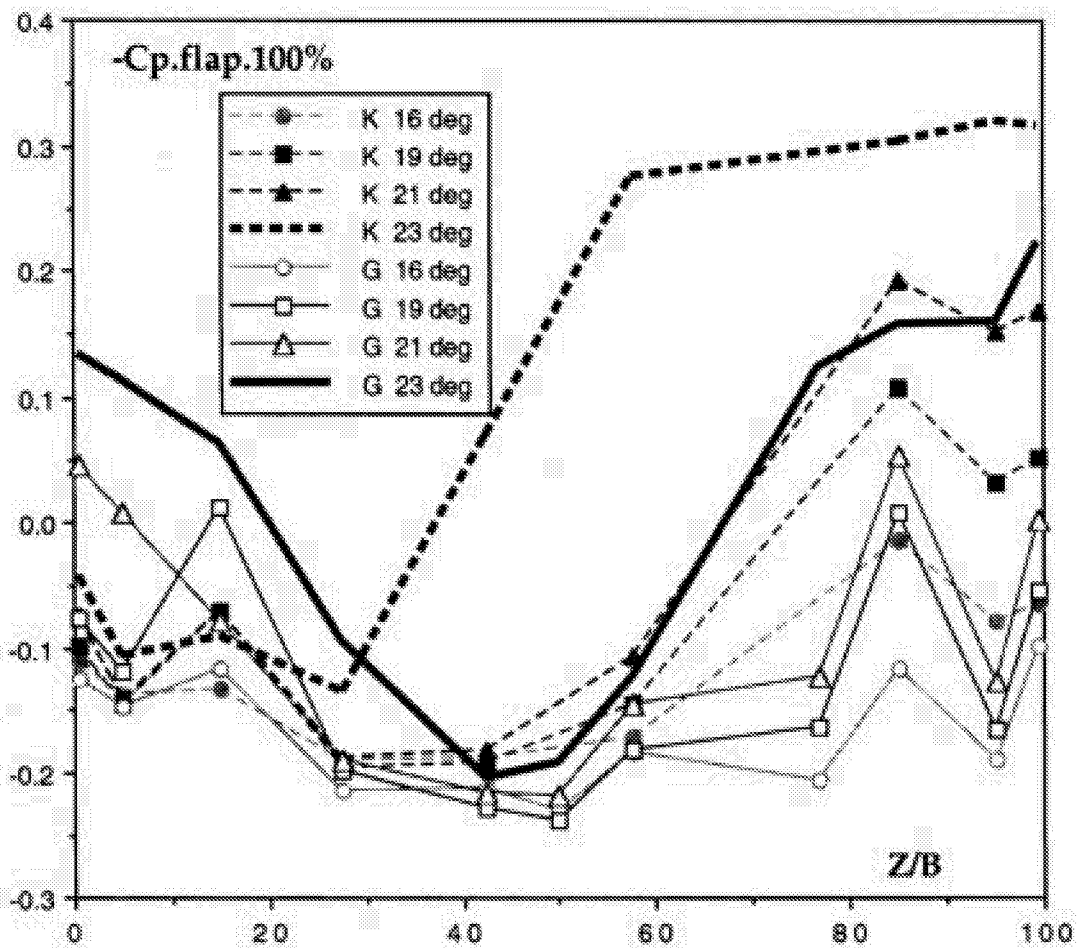


Figure A3.14d Spanwise pressure distribution, tests G and K - FLAP (Trailing edge) 30P/30N Mach=0.2, Re = 9 mill

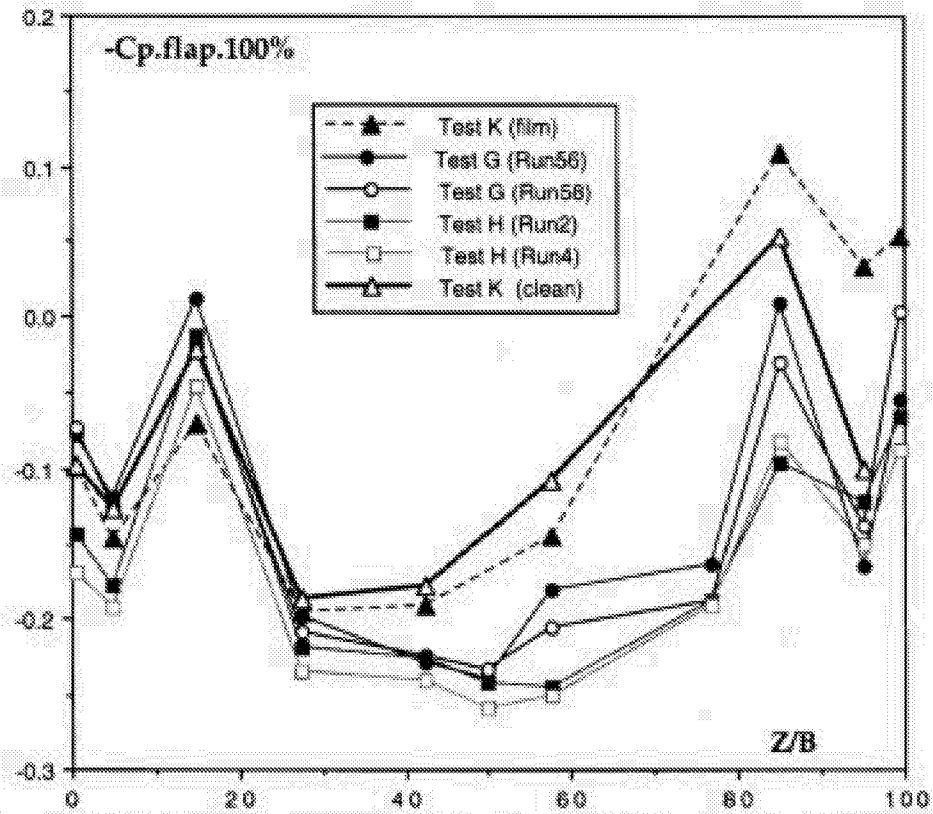


Figure A3.15 Spanwise pressure distribution, tests G,H and K including repeatability FLAP (Trailing edge). 30P/30N Mach=0.2, Re = 9 mill Alpha=19 deg

